

DESIGN AND ANALYSIS OF A LINEAR SHAPE MEMORY ALLOY
ACTUATOR

A THESIS SUBMITTED TO
THE GRADUATE SCHOOL OF NATURAL AND APPLIED SCIENCES
OF
MIDDLE EAST TECHNICAL UNIVERSITY

BY

BURCU SÖYLEMEZ

IN PARTIAL FULFILLMENT OF THE REQUIREMENTS
FOR
THE DEGREE OF DOCTOR OF PHILOSOPHY
IN
MECHANICAL ENGINEERING

JANUARY 2009

Approval of the thesis:

DESIGN AND ANALYSIS OF A LINEAR SHAPE MEMORY ALLOY ACTUATOR

submitted by **BURCU SÖYLEMEZ** in partial fulfillment of the requirements for the degree of **Doctor of Philosophy in Mechanical Engineering Department, Middle East Technical University** by,

Prof. Dr. Canan Özgen
Dean, Graduate School of **Natural and Applied Sciences**

Prof. Dr. Suha Oral
Head of Department, **Mechanical Engineering**

Prof. Dr. F.Suat Kadioğlu
Supervisor, **Mechanical Engineering Dept., METU**

Dr. Bülent Özkan
Co-Supervisor, **Mechatronics Division, TÜBİTAK-SAGE**

Examining Committee Members:

Prof. Dr. Tuna Balkan
Mechanical Engineering Dept., METU

Prof. Dr. F.Suat Kadioğlu
Mechanical Engineering Dept., METU

Prof. Dr. Şakir Bor
Metallurgical and Materials Engineering Dept., METU

Assoc. Prof.Dr. Buğra Koku
Mechanical Engineering Dept., METU

Prof. Dr. Yücel Ercan
Mechanical Engineering Dept., TOBB-ETU

Date: 21.01.2009

I hereby declare that all information in this document has been obtained and presented in accordance with academic rules and ethical conduct. I also declare that, as required by these rules and conduct, I have fully cited and referenced all material and results that are not original to this work.

Name, Last Name : Burcu Söylemez

Signature :

ABSTRACT

DESIGN AND ANALYSIS OF A LINEAR SHAPE MEMORY ALLOY ACTUATOR

Söylemez, Burcu

Ph. D., Department of Mechanical Engineering

Supervisor : Prof. Dr. F. Suat Kadiođlu

Co-Supervisor: Dr. Bülent Özkan

January 2009, 196 pages

Shape memory alloys are new, functional materials used in actuator applications with their high power to weight ratio. The high strength or displacement usage of shape memory alloys makes them suitable for direct drive applications, which eliminate use of power transmission elements.

The aim of this research is to develop the methodology and the necessary tools to design and produce linear shape memory alloy actuators to be used in missile systems, space applications, and test equipments.

In this study, the test apparatus designed and built to characterize shape memory alloy thin wires is described, and then the characterization tests, modeling and control studies performed on a wire are explained. In the control studies, displacement control through strain, resistance and power feedback is investigated and different control strategies (proportional-integral, proportional-integral with feedforward loop, and neural network) are employed. The results of the characterization tests, simulations and experiments are all presented in graphical and tabular form. From the results it is concluded that through careful characterization, the behavior of SMA wire can be closely approximated through models which can be used effectively to test various control strategies in

simulations. Also, satisfactory position control of SMA wires can be achieved through both classical and NN control strategies by using appropriate feedback variables and power is found to be a viable feedback variable.

Lastly, a linear SMA wire actuator is designed as a case study. The actuator prototype is produced, suitable control strategies are applied and actuator is experimented to validate the theoretical assumptions.

The actuator developed through this work is a technology demonstration and shows that shape memory alloy elements can be utilized in several defense and space applications contracted to TÜBİTAK-SAGE as well as certification test equipments. The development of shape memory alloy actuators that can be used in defense and later in aeronautical/space applications is a critical research and development project for national defense industry.

Keywords: Shape memory alloy, SMA, shape memory alloy actuator, shape memory alloy wire actuator, control, shape memory alloy wire characterization, strain feedback, resistance feedback, power feedback, neural network.

ÖZ

ŞEKİL BELLEKLİ ALAŞIMLAR KULLANILAN DOĞRUSAL BİR EYLEYİCİNİN TASARIM VE ANALİZİ

Söylemez, Burcu

Doktora, Makina Mühendisliği Bölümü

Tez Yöneticisi : Prof. Dr. F. Suat Kadiođlu

Ortak Tez Yöneticisi: Dr. Bülent Özkan

Ocak 2009, 196 sayfa

Şekil bellekli alaşımlar yüksek birim ağırlık başına düşen güç çıktısı oranlarıyla eyleyici uygulamalarında kullanılan yeni, işlevsel malzemelerdir. Şekil bellekli alaşımlar, yüksek kuvvet veya deplasman kullanımlarıyla doğrudan tahrik uygulamalarında, güç aktarım elemanlarına ihtiyaç bırakmadan kullanılmaya uygundurlar.

Bu araştırmanın amacı, füze sistemleri, uzay uygulamaları ve test ekipmanlarında kullanılmak üzere şekil bellekli alaşımlar ile eyleyici tasarım ve üretiminde izlenecek yol ve gerekli araçların geliştirilmesidir.

Bu çalışmada ince şekil bellekli tellerin karakterizasyonu için tasarlanmış ve üretilmiş test cihazı anlatılmış daha sonra bir tel üzerinde gerçekleştirilen karakterizasyon testleri, modelleme ve kontrol çalışmaları açıklanmıştır. Kontrol çalışmalarında gerinim, elektriksel direnç ve tüketilen güç geri besleme değişkenleri kullanılan değişik kontrol stratejileri (oransal-integral, ileri besleme takviyeli oransal-integral ve yapay sinir ağları) ile deplasman kontrolü gerçekleştirilmiştir. Karakterizasyon testlerinin, simülasyonların ve deneylerin sonuçları hem grafik hem de tablo halinde sunulmuştur. Bu sonuçlara göre, titiz bir karakterizasyon ile şekil bellekli alaşımlı tellerin davranışlarının değişik kontrol

stratejilerini simülasyonlarla test etmek üzere modellenebileceği gösterilmiştir. Ayrıca, uygun geri besleme değişkenleri ile şekil bellekli tellerin tatmin edici pozisyon kontrolünün hem klasik hem de yapay sinir ağları kullanılan kontrolcülerle sağlanabileceği ve tüketilen gücün uygun bir geri besleme değişkeni olduğu anlaşılmıştır.

Nihayet, örnek çalışma olarak şekil bellekli tel kullanılan doğrusal bir eyleyici tasarlanmıştır. Geliştirilen eyleyici üretilmiş, uygun kontrol stratejileri uygulanmış ve teorik öngörülerini doğrulamak amacıyla gerekli testler gerçekleştirilmiştir.

Bu çalışma sonucunda geliştirilen eyleyici ve yöntemler, esas itibarıyla bir teknoloji gösterimi olup, şekil bellekli alaşımların TÜBİTAK-SAGE kapsamında yürütülen çeşitli savunma sanayii ve uzay projeleriyle tasarlanan test ekipmanlarında kullanılabileceğini göstermektedir. Öncelikle savunma daha sonra havacılık ve uzay uygulamalarında kullanılacak şekil bellekli alaşım kullanılan eyleyicilerin geliştirilmesi ulusal savunma sanayii için kritik bir AR-GE yaklaşımıdır.

Anahtar Kelimeler: Şekil bellekli alaşım, ŞBA, şekil bellekli alaşım kullanılan eyleyici, şekil bellekli alaşım tel kullanılan eyleyici, kontrol, şekil bellekli alaşım tellerin karakterizasyonu, gerinim geribesleme, direnç geribesleme, güç geribesleme, yapay sinir ağı.

ACKNOWLEDGEMENTS

First, I would like to express my gratitude to my co-supervisor, friend and colleague Dr. Bülent ÖZKAN for his guidance, prompt feedbacks and endless patience. I am grateful to him.

I sincerely appreciate my supervisor Prof. Dr. F. Suat KADIOĞLU for his valuable comments and careful editing of the text.

My special thanks go to Mr. Evran ZİHNİOĞLU for his help during construction of the experimental set-up and Mr. Fatih YAŞAR for sharing his accumulated knowledge and experience on shape memory alloys.

Also, I would like to thank my colleagues and my friends Mr. G. Tuna TÜRKBEY, Dr. Erdinç N. YILDIZ, Dr. A. Serkan GÖZÜBÜYÜK and other friends in TÜBİTAK-SAGE for their friendship and help.

The support of TÜBİTAK-SAGE in this thesis especially in experimental studies is also acknowledged.

My greatest thanks go to my parents, Prof. Dr. Feride SÖYLEMEZ and Prof. Dr. Eres SÖYLEMEZ for their support, guidance and inspiration all through my life, my sister Başak SÖYLEMEZ who is always there for me and my loving husband Mete DÖNMEZ for his patience and support during hard times. I love them very much.

TABLE OF CONTENTS

ABSTRACT	iv
ÖZ.....	vi
ACKNOWLEDGEMENTS	viii
TABLE OF CONTENTS.....	ix
LIST OF TABLES	xiii
LIST OF FIGURES	xiv
LIST OF SYMBOLS.....	xxiii
LIST OF ABBREVIATIONS	xxv
CHAPTERS	
1. INTRODUCTION.....	1
1.1. Shape Memory Alloys	1
1.2. Review of Applications of Shape Memory Alloys	4
1.2.1. Free Recovery.....	5
1.2.2. Constrained Recovery.....	6
1.2.3. Actuators.....	6
1.2.4. Superelasticity.....	7
1.3. SMA-Based Actuators	7
1.3.1. Thermal Actuators.....	10
1.3.2. Electrical Actuators	11
1.4. Survey of Recent Patents Issued	12
1.4.1. Actuator Device with a Flexible Cable Incorporating a Shape Memory Element	13
1.4.2. Prolonged Life Shape Memory Alloy Actuator	14
1.4.3. Shape Memory Bi-Directional Rotary Actuator	16
1.5. SMA Actuators Used in Aerospace Applications	17
1.6. Scope of the Thesis.....	22
2. SHAPE MEMORY BEHAVIOR AND MODELING	25
2.1. Memory Effect	25
2.1.1. Phase Transformation.....	26
2.1.2. Martensite Re-Orientation	28
2.2. Thermomechanical Behavior	29

2.3. Material Selection.....	31
2.4. Training SMA Elements.....	32
2.5. Shape of the Active Element	33
2.6. Review of Shape Memory Alloy Models	36
2.6.1. Models with Assumed Phase Transformation Kinetics	38
2.7. Characterization of Shape Memory Alloy Wires.....	48
2.7.1. Parameters Required for Modeling.....	49
2.7.2. Characterization Tests	52
2.7.3. Description of the Test Apparatus	52
2.7.4. Test Procedure and Results.....	55
2.7.5. Estimation of Characteristic Parameters.....	60
2.7.6. Comparing Test Results with Theoretical Models.....	61
2.8. Modeling of Shape Memory Alloy Wires	62
2.8.1. Strain-Current Relation.....	64
2.8.2. Resistance-Current Relation	68
2.8.3. Power-Current Relation.....	72
3. POSITION CONTROL OF SHAPE MEMORY ALLOY WIRES.....	77
3.1. Overview of Control Methods Applied to SMA Actuators	77
3.2. Position Control of SMA Wires	80
3.3. Strain Feedback	81
3.3.1. P-Type Control.....	83
3.3.2. PI-Type Control.....	84
3.3.3. PI-Type Control with Feedforward Loop	86
3.3.4. Neural Network Narma-L2 Control	88
3.4. Resistance Feedback.....	94
3.4.1. P-Type Control.....	95
3.4.2. PI-Type Control.....	96
3.4.3. PI-Type Control with Feedforward Loop	97
3.4.4. Neural Network Narma-L2 Control	99
3.5. Power Feedback	100
3.5.1. P-Type Control.....	102
3.5.2. PI-Type Control.....	102
3.5.3. PI-Type Control with Feedforward Loop	103
3.5.4. Neural Network Narma-L2 Control	105
3.6. Strain-Resistance Relation	107

3.7. Strain-Power Relation	109
3.8. Validation of Control Schemes under Different Loads	111
3.8.1. Simulations with 90 MPa Stress	112
3.8.2. Simulations with 210 MPa Stress	115
4. EXPERIMENTS ON THE POSITION CONTROL OF SHAPE MEMORY ALLOY WIRES	119
4.1. Control Set-up	119
4.2. Strain Feedback	124
4.2.1. PI-Type Control	125
4.2.2. PI-Type Control with Feedforward Loop	126
4.2.3. Neural Network Narma-L2 Controller	127
4.3. Resistance Feedback	130
4.3.1. PI-Type Control	131
4.3.2. PI-Type Control with Feedforward Loop	132
4.3.3. Neural Network Narma L2 Controller	134
4.4. Power Feedback	136
4.4.1. PI-Type Control	136
4.4.2. PI-Type Control with Feedforward Loop	138
4.4.3. Neural Network Narma L2 Controller	139
4.5. Strain- Resistance Relation	141
4.6. Strain- Power Relation	143
4.7. Validation of Control Schemes under Different Loads	144
4.7.1. Tests with 90 MPa Stress	144
4.7.2. Tests with 210 MPa Stress	150
4.7.3. Tests Against a Spring	155
5. DESIGN AND EXPERIMENTAL INVESTIGATION OF A LINEAR SHAPE MEMORY ALLOY ACTUATOR	163
5.1. Actuator Design	163
5.1.1. Conceptual Design	163
5.1.2. Mechanical Design	164
5.2. Actuator Test-Bed	165
5.3. Control Experiments on the Actuator	167
5.3.1. Strain Feedback	169
5.3.2. Resistance Feedback	170
5.3.3. Power Feedback	172

6. DISCUSSION AND CONCLUSION.....	176
6.1. Summary and Conclusions.....	176
6.2. Design Methodology for SMA Wire Actuators.....	180
6.3. Future Work	182
REFERENCES.....	183
APPENDIX A: POLYNOMIALS THAT CAN BE USED IN POLE PLACEMENT.....	
.....	189
CURRICULUM VITAE.....	194

LIST OF TABLES

TABLES

Table 1. Comparison of properties of Ni-Ti and Cu-Zn-Al [4]	4
Table 2. Main properties of typical SMAs [39]	32
Table 3. Classification of SMA elements	34
Table 4. Comparison of load cases for SMA actuators [42]	35
Table 5. Properties of the selected wire [43].....	36
Table 6. Constants needed to be characterized for corresponding models.....	49
Table 7. Instruments used in the test apparatus	54
Table 8. Instruments used in the experiments	120
Table 9. Comparison of experimental results of strain control methods.....	129
Table 10. Comparison of experimental results of resistance control methods .	135
Table 11. Comparison of experimental results of power control methods	140

LIST OF FIGURES

FIGURES

Figure 1. Schematic representation of SME and superelasticity [3]	2
Figure 2. Schematic representation of hysteresis loop [2]	3
Figure 3. Shape memory events in the stress/strain perspective [3].....	5
Figure 4. SMA coupling [4]	6
Figure 5. Power/weight ratio vs. weight diagram of different actuators [14].	8
Figure 6. Opposing constant force.....	9
Figure 7. Opposing spring	9
Figure 8. Two one-way SMAs	10
Figure 9. Early shape-memory alloy engine [16].....	11
Figure 10. Linear motion SMA actuator [17]	12
Figure 11. SMA rotary actuator [18].....	12
Figure 12. Shape memory alloy actuator device.....	13
Figure 13. Detailed figure of shape memory alloy actuator device.....	14
Figure 14. Figure of prolonged life shape memory alloy actuator	15
Figure 15. Figure of shape memory bi-directional rotary actuator.....	17
Figure 16. Various SMA Pin Pullers by TiNi Aerospace Inc.[21]	18
Figure 17. Deployable antenna actuated by shape memory alloy hinge [24]	19
Figure 18. Representative drawings of conventional flap control and smart wing (DARPA) [28]	20
Figure 19. Variable area exhaust nozzle [29]	21
Figure 20. Tracking of helicopter rotor blades [30].....	22
Figure 21. Shape memory alloy behavior [32]	26
Figure 22. Idealized hysteresis curves for SME (fixed load) and super elasticity (fixed temperature) [34]	28
Figure 23: Stress- Strain curves of SMAs in (a) full martensite and (b) full martensite to full austenite [36].....	30
Figure 24. Work extraction from SMAs	30
Figure 25. Strain-temperature characteristics at constant stress levels [38]	31
Figure 26. Stress- transformation temperature plot [37].....	41
Figure 27. Exponential function phase transformation model by Tanaka.....	42

Figure 28. Cosine function phase transformation model by Liang and Rogers'	.44
Figure 29. Modified stress-transformation temperature plot [51]	46
Figure 30. Schematic DSC plot [2]	50
Figure 31. Transformation temperatures vs. stress plot (Tanaka's and Liang and Rogers' Models) [37]	51
Figure 32. Transformation temperatures versus stress plot (Brinson's Model) [51]	51
Figure 33. Schematic view of the characterization test bench	53
Figure 34. SMA characterization test bench	54
Figure 35. Circuit design of the set-up	55
Figure 36. Current profile supplied for characterization	56
Figure 37. Temperature profile of the wire	56
Figure 38. Strain-temperature results of the experiments under various stress levels	57
Figure 39. Strain-current results of the experiments under various stress levels	57
Figure 40. Hysteresis width-stress plot	58
Figure 41. Resistance-temperature results of the experiments under various stress levels	59
Figure 42. Resistance-current results of the experiments under various stress levels	59
Figure 43. Map of characterization on stress-strain diagram	60
Figure 44. Variation of transformation temperatures with the applied loads	61
Figure 45. Strain-temperature plot under 90 MPa stress	61
Figure 46. Strain-temperature plot under 140 MPa stress	62
Figure 47. Strain-current model	65
Figure 48. Experiment and model results for strain model with ramp input	65
Figure 49. Experiment and simulation results of strain of SMA wire to step current input	66
Figure 50. Block diagram for frequency response analysis of strain model	67
Figure 51. Current supplied to the model	67
Figure 52. Bode Plot for strain model	68
Figure 53. Resistance-current model	69
Figure 54. Experiment and model results for resistance with ramp input	70
Figure 55. Experiment and simulation results of SMA resistance model with step input	71

Figure 56. Block diagram for frequency response analysis of resistance model	71
Figure 57. Bode Plot for resistance model.....	72
Figure 58. Power-current model.....	73
Figure 59. Experiment and model results for power of the wire using ramp input	74
Figure 60. Experiment and simulation results of power of SMA wire to step current input.....	74
Figure 61. Block diagram for frequency response analysis of power model.....	75
Figure 62. Bode Plot for power model.....	76
Figure 63. Resistance versus martensite fraction.....	78
Figure 64. Linear strain model.....	82
Figure 65. General block diagram of the strain control system.....	82
Figure 66. Strain command-model response using PI controller ($K_p=300$ and $K_i=55$).....	85
Figure 67. Strain command-model response using PI controller ($K_p=300$ and $K_i=110$).....	86
Figure 68. Inverse strain-current model.....	86
Figure 69. PI-type control with feedforward loop.....	87
Figure 70. Strain command and model response using PI controller with feedforward loop ($K_p=300$, $K_i=55$, and $K=0.8$).....	87
Figure 71. Strain command and model response using PI controller with feedforward loop ($K_p=300$, $K_i=110$, and $K=0.8$).....	88
Figure 72. Structure of a neural network representation [68].....	90
Figure 73. Block diagram of the NARMA-L2 controller [68].....	91
Figure 74. Performance index with respect to number of hidden layers (strain feedback).....	92
Figure 75. Performance index with respect to number of maximum iterations (strain feedback).....	93
Figure 76. Block diagram of the system with Narma L2 controller.....	93
Figure 77. Strain command and model response using Narma-L2 controller.....	93
Figure 78. Linear resistance model.....	94
Figure 79. General block diagram of the resistance control system.....	94
Figure 80. Resistance command and model response using PI controller ($K_p=300$ and $K_i=35$).....	96

Figure 81. Resistance command and model response using PI controller ($K_p=300$ and $K_i=70$)	97
Figure 82. Inverse resistance-current model	97
Figure 83. PI-type control with feedforward loop.....	98
Figure 84. Resistance command and model response using PI controller with feedforward loop	98
Figure 85. Block diagram of the system with Narma L2 controller with resistance f/b.....	99
Figure 86. Performance index with respect to number of hidden layers (resistance f/b)	99
Figure 87. Performance index with respect to number of maximum iterations (resistance f/b)	100
Figure 88. Resistance command and model response using Narma L2 controller	100
Figure 89. Linear power model.....	101
Figure 90. General block diagram of the power feedback control system.....	101
Figure 91. Power command and model response using PI controller ($K_p=100$ and $K_i=49$).....	103
Figure 92. Power command and model response using PI controller ($K_p=100$ and $K_i=99$).....	103
Figure 93. Inverse power-current model.....	104
Figure 94. PI-type control with feedforward loop.....	104
Figure 95. Power command and model response using PI controller with feedforward loop	105
Figure 96. Block diagram of the system with Narma L2 controller	105
Figure 97. Performance index with respect to number of hidden layers (power f/b).....	106
Figure 98. Performance index with respect to number of maximum iterations (power f/b).....	106
Figure 99. Power command and model response using Narma L2 controller ..	107
Figure 100. Resistance-strain relation	108
Figure 101. Block diagram of resistance control using strain input	108
Figure 102. Resistance response using strain input	109
Figure 103. Strain response of resistance control using strain input.....	109
Figure 104. Strain-power relation	110

Figure 105. Block diagram of power control using strain input.....	110
Figure 106. Power response using strain input.....	111
Figure 107. Strain response using power control with strain input.....	111
Figure 108. Strain model with 90 MPa stress	112
Figure 109. Strain response with 90 MPa stress	112
Figure 110. Resistance model with 90 MPa stress	113
Figure 111. Resistance response with 90 MPa stress	113
Figure 112. Power model with 90 MPa stress.....	114
Figure 113. Power response with 90 MPa stress.....	115
Figure 114. Strain model with 210 MPa stress	115
Figure 115. Strain response with 210 MPa stress	116
Figure 116. Resistance model with 210 MPa stress	117
Figure 117. Resistance response with 210 MPa stress	117
Figure 118. Power model with 210 MPa stress.....	118
Figure 119. Power response with 210 MPa stress.....	118
Figure 120. Conceptual circuit diagram for the experiment set-up.....	120
Figure 121. Current versus control signal voltage plot and linear fit.....	121
Figure 122. PSDs of raw strain, voltage, and current data.....	122
Figure 123. Raw and filtered data for 10 mA and 100 mA constant current	123
Figure 124. Simulink model for strain feedback control system	125
Figure 125. Simulink model for PI-type controller for strain feedback	125
Figure 126. Strain feedback with PI control ($K_p=300$ and $K_i=55$).....	126
Figure 127. Strain feedback with PI control ($K_p=300$ and $K_i=110$).....	126
Figure 128. Simulink model for PI-type control with feedforward loop for strain feedback	127
Figure 129. Strain feedback with PI control with feedforward loop ($K_p=300$ and $K_i=55$).....	127
Figure 130. Simulink model for Neural network Narma-L2 control for strain feedback	128
Figure 131. Strain feedback with NN Narma-L2 control.....	128
Figure 132. Simulink model for resistance feedback control system.....	130
Figure 133. Simulink model for PI-type controller for resistance feedback.....	131
Figure 134. Resistance feedback with PI control ($K_p=300$ and $K_i=35$)	131
Figure 135. Resistance feedback with PI control ($K_p=300$ and $K_i=70$)	132

Figure 136. Simulink model for PI-type control with feedforward loop for resistance feedback	133
Figure 137. Resistance feedback with PI control with feedforward loop ($K_p=300$, $K_i=35$, $K=0.8$)	133
Figure 138. Resistance feedback with NN Narma-L2 control.....	134
Figure 139. Simulink model for power feedback control system	136
Figure 140. Simulink model for PI-type controller for power feedback	137
Figure 141. Power feedback with PI control ($K_p=100$ and $K_i=49$).....	137
Figure 142. Power feedback with PI control ($K_p=100$ and $K_i=99$).....	137
Figure 143. Simulink model for PI-type control with feedforward loop for power feedback	138
Figure 144. Power feedback with PI control with feedforward loop ($K_p=100$ and $K_i=49$).....	138
Figure 145. Power feedback with NN Narma-L2 control	139
Figure 146. The Simulink model for strain control through resistance feedback	141
Figure 147. Strain command and response using resistance feedback with PI control ($K_p=300$ and $K_i=70$)	142
Figure 148. Resistance command and response using resistance feedback with PI control ($K_p=300$ and $K_i=70$)	142
Figure 149. The Simulink model for strain control through power feedback.....	143
Figure 150. Strain command and response using power feedback with PI control ($K_p=100$ and $K_i=99$)	143
Figure 151. Power command and response using power feedback with PI control ($K_p=100$ and $K_i=99$)	144
Figure 152. Strain feedback control with PI controller ($K_p=300$ and $K_i=55$) under 90 MPa stress	145
Figure 153. Strain feedback control with PI controller with feedforward loop ($K_p=300$, $K_i=55$, and $K=0.8$) under 90 MPa stress	145
Figure 154. Strain feedback control with NN-Narma L2 controller under 90 MPa stress	146
Figure 155. Resistance feedback control with PI controller ($K_p=300$ and $K_i=35$) under 90 MPa stress	147
Figure 156. Resistance feedback control with PI controller with feedforward loop ($K_p=300$, $K_i=35$, and $K=0.8$) under 90 MPa stress	147

Figure 157. Resistance feedback control with NN-Narma L2 controller under 90 MPa stress	148
Figure 158. Power feedback control with PI controller ($K_p=100$ and $K_i=99$) under 90 MPa stress	149
Figure 159. Power feedback control with PI controller with feedforward loop ($K_p=100$, $K_i=99$, and $K=0.8$) under 90 MPa stress	149
Figure 160. Power feedback control with NN-Narma L2 controller under 90 MPa stress	150
Figure 161. Strain feedback control with PI controller ($K_p=300$ and $K_i=55$) under 210 MPa stress	151
Figure 162. Strain feedback control with PI controller with feedforward loop ($K_p=300$, $K_i=55$, and $K=0.8$) under 210 MPa stress	151
Figure 163. Strain feedback control with NN-Narma L2 controller under 210 MPa stress	152
Figure 164. Resistance feedback control with PI controller ($K_p=300$ and $K_i=35$) under 210 MPa stress	152
Figure 165. Resistance feedback control with PI controller with feedforward loop ($K_p=300$, $K_i=35$, and $K=0.8$) under 210 MPa stress	153
Figure 166. Resistance feedback control with NN-Narma L2 controller under 210 MPa stress	153
Figure 167. Power feedback control with PI controller ($K_p=100$ and $K_i=99$) under 210 MPa stress	154
Figure 168. Power feedback control with PI controller with feedforward loop ($K_p=100$, $K_i=99$, and $K=0.8$) under 210 MPa stress	154
Figure 169. Power feedback control with NN-Narma L2 controller under 210 MPa stress	155
Figure 170. Strain-current curve of the wire working against the spring.....	156
Figure 171. Resistance-current curve of the wire working against the spring ..	156
Figure 172. Power-current curve of the wire working against the spring	157
Figure 173. Strain feedback control with PI controller ($K_p=300$ and $K_i=55$) against spring	158
Figure 174. Strain feedback control with PI controller with feedforward loop ($K_p=300$ and $K_i=55$) against spring	158
Figure 175. Strain feedback control with NN Narma-L2 controller against spring	159

Figure 176. Resistance feedback control with PI controller ($K_p=300$ and $K_i=35$) against spring.....	159
Figure 177. Resistance feedback control with PI controller with feedforward loop ($K_p=300$, $K_i=35$, and $K=0.8$) against spring.....	160
Figure 178. Resistance feedback control with NN Narma-L2 controller against spring.....	160
Figure 179. Power feedback control with PI controller ($K_p=100$ and $K_i=99$) against spring.....	161
Figure 180. Power feedback control with PI controller with feedforward loop ($K_p=100$, $K_i=99$, and $K=0.8$) against spring.....	161
Figure 181. Power feedback control with NN Narma-L2 controller against spring.....	162
Figure 182. 2-D Layout of the actuator.....	164
Figure 183. 3-D views of the actuator.....	165
Figure 184. SMA linear actuator.....	165
Figure 185. Actuator test-bed rear view.....	166
Figure 186. Actuator test-bed front view.....	166
Figure 187. Displacement characteristic of the actuator.....	167
Figure 188. Strain curve of the actuator.....	167
Figure 189. Resistance curve of the actuator.....	168
Figure 190. Power consumption curve of the actuator.....	168
Figure 191. Strain feedback control of the actuator with PI controller ($K_p=300$ and $K_i=55$).....	169
Figure 192. Strain feedback control of the actuator with PI controller ($K_p=300$ and $K_i=110$).....	169
Figure 193. Strain feedback control of the actuator with PI controller with feedforward loop ($K_p=300$, $K_i=55$ and $K=0.8$).....	170
Figure 194. Strain feedback control of the actuator with NN Narma-L2 controller.....	170
Figure 195. Resistance feedback control of the actuator with PI controller ($K_p=300$ and $K_i=35$).....	171
Figure 196. Resistance feedback control of the actuator with PI controller ($K_p=300$ and $K_i=70$).....	171
Figure 197. Resistance feedback control of the actuator with PI controller with feedforward loop ($K_p=300$, $K_i=35$, and $K=0.8$).....	172

Figure 198. Resistance feedback control of the actuator with NN Narma-L2 controller	172
Figure 199. Power feedback control of the actuator with PI controller ($K_p=100$ and $K_i=49$).....	173
Figure 200. Power feedback control of the actuator with PI controller ($K_p=100$ and $K_i=99$).....	173
Figure 201. Power feedback control of the actuator with PI controller with feedforward loop ($K_p=100$, $K_i=49$, and $K=0.8$).....	174
Figure 202. Power feedback control of the actuator with NN Narma-L2 controller	174
Figure 203. Strain feedback control simulation and experiment result, PI type control	177
Figure 204. Resistance feedback control simulation and experiment result, PI type control with feedforward loop	178
Figure 205. Power feedback control simulation and experiment result, NN controller	178
Figure 206. Power to weight ratios of common actuators	179

LIST OF SYMBOLS

A_f	: Austenite finish temperature
A_s	: Austenite start temperature
C	: Current
E_a	: Austenitic elastic modulus
E_m	: Martensitic elastic modulus
ε	: Strain
ε_d	: Desired strain
ε_e	: Strain error
ε_L	: Maximum recoverable strain
ε_m	: Measured strain
G_c	: Controller transfer function
G_s	: Closed loop system transfer function
I	: Current
K	: Feedforward gain
K_i	: Integral gain
K_p	: Proportional gain
M_f	: Martensite finish temperature
M_s	: Martensite start temperature
P	: Dissipated power per unit length
P_d	: Desired power dissipation per unit length
P_e	: Error in power dissipation per unit length
P_m	: Measured power dissipation per unit length
R	: Resistance per unit length

- R_d : Desired resistance per unit length
- R_e : Error in resistance per unit length
- R_m : Measured resistance per unit length
- R_{max} : Maximum resistance per unit length
- R_{min} : Minimum resistance per unit length
- T : Temperature
- W : Weight
- ω_c : Bandwidth frequency

LIST OF ABBREVIATIONS

DSC	:	Differential Scanning Calorimetry
FF	:	Feed forward
LVDT	:	Linear Variable Displacement Transducer
Ni-Ti	:	Nickel-Titanium
NN	:	Neural Network
P	:	Proportional
PI	:	Proportional-Integral
PID	:	Proportional-Integral-Derivative
PSD	:	Power Spectral Density
SMA	:	Shape Memory Alloy
SME	:	Shape Memory Effect
SS	:	Steady State
TDL	:	Tapped Delay Line

CHAPTER 1

INTRODUCTION

The trend towards miniaturization of control and robotic systems requires a decrease in size and weight of their components. One of the important elements of these systems is the actuators which are generally electrical, hydraulic or pneumatic. The power outputs of electrical, hydraulic, and pneumatic systems are drastically reduced with the reduction in their size and weight. The problem of scaling down brings novel technologies such as piezoelectric materials, polymer gels, magneto-restrictive fluids, and shape memory alloys to attention. Of all these technologies, shape memory alloys are among the most advantageous in actuator applications with their high power to weight ratio.

Shape memory alloys are easily adapted to miniaturization in design with their silent, smooth and lifelike motions eliminating the need for power transmission elements. As shape memory alloy manufacturing techniques improve and design objectives become more severe, they will find increasing use in almost all engineering domains.

1.1. Shape Memory Alloys

The term “Shape Memory” refers to ability of certain materials to “remember” a shape, even after rather severe deformations: once deformed at low temperatures, these materials will stay deformed until heated, whereupon they will return to their original, pre-deformed “learned” shape. This unique effect of returning to an original geometry after a large inelastic deformation (near 8%) is known as the Shape Memory Effect (SME) [1]. The same materials have another unique property called “super elasticity” at a higher temperature, which is associated with a large (near 18%) nonlinear recoverable strain upon loading and unloading [2].

Shape memory phenomenon results from crystalline phase change known as “thermoelastic martensitic transformation”. At temperatures below transformation temperature, shape memory alloys are martensitic. In this condition, their microstructure is characterized by “self-accommodating twins”. The martensite is soft and can easily be deformed by de-twinning (Figure 1). Heating above the transformation temperature recovers the original shape and converts the material to its high strength, austenitic condition. If a stress is applied to a shape memory alloy in temperature range between austenite finish temperature and a maximum temperature, martensite can be stress-induced. As austenite is the thermodynamically stable phase at this temperature under no load conditions, the material springs back into its original shape when the stress is no longer applied. This phenomenon is known as “pseudoelasticity” or “transformational superelasticity” [2].

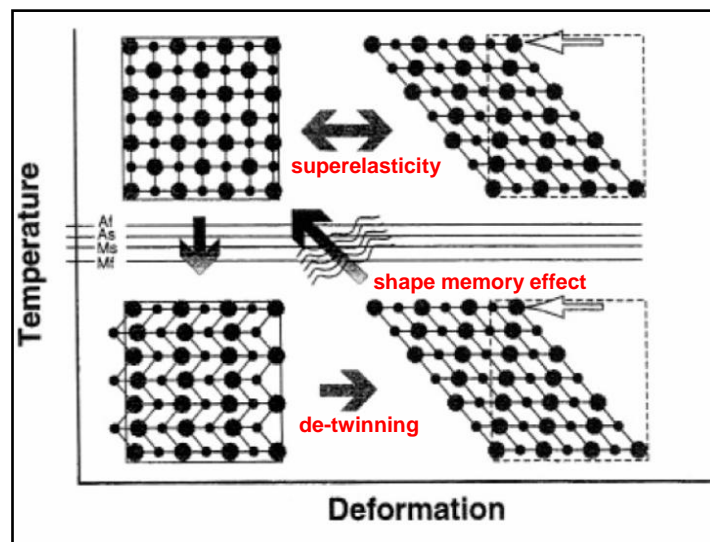


Figure 1. Schematic representation of SME and superelasticity [3]

The complete transformation cycle is characterized by the following temperatures: austenite start temperature (A_s), austenite finish temperature (A_f), martensite start temperature (M_s), and martensite finish temperature (M_f). A plot of volume fraction of martensite as a function of temperature provides a curve of type shown schematically in Figure 2.

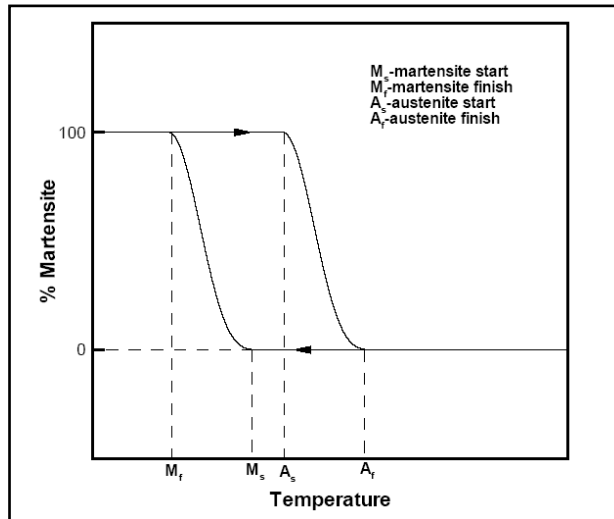


Figure 2. Schematic representation of hysteresis loop [2]

The shape memory effect was first observed in 1932 by a Swedish physicist Arne Olander in a gold-cadmium alloy. Chang and Read used gold-cadmium alloy to lift weight in 1958 at the Brussels World's Fair. In 1961, at the U.S. Naval Ordnance Laboratory, William Beuhler discovered the shape memory behavior of nickel-titanium (Ni-Ti) alloy. The Ni-Ti alloy proved to be both cost-effective and non-toxic. The name derived for Ni-Ti discovered in Naval Ordnance Laboratory, "NITINOL" later became a commercially recognized name for this family of alloys.

The transformation temperatures of shape memory alloys can be adjusted through changes in composition. Nickel-titanium and copper-zinc-aluminum (Cu-Zn-Al) alloys show transformation temperatures between -100°C and $+100^{\circ}\text{C}$, but a difference of less than 1 % in the composition can change the transformation temperatures by as much as 150°C . Copper-aluminum-nickel (Cu-Al-Ni) alloys show transformation temperature up to 200°C , however these alloys are unstable in cyclic applications [1]. A simple comparison of some properties of commonly used alloys that exhibit shape memory behavior is given in Table 1. Due to superior properties of Ni-Ti alloys in many aspects research, production and application efforts are generally directed towards this alloy.

Table 1. Comparison of properties of Ni-Ti and Cu-Zn-Al [4]

	Ni-Ti	Cu-Zn-Al
Recovery Strain	8 %	4 %
Recovery Stress	500 MPa	200 MPa
Number of Cycles	10 ⁵	10 ²
Corrosion Resistance	Good	Problematic
Machinability	Poor	Fair

Through 1970's the potential use of shape memory effect was recognized and a variety of SMA implemented products were realized [2]. In 1971, Sawyer used Ni-Ti to activate an artificial heart. Delta Metal Company used shape memory alloys both as thermal sensors and actuators.

In 1982, Sharp employed SMA actuators in electric oven dampers, and in 1983, Matsushita Electric used SMAs as actuators for louvers in the air conditioners.

Research on the modeling, application, and control of shape memory alloys has continued and expanded through the present.

1.2. Review of Applications of Shape Memory Alloys

Throughout the time, researchers, designers, and companies recognized the potential to use the SMAs in engineering applications.

Shape memory alloys acted as connecting elements, actuators, sensors, and other means in a variety of electronic, mechanical, hydraulic, thermal, and medical applications [5].

Shape memory alloy applications are grouped in four main categories according to their primary function in the application; those categories are free recovery, constrained recovery, actuators, and superelasticity. The stress-strain graphs of the shape memory events which are three of the above mentioned categories; free recovery, constrained recovery, and actuators are shown in Figure 3.

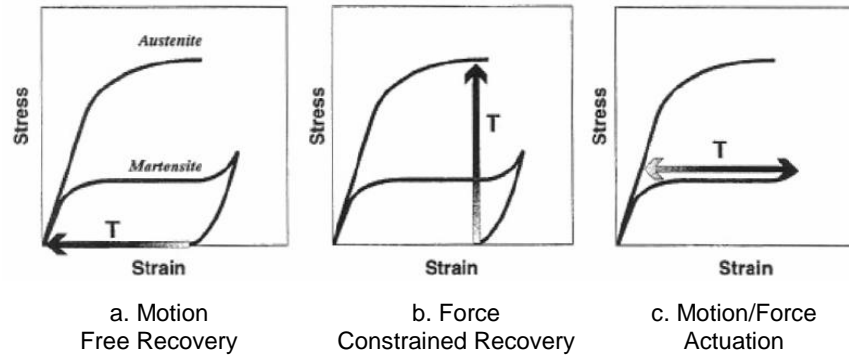


Figure 3. Shape memory events in the stress/strain perspective [3]

The stress-strain graphs given above can be explained by considering a straight SMA wire fixed at one end. Stretching it at room temperature generates elongation after unloading (martensitic phase). The wire remains in the stretched condition until it is heated above transformation temperature of this particular alloy. If no load is applied, heating will cause transformation to austenitic phase without any stress residue thus it will shrink to its original length; this is called free recovery, Figure 3 (a). Subsequent cooling below transformation temperature (to martensitic phase) does not cause a macroscopic shape change.

If, after stretching at room temperature, the wire is prevented from returning to its original length (in martensitic phase), i.e. if constrained to the extended length upon heating above transformation temperature (transformation to austenitic phase); it can generate a considerable force. This is called constrained recovery, Figure 3 (b).

If the opposing force can be overcome by the shape memory wire upon heating, it will generate motion against a force, and thus do work. This event is actuation using SMA, Figure 3 (c). Upon heating the wire will contract and lift a load, for instance. Actuation using SMAs will be discussed in detail in the following sections.

1.2.1. Free Recovery

This group of applications employs SMAs to cause motion or strain. Examples for these applications include free deployment mechanisms and deployable structures where shape memory alloy is used to maintain the original shape even after deformation with the simple application of heat.

1.2.2. Constrained Recovery

Constrained recovery includes applications in which the SMA is prevented from changing shape and thereby generates stress (Figure 4).

The first large scale application of SMAs in 1971 was as a coupling to connect hydraulic tubing in F-14 aircraft. SMAs were used in defense industry as electrical connectors and fasteners such as rivets, clamps and seals, etc. [6].

Ni-Ti SMA couplings are reliable joints for demanding applications; however copper and iron based couplings are preferred for their low cost despite their lower performance.

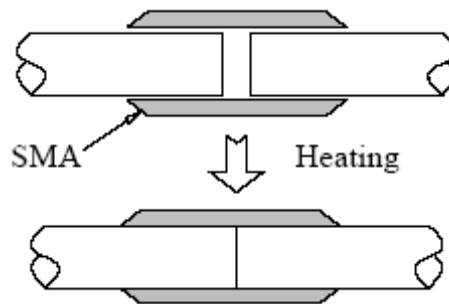


Figure 4. SMA coupling [4]

1.2.3. Actuators

Actuators employing shape memory alloys can be classified into two groups: those driven by the changes in the ambient temperature and those driven electrically. Thermal actuators are in competition with thermal bimetals, whereas electrical actuators compete with servo motors, solenoids, linear motors, etc.

SMA actuators are also used in micro-electro-mechanical (MEM) devices, static and dynamic structural control (external to a structure or embedded within the structure) for active vibration and shape control.

The more advanced applications of the SMA actuators are observed in passive/active control systems [7], [8], smart/adaptive structures [9], and composite structures [10]. It has been shown that the natural frequency of a cantilever beam with a SMA spring support at one end can be significantly changed by changing the stiffness of SMA spring when it is heated. Hybrid

composite embedded with SMA fibers can be used for vibration control and shape control by using the distributed force applied by SMA fibers. SMA based actuators will be discussed in detail in the following sections.

1.2.4. Superelasticity

The property of superelasticity of shape memory alloys has generally been used in medical applications. Orthodontic arch wires, stents, retractable spatulas, and hingeless instruments can be given as examples of medical applications.

Another application of superelastic behavior is in passive vibration control through SMA dampers [11] and isolators [12] due to SMAs' high internal friction. Aiken et al., [13] have suggested using SMA as passive energy dissipater to increase the hysteresis damping in structure under earthquake.

1.3. SMA-Based Actuators

Shape memory actuators are used where a large force or large stroke is required and thermodynamic efficiency is not essential. The reason for using shape-memory alloys as actuators is that a large amount of work can be obtained from a small volume of material. Repeated cycling at approximately 5 percent strain and more than 200 MPa stress produces more than a Joule of work output per cycle, among the highest work densities (the amount of work output per unit weight of the actuating element) known (Figure 5).

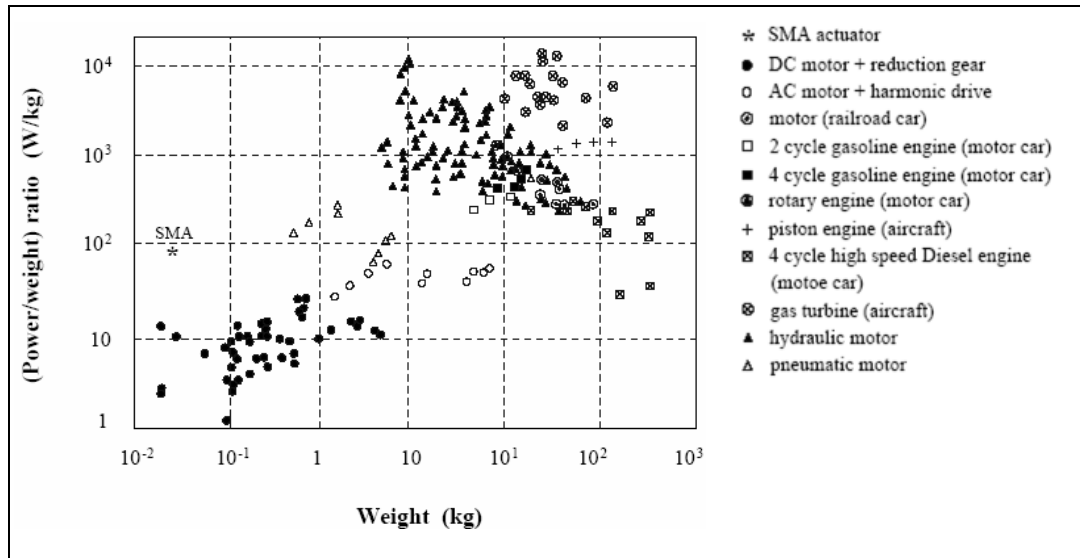


Figure 5. Power/weight ratio vs. weight diagram of different actuators [14].

SMA elements can either be trained to remember only high temperature austenite shape, one-way SMA; or both low and high temperature shapes, two-way SMA. The phase transformation strain of two-way SMAs is significantly less and their stability and repeatability are uncertain [15].

Both one-way and two-way SMA elements may be used for actuator applications. Although two-way SMA can perform in two directions, however its transformation strain is normally only half of that in one-way SMA and the actuation cycle may not always be accurately repeated. Instead of two-way shape memory alloys, two one-way shape memory alloy elements are arranged to work in bias to obtain the same actuation.

Actuators employing one-way SMA elements should be reset using a biasing mechanism or a resetting force to complete the work cycle. Different force/displacement characteristics may be obtained by changing the kind of the biasing mechanism used in the actuator. Three basic types of SMA actuators using only one-way SMA elements are given in the following paragraphs.

In the first type, the dead weight of a load or any other external force causes the SMA wire to elongate in martensitic phase, upon heating, the load is raised by the constant force which is its weight or the opposing force (Figure 6). Upon cooling, the weight or the force causes the wire to stretch back. Actuators using gravity or a constant reaction as a resetting force give a horizontal force/displacement characteristic.

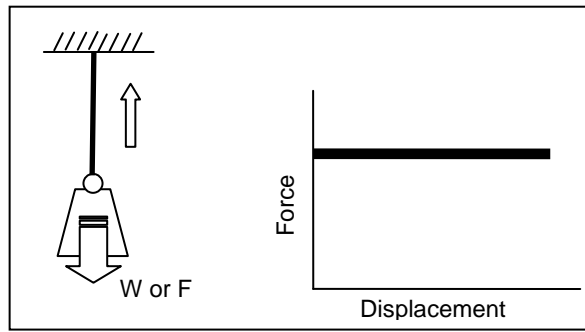


Figure 6. Opposing constant force

The second kind of biasing mechanism is the spring, in which the shape memory alloy works against a spring, when the SMA element is heated the spring is stretched, storing energy upon cooling the energy stored in the spring is released and the SMA element deforms back, to the original deflection thus completing the cycle (Figure 7). The slope in the force displacement line simply represents the spring rate. However, this application is not recommended in terms of life of the SMA since the opposing force increases as the SMA goes through transformation.

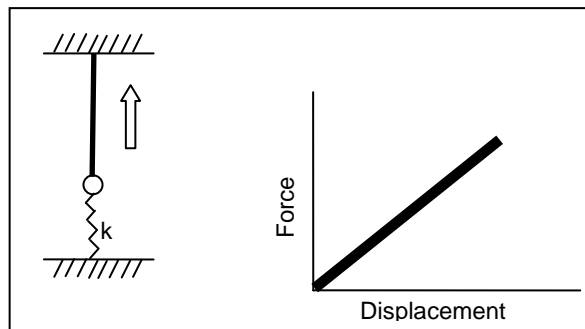


Figure 7. Opposing spring

As described above, two one-way SMA elements can be arranged to work against each other as the third method. While one of the wires is heated, thus contracted doing work, the other one is elongated (Figure 8). Upon heating the next wire, the motion is reversed, thus the work cycle is completed.

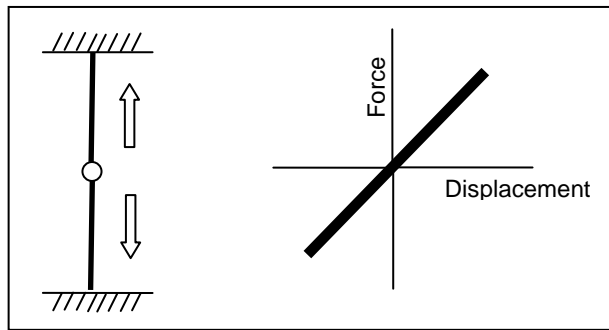


Figure 8. Two one-way SMAs

Another classification of SMA actuators can be made according to their heating methods. Shape memory based actuators can either be driven by thermal changes or by electrical means. The two actuation types are very much different from design point of view, so a brief literature survey on both kinds will be presented in the following sections.

1.3.1. Thermal Actuators

Heating an SMA element by thermal changes can be achieved by passing an electrical current through a high resistance wire or tape wrapped around the SMA element as an active thermal method or by exposing the SMA component to thermal radiation, which is a passive method. In the latter method no additional heating system is required; however, this method is inflexible, and it could be very difficult to actuate the device.

The first known thermal actuator was greenhouse window opener which used a Cu-Zn-Al spring to adjust the internal temperature of a green house. Other thermal actuators include air conditioning louvers that deflect air up or down depending upon its temperature; SMA springs used to control the shifting of automatic automobile transmissions and to compensate for changes in the ambient temperature; an SMA element in the coffee maker controlling brewing temperature; an SMA spring in an anti-scald device shutting off hot water when it becomes too hot or an SMA element being used as a circuit breaker.

Another example of this type worth mentioning is heat engines [16]. SMA elements made it easy to convert heat to mechanical energy where significant sources of waste heat are available. Several inventors produced working heat engines employing SMAs. Figure 9 shows one of these inventions. These

engines had low efficiency, but high power density (power delivered by the actuator per unit weight of the actuating element). The engines required delivering hundreds of kilowatts in practical, but this proved to be much more difficult than it was anticipated. Scale-up stopped at about one kilowatt: it failed for engineering and economic reasons. Large masses of metal must be rapidly cycled to achieve high power, requiring accurate control of flows, temperatures, large forces, and friction.

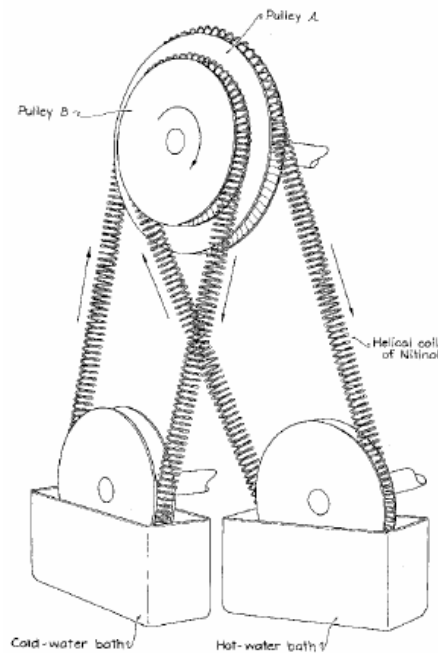


Figure 9. Early shape-memory alloy engine [16]

1.3.2. Electrical Actuators

In this method, SMA elements are actuated by passing an electrical current through them. This method is only applicable where a small diameter SMA wire or spring is used; otherwise the electrical resistance is too small to produce enough heating. The main advantage is simplicity, while the big disadvantage is that the SMA element needs to be electrically insulated.

As the applications of SMA actuators, linear motion actuators (Figure 10), and rotary joint actuators (Figure 11) which are actuated by passing electrical current through SMA element are available. In the joint actuator (Figure 11) the joint can rotate back and forth by heating two SMA springs alternately.

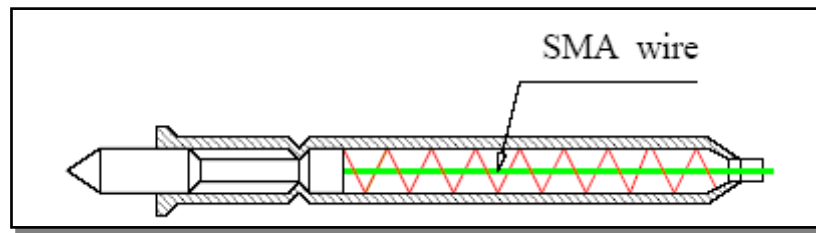


Figure 10. Linear motion SMA actuator [17]

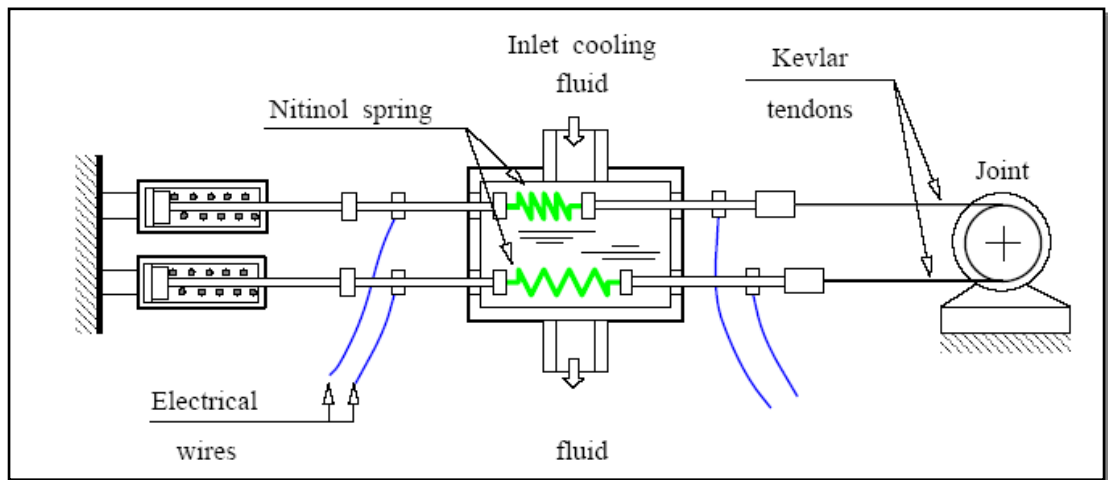


Figure 11. SMA rotary actuator [18]

One of the major problems of SMA actuators, especially those heated by electrical current is the cooling rate of the SMA to complete the martensitic transformation. Generally, cooling rate is the limiting factor in the bandwidth of the actuators. In most of the applications, a cooling liquid (Figure 11) is used to improve the bandwidth of SMAs; sometimes mobile heat sinks [19], and semiconductors [20] are also used.

1.4. Survey of Recent Patents Issued

Many patents have been issued for devices that exploit shape memory effect in the recent years. Some of these, which are more closely related to the current work, are briefly reviewed below.

1.4.1. Actuator Device with a Flexible Cable Incorporating a Shape Memory Element

Publication No. : US 2003/0173863 A1

Publication Date: July 18, 2003

In this patent, a shape memory alloy actuator which is used as a car truck door unlocking device comprises a flexible cable. One of the ends is connected to the control member and the other to the controlled member. A portion of the flexible cable is made of a shape memory material in such a way that the device can be used both as a mechanical element of flexible transmission between the control member and the controlled member, and as a shape memory actuator, designed to operate the controlled member following upon a variation in length of mentioned shape memory portion.

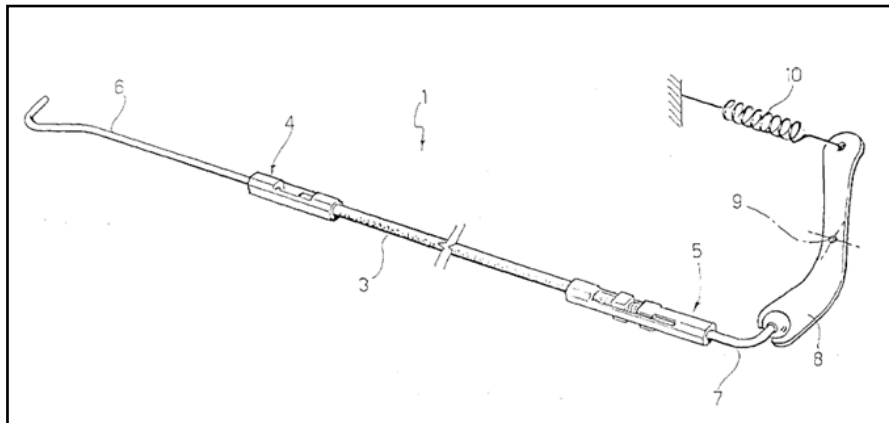


Figure 12. Shape memory alloy actuator device

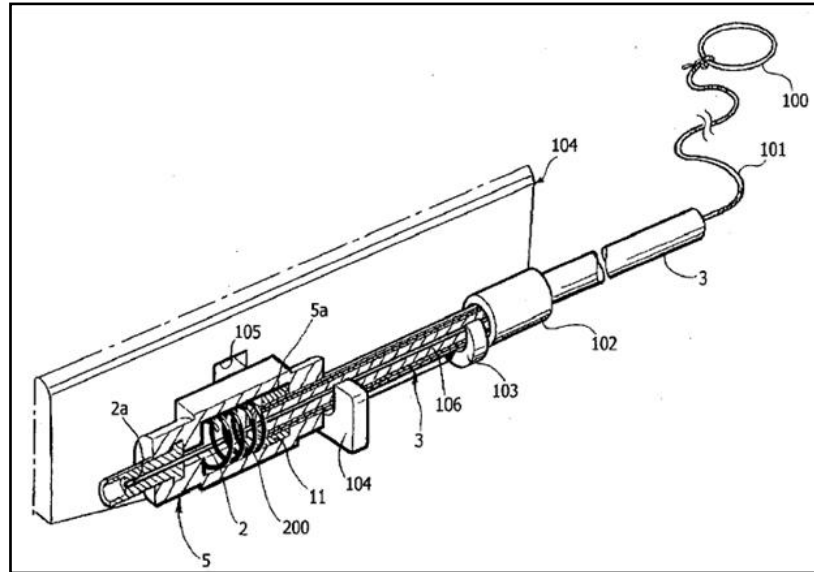


Figure 13. Detailed figure of shape memory alloy actuator device

The actuator **1** presented can be operated manually by means of applying a tensile force on the hook **6**. This force is then transmitted to controlled member **8**. When the tensile force is interrupted, the spring **10** tends to bring controlled member **8** back into resting position.

The actuator can be operated automatically by simply applying electric current through the flexible cable **2**. Shape memory alloy flexible cable **2** is heated by Joule effect, above its transformation temperature; as a result the cable retracts. Consequently, end hook **7** approaches the hook **6**, causing the movement of the controlled member **8**. As the electric current ceases to circulate through flexible cable **2**, the spring **10** brings the controlled member **8** back into resting position.

1.4.2. Prolonged Life Shape Memory Alloy Actuator

Publication No. : JP2006038931

Publication Date: Feb. 9, 2006

In this patent, it is aimed to provide an actuator using a wire made of shape memory alloy, whose life in terms of repeated operation is prolonged by reducing stress generated in the wire of the actuator.

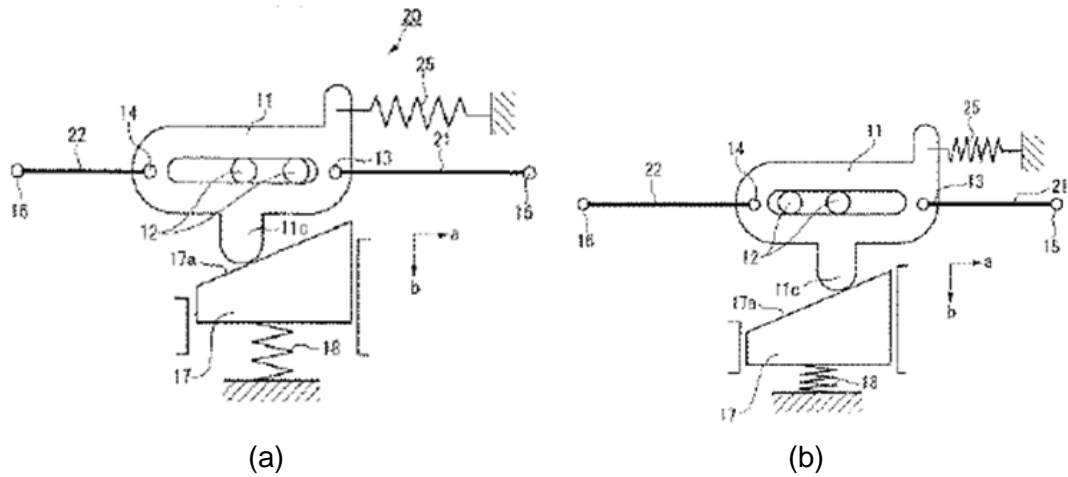


Figure 14. Figure of prolonged life shape memory alloy actuator

By energizing the first wire **21** made of shape memory alloy when the actuator is in the first state shown by Figure 14(a), the wire is contracted to memorized shape so that tensile force is generated, and a driving member **11** moves in a direction shown by direction 'a' and pushes down a driving object **17** in the direction shown by 'b', whereby the actuator gets in a second state shown by Figure 14(b). By stopping energizing the wire **21** and energizing the second wire **22** made of shape memory alloy, the wire **22** is contracted to memorized shape so that tensile force is generated, and the driving member **11** moves in an opposite direction to the direction shown by 'a', whereby the amount of force pushing-down is decreased and the driving object **17** ascends to restore the actuator in the first state. The stress generated by energizing the wire **22** is increased because the force of a tension spring **25** is added, but the stress generated by energizing the wire **21** is decreased by an amount equivalent to the force of the tension spring **25**, so that the life in terms of the repeated operation is prolonged.

1.4.3. Shape Memory Bi-Directional Rotary Actuator

Publication No. : US 5 127 228

Publication Date: July 7, 1992

The shape memory actuator presented in this patent is capable of high torque densities capable of being used on space applications and other fields.

The actuator in Figure 15 is comprised of two concentric tubular SMA members, namely an inner SMA member **12** and an outer SMA member **14**. The end of the SMA members are mechanically connected and restrained to an indexed position relative to each other. Internal splines of indexing standoffs **20** engage the external splines of the inner SMA member **12**. The indexing end caps **22** have internal splines that engage the external splines of both the outer SMA member **14** and the indexing standoffs **20**. The spline arrangement mechanically restrains the ends relative to each other and provides adjustability in the relative twist of the SMA members. Heaters can be located either on the inside or the outside of the SMA members provide that they are thermally insulated to prevent from heating the wrong SMA member. The preferred embodiment has the inner SMA member heater **16** located inside the inner SMA member **12**. The outer SMA member heater **18** is located on the outside of the outer SMA member **14**.

In the actuator the SMA members are designed to provide equal torque outputs in either direction. The inner and outer diameters of SMA members are selected for the desired output torque and to match the polar moments of inertia. The lengths are selected to provide the desired rotary motion and to most closely match the individual torque curves. It has been found that a design with ten percent strain developed in either SMA member between positions gives satisfactory results.

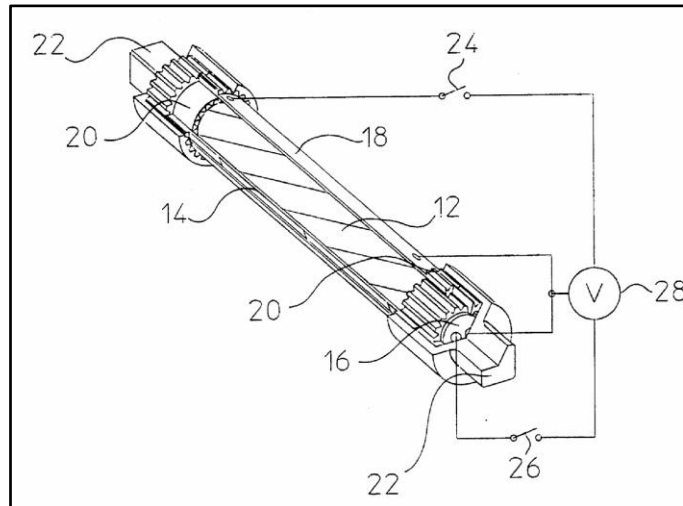


Figure 15. Figure of shape memory bi-directional rotary actuator

Initially both SMA members are martensite with the inner SMA member **12** twisted relative the outer SMA member **14**. Actuation is accomplished by closing the inner heater switch **26** to apply power from the voltage supply **28** to the inner SMA member heater **16** heating the inner SMA member above its austenite finish temperature. Strain recovery proceeds at the elevated stress until the strain coincides with the yield point. The output torque driven by the internal stress then drops off as function of the austenite modulus. Simultaneous to this the outer SMA member **14** is being deformed in its martensite form by the inner SMA member **12** which is in its austenite form. The actuation stops when the torques of the two SMA members balances. Reverse actuation is accomplished by allowing the inner SMA member **12** to first cool to the martensite finish temperature. Closing the outer heater switch **24** in order to apply power from the voltage supply **28** to the outer SMA member heater **18** heating the now deformed outer SMA member **14** above the austenite finish temperature. The actuation proceeds as it did in the opposite direction with the roles of the inner and outer SMA member reversed.

1.5. SMA Actuators Used in Aerospace Applications

Shape memory alloy elements are used in actuators due to their advantage over conventional methods by their high power to weight ratio, noiseless operation, and fewer parts needed to operate.

Shape memory actuators, like other technologies, have unique characteristics which make them suitable for some aerospace applications but not all. The following issues should be considered while using SMAs as actuators in aerospace applications: SMAs are more useful as small actuators; applications should not be time critical since activation of SMA elements are affected by initial temperature, and variations in the input energy levels combined with their low efficiency values (nearly 1% in practical); lower bandwidths should be acceptable since bandwidth of actuation depends on cooling of the shape memory element; and applications where SMA elements can be heated via passing current through them (Joule heating) are more appropriate for aerospace usage. In this section a few of the implementations of shape memory alloys in aerospace applications are discussed.

One of the examples of actuators used in aerospace applications employing SMA element is the pin-puller. The conventional solenoid or pyrotechnic activated pin-pullers are replaced with shape memory actuated systems. The use of SMA elements reduces weight, enhances reliability and extends the operational life of the system. Pin retraction is achieved by coupling the recovery characteristics of shape memory alloy material with a detent mechanism. Pin pullers are on-off type actuators where Ni-Ti wire is used to trigger the release of the energy stored in a loaded compression spring. Various sizes of Pin Pullers by TiNi Aerospace Inc. (Figure 16) were used in a variety of space missions and they are flight qualified [21].



Figure 16. Various SMA Pin Pullers by TiNi Aerospace Inc.[21]

Shape memory alloys are used for positioning solar panels in the satellites where the actuation speed is not important. Proportional positioning with closed loop control system using a position sensor is generally applied. The

implementation of SMA elements in these applications provides simplicity, and increases reliability [22].

Shape memory alloys are also employed in deployment mechanisms for both controlled and free deployment cases [23]. SMA based deployable structures can be folded easily owing to large deformation capability (Figure 17) [24]. Actuation is then accomplished by heating the SMA above its transformation temperature that forces it to recover its original shape. The deployment mechanism can be built reversible simply by using another set of SMA in bias. SMA actuated deployment mechanisms are used in satellite antennas, solar panels, space truss structures with their advantage of mass/volume savings and avoidance of end-of-deployment shock loadings, which are always associated with spring-deployed structures.

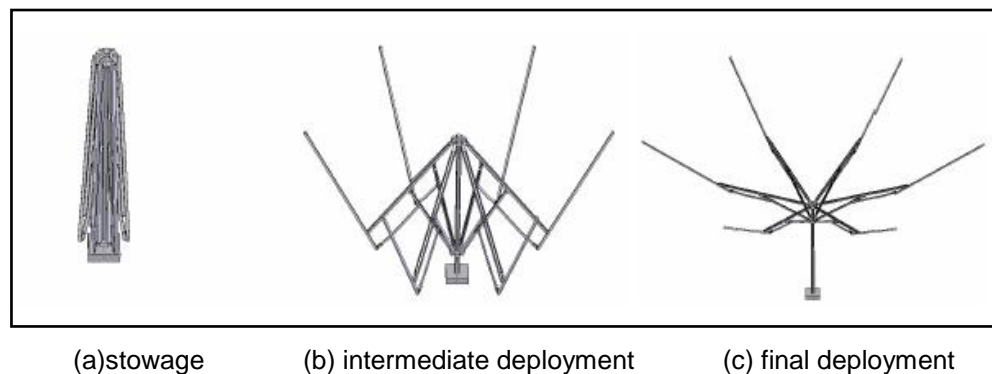


Figure 17. Deployable antenna actuated by shape memory alloy hinge [24]

Smart structures in which shape memory element is an integral part of the structure are recently one of the most frequently used forms of shape memory effect in actuation. The SMA element is embedded within the body so that when it is actuated the whole structure changes shape due to the created internal force.

Composite structures employing shape memory alloy materials are used in space systems as active vibration dampers to reduce the motion caused by the vibrations [25]. When the vibration in the system is detected the SMA element is activated changing the shape thus changing the damping characteristics of the structure.

Another successful example of smart structures is the U.S. Defense Advanced Research Projects Agency's (DARPA) "Smart Wing Program". An optimized lift-drag relationship of an airfoil can be achieved when the camber can be varied according to the different operating conditions [26]. "Smart Wing Program" involves the development of an SMA based, hingeless, smoothly contoured trailing edge with SMA integrated actuation mechanisms to replace standard hinged control surfaces and provide variable, optimal aerodynamic shapes for a variety of flight regimes (Figure 18) [27].

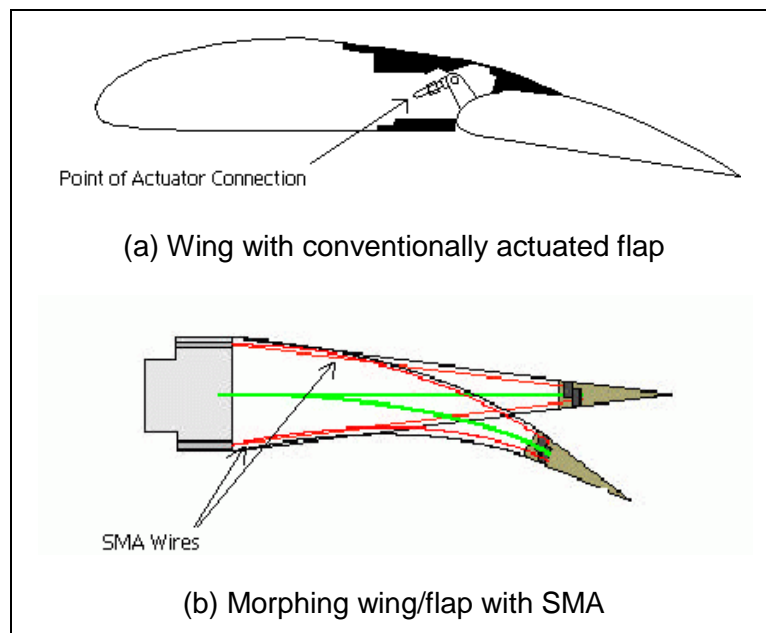


Figure 18. Representative drawings of conventional flap control and smart wing (DARPA) [28]

Adaptation of aerodynamic profiles accordingly may suitably be achieved with a smart structure. The wing is forced to change its shape when the shape memory element is heated, the actuation can be accomplished in both directions using antagonistic shape memory elements. However, bandwidth of the actuation is limited with the cooling conditions.

SMA embedded smart structures are also used in aerospace applications where a variable air inlet is required. Jet engines require air to enter the engine at approximately Mach 0.5 or less. Due to the wide range of Mach speeds, altitude, angle-of-attack, angle-of-slip, and engine airflow conditions, a fixed geometry inlet cannot provide ideal performance under all conditions. Quasi-

static shape control for inlet shaping is accomplished via compliant surfaces actuated with SMAs, [29].

As in the case of air inlet, variable area fan and exhaust nozzles are desired to improve the engine efficiency over a wider range of operation conditions. Conventionally, adjustment of the opening area of the exhaust nozzle is attained by using electric motors or hydraulic actuators. Compared to the conventional actuators, the SMA actuator dramatically reduces the actuator system weight. The SMA actuators are remotely placed away from the exhaust nozzle area so that the environmental temperature is below their transformation temperature. By electrically heating the SMA actuators, the exhaust nozzle will experience an area reduction of up to 40%. Bias springs will apply forces to return the exhaust nozzle to the open-up configuration (Figure 19) [29].

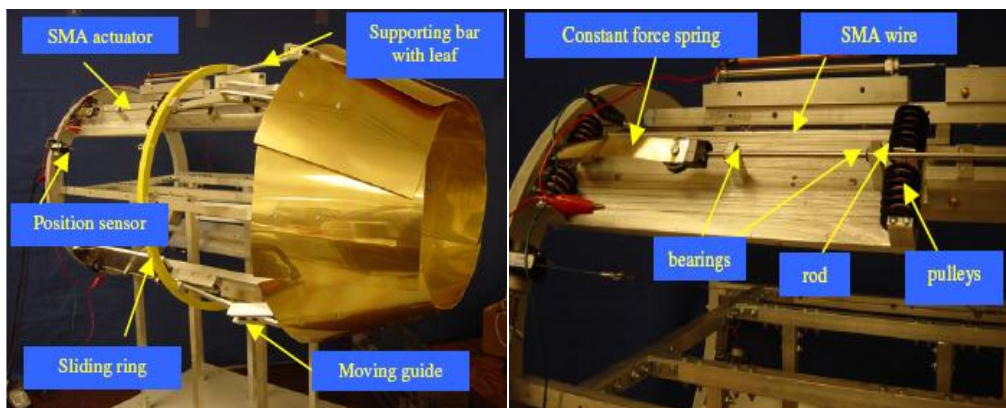


Figure 19. Variable area exhaust nozzle [29]

Helicopters encounter vibratory loads from different sources such as blade dissimilarity and the aerodynamic environment. Currently, to overcome this problem, in-shop tracking of blades is done periodically resulting in a significant increase in operating cost and helicopter downtime. The ability to track helicopter blades in-flight by using SMA wires as hinge actuators has several advantages: the minimization of low frequency vibrations; the relaxation of manufacturing tolerances of blades; a reduction in downtime; a decrease in overall operating and procurement costs; and an increase in the fatigue life of structural components and instrumentation [30].

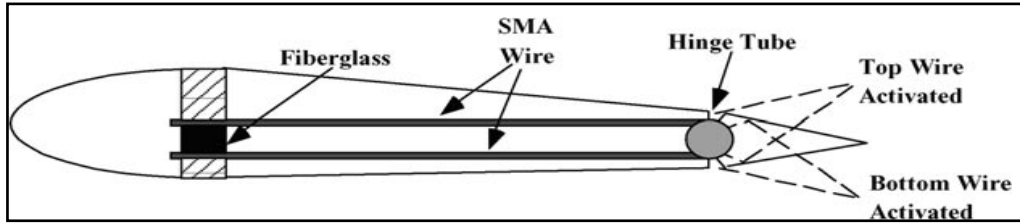


Figure 20. Tracking of helicopter rotor blades [30]

Various research activities are going on towards SMA actuated smart structures. Progress over the past is promising which can be specifically related to understanding and analytically describing SMAs' complex behavior as well as advances in manufacturing SMA reinforced composites.

1.6. Scope of the Thesis

The aim of this research is to demonstrate the use of shape memory alloys in actuators to be integrated in aerospace systems and test equipments. The intended study comprises the theoretical and experimental position control of SMA wires to be used in actuators and design and production of an actuator, application of the suitable control strategies, and relevant experiments for validating the theoretical assumptions.

In this sense, a desirable actuator features the following characteristics:

- Consistent device-to-device and cycle-to-cycle response
- Very good mechanical tolerances
- Low or predictable hysteresis
- Large force capability
- High frequency response
- Durability and reliability over time (including aging and environmental effects)
- Suitable size and weight

Current shape-memory based actuators exhibit some, but not all, of these characteristics. While there has been significant emphasis on producing and modeling SMAs [1], [2], [3], [31], [32], [34], there has, in general, been much less effort focused on developing devices that take full advantage of their unique

properties. In fact, shape memory alloy actuators provide an interesting alternative to conventional actuation methods. Their advantages create a means to drastically reduce the size, weight, and complexity of actuation systems.

Recently, like other robotic actuators, actuators and systems used in missiles and space applications are needed to become more and more compact. Although shape memory alloy materials have a significant potential in the area of actuators, only a limited number of work related to design, production and control issues of SMA actuators is available. The emphasis of this work is aimed to be the development of devices which will advance and expand the areas within which shape memory alloys can provide novel solutions and significantly increase the amount of work shape memory alloys can deliver to the system.

In this study, issues in the design of shape memory alloy actuators are outlined and accurate position control of SMA wire actuators is achieved. Also, as a part of the thesis study, SMA wire characterization and control set-up is built in TÜBİTAK-SAGE Mechatronics Laboratory. After modeling the shape memory element, control simulations and experiments are performed using three feedback variables with three different control schemes.

Finally, as a case study, a linear SMA wire actuator is designed and prototyped. The developed control methods are implemented and experimented on the actuator, and accurate control of the actuator is attained.

The thesis comprises six chapters. In Chapter 1, the results of an extensive literature survey about the shape memory alloys and their applications is presented. Also, the scope of the thesis is given.

In Chapter 2, the underlying principles of shape memory behavior are discussed. Then, the selection of material, training issues, and the effect of active element shape are explained. Afterwards, a brief literature review of SMA models and detailed explanation on selected models with their characterization requirements are presented. At this point, the SMA characterization set-up built in TÜBİTAK-SAGE and the characterization experiments performed are described. Eventually, the proposed models for the strain, resistance, and dissipated power of the SMA wire are presented with simulations and experiments. The model for power dissipated by the wire obtained in this section is a new concept for defining the behavior of the wire.

In Chapter 3, first, a literature review of the control methods applied to SMA wire actuators is given. Then, of Proportional-Integral (PI) type controller, PI-type controller with a feedforward loop, and Neural Network (NN) Narma-L2 type controllers are designed for controlling the strain, resistance per unit length, and dissipated power per unit length of the wire. While resistance and strain feedback models can be find in the literature, dissipated power is a newly introduced internal feedback variable for the SMA wires to be used as a self-sensor. In this content, the computer simulations of the designed controllers are performed on the selected data set. Since the ultimate motive to control internal variables (resistance and power) is to control the position of the wire, strain-resistance and strain-power relations are simulated and indirect strain control of the wire is demonstrated. Finally, the designed control systems are validated for other data sets.

Chapter 4 starts with the description of the control set-up, derivation of the driver function and selection of the filter to eliminate the noise in the data. Afterwards, the previously designed control systems are implemented and real time strain, resistance, and power control of the SMA wire is accomplished. Furthermore, strain-resistance, strain-power relations and validation of control schemes under different loads and against a spring are also experimented. In this part of the study, effective control of an SMA wire is demonstrated.

In Chapter 5, a linear SMA wire actuator to displace 10 N of load 10 mm is designed and controlled as a case study. In this chapter, firstly actuator design is described in two sections: conceptual design and mechanical design sections. In conceptual design part, the general characteristics of the actuator to achieve the requirements are indicated and in mechanical design, detailed mechanical design of the actuator is discussed. Then, actuator test-bed and control experiments on the actuator are presented. The designed, simulated, and experimented control schemes are implemented and very satisfactory results are obtained.

In Chapter 6, the outcomes of the study are discussed. A design methodology for shape memory alloy wire based actuators is outlined for future reference. Finally, some future work recommendations are made.

CHAPTER 2

SHAPE MEMORY BEHAVIOR AND MODELING

Ever since the shape memory effect is observed, engineers and scientists have tried to discover the driving phenomena behind this unexpected behavior. In recent years, the micro-structural phase transformation is understood however the underlying microscopic mechanism, the relation between microscopic and macroscopic behavior, is still a research topic.

In order to implement shape memory alloy elements into engineered components and systems, modeling is needed as a quantitative tool to guide the engineer through the design process. In this sense, modeling of material behavior is traditionally motivated by one of the two requirements explained as [31]:

(1) Constitutive models developed for implementation into explicit engineering analysis tools such as the finite element method. These models are usually deemed phenomenological constitutive models. They also cover the “internal state variable models” that implicitly account for micro-mechanical material behavior in the stress-strain response.

(2) Constitutive models developed exclusively to gain a quantitative insight into the relationships between micro-structural input variables and the macroscopic stress-strain response, which are usually referred to micro-mechanical models. These models explicitly account for micro-mechanical behavior in the stress-strain response.

2.1. Memory Effect

The observable mechanical behavior of shape memory alloys (SMAs) can be investigated in two categories. One of them is the ‘Shape Memory Effect’ (SME) in which an element exhibits a large residual (seemingly plastic) strain upon loading and unloading at low temperature that is fully recovered by simply increasing the temperature of the material. The other category is the

‘Pseudoelastic Effect’ or ‘Superelasticity’ in which the element achieves a very large residual (seemingly plastic) strain upon loading that is then fully recovered in a hysteresis loop upon unloading. The graphical representations of the mentioned categories are presented in Figure 21, where σ and ϵ stand for the stress and strain quantities respectively.

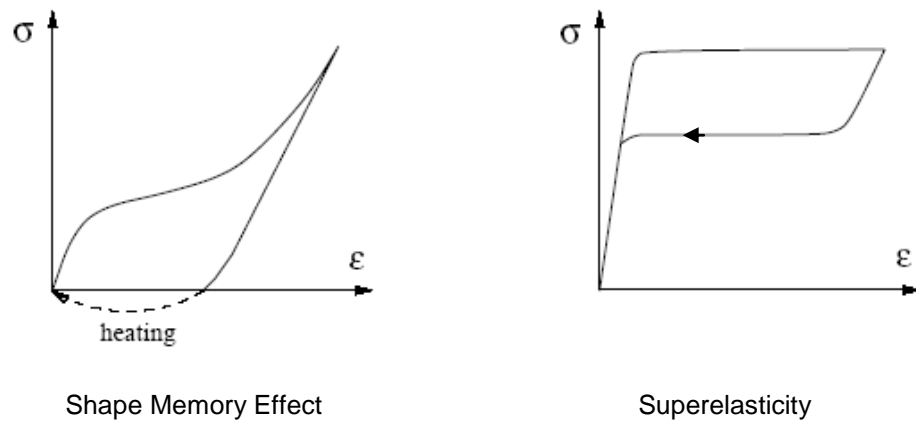


Figure 21. Shape memory alloy behavior [32]

These two behaviors are related to two different micro-structural transformations which are phase transformation and martensite re-orientation.

2.1.1. Phase Transformation

“Phase Transformation” is the “Martensitic Transformation” (from austenite to martensite) and its reverse transformation is the lattice transformation involving a shearing deformation that results from cooperative atomic movements. The martensitic transformation is a diffusionless phase transformation in solids, in which atoms move cooperatively, and often by a shear-like mechanism. Basically, this transformation is caused by the difference in free energy which is the total amount of energy in a physical system which can be converted to do work, between the two phases; austenite being the high-energy phase [33]. Usually the parent phase (high temperature phase) is cubic and the martensite (lower temperature phase) has a lower symmetry. When the temperature is lowered below a critical one, martensitic transformation starts by a shear-like mechanism. Then, if the temperature is raised and martensite becomes unstable, then the reverse transformation occurs, and if the

transformation is crystallographically reversible, the martensite reverts to the parent phase in the original orientation. Even though the relative atomic displacements are small (compared with inter-atomic distance), a macroscopic shape change appears associated with martensitic transformation [2].

Transformations can be induced either by a temperature change, or by an applied stress both of which change the free energy of the material. The volume change associated with them is very small and all deformation in transformations is recoverable.

Since the martensitic transformations are not associated with a compositional change, in order to induce the austenite to martensite transformation, the chemical free energy (Gibbs free energy) of the martensite phase must be lower than that of the austenite phase. However, since the transformation also requires non-chemical free energy, such as transformation strain energy, friction energy, etc., the transformation can happen only when the difference between the chemical free energies of the two phases is greater than the necessary non-chemical free energy. Similarly, the transformation from martensite to austenite will occur when the difference between the above stated energies is sufficiently large. Because of this, supercooling is necessary for the nucleation of a martensite, and superheating is necessary for the reverse transformation. By the same reasoning, M_s (martensite start temperature) is not same as M_f (martensite finish temperature), since the elastic energy around the martensite resists the growth of the martensite nucleation unless a further driving force (cooling) is given; the same reason applies to the difference between A_s (austenite start temperature) and A_f (austenite finish temperature). Thus, a distinguishing characteristic of SMAs is the 'hysteresis' behavior which can be defined as the difference between the forward and reverse transformation paths (Figure 22).

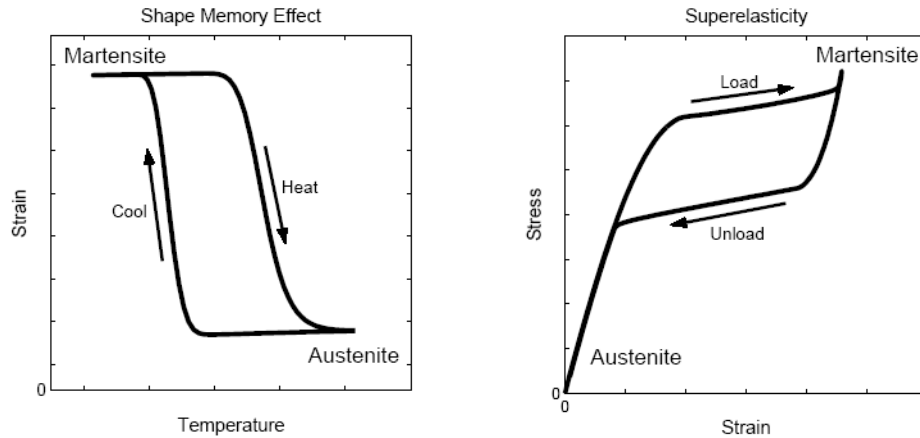


Figure 22. Idealized hysteresis curves for SME (fixed load) and super elasticity (fixed temperature) [34]

2.1.2. Martensite Re-Orientation

Martensite re-orientation is a transformation between martensite variants, where no phase change is involved. This transformation is always stress related and the corresponding recoverable strain is associated with the conversion between variants of the martensite.

If an SMA element which consists only of twinned martensite is subjected to gradually increasing uniaxial stress, transformations will occur between variants within each twinning group, leading to the growth of a preferred variant. This process minimizes the elastic energy in this group, as the change of internal stress partially counteracts the externally applied stress.

As the stress level increase, similar conversions will take place among martensite groups until the entire specimen consists of only one variant in single crystal and a large macroscopic strain is produced. This process is called detwinning, and the resulting martensite is usually called 'Detwinned Martensite' [35].

After deformation, the specimen can be heated to high temperature under zero external stress, so that only austenite remains, and it will go back to the shape that it had before twinning, thus it remembers its original shape i.e. SME.

2.2. Thermomechanical Behavior

Since austenite and martensite exhibit different micro-structures, their mechanical and physical properties also differ significantly, and in the range where they co-exist a variety of nonlinearities occur.

Young's Modulus, damping, internal friction, resistance, heat capacity, latent heat of transformation, and thermal conductivity can be examples of the properties that change with the phase of the material. Most of these relationships involve hysteresis and are not only nonlinear but dependent on alloy composition, processing, and the number of activation cycles.

One of the mechanical properties that depend on the phase of the material is the stress-strain characteristic. Figure 23 shows the stress-strain curves for austenite and martensite SMAs. In the austenitic phase, the stress-strain curve appears similar to most materials, but in the martensitic phase, a plateau and different loading and unloading curves exist. The plateau is the area where detwinning occurs, the martensite transforms from 'Twinned Martensite' to 'Detwinned Martensite'. Upon loading martensite, a "normal" elastic curve is initially followed until the plateau is reached. Then for a minor increase in stress, a large strain results due to detwinning. If the load is removed at any point on the plateau, a different unloading curve is formed shown in Figure 23(a) as the broken lines. The end of the plateau represents fully detwinned martensite. If the load is further increased, elastic deformation of the detwinned martensite is observed until the plastic deformation occurs. From here any increase in stress introduces slip in lattice boundaries, causing unrecoverable strains.

During heating from A_s to A_f and cooling between M_s and M_f , the curves transform between each other. Figure 23(b) illustrates the transition from strain-stress curve of martensite to that of austenite and vice-versa. This transition plays an important role in allowing for the extraction of work from SMAs.

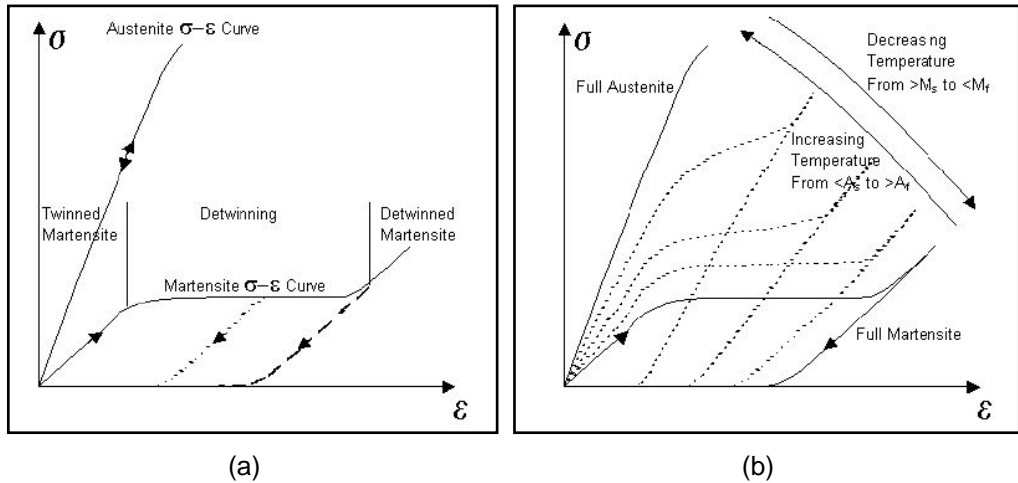


Figure 23: Stress- Strain curves of SMAs in (a) full martensite and (b) full martensite to full austenite [36]

The strain values resulting from a particular stress will be different in martensite and austenite phases. This allows work to be done on a load by heating the SMA element (Figure 24). The Young's Modulus of an SMA element will vary with its phase composition and temperature [37]. In a SMA element, the measured Young's Modulus of the austenite phase can be several times higher than that of the martensite phase.

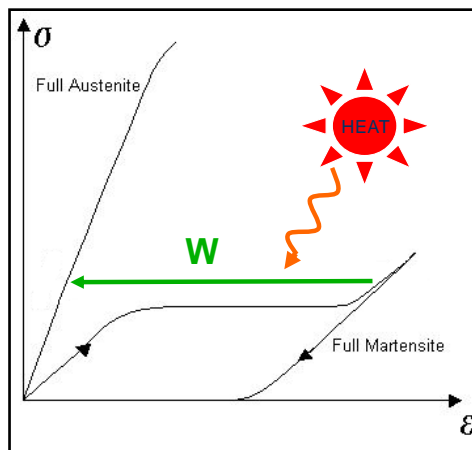


Figure 24. Work extraction from SMAs

Another thermomechanical behavior of the SMAs is the dependence of their transformation temperatures on the applied stress level. When the stress

level increases energy needed for phase transformation, thus the transformation temperatures are increased (Figure 25).

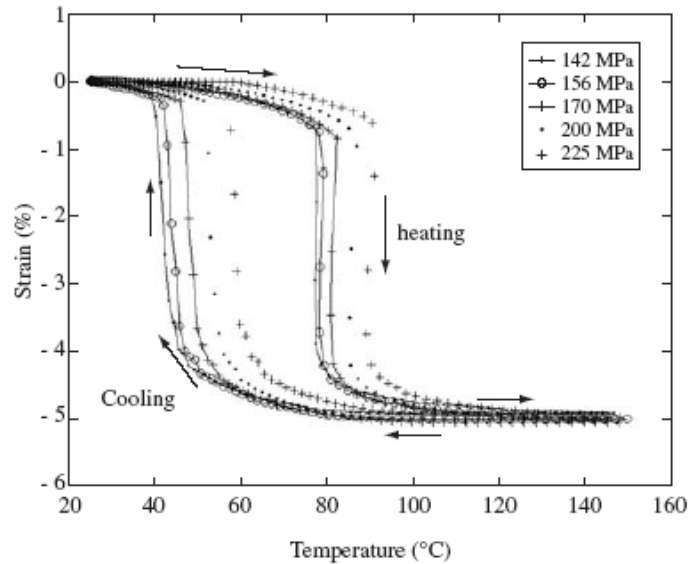


Figure 25. Strain-temperature characteristics at constant stress levels [38]

2.3. Material Selection

The properties of SMAs depend on and are very sensitive to the concentration of the elements in the alloy. In the work by W. Huang, a detailed comparison of Ni-Ti, Cu-Zn-Al, and Cu-Al-Ni is given in Table 2 [39]. In this study, some major characteristics are chosen as performance criteria and the comparison is presented in performance charts. According to the selected characteristics, Ni-Ti seems to be the most suitable of those alloys compared with a slight difference in cost. Thus, Ni-Ti is chosen for this study because it is the most readily available alloy and because of its favorable shape memory and electrical resistance characteristics.

The relatively high electrical resistance of Ni-Ti is beneficial for experimental situations involving activation of the actuators by resistive heating, since smaller currents would be sufficient for the needed actuation. Also, the functional properties are far better reproducible for Ni-Ti than for other alloys with a higher mechanical strength and allowing a higher working stress. Ni-Ti shows a higher memory strain so that a higher work density (delivered work per unit

volume) can be obtained; with better hysteresis characteristics, and has a corrosion resistance comparable to stainless steel.

Table 2. Main properties of typical SMAs [39]

	NiTi	CuZnAl	CuAlNi
Specific heat (J/Kg°C)	450–620	390–400	373–574
Thermal conductivity (20°C) (W/mK)	8.6–18	84–120	30–75
Density (Kg/m ³)	6400–6500	7540–8000	7100–7200
Latent heat (J/Kg)	19 000–32 000	7000–9000	7000–9000
Electrical resistivity (10 ⁶ Ωm)	0.5–1.1	0.07–0.12	0.1–0.14
Thermal expansion coefficient (10 ⁻⁶ /K)	6.6–11	17	17
Maximum recovery stress (Mpa)	500–900	400–700	300–600
Normal working stress (Mpa)	100–130	40	70
Fatigue strength (N = 10 ⁶) (Mpa)	350	270	350
Maximum transformation strain (%)	$N = 1$ $N < 10^2$ $N < 10^5$ $N < 10^7$	6–8 4–6 4	5–6 4
Normal number of thermal cycles	$> 10^5$	$> 10^4$	$> 5 \times 10^3$
Young's Modulus (Gpa)	28–83	70–100	80–100
Shape memory transformation temperature (°C)	–200–200	–200–150	–200–200
Hysteresis (°C)	2–50	5–20	20–40
Maximum overheating temperature (°C)	400	150	300
Damping capacity (SDC%)	15–20	30–85	10–20
Grain size (μm)	1–100	50–150	25–100
Melting, casting and composition control	Difficult	Fair	Fair
Forming (rolling, extrusion)	Difficult	Easy	Difficult
Cold-working	Fair	Restricted	Very difficult
Machinability	Difficult	Very good	Good
Cost ratio	10–100	1–10	1.5–20

2.4. Training SMA Elements

Shape memory alloy end products like bars, wires, ribbons, and sheets are normally finished by cold working to achieve the desired dimensions and enhance surface quality. Cold working suppresses the shape memory response of these alloys. It also raises the strength and decreases the ductility. However, cold work does not raise the stiffness of the material. Heat treating after cold working diminishes the effects of cold working and restores the shape memory response of these alloys. With different compositions and heat treatment processes, different transition temperature SMAs can be attained. Therefore, in order to optimize the physical and mechanical properties of an SMA product and achieve shape memory or superelasticity, the material is cold worked and then heat treated.

SMA elements can be made to remember a certain shape (shape setting) or a certain percent of strain (training) upon transformation to austenite. Shape setting or training is accomplished by deforming the SMA element to the shape

of a desired component, or elongating it by a desired percent, then constraining the element by clamping and then heat treating. This is normally done with material in the cold worked condition, for example cold drawn wire. In shape setting cold worked material, care must be taken to limit deformation strain to prevent cracking of the material.

Smith et al. [40] reviewed the types of furnaces and fixturing hardware or mandrels that have been used in heat treatment. Many types of furnaces have been used including box furnaces, continuous belt hearth furnaces, tube furnaces, heated platen presses, vacuum furnaces, induction heaters, salt baths and fluidized bed furnaces. The electrical resistance of Ni-Ti alloys makes them a good candidate for self heating by electric current. Ni-Ti alloys are oxidized when heat treated in air; therefore, surface requirements and atmosphere control are important considerations.

The shape setting heat treatment changes the physical and mechanical properties of Ni-Ti. Morgan and Broadly [41] mapped the effect of temperature and time at temperature on shape set wire properties. Their response curves illustrate that physical and mechanical properties do not always change in the same direction.

2.5. Shape of the Active Element

Since cold machining of Ni-Ti is rather difficult; the material is mainly available in simple shapes like bars, wires, pipes, rings, and strips. The SMA elements are employed in the actuators to obtain large deflection or high force. The shapes of SMA elements used in the actuators depend on the characteristics of the requirement. These elements can be classified as in Table 3.

Table 3. Classification of SMA elements

<i>Element</i>	<i>Type of deflection</i>	<i>Amount of deflection</i>	<i>Amount of force/torque</i>
Straight wire	Linear	Small	High
Helical elements (springs)	Linear	Large	Small
	Rotary	Large	Small
Torsional bars/tubes	Rotary	Large	Small
Cantilever strips	Both	Large	Small
Belleville-type discs	Linear	Small	Moderate

There are a lot of actuators designed based on shape memory springs. The main advantage of a spring is that it generates a large macroscopic displacement out of a relatively small microscopic strain; but the stress distribution over the cross-section of the spring is not constant. This implies that a greater material volume is needed for generating the same force. This has a negative effect on the efficiency and the speed of the spring based actuator. For the same output, a larger material volume has to be heated and cooled. Using wires as an active element has the advantage of optimal use of the material. The required amount of work is generated with minimal use of shape memory material.

The advantages of using SMA wires loaded in tension are presented in Table 4. As can be seen tension loading has a much higher efficiency than other load cases. There are two alternatives in order to deal with the limited stroke and force available when using straight wires, one of them is using a series system consisting of a single long wire (to generate the desired displacement) or using a parallel system of multiple wires (to generate high force and small displacement) together with a lever mechanism.

Table 4. Comparison of load cases for SMA actuators [42]

Load case	Efficiency (%)	Energy density (J/kg)
Carnot (reference)	9.9	-
Tension	1.3	466
Torsion	0.23	82
Bending	0.013	4.6

Considering the above arguments for SMA element shape selection wires are decided to be employed in this study.

The SMA wires chosen to be used in the scope of this study are Ni-Ti wires supplied by Mondotronics Inc.. The SMA wires selected are sold under the brand name 'FLEXINOL' which are heat treated and highly processed, trained to contract upon transformation, and thus ready to be used [43]. The properties of the selected wire are presented in The load capacities of the wires depend on their diameter and the load capacity is inversely proportional with the speed and time of actuation of the wire. As the diameter becomes larger, the load capacity and the energy needed to activate the wire increase. However, activation time becomes longer thus the bandwidth decreases.

Table 5.

The load capacities of the wires depend on their diameter and the load capacity is inversely proportional with the speed and time of actuation of the wire. As the diameter becomes larger, the load capacity and the energy needed to activate the wire increase. However, activation time becomes longer thus the bandwidth decreases.

Table 5. Properties of the selected wire [43]

Wire diameter (mm)	0.2
Activation start temperature, A_s (°C)	88
Activation finish temperature, A_f (°C)	98
Relaxation start temperature, M_s (°C)	72
Relaxation finish temperature, M_f (°C)	62
Density (g/cc)	6.45
Martensite phase Young modulus (GPa)	28
Austenite phase Young modulus (GPa)	75
Maximum recovery stress (MPa)	600
Recommended deformation ratio (%)	3-5
Minimum bend radius (mm)	10
Activation time (sec)	1
Relaxation time (sec)	2.2

2.6. Review of Shape Memory Alloy Models

A lot of SMA models have been developed in the late 80's and 90's, all of which try to express behavior of SMAs in different mathematical forms, [37], [42], [44], [45], [46], [47], [48]. Since shape memory material behavior depends on stress, temperature and connected with the phase of the material and the thermodynamics underlying the transformation process, formulation of adequate macroscopic constitutive laws is very complex.

One feature of many of the constitutive descriptions of shape memory behavior is that the models can generally be separated into two basic laws governing the transformation behavior: a mechanical law, which establishes the

relation between stress, strain and temperature, and a kinetic law which formulates the degree of transformation.

They can roughly be summarized into the following categories:

- Phenomenological models based on the volume fraction of martensite as the internal state variable. These models capture the dependence of the transformation behavior on temperature, including shape memory and pseudoelasticity;
- Models derived from a special free energy formulation;
- Models based on thermodynamic laws;
- Constitutive laws based on a model for hysteresis like Preisach model;
- Models based on nonlinear thermo-plasticity theory, generalized plasticity, or visco-plastic theory;
- Mathematical models for the dynamics of phase boundary motion;
- Models derived from the deformation of crystal structure during phase transformation;
- Constitutive laws that allow for micro-structural deformation during phase transformation and the free energy concept, using an energy dissipation or energy balance approach.

Each of these models aims to describe the behavior of SMAs from a certain aspect and on a different scale. However, in spite of all these efforts, no single model exists that is able to describe quantitatively the shape memory behavior of shape memory materials. The reason for this may be related to the very strong effect of micro-structure and processing on the mechanical properties.

From an engineering application point of view, the most practical and productive approach is based on phenomenological models, which fit the uniaxial experimental data, without attempting to capture the detailed underlying thermomechanical behavior. Historically, the first such model was proposed by Tanaka [44]. The models to be investigated in this study are more frequently used models in the literature; the selected models are Tanaka's, Liang and Rogers', and Brinson's phenomenological uniaxial models. These classes of

phenomenological models are known as the models with ‘assumed phase transformation kinetics’ that consider pre-established simple mathematical functions to describe phase transformation kinetics.

In the following sections, only a few of the models that aim to express the behavior of SMA elements in a mathematical form are investigated with the proposed simplifications and modifications. The advantage of using one model over another only depends upon the level of complexity required. In general, more extensive models capture a wider range of macroscopic behaviors, but also requires additional material testing for determination of the material constants.

Implementation of the models into engineering codes may also play a role in model choice due to possible numerical problems or increased coding and solving times. Thus, the model to be adopted should be chosen according to the application requirements and the experimental capabilities.

2.6.1. Models with Assumed Phase Transformation Kinetics

2.6.1.1. Tanaka’s Model

2.6.1.1.1. Development of the Constitutive Law from Thermodynamics:

Considering a one-dimensional SMA element (wire) of length L that is undergoing either martensitic transformation or its reverse transformation, from the principles of thermodynamics the energy balance (Eq.1) and Clasius-Duhem inequality (Eq.2) can be expressed as [37]:

$$\rho \dot{U} - \hat{\sigma} L + \frac{\partial q_{sur}}{\partial x} - \rho q = 0 \quad \text{Eq.1}$$

$$\rho \dot{S} - \rho \frac{q}{T} + \frac{\partial}{\partial x} \left(\frac{q_{sur}}{T} \right) \geq 0 \quad \text{Eq.2}$$

where

- U : Internal energy density
- $\hat{\sigma}$: Cauchy stress
- q : Heat production density

- q_{sur} : Heat flux
- S : Entropy density
- T : Temperature
- x : Material coordinate
- ρ : Density

According to this model, if one dimensional extension of a uniform SMA wire is considered, the phase transformations may be described in terms of three external variables, stress (σ), strain (ε), and temperature (T), and the internal variable: the martensite fraction, ξ (stage of transformation). The martensite fraction of the material varies from zero to one, with unity representing the full martensitic phase; this fraction is governed by temperature and stress.

By introducing the Helmholtz free energy $\Phi=U-TS$, Clasius-Duhem inequality (Eq.2) can be rewritten in the reference configuration as:

$$\left(\sigma - \rho_0 \frac{\partial \Phi}{\partial \varepsilon} \right) \dot{\varepsilon} - \left(S + \frac{\partial \Phi}{\partial T} \right) \dot{T} - \frac{\partial \Phi}{\partial \xi} \dot{\xi} - \frac{1}{\rho_0 T} \frac{\rho_0}{\rho} q_{sur} F^{-1} \frac{\partial T}{\partial X} \geq 0 \quad \text{Eq. 3}$$

where

- σ : 2nd Piola-Kirchhoff stress
- F : Deformation gradient
- ρ_0 : Density in reference configuration
- X : Material coordinate in reference configuration

In order for Eq. 3 to hold for every strain rate and temperature gradient, their coefficients should vanish. Hence, the two conditions are obtained as:

$$\sigma = \rho_0 \frac{\partial \Phi(\varepsilon, \xi, T)}{\partial \varepsilon} = \sigma(\varepsilon, \xi, T) \quad \text{Eq. 4}$$

$$S = - \frac{\partial \Phi(\varepsilon, \xi, T)}{\partial T} \quad \text{Eq. 5}$$

The first relation above (Eq. 4) gives the mechanical constitutive equation of the material. Using differential calculus, this equation takes the form:

$$d\sigma = \frac{\partial\sigma}{\partial\varepsilon}d\varepsilon + \frac{\partial\sigma}{\partial\xi}d\xi + \frac{\partial\sigma}{\partial T}dT \quad \text{Eq. 6}$$

leading to the most general equivalent expression

$$d\sigma = E(\varepsilon, \xi, T)d\varepsilon + \Omega(\varepsilon, \xi, T)d\xi + \theta(\varepsilon, \xi, T)dT \quad \text{Eq. 7}$$

where the material functions are defined by

$$E(\varepsilon, \xi, T) = \rho_0 \frac{\partial^2\Phi}{\partial\varepsilon^2} \quad E(\varepsilon, \xi, T) \text{ is the representative of the modulus of the SMA material}$$

$$\Omega(\varepsilon, \xi, T) = \rho_0 \frac{\partial^2\Phi}{\partial\varepsilon\partial\xi} \quad \Omega(\varepsilon, \xi, T) \text{ can be considered as the 'transformation tensor'}$$

$$\theta(\varepsilon, \xi, T) = \rho_0 \frac{\partial^2\Phi}{\partial\varepsilon\partial T} \quad \theta(\varepsilon, \xi, T) \text{ is related to the thermal coefficient of expansion for the SMA}$$

If the above defined material functions are assumed to be constants, then the constitutive relation in Eq. 7, where the subscript '0' representing the initial state of the material, can easily be derived as:

$$\sigma - \sigma_0 = E(\varepsilon - \varepsilon_0) + \Omega(\xi - \xi_0) + \theta(T - T_0) \quad \text{Eq. 8}$$

Since the maximum recoverable strain, ε_L , which is a material constant, occurs when the material is in fully martensitic phase, using the initial conditions as $\sigma_0 = \varepsilon_0 = \xi_0 = 0$ and the final conditions as $\sigma = 0$, $\varepsilon_0 = \varepsilon_L$ and $\xi = 1$, the relation between uniaxial transformation coefficient and the strain is obtained as:

$$\Omega = -\varepsilon_L E \quad \text{Eq. 9}$$

2.6.1.1.2. Estimation of the Martensite Fraction during Phase Transformation:

In the model developed by Tanaka, exponential functions are used to describe the martensitic fraction during the phase transformations.

In this model, for austenite to martensite ($A \Rightarrow M$) transformation, the following function has been proposed to represent the martensitic fraction:

$$\xi = 1 - \exp[-a_M(M_s - T) - b_M\sigma] + \xi_0 \quad \text{Eq. 10}$$

with the definition of positive material parameters a_M and b_M being $a_M = 2\ln(10)/(M_s - M_f)$ and $b_M = a_M/C_M$.

C_M is the representative of the change in the transformation temperatures M_s and M_f with the applied stress (Figure 26).

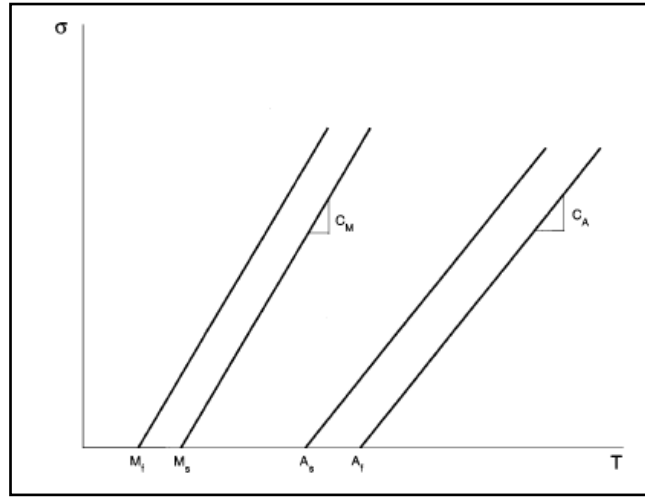


Figure 26. Stress- transformation temperature plot [37]

The critical stress for martensitic phase transformation ($A \Rightarrow M$) to initiate is given by

$$\sigma_{M_s} \geq \frac{a_M}{b_M} (T - M_s)$$

or the transformation temperature for a constant stress is:

$$T_{M_s} \leq \sigma \frac{b_M}{a_M} + M_s$$

Since an exponential function is adopted, the final bound for the phase transformation is $\xi = 0.99$ at which the transformation is considered complete.

For the reverse transformation from martensite to austenite ($M \Rightarrow A$) the exponential function is:

$$\xi = \xi_0 \exp[-a_A(T - A_s) - b_A\sigma] \quad \text{Eq. 11}$$

with the definition of the positive material parameters a_A and b_A being $a_A=2\ln(10)/(A_f-A_s)$ and $b_A=a_A/C_A$.

C_A is the representative of the change in the transformation temperatures A_s and A_f with the applied stress (Figure 26).

The critical stress for austenitic phase transformation ($M \Rightarrow A$) is given by

$$\sigma_{A_s} \geq \frac{a_A}{b_A}(T-A_s)$$

or the transformation temperature for a constant stress is:

$$T_{A_s} \leq \sigma \frac{b_A}{a_A} + A_s$$

The final bound for austenitic transformation is $\xi=0.01$ at which the material is assumed to be fully austenitic.

A representative graph for the transformation is presented in Figure 27 for the material properties $A_s=34.5^\circ\text{C}$, $A_f=49^\circ\text{C}$, $M_f=9^\circ\text{C}$, $M_s=18.4^\circ\text{C}$, $C_A=13.8$ MPa/ $^\circ\text{C}$, $C_M=13.8$ MPa/ $^\circ\text{C}$ ([37]) and under a load of 125 MPa.

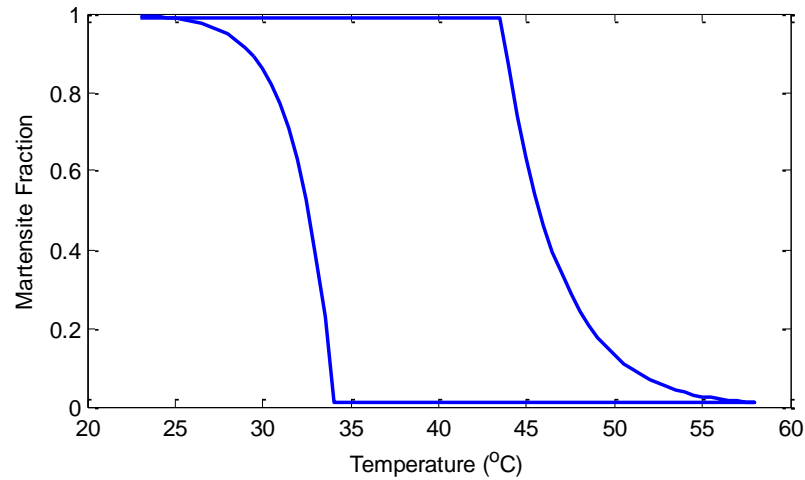


Figure 27. Exponential function phase transformation model by Tanaka

2.6.1.2. *Liang and Rogers' Model*

The constitutive law adopted by Liang and Rogers' model is same as the Tanaka's Model, the difference comes in the transformation fraction estimation

functions. This model presents an alternative evolution law for the martensite fraction base on cosine function [44], [49].

For $A \Rightarrow M$ transformation, the following function has been proposed to represent the martensitic fraction:

$$\xi = \frac{1-\xi_0}{2} \cos \left[A_M \left(T - M_f - \frac{\sigma}{C_M} \right) \right] + \frac{1+\xi_0}{2} \quad \text{Eq. 12}$$

with the definition of the positive material parameter A_M as $A_M = \pi / (M_s - M_f)$.

This representation for martensitic phase transformation holds for stresses in the range defined by:

$$C_M(T - M_s) < \sigma < C_M(T - M_f)$$

or the transformation temperature range for a constant stress is:

$$T_{M_s} < \frac{\sigma}{C_M} + M_s \text{ and } T_{M_f} < \frac{\sigma}{C_M} + M_f$$

For $M \Rightarrow A$ transformation, the following function has been proposed to represent the martensitic fraction:

$$\xi = \frac{\xi_0}{2} \left\{ \cos \left[A_A \left(T - A_s - \frac{\sigma}{C_A} \right) \right] + 1 \right\} \quad \text{Eq. 13}$$

with the definition of $A_A = \pi / (A_f - A_s)$.

This representation for martensitic phase transformation holds for stresses in the range:

$$C_A(T - A_f) < \sigma < C_A(T - A_s)$$

or the transformation temperature range for a constant stress is:

$$T_{A_f} < \frac{\sigma}{C_A} + A_f \text{ and } T_{A_s} < \frac{\sigma}{C_A} + A_s$$

A representative graph is given in Figure 28 with the same material properties given in the previous section.

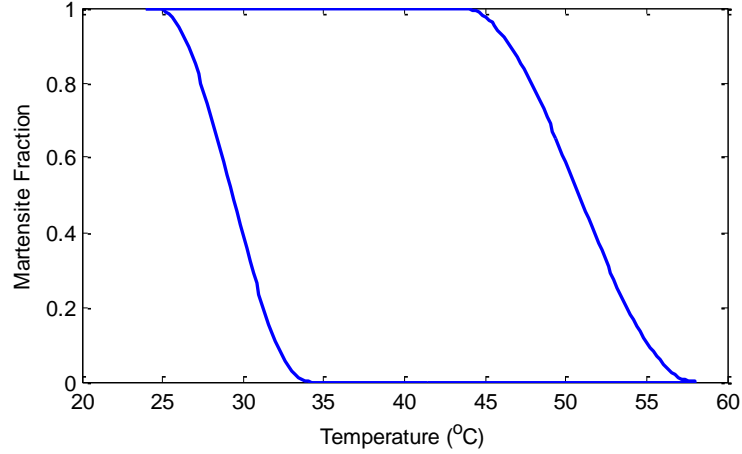


Figure 28. Cosine function phase transformation model by Liang and Rogers'

Liang and Rogers' also developed a three-dimensional model, in which it is suggested that phase transformations are driven by the associated distortion energy [50].

2.6.1.3. *Brinson's Model*

2.6.1.3.1. **Development of the Constitutive Law:**

The thermodynamical foundation of Brinson's model is same as the Tanaka's Model, however in this model the constitutive relation and the definition of the transformation fraction estimation function are redefined using a new internal state variable. This model divides the martensitic transformation into two components as temperature induced fraction, ξ_T , and stress induced fraction, ξ_S . With the introduction of $\xi = \xi_S + \xi_T$ into the constitutive equation (Eq. 6) and using differential calculus the following constitutive equation is obtained:

$$d\sigma = \frac{\partial\sigma}{\partial\varepsilon}d\varepsilon + \frac{\partial\sigma}{\partial\xi_S}d\xi_S + \frac{\partial\sigma}{\partial\xi_T}d\xi_T + \frac{\partial\sigma}{\partial T}dT \quad \text{Eq. 14}$$

leading to the most general equivalent expression

$$d\sigma = E d\varepsilon + \Omega_S d\xi_S + \Omega_T d\xi_T + \theta dT \quad \text{Eq. 15}$$

Again, assuming E , Ω_S , Ω_T , and θ to be constant, the constitutive relation in discrete form can be written as:

$$\sigma - \sigma_0 = E(\varepsilon - \varepsilon_0) + \Omega_S(\xi_S - \xi_{S0}) + \Omega_T(\xi_T - \xi_{T0}) + \theta(T - T_0) \quad \text{Eq. 16}$$

Applying the material restriction of maximum recoverable strain, ε_L , for the initially 100% austenite case, $\xi_{S0}=0$, $\xi_{T0}=0$ with $\sigma_0=0$, $\varepsilon_0=0$ and the final conditions $\xi_S=1$, $\xi_T=0$, $\sigma=0$, $\varepsilon = \varepsilon_L$, the relation between uniaxial transformation coefficient and the maximum recoverable strain should be in the following manner:

$$\Omega_S = -\varepsilon_L.E \quad \text{Eq. 17}$$

Considering the case of maximum recoverable strain with 100% twinned (undeformed) martensite, $\xi_{S0}=0$ and $\xi_{T0}=1$ and remaining conditions identical to the previous case gives the necessity that: $\Omega_T=0$.

Thus the thermomechanical constitutive law with the new separated martensite fraction becomes:

$$\sigma - \sigma_0 = E(\varepsilon - \varepsilon_0) + \Omega(\xi_S - \xi_{S0}) + \theta(T - T_0) \quad \text{Eq. 18}$$

2.6.1.3.2. Estimation of the Martensite Fraction during Phase Transformation:

In this model, two more experimentally found material constants are defined; σ_f^{cr} and σ_s^{cr} are the critical stress values for martensite transformations below which the martensitic transformation temperatures remain constant. The modified stress-transformation temperature plot for this model is given in Figure 29. The transformation for this model is investigated for three different conditions.

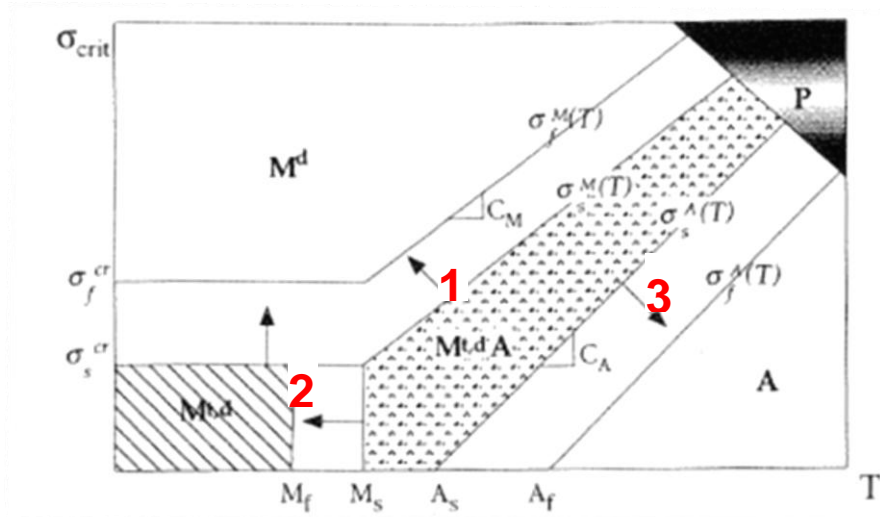


Figure 29. Modified stress-transformation temperature plot [51]

1. For transformation from austenite to detwinned martensite ($A \Rightarrow M^d$) transformation, for $T > M_s$ and under the applied stress in the range:

$$\sigma_s^{cr} + C_M(T - M_s) < \sigma < \sigma_f^{cr} + C_M(T - M_s)$$

The following functions have been proposed to represent the martensitic fractions:

$$\xi_s = \frac{1 - \xi_{s0}}{2} \cos \left[\frac{\pi}{\sigma_s^{cr} - \sigma_f^{cr}} (\sigma - \sigma_f^{cr} - C_M(T - M_s)) \right] + \frac{1 + \xi_{s0}}{2} \quad \text{Eq. 19}$$

$$\xi_T = \xi_{T0} - \frac{\xi_{T0}}{1 - \xi_{s0}} (\xi_s - \xi_{s0}) \quad \text{Eq. 20}$$

2. For $T < M_s$ and the applied stress is in the range $\sigma_s^{cr} < \sigma < \sigma_f^{cr}$, the following definitions for martensite fractions are used:

$$\xi_s = \frac{1 - \xi_{s0}}{2} \cos \left[\frac{\pi}{\sigma_s^{cr} - \sigma_f^{cr}} (\sigma - \sigma_f^{cr}) \right] + \frac{1 + \xi_{s0}}{2} \quad \text{Eq. 21}$$

$$\xi_T = \xi_{T0} - \frac{\xi_{T0}}{1 - \xi_{s0}} (\xi_s - \xi_{s0}) + \Delta_{T\xi} \quad \text{Eq. 22}$$

where, if $M_f < T < M_s$ and $T < T_0$,

$$\Delta_{T\xi} = \frac{1 - \xi_{T0}}{2} \{ \cos[A_M(T - M_f)] + 1 \}$$

else, $\Delta_{T\xi} = 0$

with the definition of A_M same as Liang and Rogers' model.

3. For $T > A_s$ and the applied stress in the range $\sigma_s^{cr} + C_M(T - M_s) < \sigma < \sigma_f^{cr} + C_M(T - M_s)$ the following definitions are used for martensite fractions:

$$\xi_s = \xi_{s0} - \frac{\xi_{s0}}{\xi_0} (\xi_0 - \xi) \quad \text{Eq. 23}$$

$$\xi_T = \xi_{T0} - \frac{\xi_{T0}}{\xi_0} (\xi_0 - \xi) \quad \text{Eq. 24}$$

where

$$\xi = \frac{\xi_0}{2} \left\{ \cos \left[A_A \left(T - A_s - \frac{\sigma}{C_A} \right) \right] + 1 \right\}$$

2.6.1.3.3. Non-Constant Material Functions and Simplifications to the Models

In the models above, the derived constitutive equation assumes constant material functions, however it is known that Young's Modulus, E , has a strong dependence on the phase thus, on the martensite fraction [51]. A reasonable assumption for modulus function of a SMA material as suggested by Liang is given in the following equation (Eq. 25).

$$E(\varepsilon, \xi, T) = E(\xi) = E_a + \xi(E_m - E_a) \quad \text{Eq. 25}$$

where

E_m : Modulus of elasticity for the material in 100% martensitic phase

E_a : Modulus of elasticity for the material in 100% austenitic phase

In order to simplify the Brinson's definition of constitutive equation, Eq. 18 is rewritten in the form:

$$\sigma - \sigma_0 = E(\varepsilon - \varepsilon_0) + \Omega(\xi_S - \xi_{S0}) + \theta(T - T_0) \quad \text{Eq. 26}$$

The equation given above can be expressed as in Eq. 27, where the term K_0 lumps the initial conditions, (Eq. 28), and it is shown by Brinson that it can be omitted without loss of generality of the constitutive equation.

$$\sigma = E(\xi_0)(\varepsilon - \varepsilon_L \xi) + \theta(T - T_0) + K_0 \quad \text{Eq. 27}$$

$$K_0 = \sigma_0 - E(\xi_0)(\varepsilon_0 - \varepsilon_L \xi_0) \quad \text{Eq. 28}$$

In the constitutive equations, T_0 is the state at which thermal strain is defined to be zero. Since thermal strains developed in operational regions are orders of magnitude smaller than the transformation strain, thermal strain component can be neglected; a much more simplified version of the constitutive equation then can be obtained (Eq. 29).

$$\sigma = E(\xi_0)(\varepsilon - \varepsilon_L \xi) \quad \text{Eq. 29}$$

2.7. Characterization of Shape Memory Alloy Wires

Using shape memory elements in actuators requires the characterization of the selected SMA before designing and modeling the application. The characterization mainly concerns with the transformation temperatures, their variations under loading, and stress-strain-temperature relationship. Characterization is important for obtaining the model of the material behavior to be used as the plant in simulations and control system design.

The characterization is generally performed using differential scanning calorimetry (DSC) analysis and electrical resistivity (ER) measurements under stress free condition. In these tests, only transformation temperatures and other physical parameters, like enthalpy and absolute electrical resistance, can be determined.

For tests involving heating-cooling cycles under external load, commercial thermo-mechanical analyzers (TMA) are used to determine both transformation temperatures and strains. These test apparatus have a built-in conditioning chamber to control heating and cooling of the SMA element.

However, SMA elements used in actuators are often heated by Joule heating method, that is, by passing an electrical current through them. In order to characterize SMAs using current as a conditioner, electrical resistance and strain

should be monitored. In the following section, parameters needed for the models are distinguished.

2.7.1. Parameters Required for Modeling

The models explained in section 2.6 require certain parameters in order to fully represent the behavior of the SMA element [52], [53]. The constants needed are given in Table 6 together with the corresponding models. In this table L&R stands for Liang and Rogers' model.

Table 6. Constants needed to be characterized for corresponding models

	Martensite	Austenite	Unit	Model
Free transformation temperatures	M_s^0, M_f^0	A_s^0, A_f^0	°C	Tanaka, L&R, and Brinson
Young's Moduli	E_m	E_a	MPa	Tanaka, L&R, and Brinson
Transformation temperature-stress coefficients	C_M	C_A	MPa/°C	Tanaka, L&R, and Brinson
Critical stresses	$\sigma_s^{cr}, \sigma_f^{cr}$	-	MPa	Brinson
Maximum recoverable strain	ϵ_L		-	Tanaka, L&R, and Brinson

2.7.1.1. Determining Free Transformation Temperatures

Free transformation temperatures can be determined using a DSC. DSC tests measure the relationship between power input/output and temperature change for a small sample of SMA material, and are the standard way of investigating temperature induced phase changes. Peaks in the plot of heat flow vs. temperature given in Figure 30 show exothermic transformations; whereas troughs mark endothermic transformations. The temperatures at which these transformations start and finish are also determined from the plot.

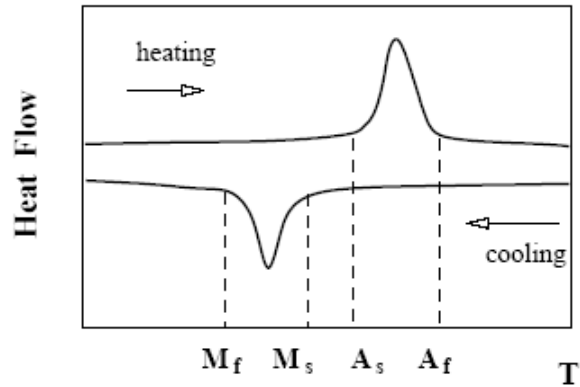


Figure 30. Schematic DSC plot [2]

2.7.1.2. **Determining the Young's Modulus**

Standard stress-strain tests can be performed to determine the Young's Modulus. However, since this parameter is dependent on the phase of the element, to determine the martensitic modulus (E_m) the material should be cooled below M_f^0 and to determine the austenitic modulus (E_a) the temperature should be kept above A_f^0 .

2.7.1.3. **Determining Transformation Temperature-Stress Coefficients**

The constants C_M and C_A can be determined by applying thermal cycling to the wire while inducing various constant stresses. Strain and temperature data should be acquired, and then the transformation temperatures should be determined at different stress levels. Afterwards, transformation temperature vs. stress are plotted (Figure 31) and the slopes of the lines (C_M and C_A) are calculated.

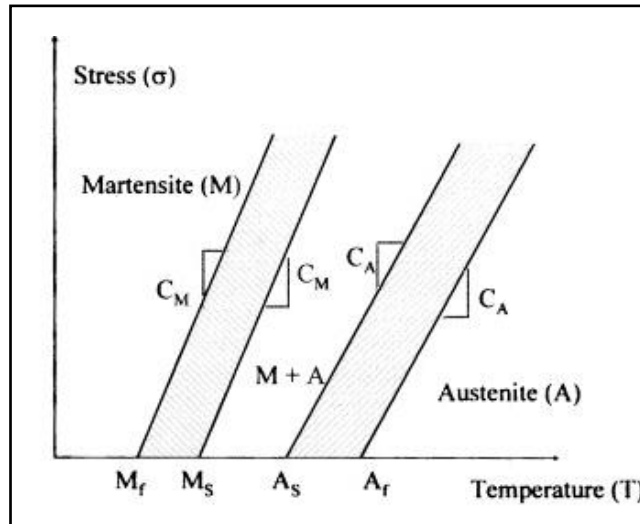


Figure 31. Transformation temperatures vs. stress plot (Tanaka's and Liang and Rogers' Models) [37]

2.7.1.4. Determining Critical Stresses

Critical stresses, σ_s^{cr} , and σ_f^{cr} , for stress induced martensite (detwinned martensite) can be determined through constant temperature stress-strain tests. The transformation stresses of the SMA wire below M_s^0 is expected to be constant in Brinson's model, thus this constant value is determined by plotting stress strain test results at different temperatures (Figure 32).

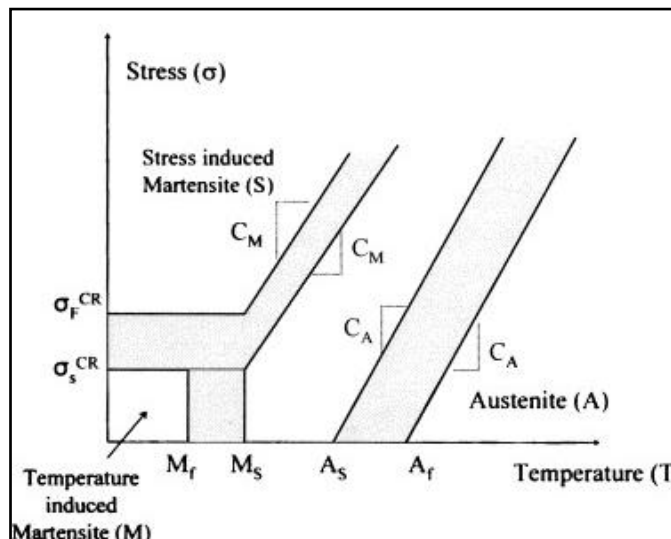


Figure 32. Transformation temperatures versus stress plot (Brinson's Model) [51]

2.7.1.5. Determining Maximum Recoverable Strain

Maximum recoverable strain (ϵ_L), can be determined by applying thermal cycling to the wire while inducing constant stress. Strain data are acquired, and then the maximum strain that the wire can recover is determined.

2.7.2. Characterization Tests

In the next sections, the set-up to characterize the SMA wires to be used in the actuators is described and the results of the experiments and their comparison with the theoretical models are shown.

The wire selected to be tested is “Flexinol 200 HT”, whose properties are presented in Table 5. The load capacities of the wires depend on their diameter and the load capacity is inversely proportional with the speed and time of actuation of the wire. As the diameter becomes larger, the load capacity and the energy needed to activate the wire increase. However, activation time becomes longer thus the bandwidth decreases.

Table 5. It is decided to perform constant stress tests to determine CM and CA to be used in the models.

In this work, an experimental set-up is specially designed to perform electro-thermomechanical cycles under a constant load in thin SMA wire measuring simultaneously its voltage, current, and strain. The apparatus is used to determine the strain-temperature (ϵ -T), electrical resistance (per meter of the wire) versus temperature (R-T), and hysteresis loops of a Ni-Ti SMA wire, being uniaxially loaded in the range of 90 to 210 MPa.

2.7.3. Description of the Test Apparatus

Figure 33 illustrates the experimental test bench specially designed to perform electro-thermomechanical characterization of thin SMA wires. This apparatus is composed basically of a simple mechanical structure, an LVDT (Linear Variable Displacement Transducer) displacement sensor, a power supply, a signal generator, an electronic load, data acquisition system, and a data acquisition computer. In the mechanical structure, an aluminum frame was manufactured using standard (50 mm x 50 mm) profiles joined by screws. On this frame a fixed guide and LVDT are assembled. A 100 mm long SMA wire is

fastened by polyamide screws through silicone plated insulated steel grips. The wire is loaded by hanging dead weight to the wire to assure a uniaxial tensile state on the SMA wire (Figure 34).

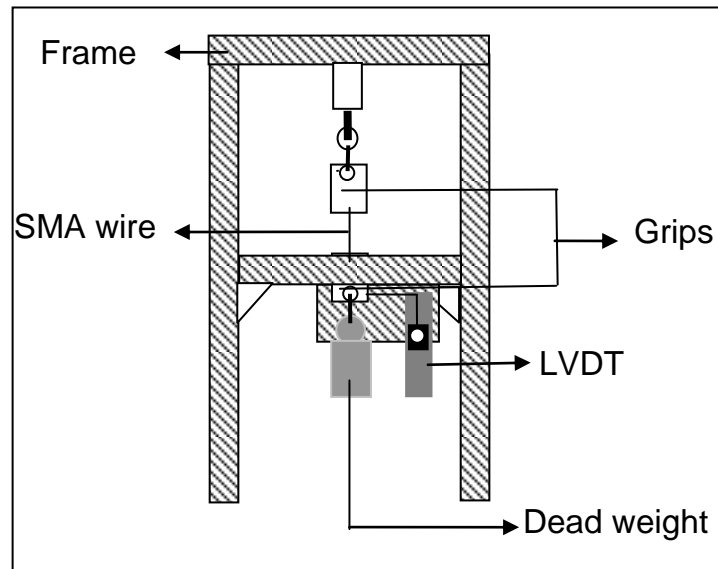


Figure 33. Schematic view of the characterization test bench

The displacement of the SMA is measured by the BALLUFF BTL05 model LVDT with system resolution less than 0.1 mV and full scale reading is 10 Volts. The current supplied to the wire by INSTEK PST3202 power supply is controlled using signal generator MITech 9301, and the electronic load DTL32A-LC by DATEL. The signal generator supplies the necessary voltage to adjust the resistance of the electronic load which is connected to the SMA wire in series so as to control the current through the circuit. Table 7 summarizes the resolution and accuracy values of the instruments used in the test apparatus. A thermocouple of 0.125 mm is attached to the wire using a thermally highly conductive and electrically insulative adhesive OMEGA BOND 101-16. The data acquisition system DAQ Book 2020 with 16 bit resolution is used to simultaneously collect current, voltage, strain, and temperature data. A ceramic resistance of 1 Ω is connected in series to the wire specimen from which the current flowing through is measured. The voltage of the SMA wire is also recorded so that the resistance and power of the wire is calculated.

Table 7. Instruments used in the test apparatus

Instrument	Brand/Model	Resolution	Accuracy
Displacement sensor	BALLUFF BTL05	< 0.1 mV/10V	0.5 μm
Power supply	INSTEK PST3202	1 mA	$\leq 0.1\% + 5\text{mA}$
Signal generator	MITech 9301	frequency	10^{-8} Hz
		amplitude	12 bit
Electronic load	DATEL DTL32A-LC	0.025 %	$\pm 1 \%$
Thermocouple	Omega CHAL -005	-	$\pm 1.5 \text{ }^\circ\text{C}$
Data acquisition system	IOtech Daqbook 2020	16 bit	$\pm 0.1 \%$

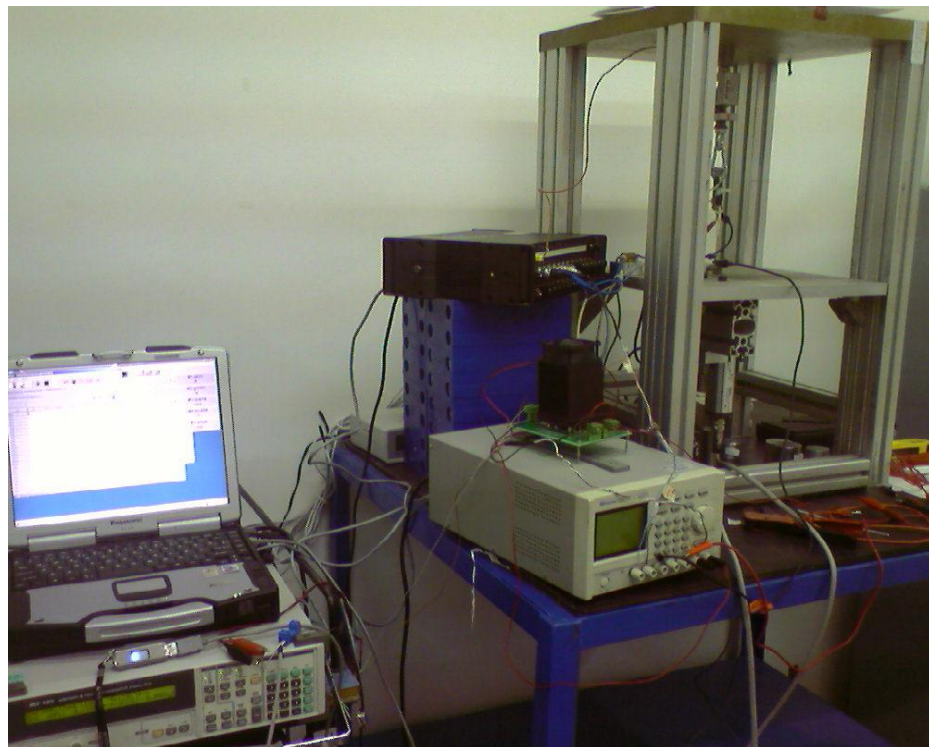


Figure 34. SMA characterization test bench

The circuit design of the set-up is given in Figure 35. The power supply, electronic load, and the wire are connected in series. As shown, the temperature, current, voltage, length of the wire, and the voltage supplied to the electronic load are collected.

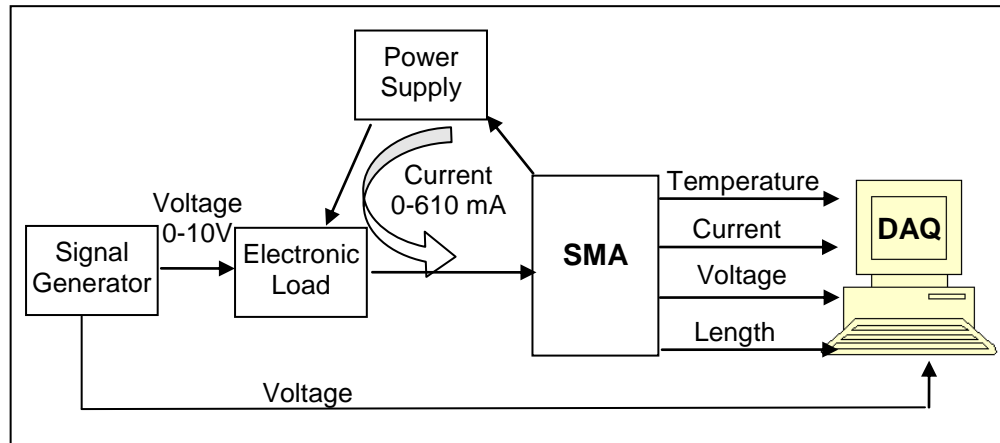


Figure 35. Circuit design of the set-up

2.7.4. Test Procedure and Results

In the experiments, constant stress tests are performed for different stress levels in which ramp current input is supplied to the electronic load thus to the SMA wire. The following steps are performed for the tests:

- Load (dead weight) is hung on the free end of the wire.
- Data acquisition is initiated. Displacement, temperature, current, and voltage data are collected.
- The current is supplied according to the profile given in Figure 36. The heating and cooling cycle takes approximately 5000 seconds to complete while the current is supplied at a rate of 0.22 mA/s.
- Data acquisition is ended.

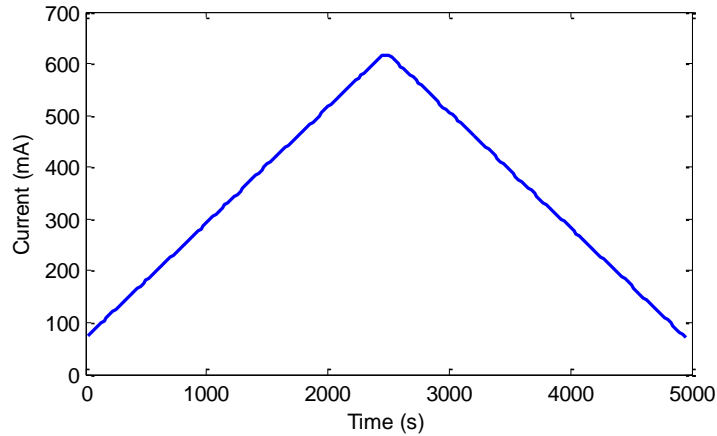


Figure 36. Current profile supplied for characterization

The temperature data of the wire collected during the tests is given in Figure 37. However, since the thermocouple may disturb the temperature of the wire and the ambient temperature is not being controlled, the temperature data may not be very accurate and these temperatures should be regarded as representative values.

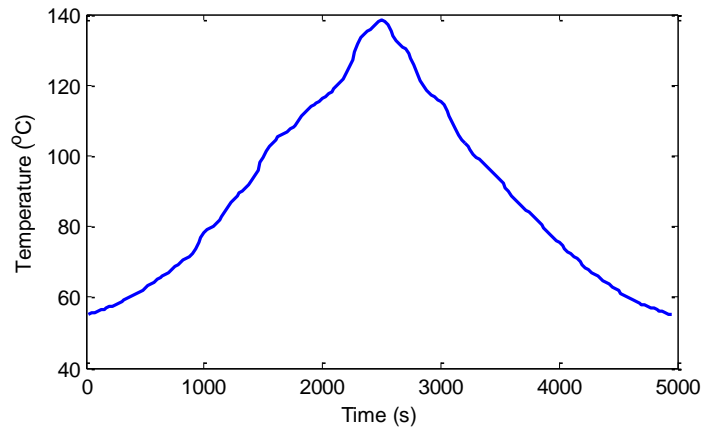


Figure 37. Temperature profile of the wire

Collected data are processed using Matlab® and an m-file which is a standard Matlab® file format developed for this purpose. Eventually, the strain-temperature (Figure 38) and strain-current (Figure 39) curves are obtained. For all the applied loads, strain of the SMA wire was practically constant between 2.9 and 3 %, indicating that a complete orientation of martensite variants occurs

between 90 and 210 MPa. It is also clearly observed that the hysteresis loops move toward the higher temperatures with an increasing stress level.

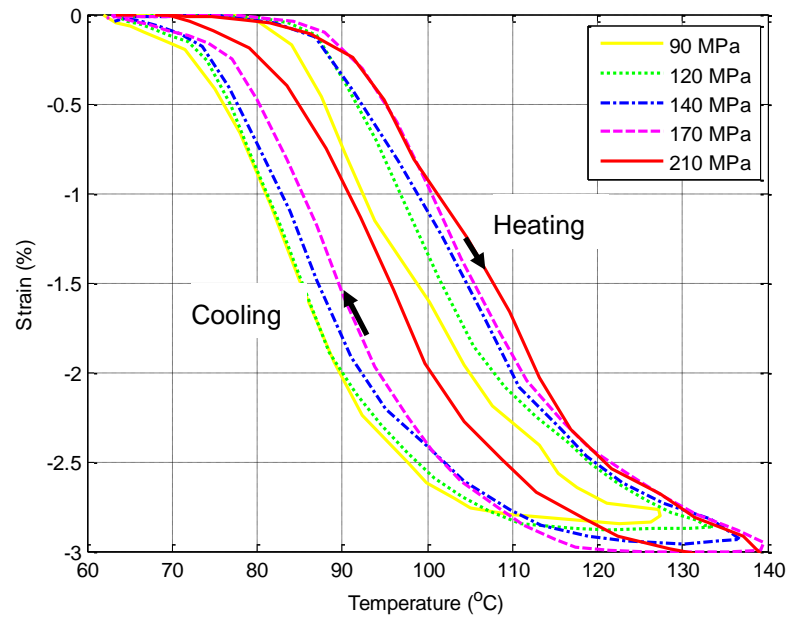


Figure 38. Strain-temperature results of the experiments under various stress levels

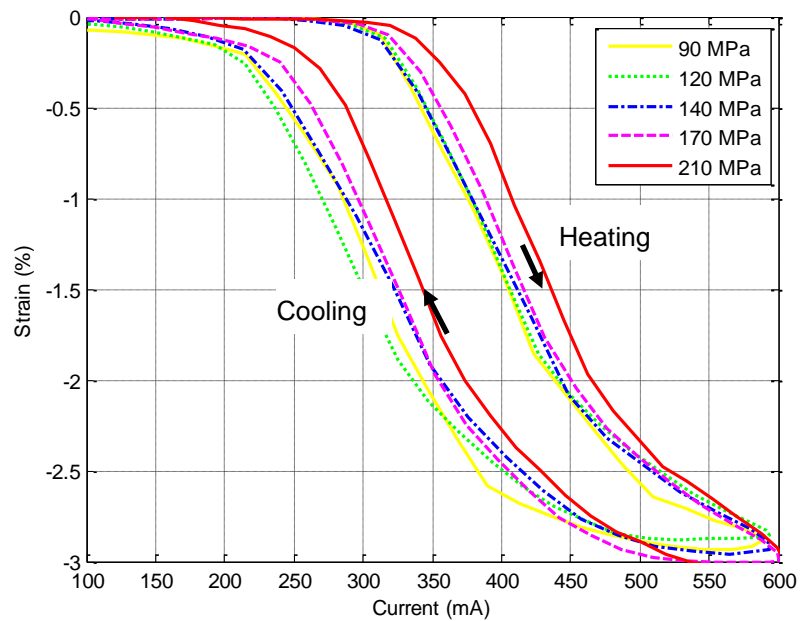


Figure 39. Strain-current results of the experiments under various stress levels

Another phenomenon to observe is the decrease in the width of the hysteresis. The hysteresis width drops of about 8°C in the range between 90 and 210 MPa as given in Figure 40.

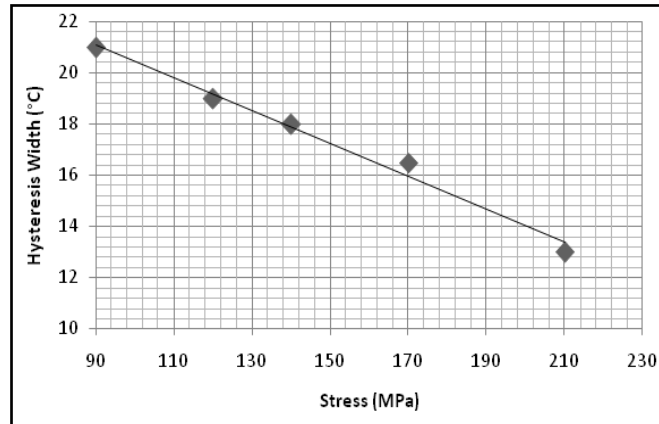


Figure 40. Hysteresis width-stress plot

Using the collected data, resistance of the wire per meter is also plotted as a function of the temperature of the wire (Figure 41) and the current passing through the wire (Figure 42). It is observed that for the loads applied, the electrical resistance reaches its maximum values between 2.5 and 3.5% higher than the resistance values at 25°C. It is also observed that the resistance values decrease by 16 to 18% during transformation.

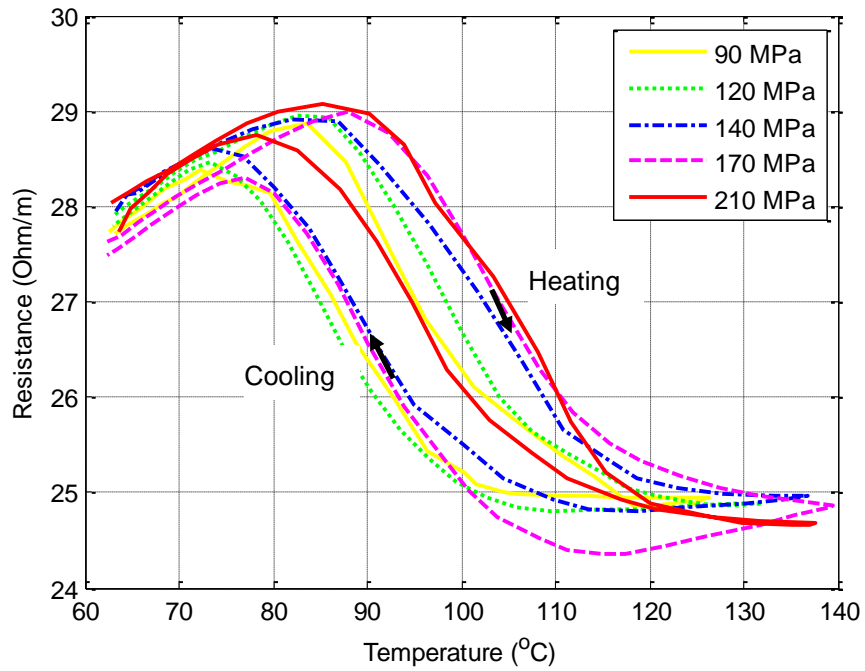


Figure 41. Resistance-temperature results of the experiments under various stress levels

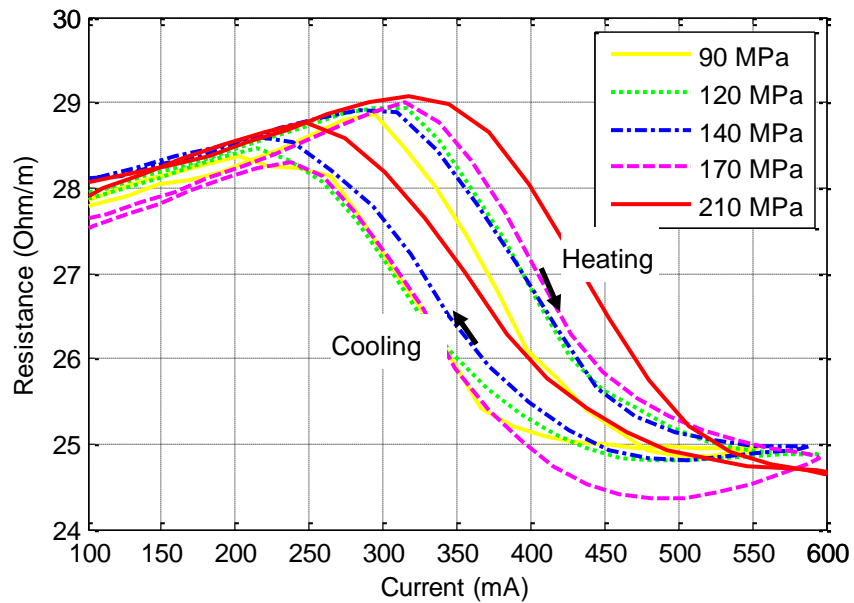


Figure 42. Resistance-current results of the experiments under various stress levels

The characterization process can be mapped into stress-strain diagram as given in Figure 43. In the figure, as a representative case, process 1 shows the path for loading wire with 210 MPa stress, process 2 is the heating process,

process 3 is cooling back to initial state under the effect of the load and process 4 shows the removal of load after deformation at low temperature.

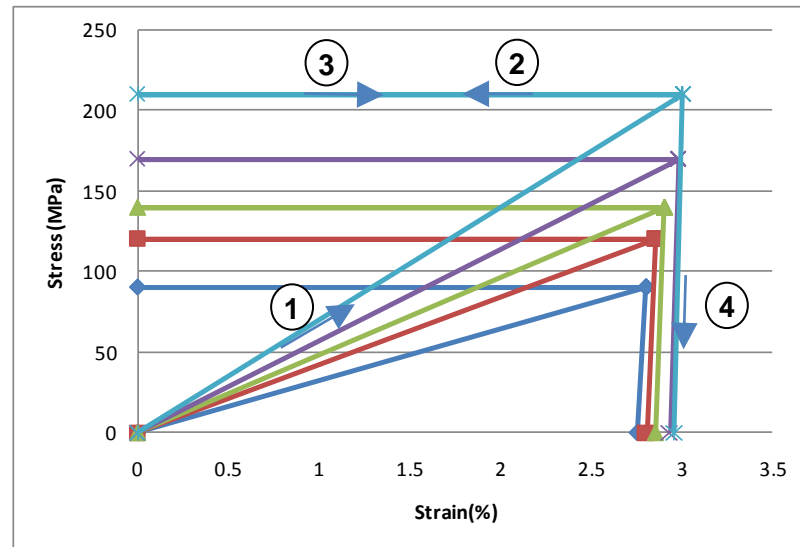


Figure 43. Map of characterization on stress-strain diagram

2.7.5. Estimation of Characteristic Parameters

The plots of strain-temperature data are used to estimate the transformation temperatures at different stress levels. After the transformation temperatures are estimated for all stress levels, the plot of transformation temperatures vs. stress levels is obtained (Figure 44). The slopes of the inclined lines in the plot give the required parameters as $C_A=7.4 \text{ MPa}/^\circ\text{C}$ and $C_M=5.8 \text{ MPa}/^\circ\text{C}$.

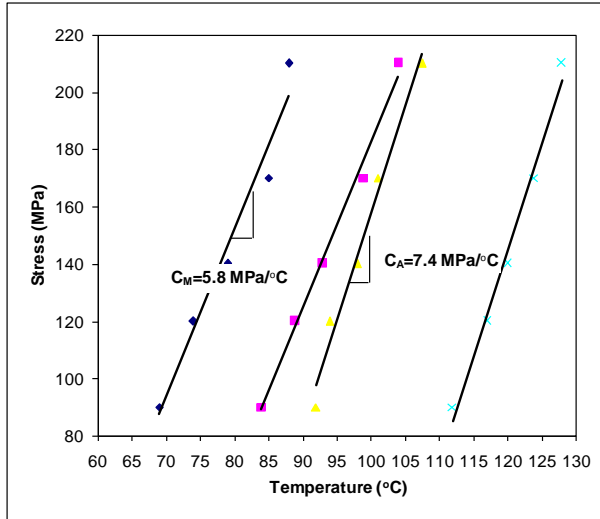


Figure 44. Variation of transformation temperatures with the applied loads

2.7.6. Comparing Test Results with Theoretical Models

Since only C_A and C_M are determined, Brinson's model cannot be simulated as mentioned in the preceding section. Tanaka's and Liang and Rogers' models for strain-temperature, ignoring thermal strain term, will be presented on the strain-temperature plots obtained directly from the experiments for different loading conditions.

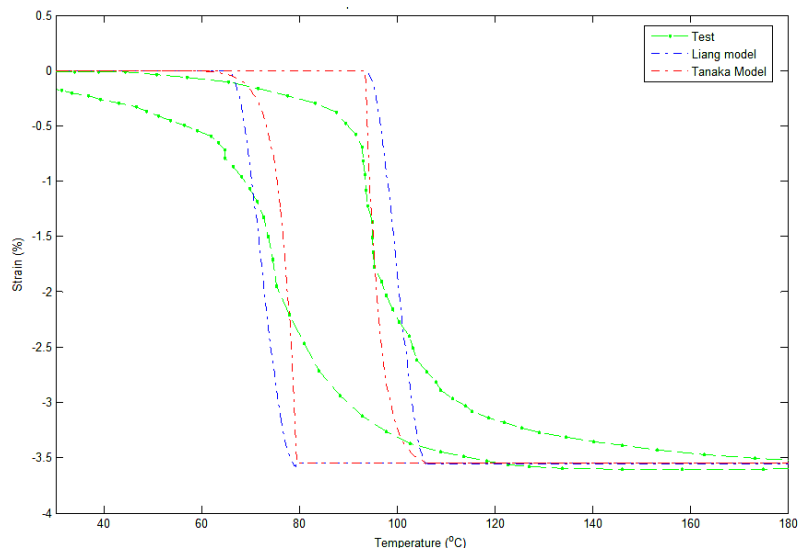


Figure 45. Strain-temperature plot under 90 MPa stress

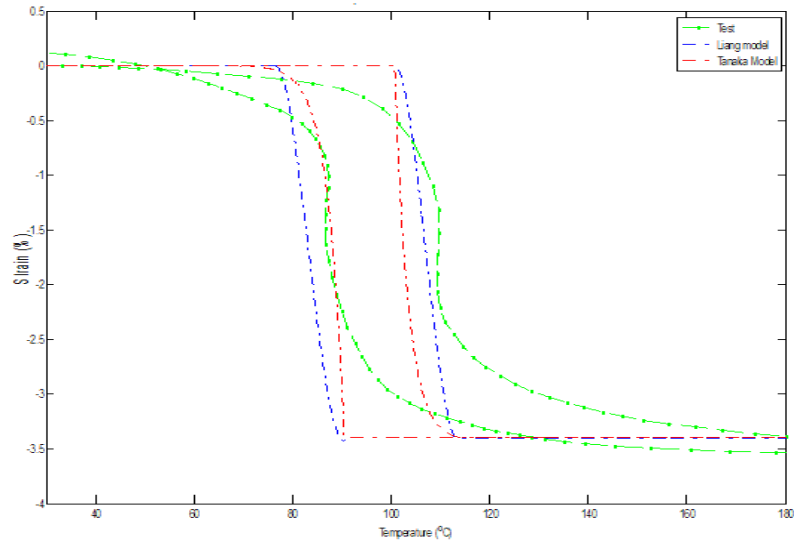


Figure 46. Strain-temperature plot under 140 MPa stress

When the plots in Figure 45 and Figure 46 are investigated, it is observed that both of the models are not sufficient to represent the behavior of the experimented shape memory alloy wire. The kinematic part of the discussed models, where transformation ratio is estimated, is a kind of curve fit on the experimental data. This may be the reason why these models do not effectively fit on the collected data. Another reason why these models do not represent the experimented wire may be the effect of heating rate in the experiments, in the literature there is no evidence how the samples are heated while obtaining these models. The modeled curves may fit on data where pseudo-thermo-static effects are ignored, i.e, the wires are heated very rapidly.

2.8. Modeling of Shape Memory Alloy Wires

In a control system design, a model is invaluable as a design aid. An accurate model of a system to be controlled permits the designer to conduct experiments with the proposed controllers through the simulation. Also, an accurate model can be used to tune the parameters of more sophisticated controllers.

Developing a mathematical model that captures the behavior of an SMA as it undergoes temperature, stress, and phase changes is a complicated and challenging problem also associated with the significant hysteresis behavior. Researchers continue to study how best to model and control the actuators that use this unique family of materials.

Transformation in SMA wires can be observed using the variables that can be classified into two categories as external variables (displacement and stress) and internal variables (temperature, martensite fraction, and electric resistance). While the stress and displacement of the elements are relatively straight forward to measure, the temperature and internal martensite fraction are not.

In order to determine martensite fraction, various parameters including resistivity can be used which is relatively easy to measure. However, in resistance calculation (voltage/current) from the obtained data involves division operation which sometimes leads to numerical problems; in this study, power consumption (voltage x current) of the SMA element is proposed to be used as an alternative. Since most actuator applications require displacing an object against an opposing force, strain, resistance, and power are chosen as control parameters, i.e controller inputs.

Considering the difficulty in directly measuring the temperature and the fact that Joule heating is going to be used as heating method, the models of force and position control need to have current as the controlling input, i.e. controller output.

The models discussed in the previous section are not suitable to be used in this study as they do not exactly match the experimental data. Since every model discussed in literature is a kind of curve fitting to an experimental data, it is decided to build a new model by curve fitting on strain-current, resistance-current, and power-current curves for a constant force applied to the SMA depending on the obtained experimental data. Then, various types of controllers will be designed using this model. In the forthcoming sections of this study, a verification of the controllers will be presented for the models where different forces are applied.

In the next section, the SMA wire is first modeled in Matlab[®] SIMULINK[®] environment with current being the input, absolute strain (the transformation causes contraction thus negative strain), resistance, and power as the output. Afterwards, the relationships between strain-resistance and strain-power are investigated. Simulations are run and the results are then compared to experimental findings for certain test inputs. As the representative data set, 140

MPa stress experiment, where a load of 450 gr hung on the SMA wire is selected.

2.8.1. Strain-Current Relation

Absolute strain output of the SMA wire is modeled using curve fitting of sigmoid type functions (Figure 47). Firstly, martensite start (M_s), martensite finish (M_f), austenite start (A_s), and austenite finish (A_f) currents are estimated and then the parameters of the indicated sigmoid functions a_A , a_M , I_A , and I_M are defined as follows:

$$a_A = \frac{5}{(A_s - A_f)} \quad a_M = \frac{5}{(M_s - M_f)}$$

$$I_A = \frac{(A_s + A_f)}{2} \quad I_M = \frac{(M_s + M_f)}{2}$$

where

$$M_f = 250 \text{ mA} \quad A_s = 300 \text{ mA}$$

$$M_s = 450 \text{ mA} \quad A_f = 550 \text{ mA}$$

As shown in Figure 47, the maximum recoverable strain (ϵ_r) occurs as 2.95%. In the Simulink model the activation strain rate is limited to 4 %/sec and relaxation strain rate is set as 1.8 %/sec using the specified values for the wire in the data sheet.

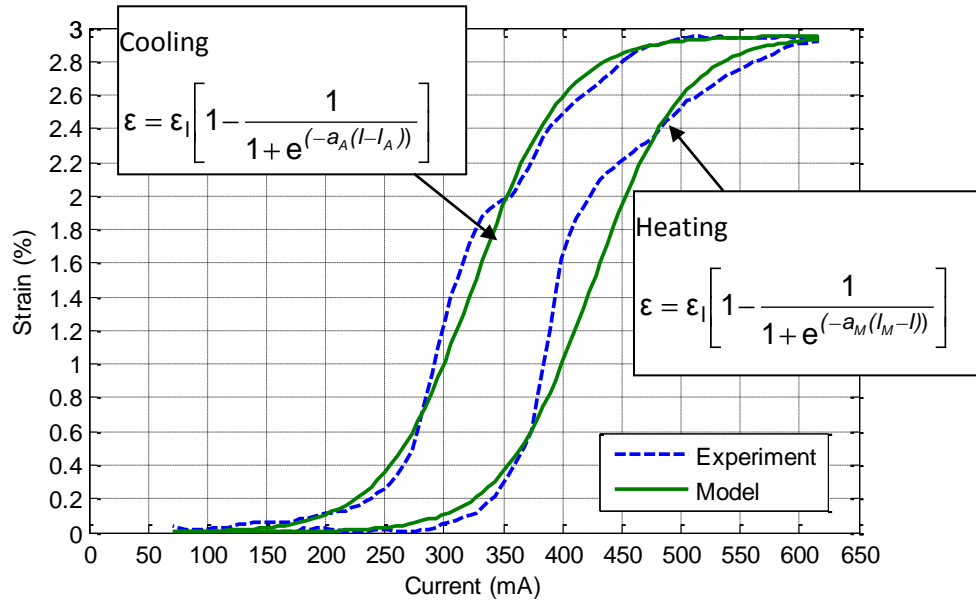


Figure 47. Strain-current model

2.8.1.1. Model Validation with Ramp Input

To this extent, the designed sigmoid type model is run with ramp current input, and experiments were conducted with the same input. For the experiments, the ramp current profile presented in Figure 36 with a maximum of 610 mA is used.

The plots of the simulation and experiment results of the strain of the wire can be seen in Figure 48.

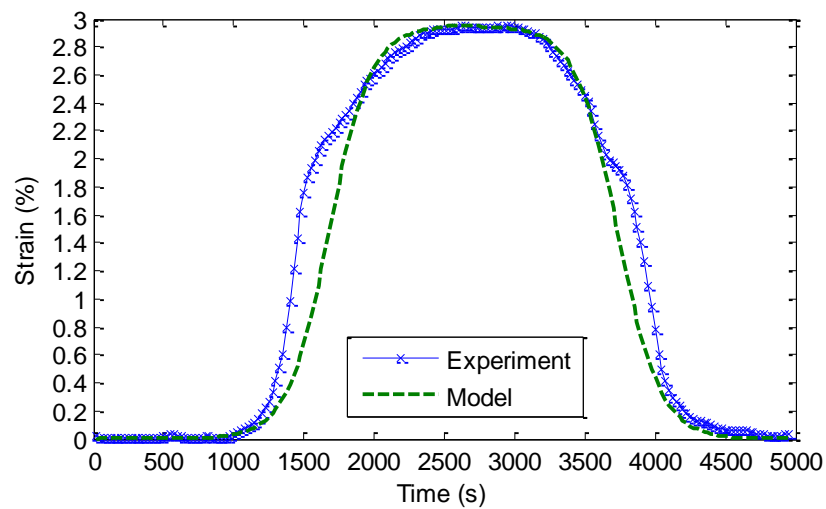


Figure 48. Experiment and model results for strain model with ramp input

2.8.1.2. Model Validation with Step Input

The experiments and simulations using step current input are also made. The aim of these experiments and simulations is to see the strain output of the SMA wire to a specific current input while heating and cooling.

As shown in Figure 49, the same current inputs are given in the experiment and in the simulation.

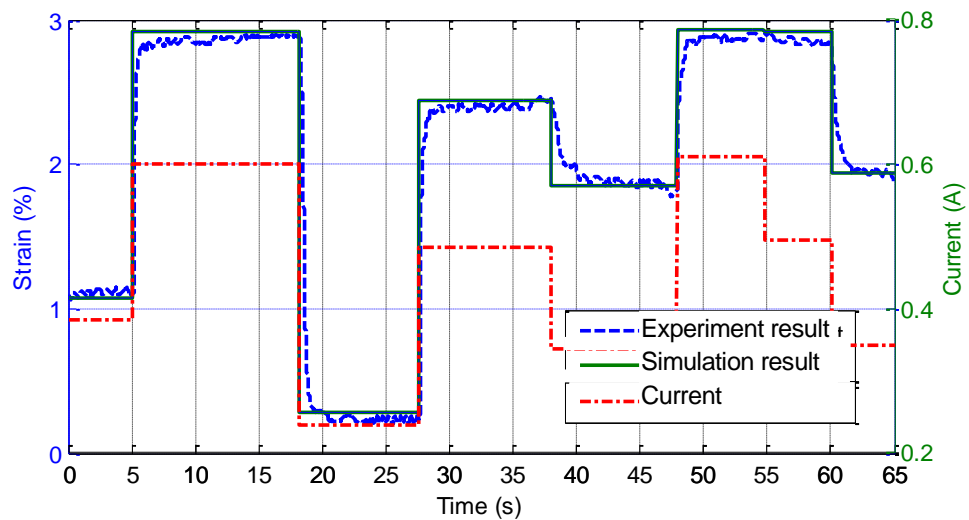


Figure 49. Experiment and simulation results of strain of SMA wire to step current input

As can be seen in Figure 49, the results obtained from the computer simulation and the relevant experiment for the same step input are the same. These results demonstrate that the model captures the behavior and hysteresis of the wire very well.

2.8.1.3. Frequency Response Analysis of Strain-Current Model

The frequency response of the strain model for the wire is also analyzed. Figure 50 shows the block diagram made for frequency analysis of the model. 0.305 A current is supplied to the model in a sine wave form with a bias of 0.305 A (Figure 51) to cover the whole transformation range with different frequency values. Bode diagrams for magnitude and phase are plotted for strain model as presented in Figure 52.

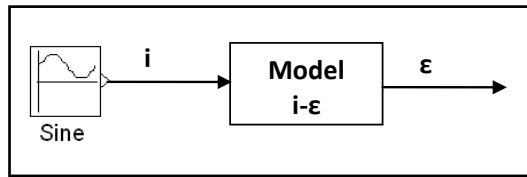


Figure 50. Block diagram for frequency response analysis of strain model

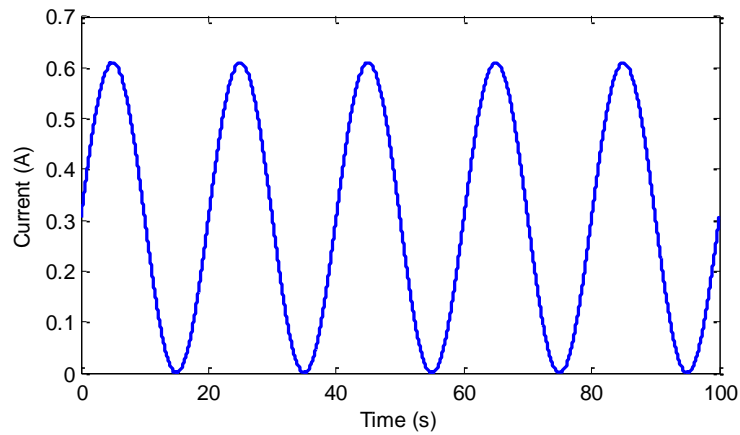


Figure 51. Current supplied to the model

The magnitude of the Bode plot is obtained using the relation:

$$M=20\log\left(\frac{\epsilon_{\max}-\epsilon_{\min}}{\epsilon_l}\right)$$

In this relation, ϵ_{\max} and ϵ_{\min} are the maximum and minimum strain values in a cycle and ϵ_l is the maximum achievable strain defined previously in 2.8.1.

Phase shift is calculated as:

$$\phi=f*(t_{\text{peak}}(\epsilon)-t_{\text{peak}}(i))*360^\circ$$

where $t_{\text{peak}}(\epsilon)$ and $t_{\text{peak}}(i)$ are the time values where strain and current become maximum in a cycle and f is the frequency of the current command.

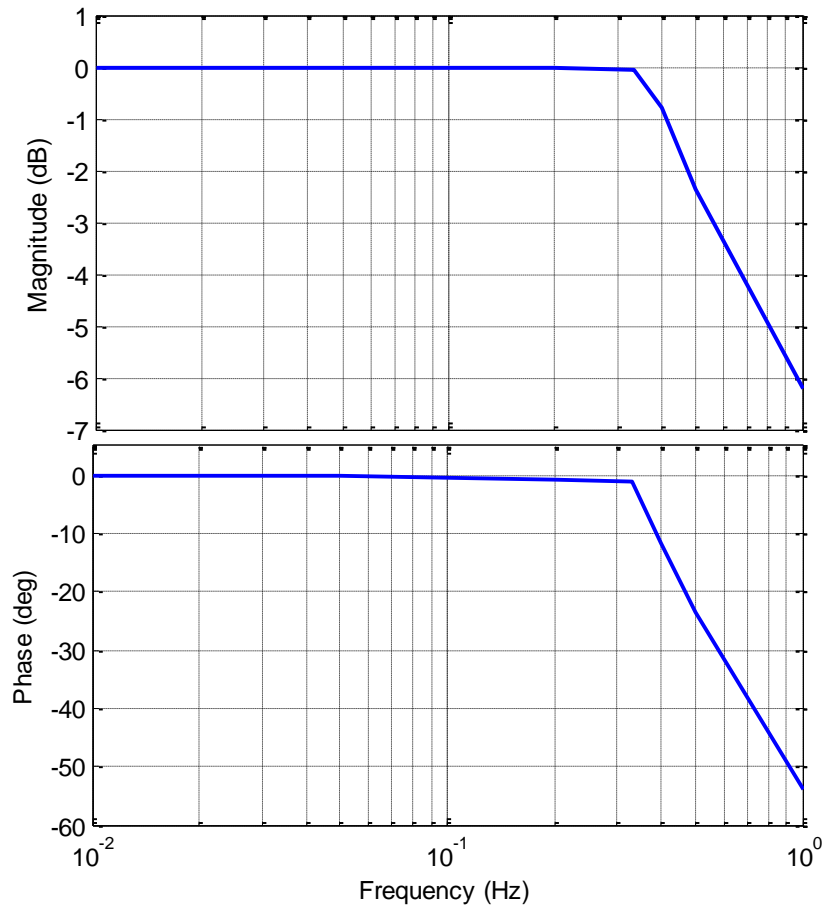


Figure 52. Bode Plot for strain model

As seen from the Bode plots the strain model can complete the full cycle for the given current commands up to nearly 0.3 Hz frequency under normal cooling conditions.

2.8.2. Resistance-Current Relation

Resistance of the SMA wire per unit length is also modeled using curve fitting of linear and exponential functions. The resistance of the wire is calculated by dividing the voltage of the wire to the current passing through the wire, and the length of the wire (Ohm/m). The resistance of the wire is calculated per unit length in order to generalize the results; so that later any length of the wire can be used obtaining the same values. While modeling the resistance-current relation, firstly, martensite start (M_s), martensite finish (M_f), austenite start (A_s), and austenite finish (A_f) currents are estimated and then a_A , a_M , I_A , and I_M are defined as follows:

$$a_A = \frac{13}{(A_s - A_f)} \qquad a_M = \frac{8}{(M_s - M_f)}$$

$$I_A = \frac{(A_s + A_f)}{2} \qquad I_M = \frac{(M_s + M_f)}{2}$$

where

$$M_f = 250 \text{ mA} \qquad A_s = 300 \text{ mA}$$

$$M_s = 450 \text{ mA} \qquad A_f = 550 \text{ mA}$$

The slope of the linear part can be defined as: $m = 0.046 \text{ Ohm}/(\text{m} \cdot \text{mA})$. R_{max} is the maximum value of the resistance in martensitic phase, 29.06 Ohm/m , and R_{min} is the minimum value of the resistance that is observed during austenitic phase, 24.79 Ohm/m . In the Simulink model the heating resistance change rate is limited to 6 Ohm/m/sec and relaxation resistance change rate is set as 2.7 Ohm/m/sec .

Hence, the model for the current-resistance relation is obtained as shown in Figure 53.

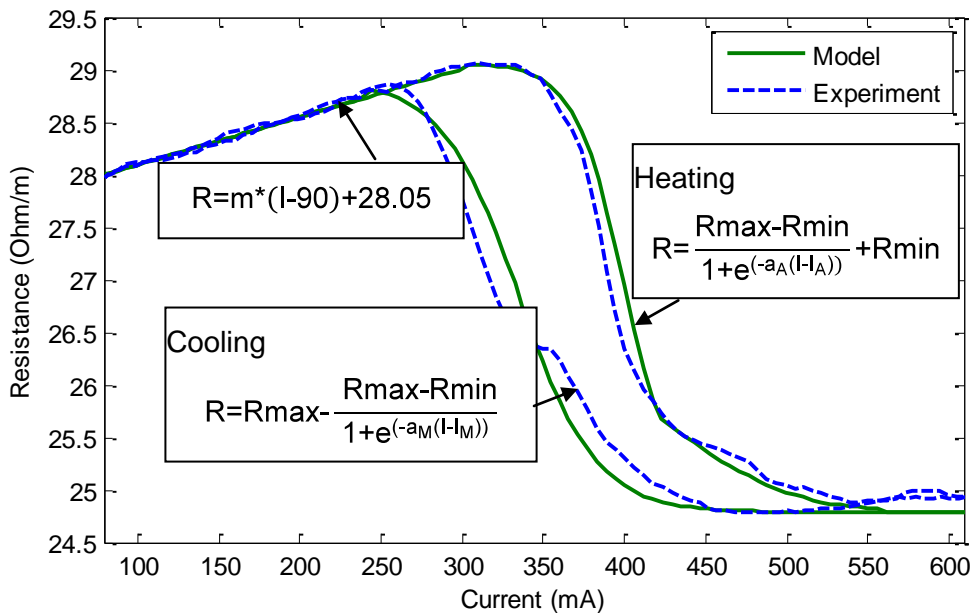


Figure 53. Resistance-current model

2.8.2.1. Model Validation with Ramp Input

The designed model is run with ramp current input, and the relevant experiments are conducted with the same input. For the experiments with ramp input, the current profile presented in Figure 36 is used.

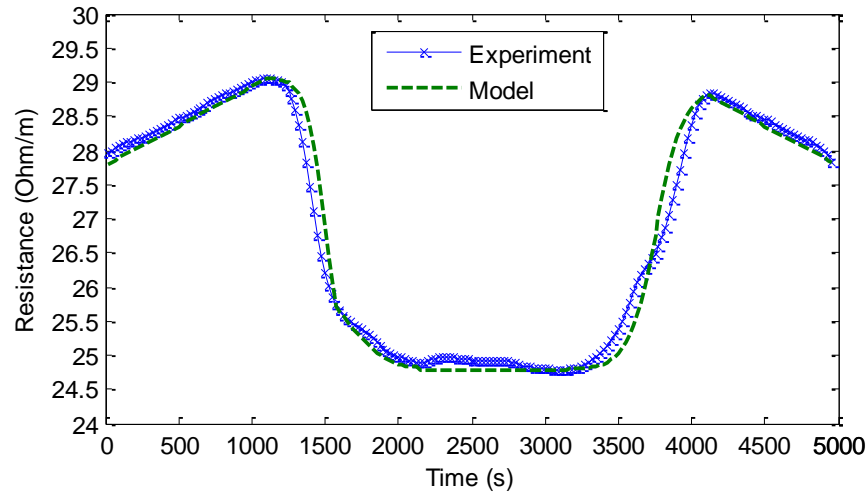


Figure 54. Experiment and model results for resistance with ramp input

The combined plot of simulation and experiment results of the resistance of the wire can be seen in Figure 54 for comparison.

2.8.2.2. Model Validation with Step Input

As done before, the computer simulations and laboratory experiments are conducted for the selected step current input sequence. The aim of these efforts is to see the resistance output of the SMA to a specific current input while heating and cooling.

The same inputs are given in the simulation and also in the experiments. As seen in Figure 55 the step input results are the same. Again, the behavior of the wire with its hysteresis characteristics is very well captured by the model.

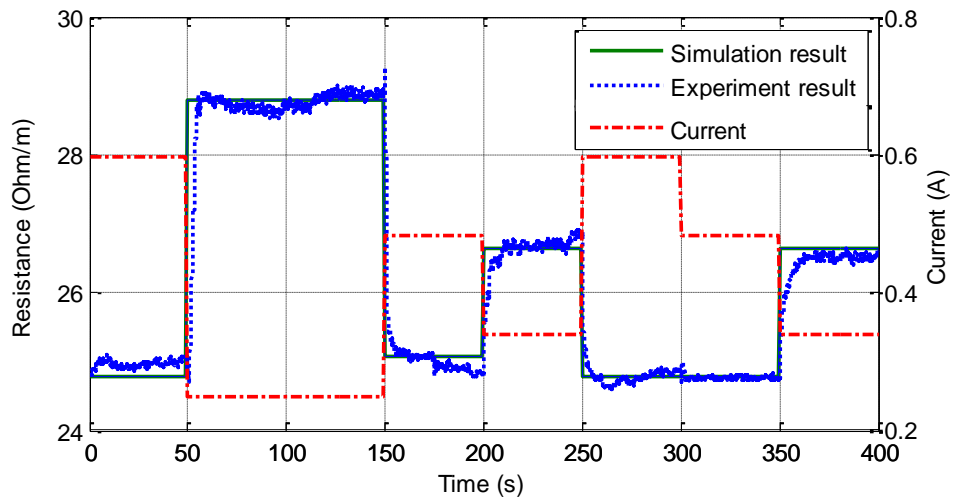


Figure 55. Experiment and simulation results of SMA resistance model with step input

2.8.2.1. Frequency Response Analysis of Resistance-Current Model

The frequency response of the resistance model is analyzed. Figure 56 shows the block diagram made for frequency analysis of the model. As for the strain model 0.305 A current is supplied to the resistance model in a sine wave form with a bias of 0.305 A (Figure 51) to cover the whole transformation range with different frequency values. Bode diagrams for magnitude and phase are plotted for resistance model as presented in Figure 52.

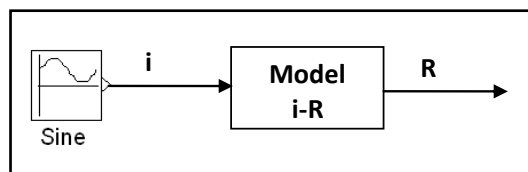


Figure 56. Block diagram for frequency response analysis of resistance model

The magnitude of the Bode plot is obtained using the relation:

$$M=20\log\left(\frac{R_{\max}-R_{\min}}{\Delta R}\right)$$

Where, R_{\max} and R_{\min} are the maximum and minimum resistance values in a cycle, ΔR is the difference between maximum and minimum resistance values in a full cycle which is 4.27 Ohm/m.

Phase shift is calculated as:

$$\phi = f * (t_{\text{peak}}(R) - t_{\text{peak}}(I)) * 360^\circ$$

In this relation, $t_{\text{peak}}(R)$ and $t_{\text{peak}}(I)$ are the time values where resistance and current are maximum in a cycle and f is the frequency of the current command.

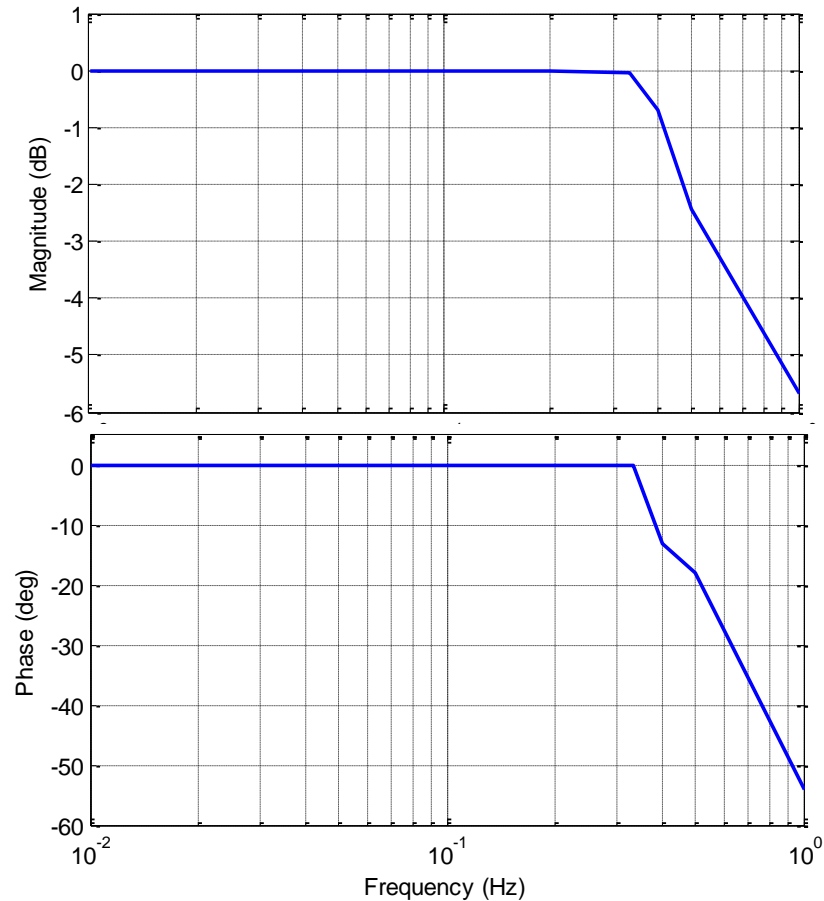


Figure 57. Bode Plot for resistance model

As seen from the Bode plots resistance model can also complete the full transformation cycle for the given current commands up to nearly 0.3 Hz frequency under normal cooling conditions.

2.8.3. Power-Current Relation

Power dissipation of the SMA wire per unit length is also modeled using curve fitting of polynomial functions. The power of the wire is calculated by multiplying the voltage of the wire with the current passing through the wire, and

dividing by the length of the wire (W/m). The power of the wire, like resistance, is calculated per unit length in order to generalize the results; so that later any length of the wire can be used obtaining the same values. Power dissipation of the SMA wire per unit length is modeled using curve fitting of a convenient fourth order polynomial function as given in Figure 58. In the Simulink model for power the power change rate is limited to 11 W/m/sec and cooling phase power change rate is set as 5 W/m /sec.

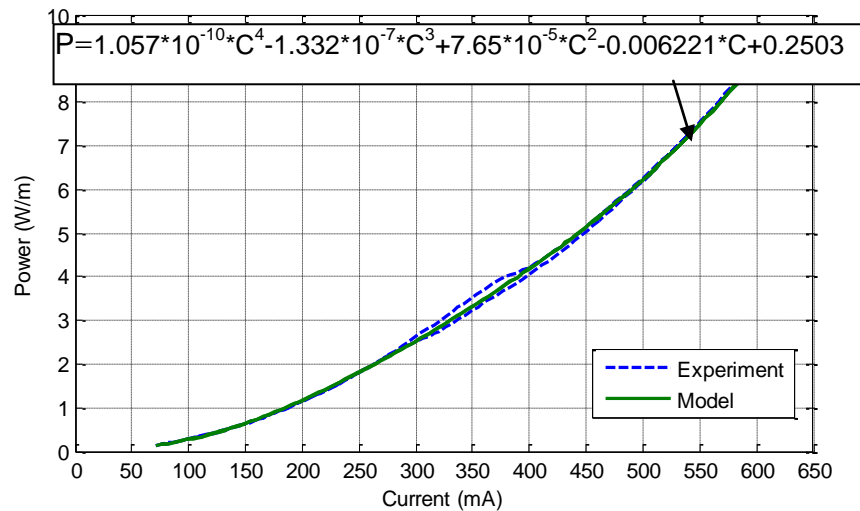


Figure 58. Power-current model

2.8.3.1. Model Validation with Ramp Input

In a similar manner, the power model is run with ramp current input, and the relevant experiments are conducted with the same current input given in Figure 36.

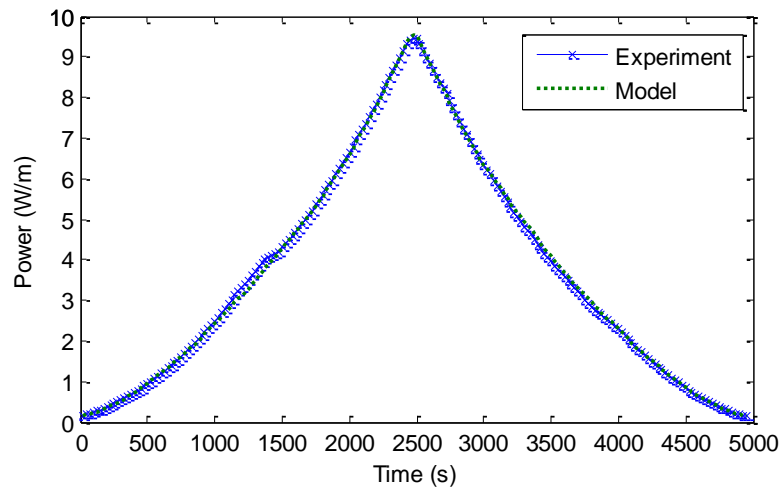


Figure 59. Experiment and model results for power of the wire using ramp input

Simulation and experiment results for the power dissipation of the SMA wire can be seen in Figure 59 for comparison.

2.8.3.2. Model Validation with Step Input

The computer simulations and laboratory experiments are conducted for step current input. The same inputs are given in the simulation and also in the experiments. As seen in Figure 60, the step input results are the same.

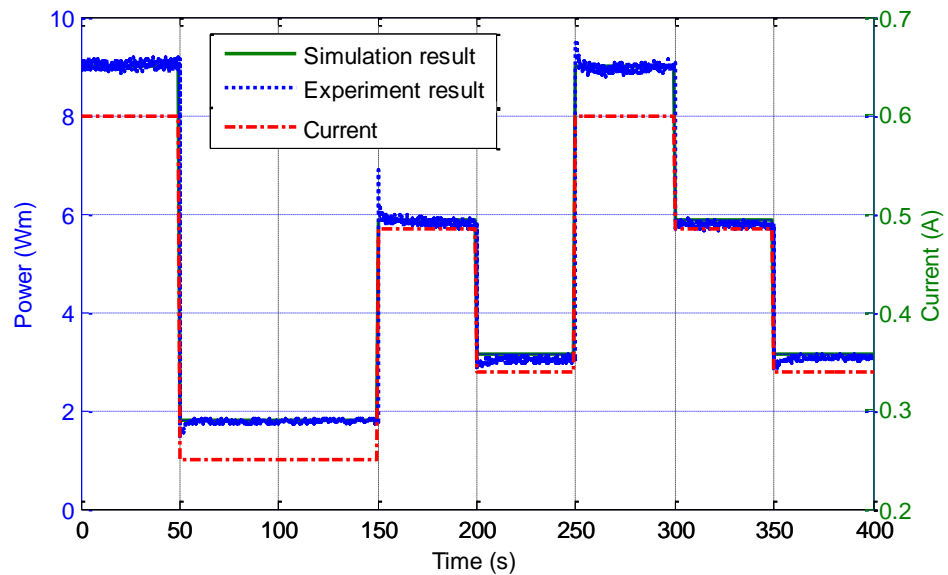


Figure 60. Experiment and simulation results of power of SMA wire to step current input

2.8.3.1. Frequency Response Analysis of Power-Current Model

The frequency response of the power model is also analyzed. Figure 65Figure 61 shows the block diagram made for frequency analysis of the power model. 0.305 A current is supplied to the power model in a sine wave form with a bias of 0.305 A as in the strain model (Figure 51). Bode diagrams for magnitude and phase are plotted for power model as presented in Figure 62.

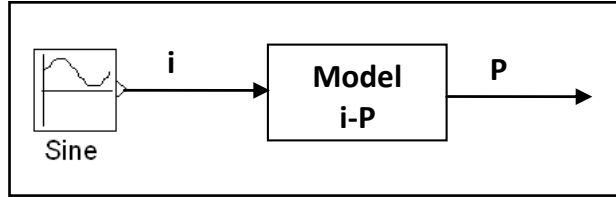


Figure 61. Block diagram for frequency response analysis of power model

The magnitude of the Bode plot is obtained using

$$M=20\log\left(\frac{P_{\max}-P_{\min}}{\Delta P}\right)$$

In this relation P_{\max} and P_{\min} are the maximum and minimum power values in a cycle; ΔP is the difference between maximum and minimum power values in a full cycle which is 9.4 W/m.

Phase shift is calculated as:

$$\phi=f*(t_{\text{peak}}(P)-t_{\text{peak}}(i))*360^{\circ}$$

Where $t_{\text{peak}}(P)$ and $t_{\text{peak}}(i)$ are the time values where power and current are maximum in a cycle and f is the frequency of the current command.

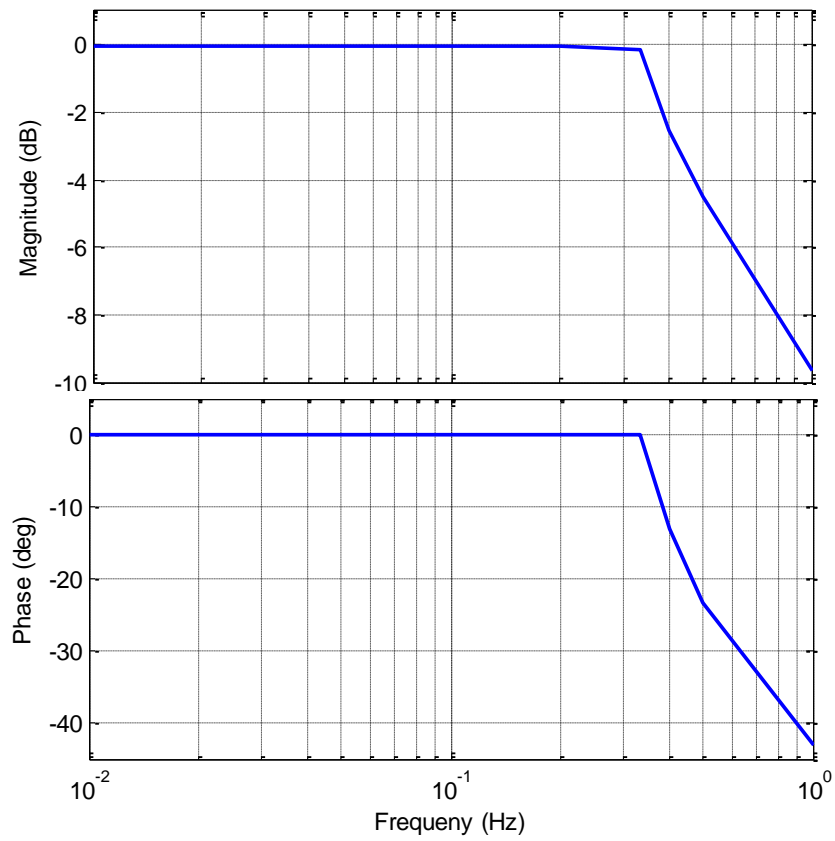


Figure 62. Bode Plot for power model

As seen from the Bode plots power model can also complete the full transformation cycle for the given current commands up to nearly 0.3 Hz frequency under normal cooling conditions.

CHAPTER 3

POSITION CONTROL OF SHAPE MEMORY ALLOY WIRES

In the actuators using shape memory alloys work can be extracted by two ways. One of them is the bias type actuation where resetting is achieved by either a bias spring or a dead weight. The second one is the differential or antagonistic type actuation where two SMA elements are actuated opposing to each other. In both cases, a sufficient control of displacement in SMAs is needed.

3.1. Overview of Control Methods Applied to SMA Actuators

Research efforts in control of actuators employing shape memory alloy elements include linear control, nonlinear control, pulse width modulation, neuro-fuzzy systems, and variable structure control. Among those methods, linear control methods such as proportional (P), proportional-integral (PI), and proportional-integral-derivative (PID), have been widely explored by several researchers. PID control strategies have been found to produce steady-state errors, to induce limit cycle problems [53].

Ikuta classified feedback control variables into two categories of external variables (displacement and stress) and internal variables (temperature and electric resistance) [55]. According to his work, electric resistance could be used as a feedback variable since it is almost a linear function of martensite fraction with negligible hysteresis as seen in Figure 63, and also easy to measure. In his work, an antagonist type gripper is introduced in which control is achieved by a PID controller using position and resistance feedback.

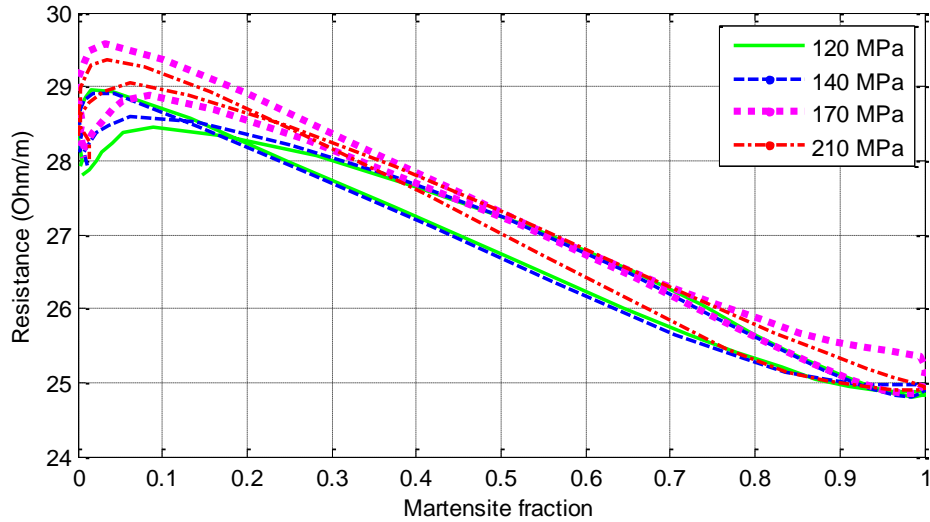


Figure 63. Resistance versus martensite fraction

Tanaka and Yamada have developed a differential rotary actuator using air for cooling [56]. PID controller with temperature feedback is employed in the actuator where a simple constitutive model (phase transformation not included) and pulse width modulation are used.

The work by Pons et al. investigates and compares different control schemes in order to avoid position overshoot while trying to maintain the fastest possible response for a given cooling method [57]. Both external and internal error sensing is used throughout the tests. PI control approach with internal resistance feedback, linearization of actuator model by direct strain feedback, and feedforward control approach have been investigated. It was shown that overall overshoot avoidance and faster response can be achieved by resistance self-sensing capability of the SMA.

Troisfontaine et al. performed two different control techniques on SMA actuators [58]. One of them is based on position feedback; whereas the second one is based on temperature feedback. They concluded that temperature feedback does not permit position control of SMA actuators.

Wijst et al., presented a control law for SMA wire actuator consisting of open and closed loop parts [59]. The open loop part takes into account the stress-strain-temperature behavior. This part estimates the required wire temperature depending on the desired position, and subsequently calculating

desired electric power as an input to the system. The mentioned input is then added up to the control input from a closed loop PI controller.

In the work by Asua et al., an experimental micro-positioning device, based on a SMA wire, is controlled [60]. Several control strategies including P, PI, sliding mode control, and PI with an anti wind-up scheme are experimented and position accuracies around one micron are achieved. PI controller with anti wind-up control scheme is observed to give very satisfactory performance.

Ma et al., presented a position control system for a SMA wire actuator using the electrical resistance feedback [61]. In this work, a neural network is employed to model the relationship between the electrical resistance and displacement so as to predict the position of the actuator using only its electrical resistance information. To enable feedback control of the SMA wire actuator using only its electrical resistance, a PID type controller is used. The results of the feedback control experiments demonstrate that the proposed position control system achieves a good control performance without using a position sensor.

Apart from the classical control approaches, neuro-fuzzy control has been used to develop dynamic models to be employed in a motion control scheme for SMA actuators. Using neuro-fuzzy logic, the system identification of the dynamic systems can be performed by observing the change of state variables (displacement and velocity) responding to a known input (supplied current). Then, using the model, the estimated current command required to follow a desired trajectory is calculated in an open-loop manner. The actual current command is the sum of this open-loop current command and the current command calculated from an ordinary linear control scheme. This neuro-fuzzy based control scheme is a generalized structure that can be used for a variety of SMA actuators [62].

The work by Lei and Yam reports two modeling and control attempts performed on a positioning system comprising of linking SMA wires [63]. The identified single wire model is then extended to a system of two SMA wires joining together at their tips. The extended model describes the position of the linking point as a function of the currents in the two SMA wires, based upon which open loop position control of the linkage is conducted. The second attempt utilizes a neuro-fuzzy based approach for positioning control of a linkage point. The second approach involves MATLAB-ANFIS (adaptive neuro-fuzzy inference

system; which is a neural network that is functionally equivalent to a fuzzy inference system) neuro-networks with hybrid learning algorithm trained to model the currents to the SMA wires as functions of present and target positions of the linkage point.

In order to control SMA actuators with hysteresis compensation Song et al. presented a new approach by using a neural network feed-forward controller and a sliding-mode based robust feedback controller [64]. Actually, this scheme includes two major parts: a feedforward neural network controller, which is used to cancel or reduce the hysteresis, and a sliding-mode based robust feedback controller, which is employed to compensate uncertainties such as the error in hysteresis cancellation and ensures the system's stability. The feedforward neural network controller is designed based on the experimental results of the open-loop testing of the wire actuator.

Grant and Hayward used variable structure control for a specific SMA actuator [65]. They developed two-stage linear and two-stage constant magnitude controllers. They showed that two-stage constant magnitude relay controller is more robust and has a simpler design.

3.2. Position Control of SMA Wires

In this section, the position control of the SMA wire with the selected representative data set will be demonstrated and later the verification of these controllers under different stress conditions will be presented.

Although the main purpose is to control the position of the wire, in this study, control of indirect feedback variables, namely, resistance and dissipated power are also performed. By using these variables, self sensing capability of the wire is utilized, which helps making smaller actuators. On the other hand, this has the drawback of introducing operational state dependent modeling requirements.

In this study, no disturbance has been modeled. Only, servo characteristics (i.e. how closely the control commands are being followed) are examined. No systematic study of disturbance effects like ambient temperature, modeling inaccuracies have been undertaken within the scope of this thesis.

At the beginning of this study, the open loop position control of the wire is considered. However, this approach is evaluated to be inapplicable due to the following reasons:

- Temperature of the wire, thus the current needed to actuate the wire depends on the environmental conditions and the controller must be robust to these variations.
- Stress also influences the activation temperature so for every stress condition the controller should be tuned.
- The control system should be robust to errors caused by modeling inaccuracies.

Hence, the composed closed loop models with strain, resistance, and power feedback are controlled by PI, PI with feedforward loop, and neural network based Narma L2 controllers. P-type control is also investigated but proved to be insufficient in the following sections. PID-type control is not considered in the scope of this work since addition of the derivative (D) term to the current control would cause the system to become unstable by amplifying the noise in the feedback loop. Furthermore, this action leads to an extra zero in the control system dynamics that may turn the system into a non-minimum phase form [66]. For these reasons, the D-action is not often chosen in design of a control system and most of the control systems discussed in the literature is based on either PI or neural network control methods.

In the control system design, some researchers have chosen to greatly simplify the material's behavior by creating a model where the phase transition temperature is single and same for heating and cooling by completely ignoring the effects of the large hysteresis.

In this study, the controller design studies begin with modeling the SMA wire with simple linear models. The calculated parameters are then used to control the non-linear realistic models described in the previous section. In all of the simulations the current is limited to 650 mA to avoid overheating of the SMA wire.

3.3. Strain Feedback

The simplest and straight forward method to control the position of an SMA wire is to use its position or calculated strain as feedback.

In general, control studies start with the simplest models that can be obtained by reasonable assumptions. Since a large portion of the phase transformation is approximately linear, a linear relation between current and strain can be used to capture their relationship as shown in Figure 64. A general block diagram of the control system is given in Figure 65, where the output of the controller is saturated outside 0 - 650 mA range.

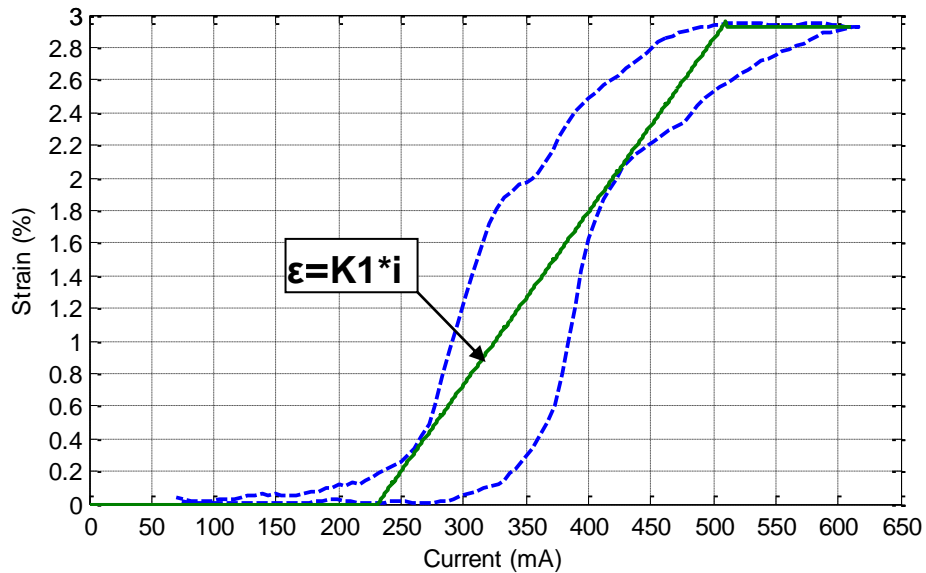


Figure 64. Linear strain model

Regarding the block diagram in Figure 65, the following equalities can be written:

$$\epsilon_m = \epsilon_e \cdot G_c(s) \cdot G_{i\epsilon}(s) \quad \text{Eq. 30}$$

$$\epsilon_e = \epsilon_d - \epsilon_m \quad \text{Eq. 31}$$

$$\epsilon_m = (\epsilon_d - \epsilon_m) \cdot G_c(s) \cdot G_{i\epsilon}(s) \quad \text{Eq. 32}$$

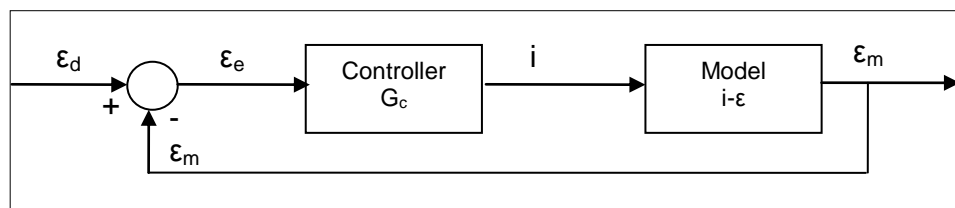


Figure 65. General block diagram of the strain control system

In Figure 65, G_c is the controller transfer function; i is the current; ϵ_d , ϵ_m , and ϵ_e represent the desired strain, measured strain, and strain error respectively. The constructed control system can be evaluated for different type of controllers as done in the following sections.

Using the block diagram algebra, the overall transfer function of the closed-loop control system can be obtained from the previous expressions in the following manner:

$$G_s(s) = \frac{\epsilon_m}{\epsilon_d} = \frac{G_c(s) \cdot G_{i\epsilon}(s)}{1 + G_c(s) \cdot G_{i\epsilon}(s)} \quad \text{Eq. 33}$$

3.3.1. P-Type Control

In this section the control studies begin with designing a P-type controller to control the strain of the wire. In this type of controller a proportional (P) gain is multiplied with the error in the strain. The proportional gain is tuned manually to obtain satisfactory controller performance in terms of steady state error. The transfer function for P controller is simply:

$$G_c(s) = K_p \quad \text{Eq. 34}$$

where K_p is the proportional gain of the controller. Then the closed loop transfer function becomes:

$$G_s(s) = \frac{\epsilon_m}{\epsilon_d} = \frac{G_c(s) \cdot G_{i\epsilon}(s)}{1 + G_c(s) \cdot G_{i\epsilon}(s)} = \frac{K_1 K_p}{1 + K_1 K_p} \quad \text{Eq. 35}$$

In order to obtain the condition for the measured strain (ϵ_m) to be equal to desired strain (ϵ_d) the relation given above should be equal to unity. This can be achieved if and only if the product $K_1 K_p$ is very large than 1 so that the effect of 1 in the denominator is cancelled and the measured strain is approximately equal to the desired strain. However, in this system, with this type of controller steady state error can never be nullified. Thus, P-type controller is not considered in the scope of this study for strain feedback control.

3.3.2. PI-Type Control

In order to control the strain of the SMA wire, a control system is designed regarding a PI-type controller. In this type of controller, the control signal to be sent to the plant, or the system to be controlled, is generated by multiplying the error between the desired and actual values of the strain and sum of the error within a certain interval with the proportional (P) and integral (I) gains, respectively. Here, the parameters of the controller are tuned to obtain a satisfactory control performance following their determination by some analytical methods. The transfer function of the PI controller can be written as:

$$G_c(s) = K_p + \frac{K_i}{s} = \frac{K_p \cdot s + K_i}{s} \quad \text{Eq. 36}$$

where K_p and K_i denote the proportional and integral gains of the controller.

Using $G_c(s)$, the system transfer function between the desired and measured strain values then becomes:

$$G_s(s) = \frac{\varepsilon_m}{\varepsilon_d} = \frac{G_c(s) \cdot G_{i\varepsilon}(s)}{1 + G_c(s) \cdot G_{i\varepsilon}(s)} = \frac{K_1 K_p \cdot s + K_1 K_i}{(K_1 K_p + 1)s + K_1 K_i} \quad \text{Eq. 37}$$

The controller parameters can be tuned using various techniques. In this context, one of the most frequently used techniques is pole-placement of closed loop transfer function. According to this technique, poles can be placed using specified polynomials. The more known kinds of these polynomials are Butterworth and Chebyshev polynomials. The mentioned polynomials can be used to place the poles of the closed loop system to make the system stable with the required bandwidth.

The system response obtained using Butterworth polynomials is observed to be better than the response using Chebyshev polynomials, thus in this design Butterworth polynomials will be used. According to this, the poles of the Butterworth polynomial is placed on the semi-circle whose radius is the required bandwidth and the number of poles is decided by the order of the characteristic polynomial i.e. the denominator polynomial of the transfer function of the closed loop system [67].

Thus, using the second order Butterworth polynomial for pole placement the integral gain K_i is calculated as a function of selected bandwidth (ω_c) and the proportional gain (K_p). Here, K_p is chosen as 300 assuming that nearly 300 mA is needed for 1% strain error and K_i is calculated to be 0.014 from the linear fit.

$$\frac{(K_1 K_p + 1)}{K_1 K_i} \cdot s + 1 = \frac{s}{\omega_c} + 1 \quad \text{Eq. 38}$$

$$K_i = \frac{(K_1 K_p + 1) \cdot \omega_c}{K_1} \quad \text{Eq. 39}$$

The simulation results for $K_p=300$, $K_i=55$ (with 0.025 Hz bandwidth), and $K_p=300$, $K_i=110$ (with 0.05 Hz bandwidth) are obtained; the strain command and the model (obtained in section 2.8.1) responses for both gain sets are given in Figure 66 and Figure 67 respectively.

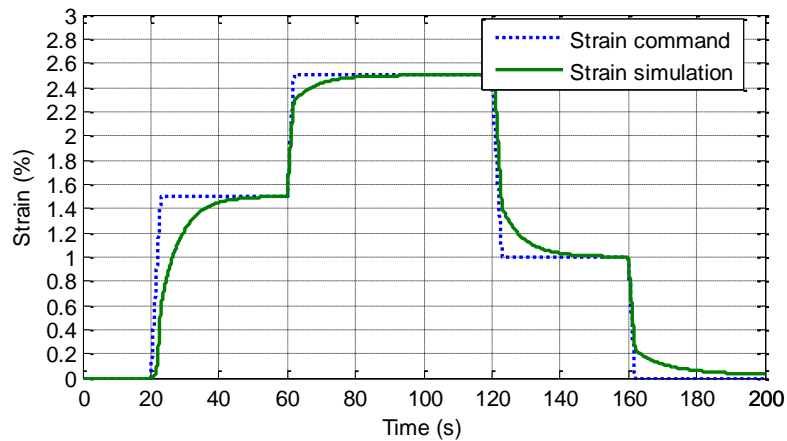


Figure 66. Strain command-model response using PI controller ($K_p=300$ and $K_i=55$)

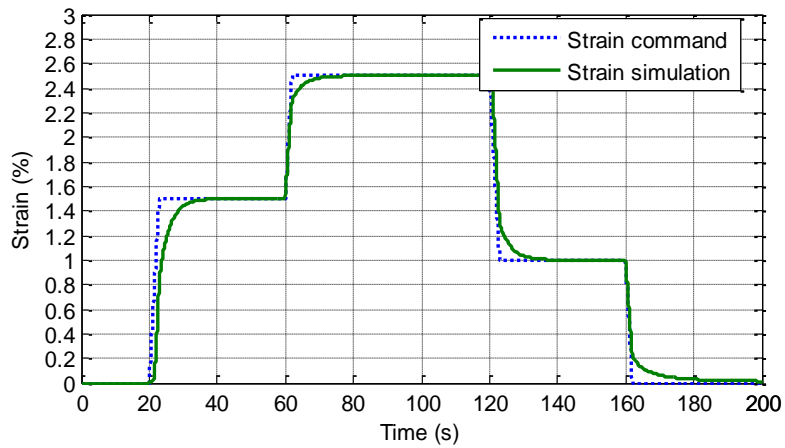


Figure 67. Strain command-model response using PI controller ($K_p=300$ and $K_i=110$)

3.3.3. PI-Type Control with Feedforward Loop

In this control scheme, an inverse model for current-strain relation is obtained for heating and cooling states of the wire using curve fitting toolbox of MATLAB (Figure 68). The aim of adding the feedforward loop is to speed up the response of the system.

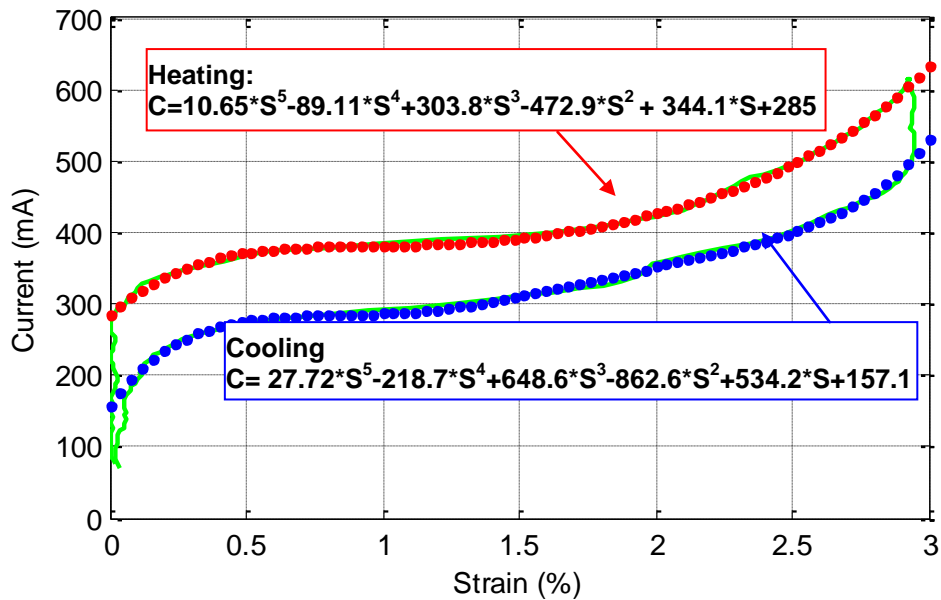


Figure 68. Inverse strain-current model

Then, this model is integrated to the control system as given in Figure 69, the current command from the feedforward loop is adjusted using the gain block

to avoid overshooting of the response, and the remaining error is suppressed by the PI controller. Since the working data set is the data obtained for 140 MPa stress level to compensate the curve fit shifts due to change in load the feedforward gain is used. In this content, feedforward loop would not compensate for disturbances but improves servo characteristics.

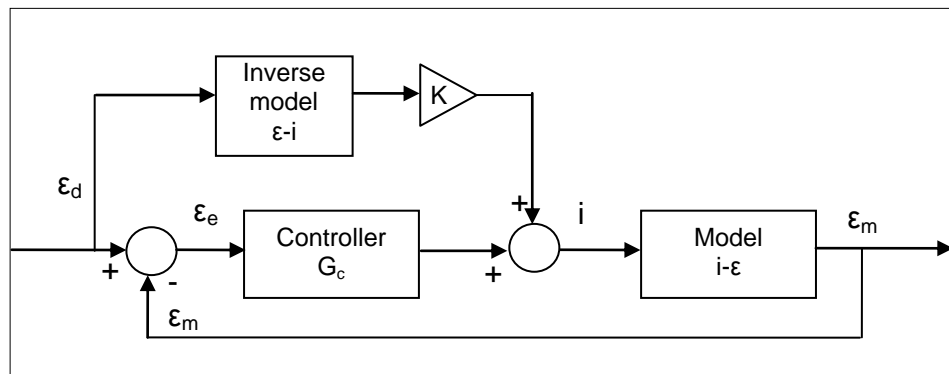


Figure 69. PI-type control with feedforward loop

The simulation results of this model with $K_p=300$, $K_i=55$, and $K_p=300$, $K_i=110$, the feedforward gain, K , adjusted to 0.8 are presented in Figure 70 and Figure 71.

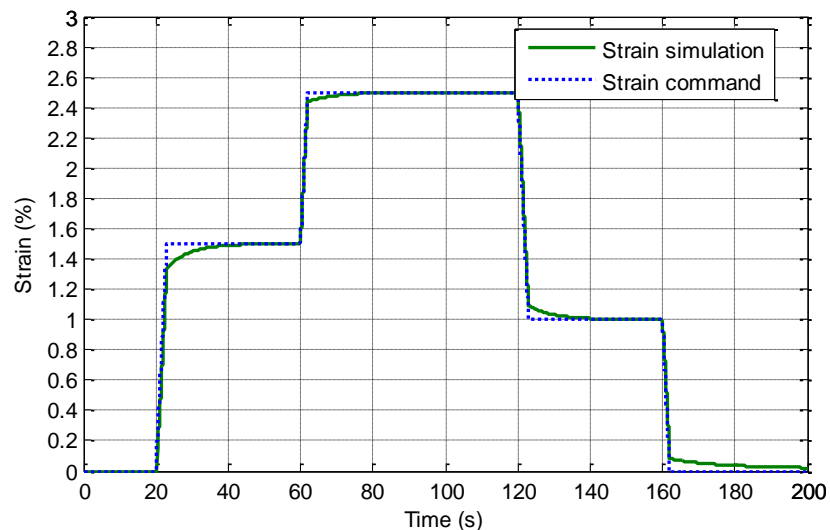


Figure 70. Strain command and model response using PI controller with feedforward loop ($K_p=300$, $K_i=55$, and $K=0.8$)

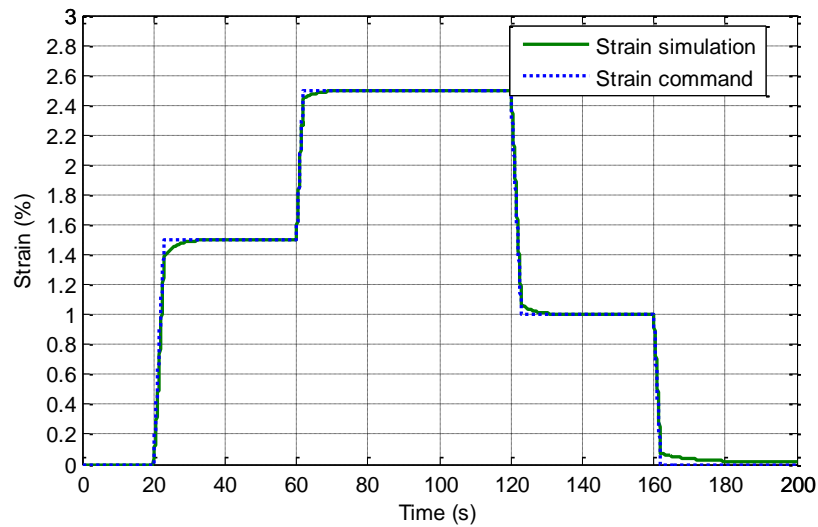


Figure 71. Strain command and model response using PI controller with feedforward loop ($K_p=300$, $K_i=110$, and $K=0.8$)

When the simulation results are compared with the regular PI controller the response time is observed to be shorter for PI controller with feedforward loop.

3.3.4. Neural Network Narma-L2 Control

In this portion of the study, the position of the SMA wire is controlled by a neural network control scheme. The implemented controller is NARMA L2 which is a built-in controller in Matlab® SIMULINK®, Neural Network Toolbox™ blockset [68].

Neural networks (NN) are composed of simple elements operating in parallel. In a neural network, the connections between elements largely determine the network function. A neural network can be trained to perform a particular function by adjusting the values of the connections (weights) between elements.

Typically, neural networks are adjusted, or trained, so that a particular input leads to a specific target output. A lot of input/target pairs, i.e. input and output data sets are needed to train a network.

In Narma-L2 control scheme, the plant model can be approximated by the companion form. The main idea of this type of control is to transform nonlinear system dynamics into linear dynamics by canceling the nonlinearities.

In the next section, firstly, the companion form system model is presented and using a neural network to identify this model is demonstrated. Then, development of a controller using the identified neural network model is described briefly.

3.3.4.1. Identification of the NARMA-L2 Model

The first step in using NARMA-L2 control is to identify the system to be controlled. The neural network is trained to represent the forward dynamics of the system. The first step is to choose a model structure to use. One standard model that is used to represent general discrete-time nonlinear systems is the nonlinear autoregressive-moving average (NARMA) model:

$$y(k+d)=N[y(k), y(k-1), \dots, y(k-n+1), u(k), u(k-1), \dots, u(k-n+1)] \quad \text{Eq. 40}$$

where $u(k)$ is the system input, and $y(k)$ is the system output. For the identification phase, a neural network can be trained to approximate the nonlinear function N .

If system output is required to follow some reference trajectory $y(k + d) = y_r(k + d)$, the then nonlinear controller of the form given in Eq. 41 is obtained.

$$u(k)=G[y(k), y(k-1), \dots, y(k-n+1), y_r(k+d), u(k-1), \dots, u(k-m+1)] \quad \text{Eq. 41}$$

The problem with using this controller is that if it is wanted to train a neural network to create the function G to minimize mean square error, dynamic back propagation need to be used [69] which is a slow process. One solution, proposed by Narendra and Mukhopadhyay [70], is to use approximate models to represent the system. The controller used in this context is based on the NARMA-L2 approximate model:

$$\hat{y}(k+d)=f[y(k), y(k-1), \dots, y(k-n+1), u(k-1), \dots, u(k-m+1)]+ \\ g[y(k), y(k-1), \dots, y(k-n+1), u(k-1), \dots, u(k-m+1)] \cdot u(k) \quad \text{Eq. 42}$$

This model is in companion form, where the next controller input $u(k)$ is not contained inside the nonlinearity. The advantage of this form is that it can be solved for the control input that causes the system output to follow the reference $y(k + d) = y_r(k + d)$. The resulting controller would have the form given in Eq. 43.

$$u(k) = \frac{y_r(k+d) - f[y(k), y(k-1), \dots, y(k-n+1), u(k-1), \dots, u(k-n+1)]}{g[y(k), y(k-1), \dots, y(k-n+1), u(k-1), \dots, u(k-n+1)]} \quad \text{Eq. 43}$$

Using this equation directly can cause realization problems, because the control input $u(k)$ based on the output at the same time, $y(k)$ must be determined. So, instead, the model given below is used.

$$y(k+d) = f[y(k), y(k-1), \dots, y(k-n+1), u(k), u(k-1), \dots, u(k-n+1)] + g[y(k), y(k-1), \dots, y(k-n+1), u(k), \dots, u(k-n+1)] \cdot u(k+1) \quad \text{Eq. 44}$$

where ($d \geq 2$). Figure 72 shows the structure of a neural network representation.

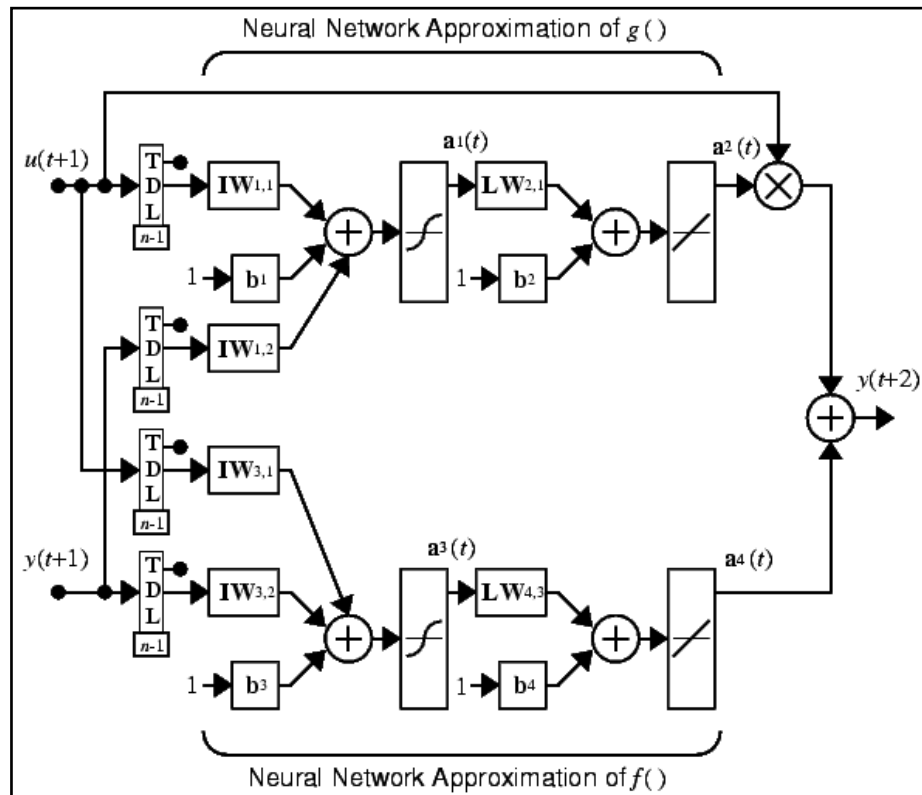


Figure 72. Structure of a neural network representation [68]

3.3.4.2. NARMA-L2 Controller

Using the NARMA-L2 model, the controller can be obtained as:

$$u(k+1) = \frac{y_r(k+d) - f[y(k), y(k-1), \dots, y(k-n+1), u(k), \dots, u(k-n+1)]}{g[y(k), y(k-1), \dots, y(k-n+1), u(k), \dots, u(k-n+1)]} \quad \text{Eq. 45}$$

This equation is realizable for ($d \geq 2$). This controller can be implemented with the previously identified NARMA-L2 plant model, as shown in Figure 73. In the figure, TDL blocks represent the tapped delay lines that store the previous values of the input signal.

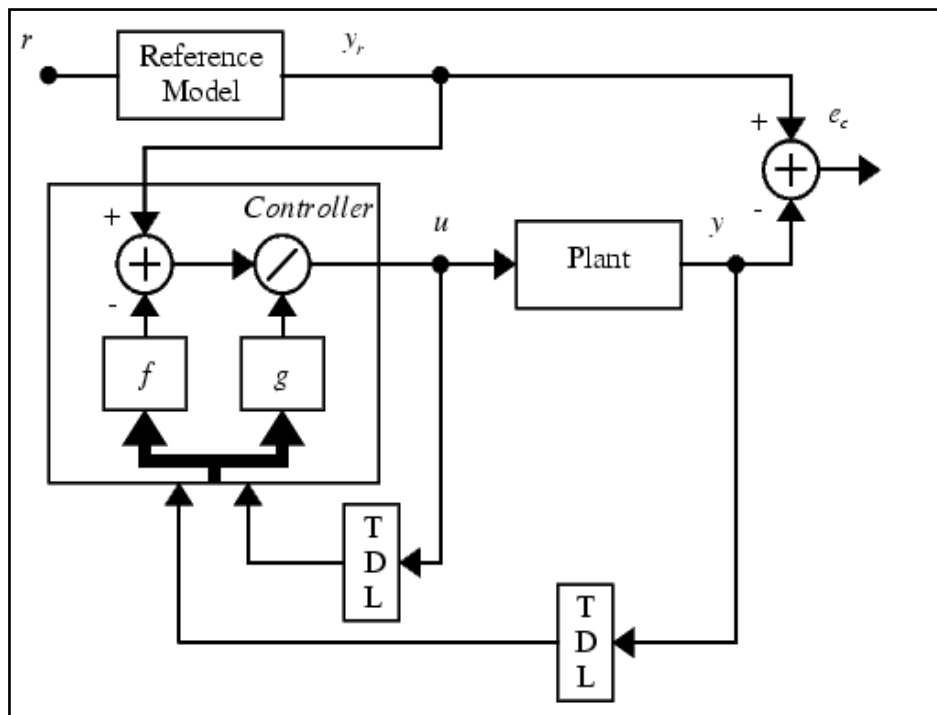


Figure 73. Block diagram of the NARMA-L2 controller [68]

The neural network Narma-L2 controller is trained using the data from the characterization experiments under 140 MPa stress with minimum 100 mA current output. The training data consist of the current input and the strain output of the SMA wire under this stress. The Levenberg-Marquard algorithm, which is generally used and very efficient back propagation procedure, is chosen for training the network.

The number of hidden layers in the network is determined by a convergence study on the performance index of the selected training algorithm. The performance index is based on the minimization of the mean square error with gradient descent optimization procedure. The number of layers determines the accuracy of the controller, however, as the number of hidden layers grows the computation time for each step increases. Figure 74 shows the convergence curve for the performance index obtained using different number of layers. As can be seen from the plot, the index seems to converge after 5 layers. Thus, 5 hidden layers are chosen to be used in the model.

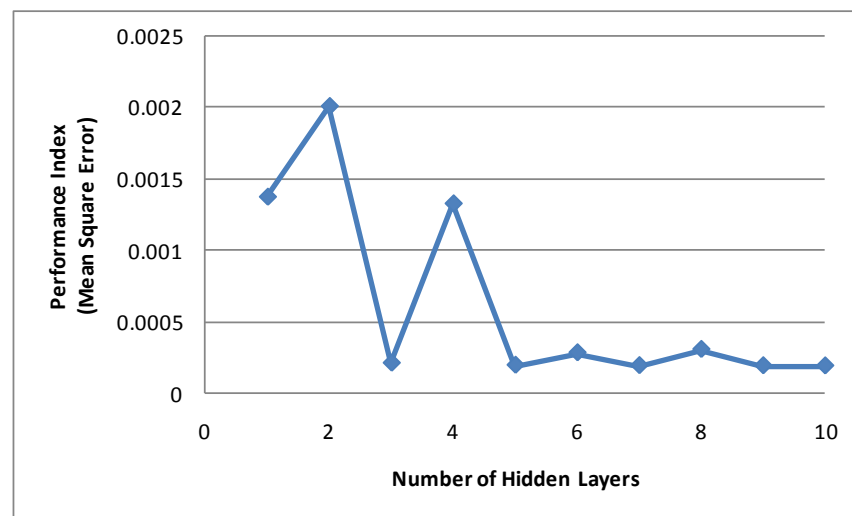


Figure 74. Performance index with respect to number of hidden layers (strain feedback)

Another factor that affects the performance of the controller is the maximum number of iterations used in training, i.e. epoch (the number of steps used in estimation of the weightings). The use of greater number of iterations does not necessarily mean better results, and generally the gradient criterion is satisfied before the maximum number of iterations is reached. A test is carried out in order to determine the optimum number of iterations, in which the maximum number of iterations is changed for the chosen number of hidden layers. As seen in Figure 75, the plot has the minimum value when the maximum number of iterations is 1000, so this value is chosen to be used in training.

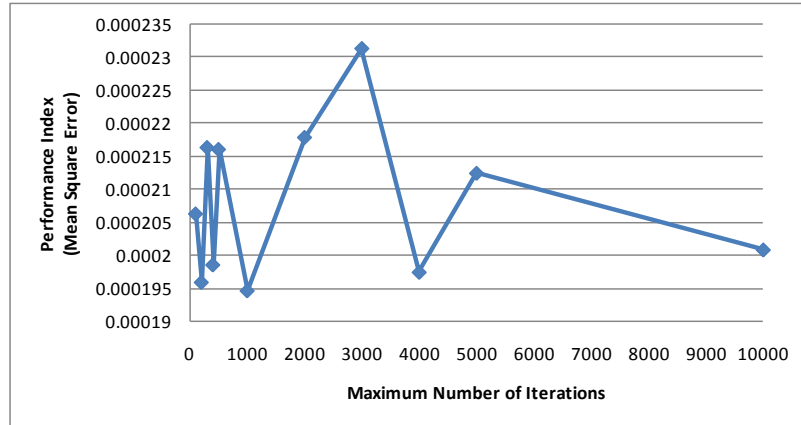


Figure 75. Performance index with respect to number of maximum iterations (strain feedback)

The simulation result of the NN Narma-L2 controller implemented system (Figure 76) is given in Figure 77.

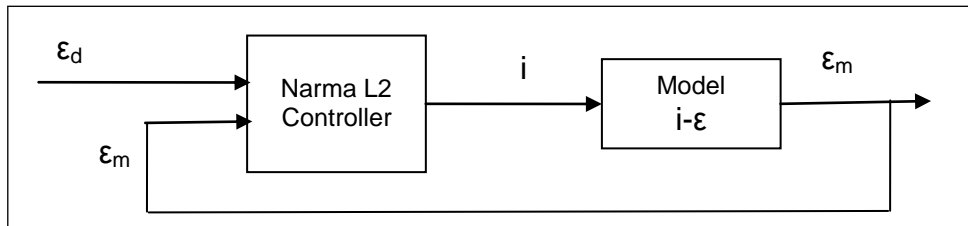


Figure 76. Block diagram of the system with Narma L2 controller

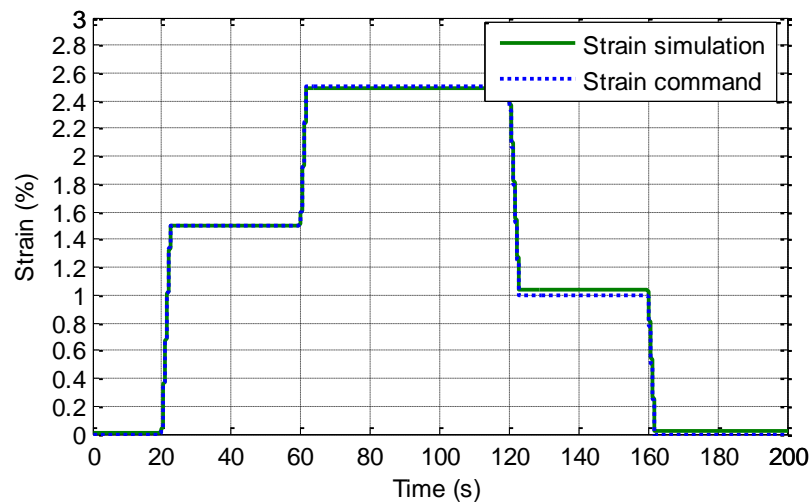


Figure 77. Strain command and model response using Narma-L2 controller

3.4. Resistance Feedback

The resistance feedback is a simpler way in the closed-loop control of an SMA wire because the resistance of the wire can easily be measured. So, in this section resistance feedback will be used to control the position of the SMA wire.

As in the strain feedback model, since a large portion of the phase transformation is almost linear, a linear relation between current and resistance is going to be used to capture their relationship as shown in Figure 78. A general block diagram of the control system is submitted in Figure 79, where the output of the controller is saturated outside 0 - 650 mA range.

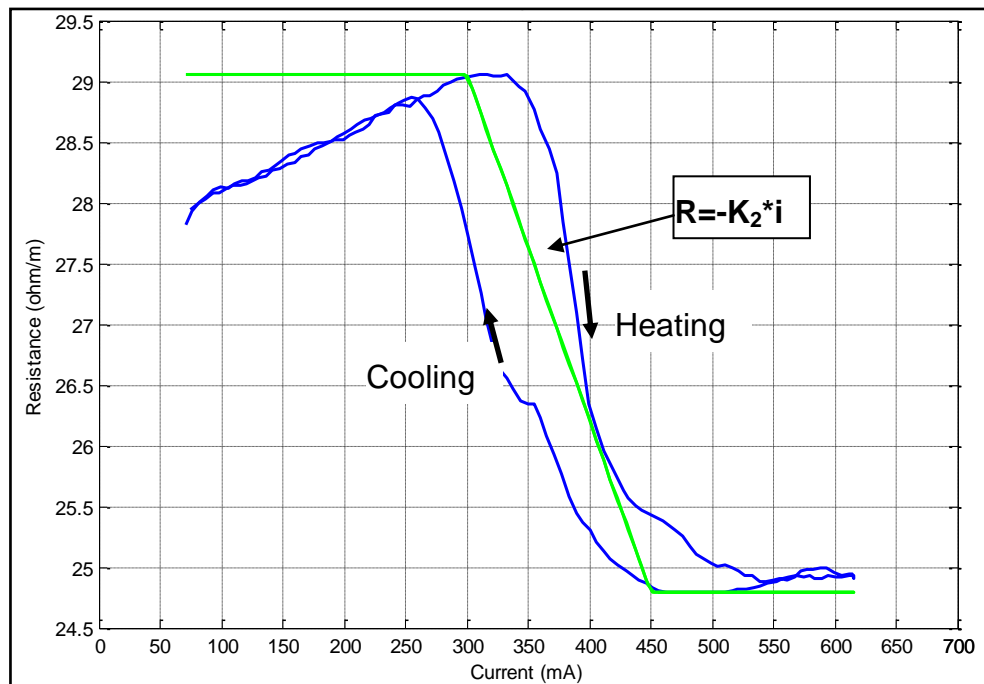


Figure 78. Linear resistance model

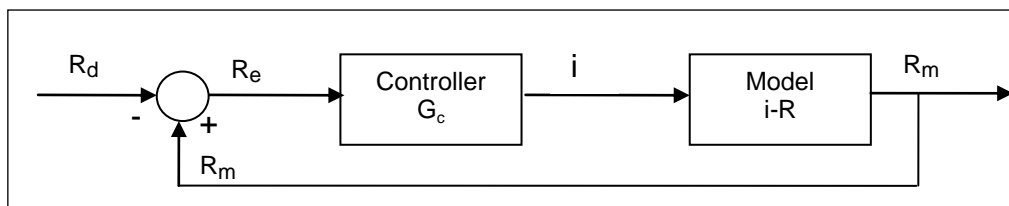


Figure 79. General block diagram of the resistance control system

For this case, since positive current command should be produced for negative resistance errors positive resistance feedback is used. Hence, the control system transfer function between the desired and measured resistance values (R_d and R_m) can be obtained as follows:

$$R_m = R_e \cdot G_c(s) \cdot G_{iR}(s) \quad \text{Eq. 46}$$

$$R_e = R_m - R_d \quad \text{Eq. 47}$$

$$R_m = (R_m - R_d) \cdot G_c(s) \cdot G_{iR}(s) \quad \text{Eq. 48}$$

$$G_s(s) = \frac{R_m(s)}{R_d(s)} = \frac{G_c(s) \cdot G_{iR}(s)}{G_c(s) \cdot G_{iR}(s) - 1} \quad \text{Eq. 49}$$

3.4.1. P-Type Control

In this section, a P-type controller to control the resistance of the wire is designed. In this type of controller for resistance feedback a proportional (P) gain is multiplied with the difference between the measured and the desired values of the resistance. The closed loop transfer function becomes:

$$G_s(s) = \frac{R_m}{R_d} = \frac{G_c(s) \cdot G_{iR}(s)}{G_c(s) \cdot G_{iR}(s) - 1} = \frac{K_2 K_p}{K_2 K_p - 1} \quad \text{Eq. 50}$$

Here, same as the P controller for strain feedback, in order to eliminate steady state error, the relation given above should be equal to unity. This can be achieved if and only if the product $K_2 K_p$ is very large than 1 so that the effect of 1 in the denominator is cancelled and the measured resistance is approximately equal to the desired resistance value. However, again, with this type of controller applied to this system, steady state error is inevitable. Thus, P-type controller is not considered in the scope of this study for resistance feedback control.

3.4.2. PI-Type Control

In order to control the resistance of the SMA wire, a control system is designed employing a PI controller. Here, using the same method discussed in section 3.3.1, the parameters of the controller are tuned to obtain a satisfactory control performance. K_p is chosen to be 300 since nearly 300 mA of current is needed to correct an error of 1 Ohm/m on the resistance of the wire, and K_2 is 0.02 from the linear fit.

The simulation results for $K_p=300$, $K_i=35$ with 0.025 Hz bandwidth and $K_p=300$, $K_i=70$ with 0.05 Hz bandwidth on the resistance model (obtained in section 2.8.2) are given. The resistance command and the model response graphics are submitted in Figure 80 and Figure 81.

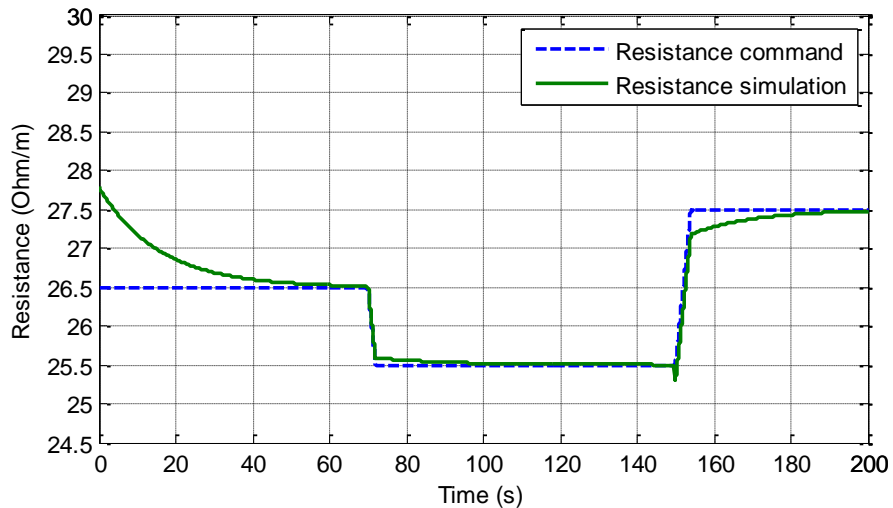


Figure 80. Resistance command and model response using PI controller ($K_p=300$ and $K_i=35$)

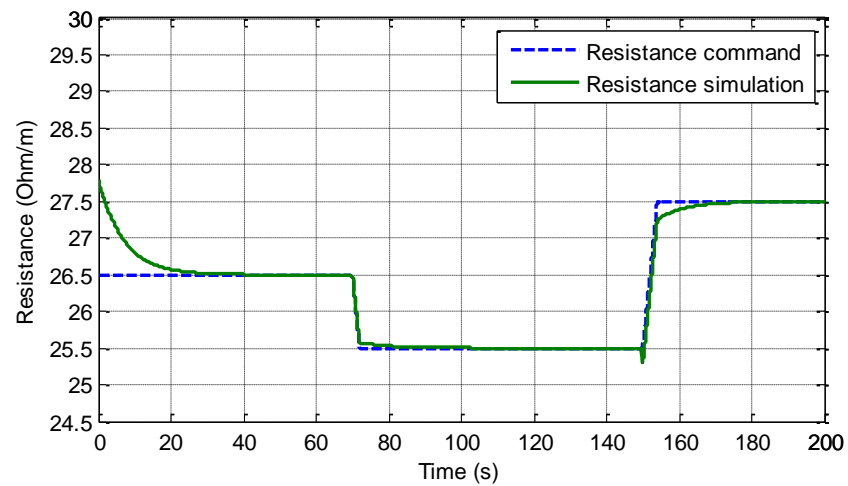


Figure 81. Resistance command and model response using PI controller ($K_p=300$ and $K_i=70$)

3.4.3. PI-Type Control with Feedforward Loop

In this control scheme, an inverse model for resistance-current relationship is obtained for heating and cooling states of the wire using curve fitting toolbox of MATLAB (Figure 82).

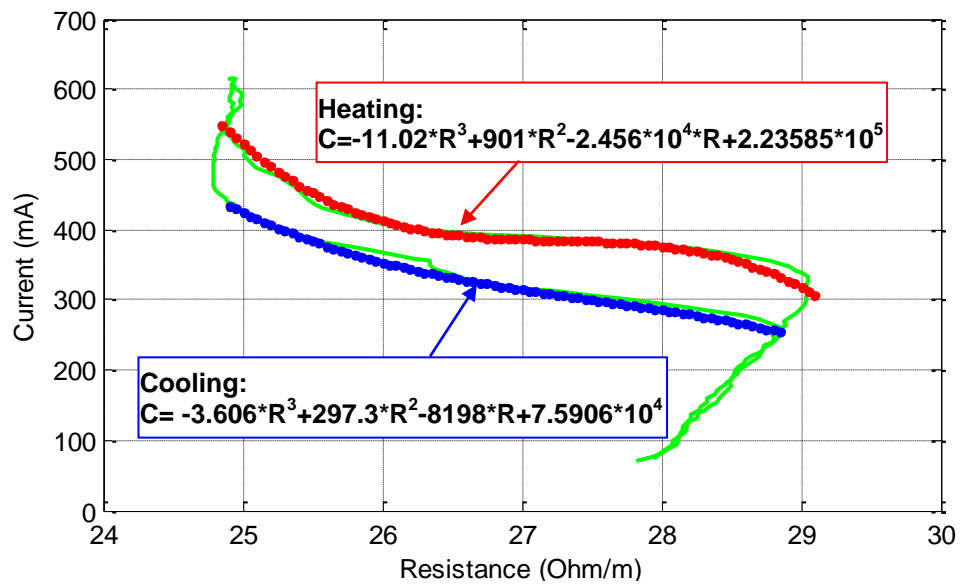


Figure 82. Inverse resistance-current model

Then, this model is integrated to the control system as given in Figure 83, the current command from the feedforward loop is adjusted using the gain block, the remaining error is suppressed by the PI controller.

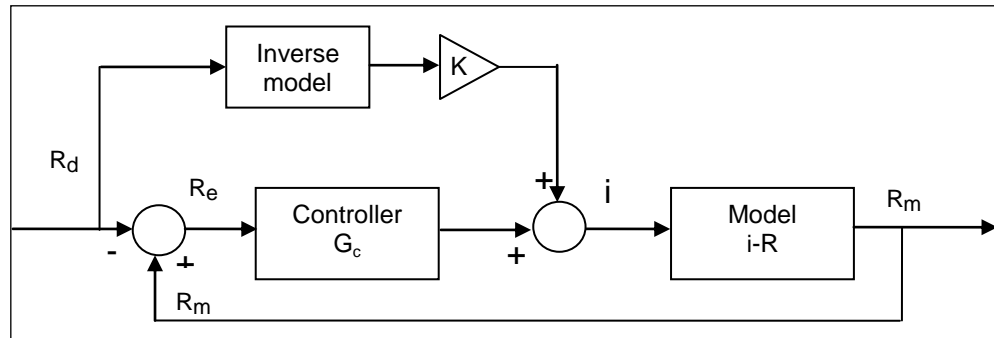


Figure 83. PI-type control with feedforward loop

The simulation results of this model with $K_p=300$, $K_i=35$, and the feedforward gain, K , adjusted to 0.8 is given in Figure 84.

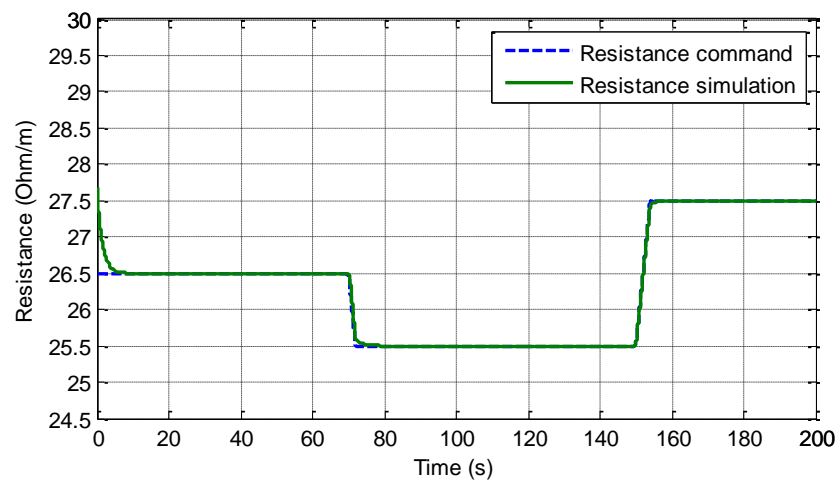


Figure 84. Resistance command and model response using PI controller with feedforward loop

It can be observed that using PI controller with feedforward loop reduces the response time.

3.4.4. Neural Network Narma-L2 Control

The NN Narma-L2 controller is implemented to the control system as given in Figure 85, the controller is trained using the data from the characterization experiments under 140 MPa stress. The training data consist of the current input and the resistance output of the SMA wire under this stress. The convergence test for determination of the number of layers (Figure 86) and a test for determining maximum number of iterations (Figure 87) are performed; a layer size of 5 and maximum 1000 iterations are chosen to be used. It is observed that the performance indices, which are indication of error in calculations, of the resistance training are higher than that of strain training.

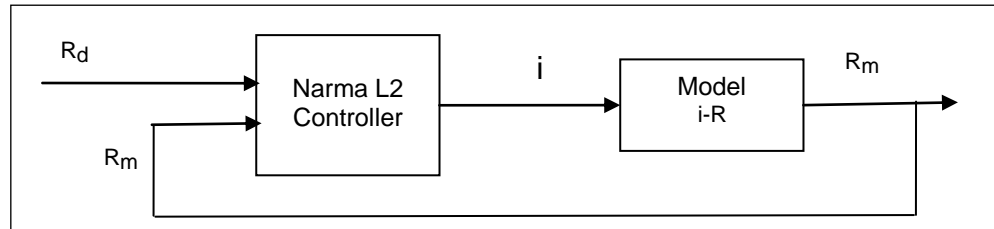


Figure 85. Block diagram of the system with Narma L2 controller with resistance f/b

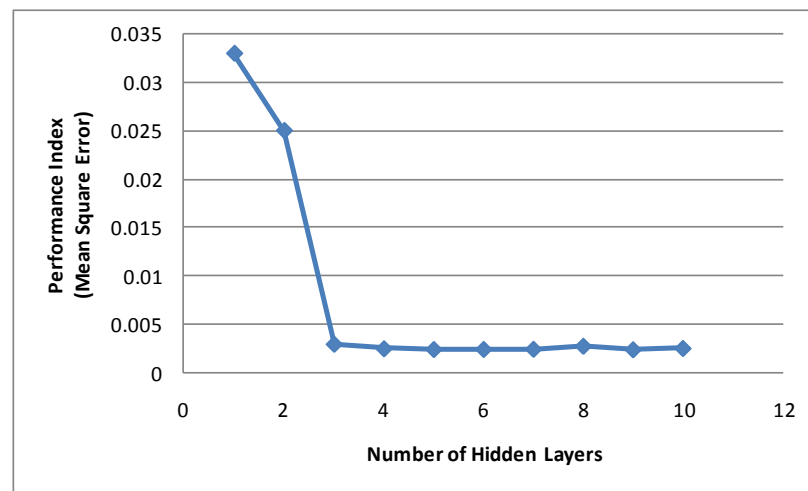


Figure 86. Performance index with respect to number of hidden layers (resistance f/b)

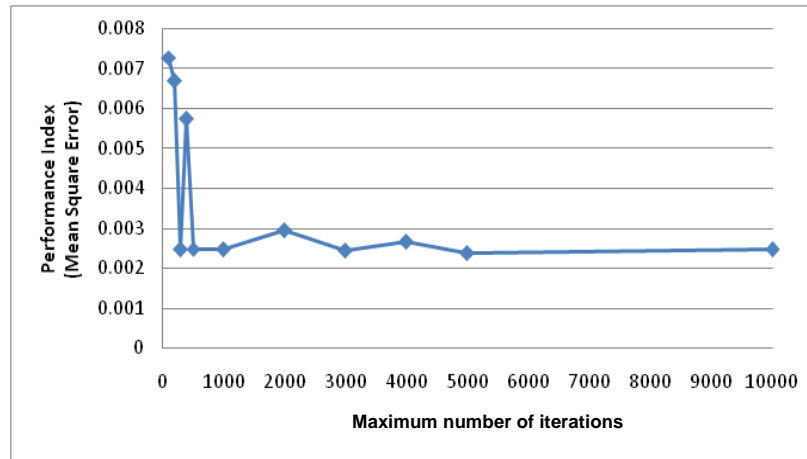


Figure 87. Performance index with respect to number of maximum iterations (resistance f/b)

The simulation result of NN Narma L2 control with resistance feedback is presented in Figure 88.

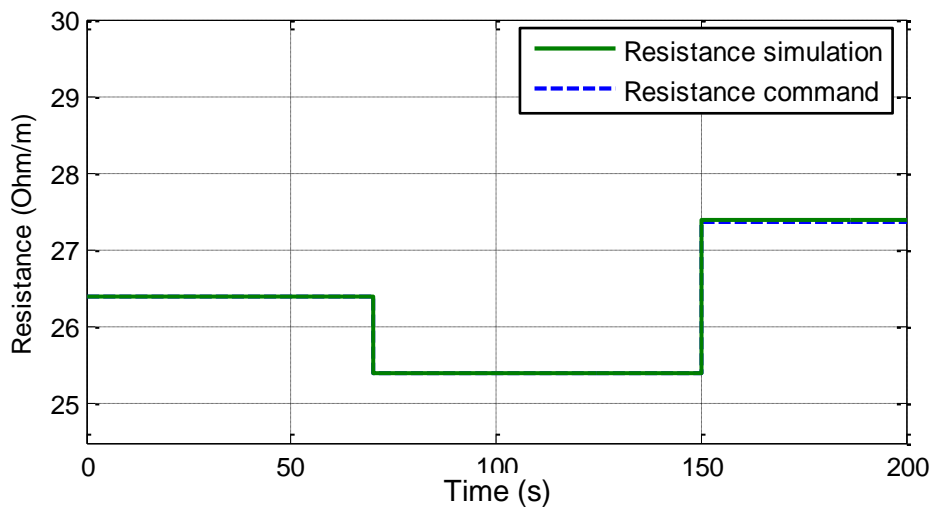


Figure 88. Resistance command and model response using Narma L2 controller

3.5. Power Feedback

Since the resistance feedback uses division in feedback calculation, the noise in voltage data is amplified by the noise in current data in real applications. Hence, power dissipation of the SMA wire is used as an alternative feedback to the resistance to control the position of an SMA wire.

In the control studies with the power feedback firstly, a linear approximation of the power-current model is obtained (Figure 89). A general block diagram of the control system is given in Figure 90.

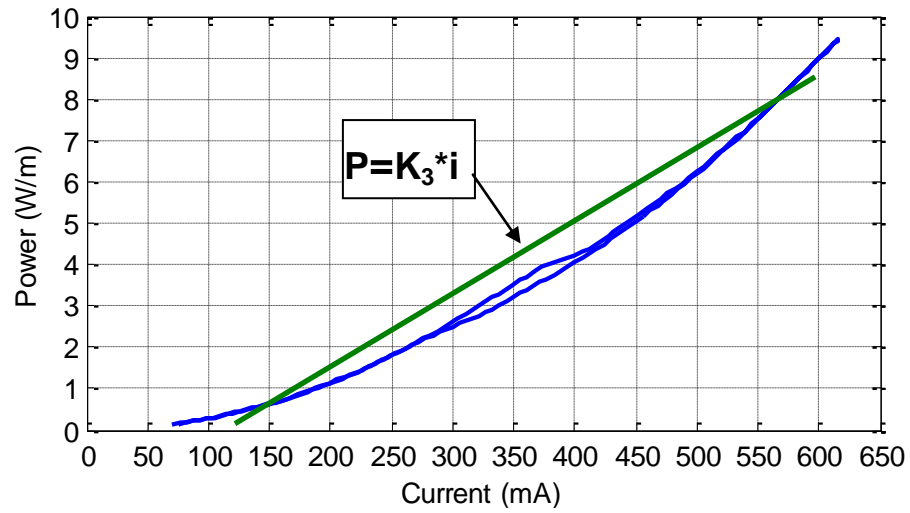


Figure 89. Linear power model

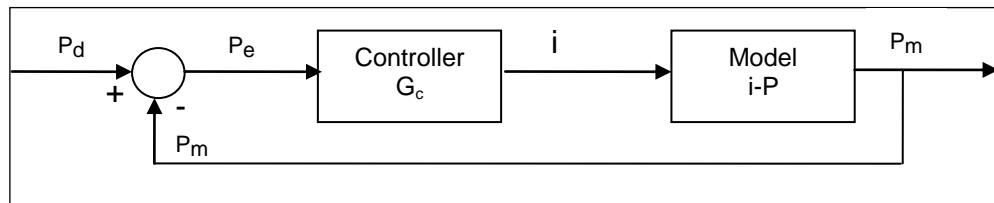


Figure 90. General block diagram of the power feedback control system

Regarding the block diagram in Figure 90 the control system transfer function can be obtained as follows:

$$P_m = P_e \cdot G_c(s) \cdot G_{iP}(s) \quad \text{Eq. 51}$$

$$P_e = P_d - P_m \quad \text{Eq. 52}$$

$$P_m = (P_d - P_m) \cdot G_c(s) \cdot G_{iP}(s) \quad \text{Eq. 53}$$

$$G_s(s) = \frac{P_m(s)}{P_d(s)} = \frac{G_c(s).G_{iP}(s)}{1 + G_c(s).G_{iP}(s)} \quad \text{Eq. 54}$$

Then, in the following sections, the P-type, PI-type, PI type with feedforward loop, and neural network control schemes are utilized to control power dissipation of the wire.

3.5.1. P-Type Control

In order to control the power dissipated by the wire firstly a P-type controller considered. In this type of controller the closed loop transfer function becomes:

$$G_s(s) = \frac{P_m}{P_d} = \frac{G_c(s).G_{iP}(s)}{1 + G_c(s).G_{iP}(s)} = \frac{K_3K_p}{1 + K_3K_p} \quad \text{Eq. 55}$$

Here, same as the P controller for strain and resistance feedback, in order to eliminate steady state error in power command, the relation given above should be equal to unity. This can be achieved if and only if the product K_3K_p is very large than 1 so that the effect of 1 in the denominator is cancelled and the measured power is approximately equal to the desired power value. However, steady state error is inevitable using this type of controller in this system. Thus, P-type controller is not utilized in the scope of this study for power feedback control.

3.5.2. PI-Type Control

In order to control the power of the SMA wire, a control system is designed employing a PI controller. Here, using the same method discussed in section 3.3.1, the parameters of the controller are tuned to obtain a satisfactory control performance. The power-current model obtained in section 2.8.3 is used in the simulations. In the simulations, proportional gain (K_p) is chosen as 100, by the approximation that in the linear model nearly 220 mA is needed for initial 2 W/m rise in power, and K_3 is found to be 0.018.

The simulation results for $K_p=100$ and $K_i=49$ with 0.05 Hz bandwidth, and $K_p=100$ and $K_i=99$ with 0.1 Hz bandwidth are given. The power command and the model response graphics are submitted in Figure 91 and Figure 92.

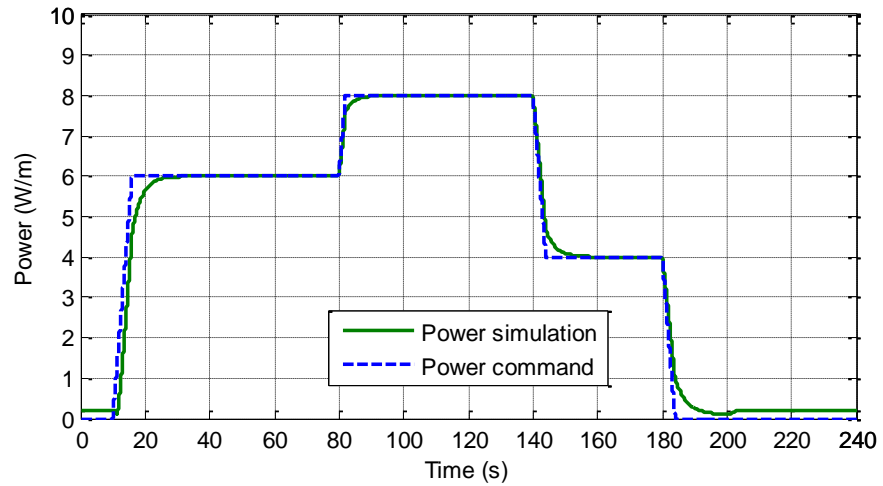


Figure 91. Power command and model response using PI controller ($K_p=100$ and $K_i=49$)

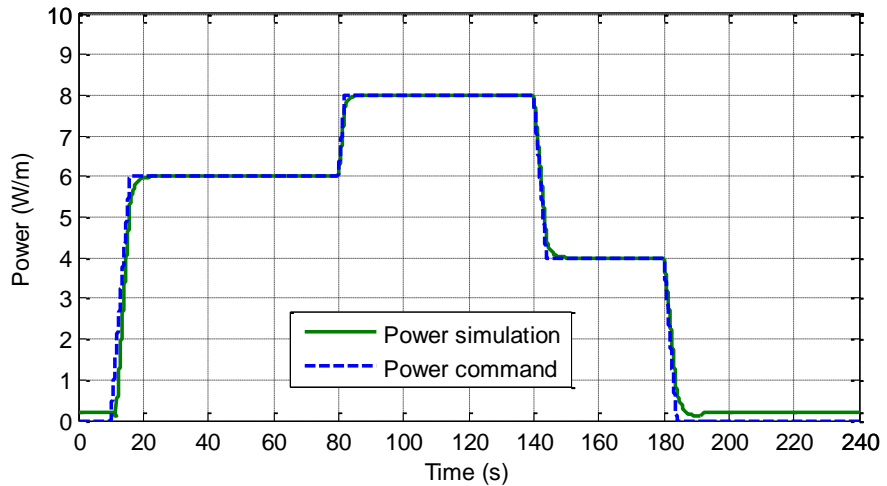


Figure 92. Power command and model response using PI controller ($K_p=100$ and $K_i=99$)

The steady state error observed in zero power dissipation commands is due to the asymptotic nature of the power model.

3.5.3. PI-Type Control with Feedforward Loop

In this control scheme, an inverse model for power-current relation is obtained for the wire using curve fitting toolbox of MATLAB®. Here, the following function seems to be best fit to the handled data as given in Figure 93 as well:

$$C = -0.08932.P^4 + 2.035.P^3 - 18.82.P^2 + 128.7.P + 68.97$$

Here C is the current in mA and P denotes the power of the wire in Watts per meter.

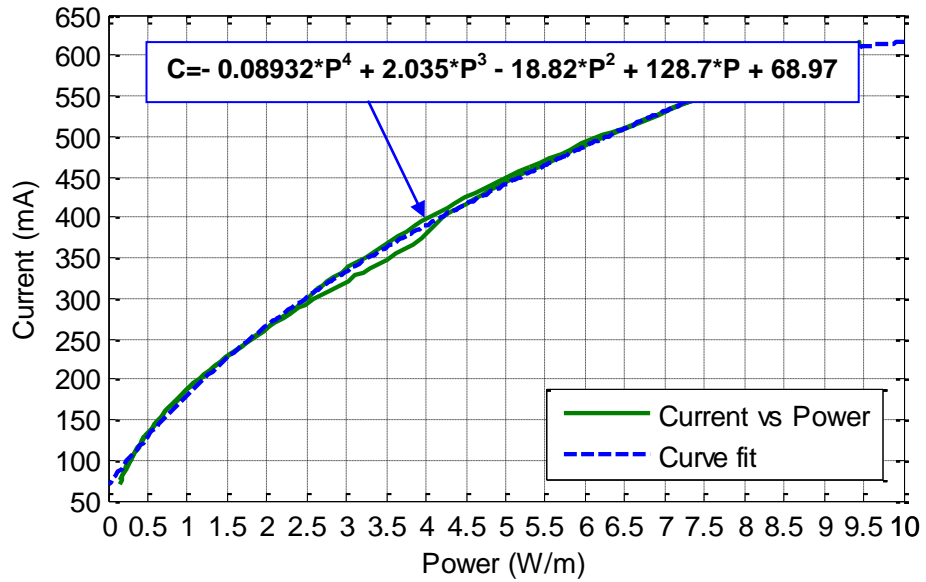


Figure 93. Inverse power-current model

Then, this model is integrated to the control system as given in Figure 94.

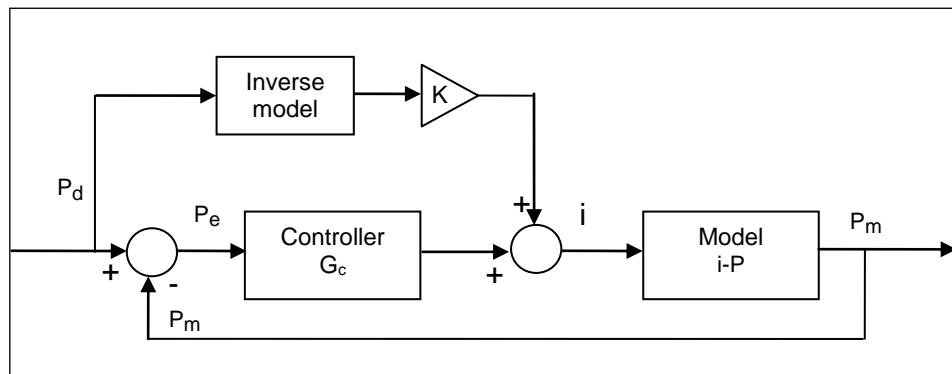


Figure 94. PI-type control with feedforward loop

The simulation results of this model with $K_p=100$, $K_i=49$ and the feedforward gain, K , adjusted to 0.8 is given in Figure 95.

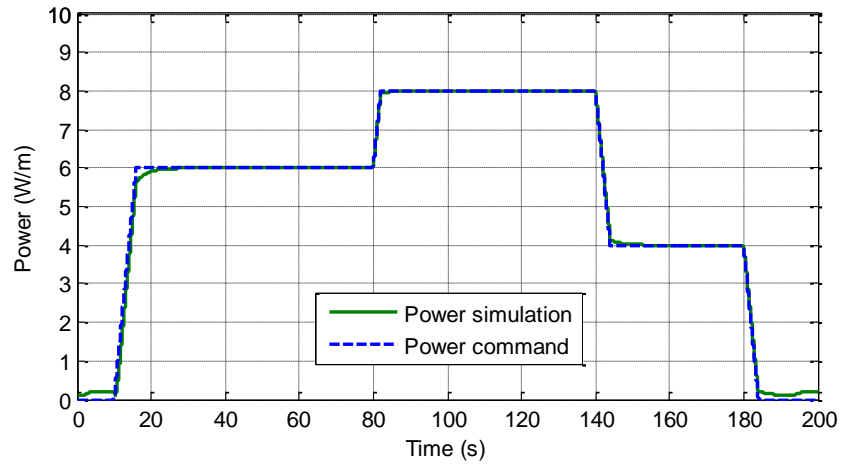


Figure 95. Power command and model response using PI controller with feedforward loop

3.5.4. Neural Network Narma-L2 Control

The NN Narma-L2 controller is implemented to the control system as given in Figure 96, the controller is trained using the data from the characterization experiments under 140 MPa stress. The training performed using the data consist of the current input and the power output of the SMA wire under 140 MPa stress.

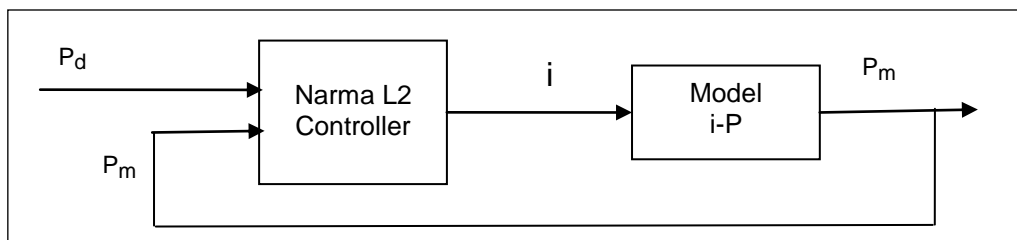


Figure 96. Block diagram of the system with Narma L2 controller

The convergence test for determination of the number of layers (Figure 97) and the test for selection of maximum number of iterations (Figure 98) are performed; a layer size of 5 and maximum 3000 iterations are chosen to be used.

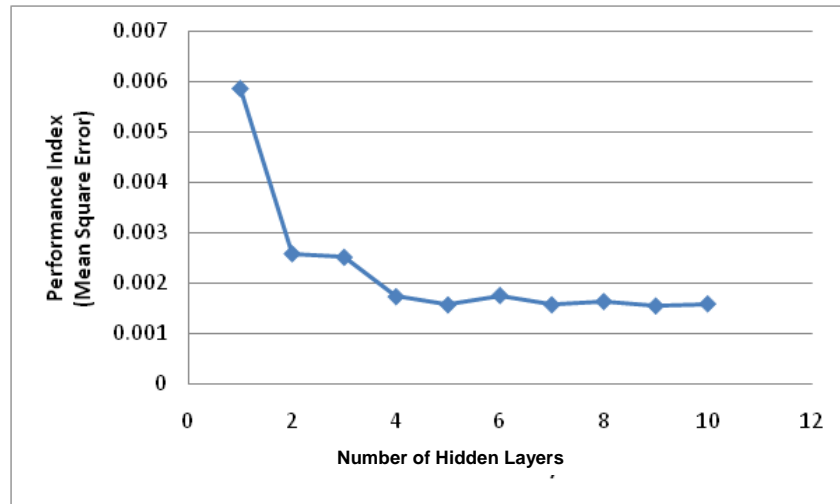


Figure 97. Performance index with respect to number of hidden layers (power f/b)

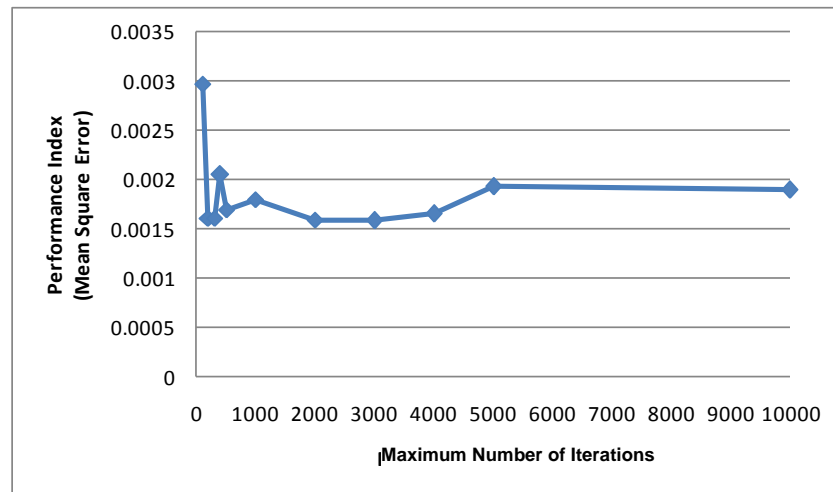


Figure 98. Performance index with respect to number of maximum iterations (power f/b)

The simulation result of this model is given in Figure 99.

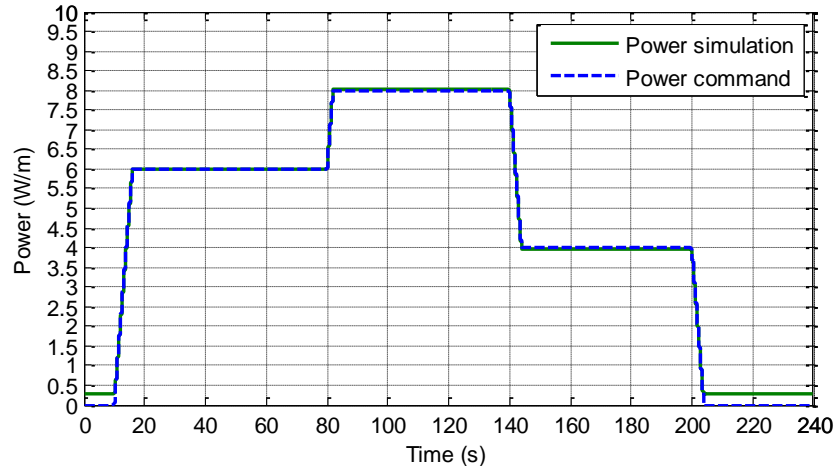


Figure 99. Power command and model response using Narma L2 controller

3.6. Strain-Resistance Relation

The aim of controlling the resistance of the wire is to control its displacement eventually. Therefore, a relationship between strain and resistance should be established. When the resistance-strain curve given in Figure 100 is observed, a fifth order curve as seen on the figure passing through the mid-points of the heating and cooling curves reflects the relation with maximum 0.1% error in strain. For a wire of 100 mm in length, this would represent a position error of only 0.1 mm out of overall stroke of about 3 mm.

In Figure 100, the lower curve represents the experimental data obtained when the wire is heated and fully recovers the displacement imposed by the bias force. The upper curve represents the experimental data when the wire is cooled to martensite phase, thus allowing the deformation caused by the bias force. The middle line is the polynomial that fits the experimental data given by the equation:

$$R=0.235*\epsilon^5-1.84*\epsilon^4+5.49*\epsilon^3-7.77*\epsilon^2+3.37*\epsilon+28.4$$

Where, R is the resistance in Ohm/m and ϵ is the percent strain of the wire.

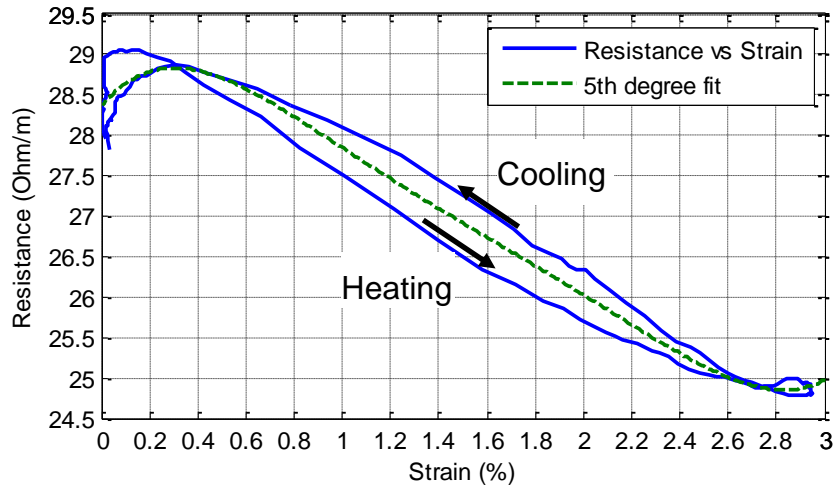


Figure 100. Resistance-strain relation

As stated before, the simulation for resistance feedback control is used to observe the strain-resistance relation. The current supplied to resistance model is also supplied to the strain model (Figure 101). The desired strain input is transformed to the resistance input using the fifth order equation. Thus, the resistance and strain responses can be seen in Figure 102 and Figure 103.

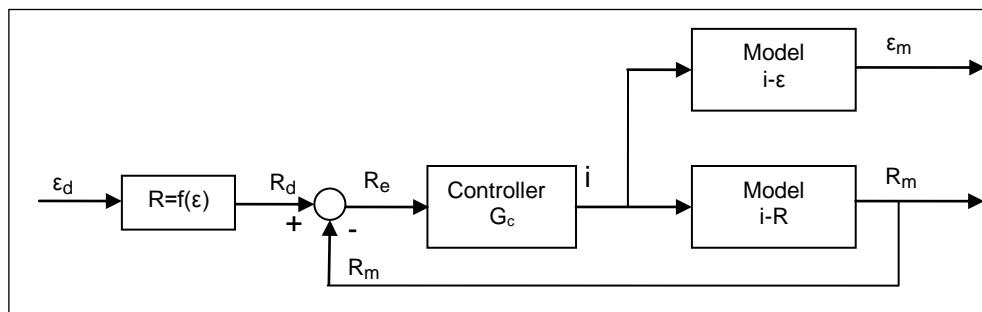


Figure 101. Block diagram of resistance control using strain input

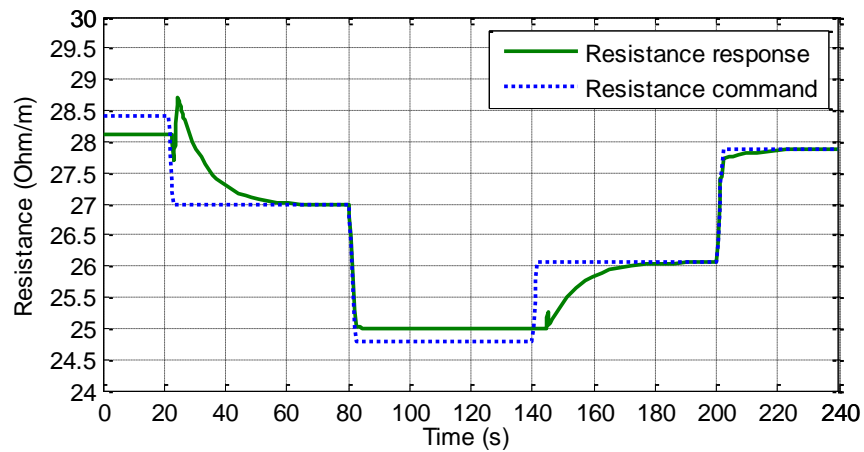


Figure 102. Resistance response using strain input

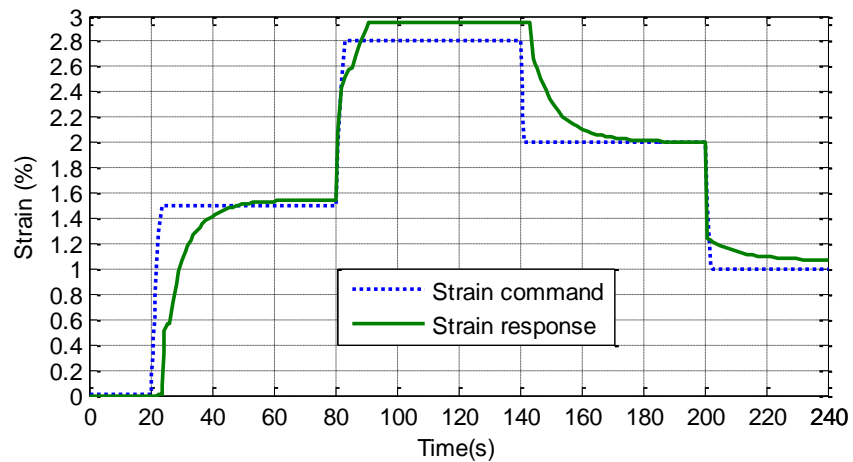


Figure 103. Strain response of resistance control using strain input

When Figure 103 is examined it can be observed that strain commands can be tracked by maximum 5 % error using resistance as the feedback in the control system.

3.7. Strain-Power Relation

The aim of controlling the power of the wire is also to control the strain response of the wire, thus a relationship between strain and power should be established. The relation obtained in the form of third order curves is presented in strain-power curve given in Figure 104.

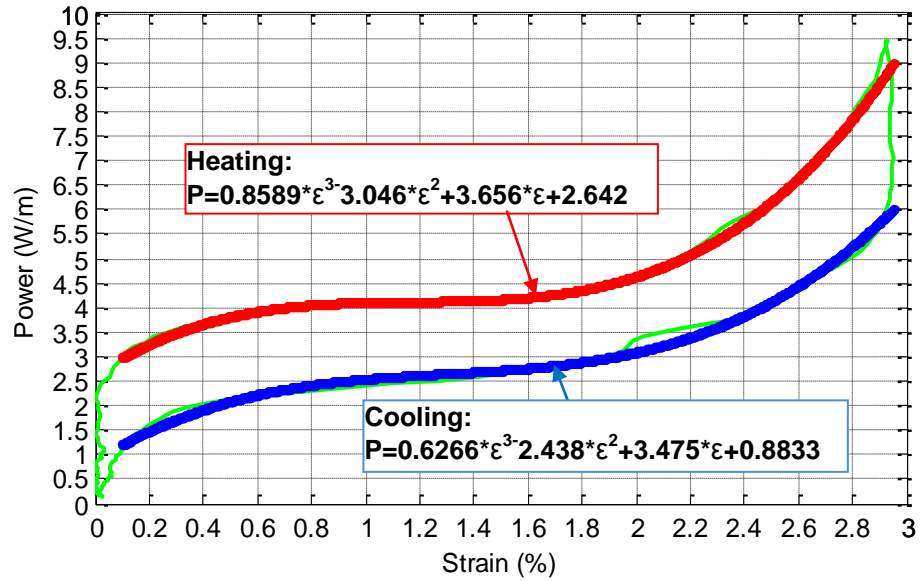


Figure 104. Strain-power relation

The relevant control system is then constructed as in the block diagram in Figure 105. The desired strain input is transformed to the power input using the model. The current supplied to power model is also supplied to the strain model. Thus, the power and strain responses are obtained as in Figure 106 and Figure 107.

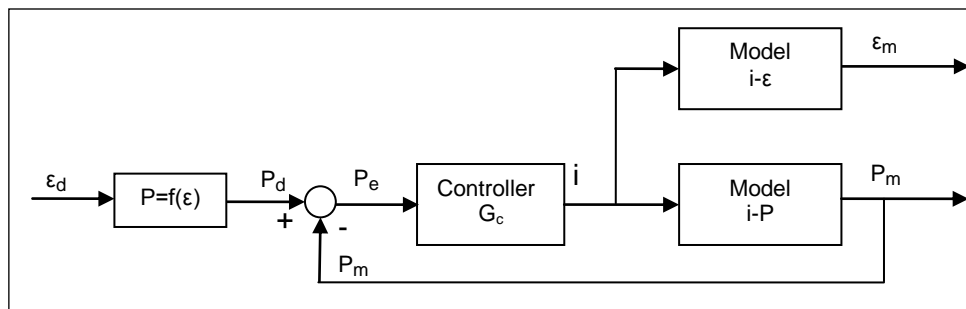


Figure 105. Block diagram of power control using strain input

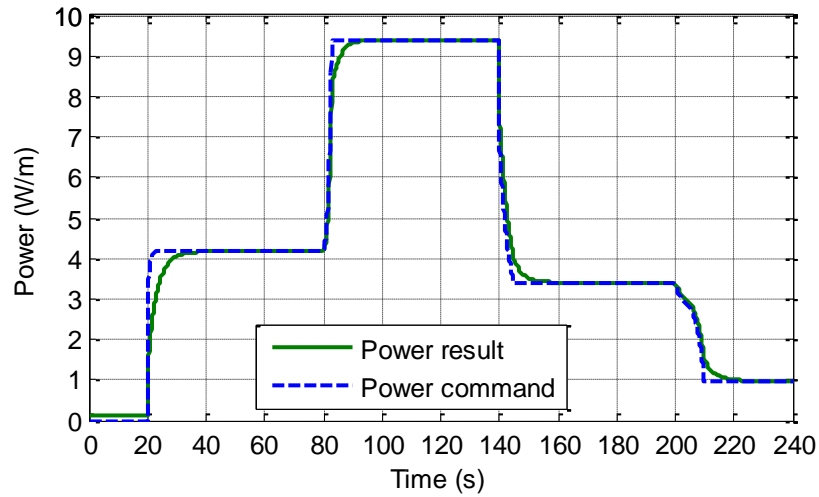


Figure 106. Power response using strain input

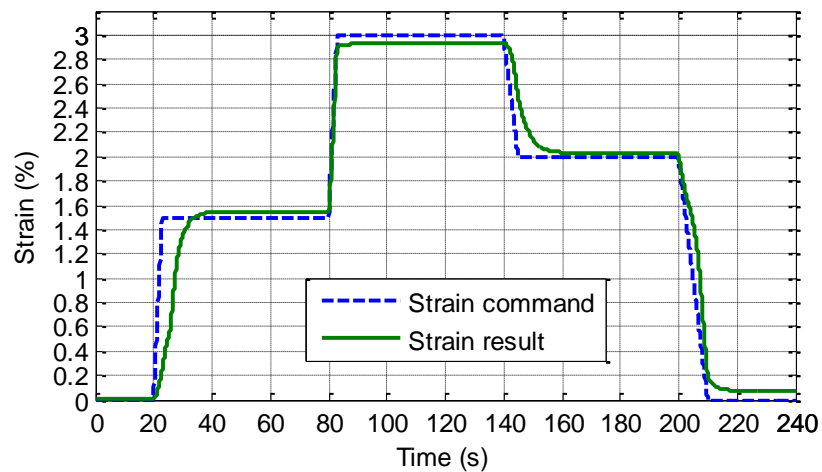


Figure 107. Strain response using power control with strain input

If the strain results are examined it can be observed that errors less than 3% can be achieved using power to control strain.

3.8. Validation of Control Schemes under Different Loads

In this section, the controllers designed in the previous sections for strain and resistance feedback are validated under different loads. The wire models are replaced by the models obtained using the data collected from the tests where 286 gr (90 MPa) and 660 gr loads (210 MPa) are carried by the SMA wire.

3.8.1. Simulations with 90 MPa Stress

3.8.1.1. Strain Feedback

The strain-current model for the load leading to the stress of 90 MPa load is given in Figure 108. In the simulations, the PI controller for strain feedback has been used with $K_p=300$ and $K_i=55$.

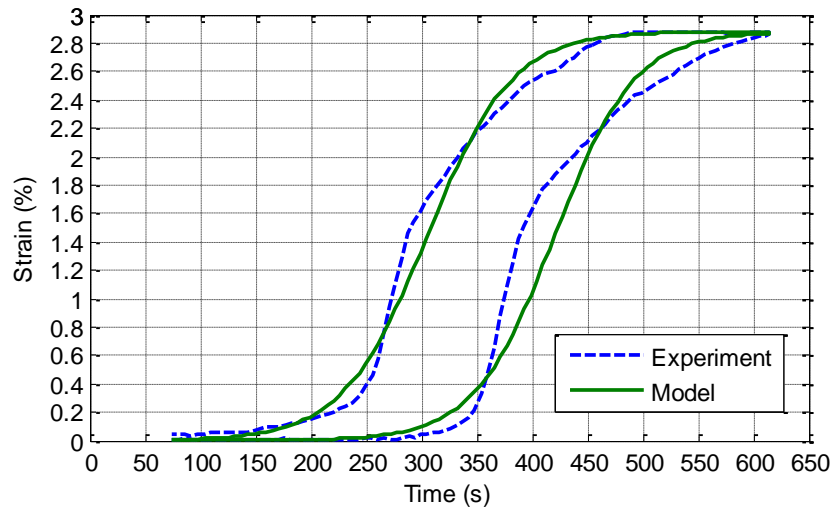


Figure 108. Strain model with 90 MPa stress

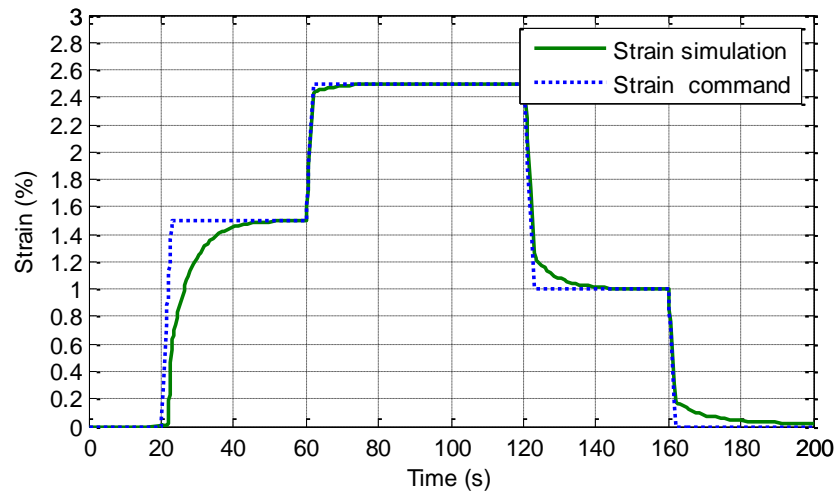


Figure 109. Strain response with 90 MPa stress

As can be seen from Figure 109 the controller parameters obtained for 140 MPa load can sufficiently be used for strain control under 90 MPa load.

3.8.1.2. Resistance Feedback

The resistance-current model for the load creating 90 MPa stress is given in Figure 110. The PI controller for resistance feedback has been used in the simulations with $K_p=300$ and $K_i=35$.

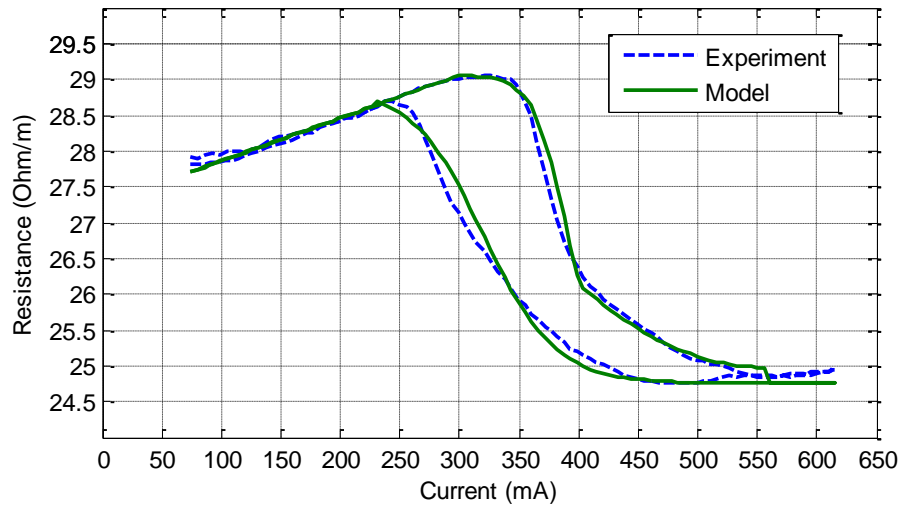


Figure 110. Resistance model with 90 MPa stress

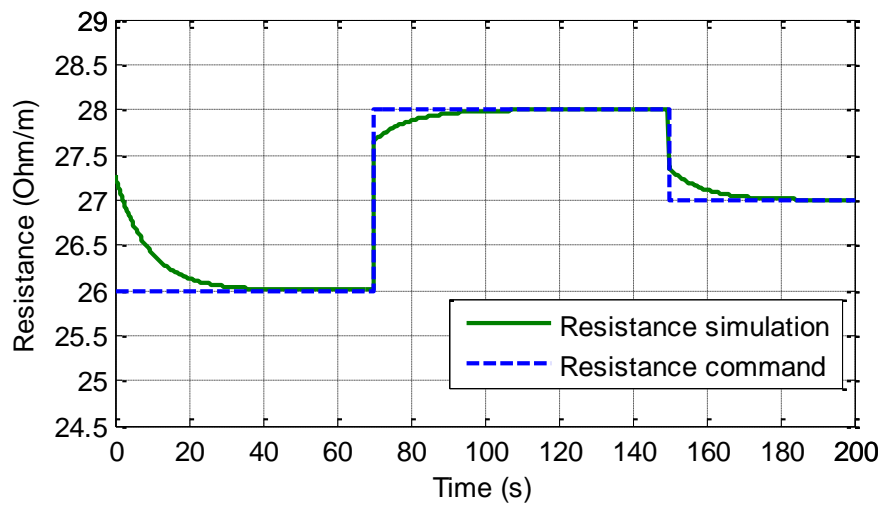


Figure 111. Resistance response with 90 MPa stress

If Figure 111 is examined, it can be concluded that resistance feedback controller obtained previously can be used for this data set.

3.8.1.3. Power Feedback

The power-current model for stress of 90 MPa presented in Figure 112. The PI controller for power feedback has been used in the simulations with $K_p=100$ and $K_i=99$. The simulation results presented in Figure 113 show that effective control of power under 90 MPa stress can be achieved.

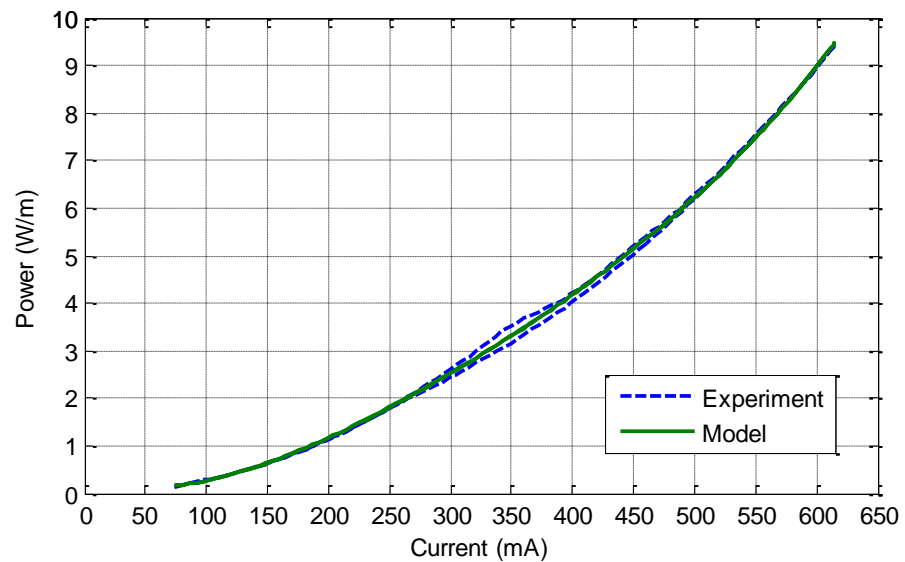


Figure 112. Power model with 90 MPa stress

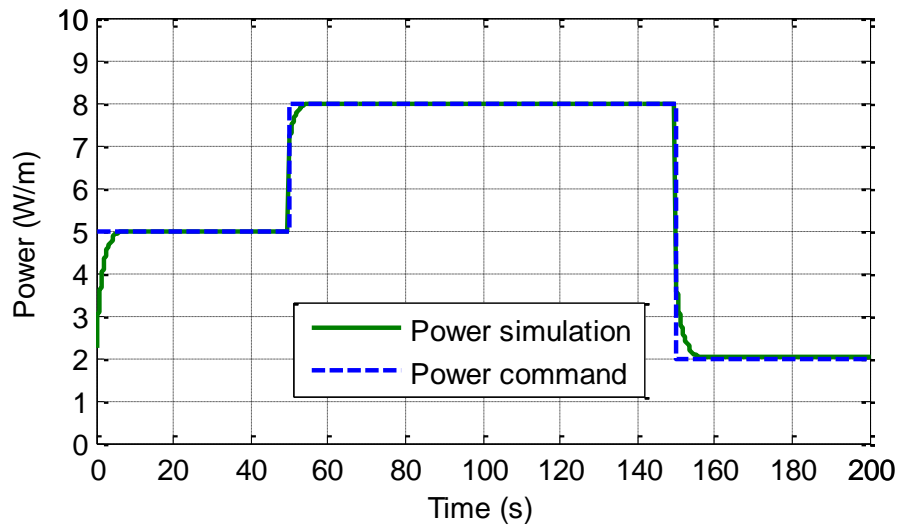


Figure 113. Power response with 90 MPa stress

3.8.2. Simulations with 210 MPa Stress

3.8.2.1. Strain Feedback

The strain-current model for 210 MPa stress is given in Figure 114. The PI controller for strain feedback with $K_p=300$ and $K_i=55$ has been used in the simulations.

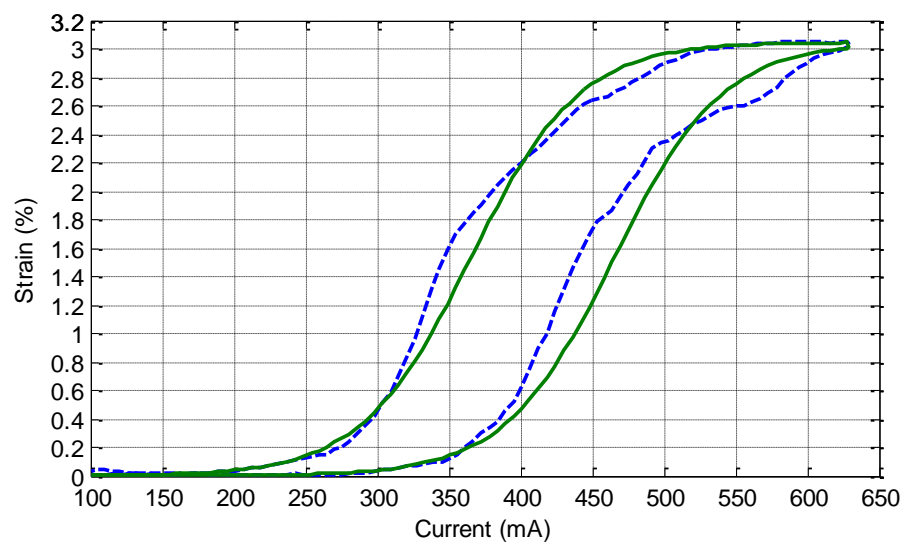


Figure 114. Strain model with 210 MPa stress

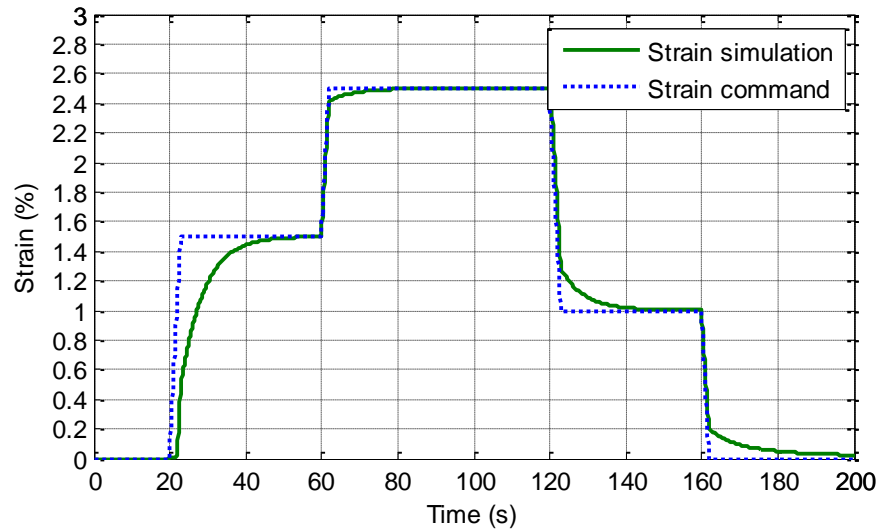


Figure 115. Strain response with 210 MPa stress

As can be observed in Figure 115, the controller parameters obtained for 140 MPa load can also sufficiently be used for strain control under 210 MPa load.

3.8.2.2. Resistance Feedback

The resistance-current model for 210 MPa stress is given in Figure 116. The PI controller for resistance feedback with the model of the wire under 210 MPa stress has been used in the simulations with the parameters $K_p=300$ and $K_i=35$.

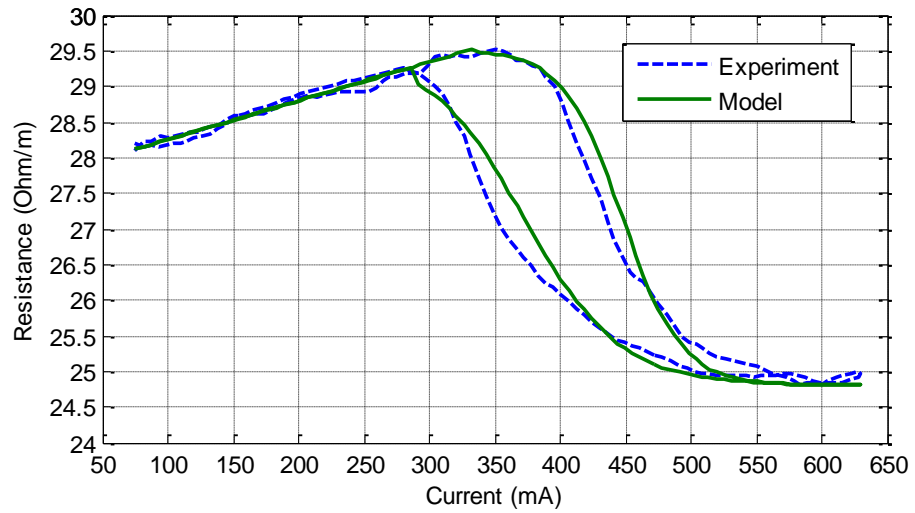


Figure 116. Resistance model with 210 MPa stress

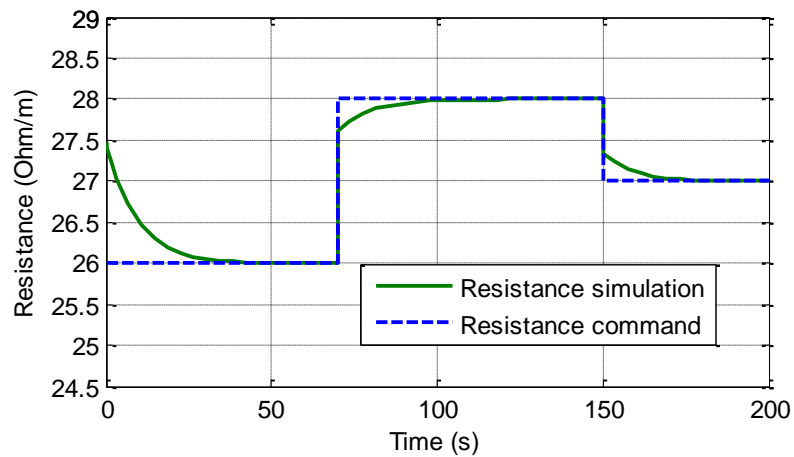


Figure 117. Resistance response with 210 MPa stress

Resistance of the wire under 210 MPa load can be controlled with the controller parameters obtained for 140 MPa load (Figure 117).

3.8.2.3. Power Feedback

The power-current model for 210 MPa stress is presented in Figure 118. The PI controller for power feedback has been used in the simulations with $K_p=100$ and $K_i=99$.

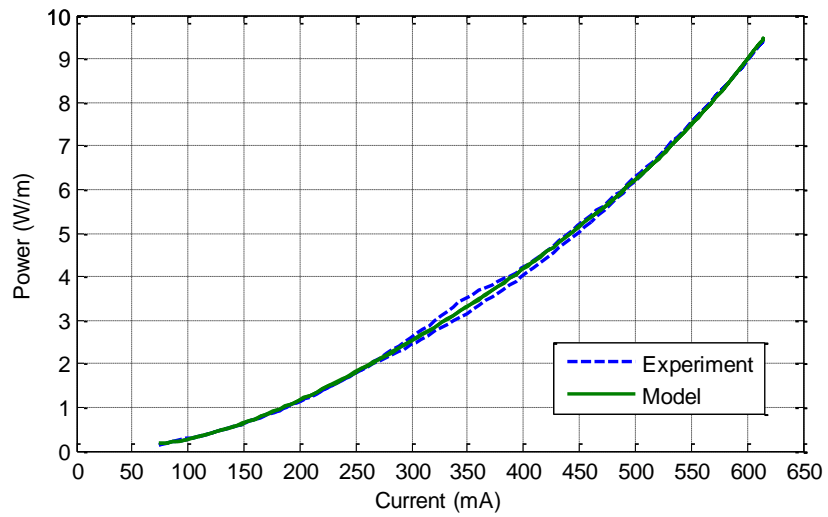


Figure 118. Power model with 210 MPa stress

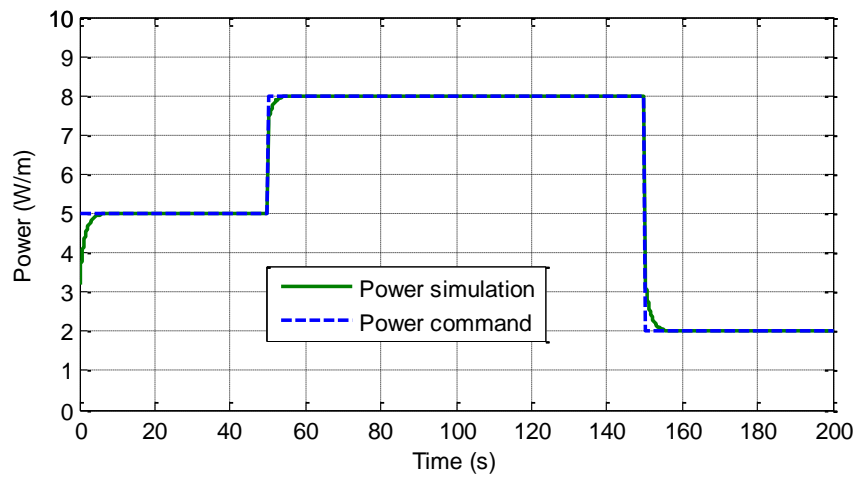


Figure 119. Power response with 210 MPa stress

If the response presented in Figure 119 is examined, it can be concluded that, controllers developed using the data for 140 MPa stress can be used for other loading states.

CHAPTER 4

EXPERIMENTS ON THE POSITION CONTROL OF SHAPE MEMORY ALLOY WIRES

4.1. Control Set-up

The available SMA wire characterization set-up is modified to experiment the control strategies developed on the SMA wire. In this scheme, the data acquisition and control card National Instruments 6036E is integrated in the system to send the control signals from the computer to the electronic load in order to control the current through the wire and to collect the current, voltage and displacement data for feedback and monitoring. Since the transformation takes place around 1-2 Hz, and control is performed with a much lower bandwidth data collection and control algorithms are run with a sampling frequency of 100 Hz to eliminate the collection of higher frequency noise in the data. A conceptual block diagram for the experimental set-up is presented in Figure 120. The resolution and accuracy of the instruments used in the experiments are presented in Table 8. Windows© XP is used as the operating system, and Real-Time Windows Target™ is used run Matlab® Simulink® models in real time.

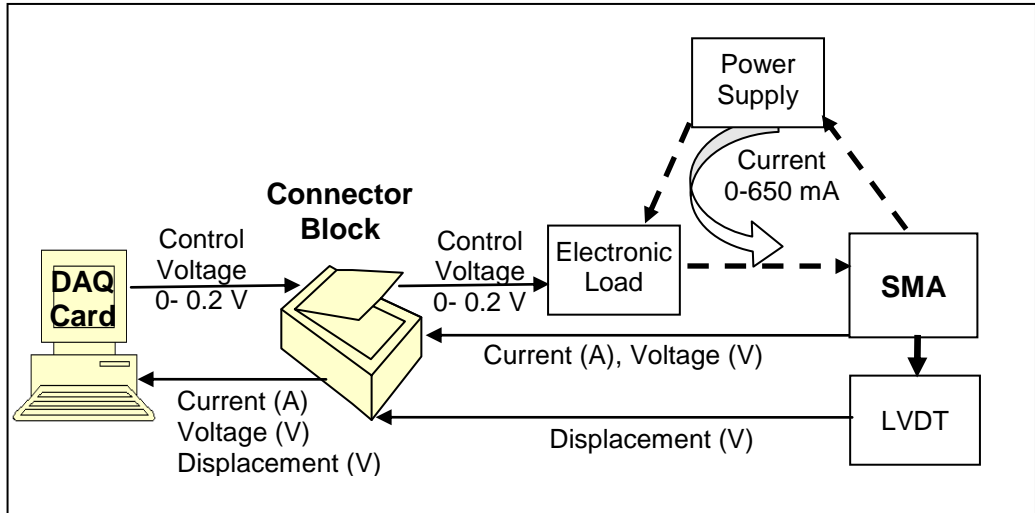


Figure 120. Conceptual circuit diagram for the experiment set-up

Table 8. Instruments used in the experiments

Instrument	Brand/Model	Resolution	Accuracy
Displacement sensor	BALLUFF BTL05	< 0.1 mV/10V	0.5 μ m
Power supply	INSTEK PST3202	1 mA	$\leq 0.1\% + 5\text{mA}$
Electronic load	DATEL DTL32A-LC	0.025 %	$\pm 1\%$
Data acquisition and control card	National Instruments NI 6036E	16 bit	0.1085 mV
Connector block	National Instruments SCB 68	–	–

In order to convert the control current signals to the electronic load control voltage signals a driver gain function is used. This function is estimated by linear curve fitting to the experimental data of current versus control signal plot (Figure 121).

The conversion function to convert current commands in milliamperes to control signal voltage in milivolts is:

$$V(\text{mV}) = 0.20029 \cdot I(\text{mA}) - 2.2359$$

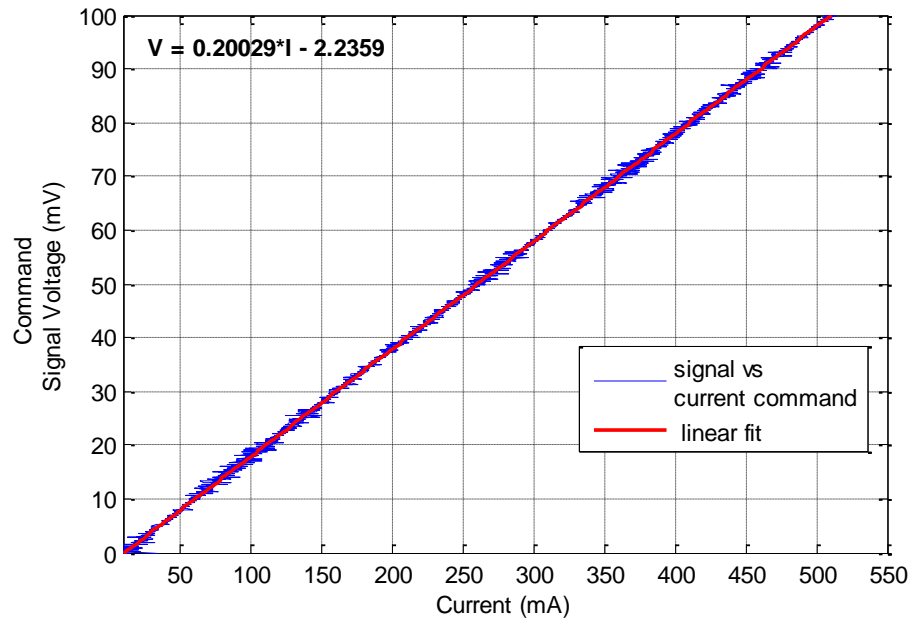


Figure 121. Current versus control signal voltage plot and linear fit

Since the noise from any data acquisition system is inevitable, the data used as feedback should be filtered during the experiments. In order to design the filter, the frequency response of the raw of strain, voltage, and current data collected for 10 and 100 mA constant current values are analyzed using power spectral densities (PSD) of the data after the mean is removed (Figure 122). When the graphs are investigated, it is observed that the noise level of the current data is higher in the order of magnitude of 10^5 than the data collected for voltage and strain.

Since the SMA is generally controlled at a maximum rate of 0.5 Hz and the transformation phenomenon can be observed around 1-2 Hz, a low pass filter with a cut-off frequency of 5 Hz is designed to remove the higher frequency noise thus smoothen the data used as feedback.

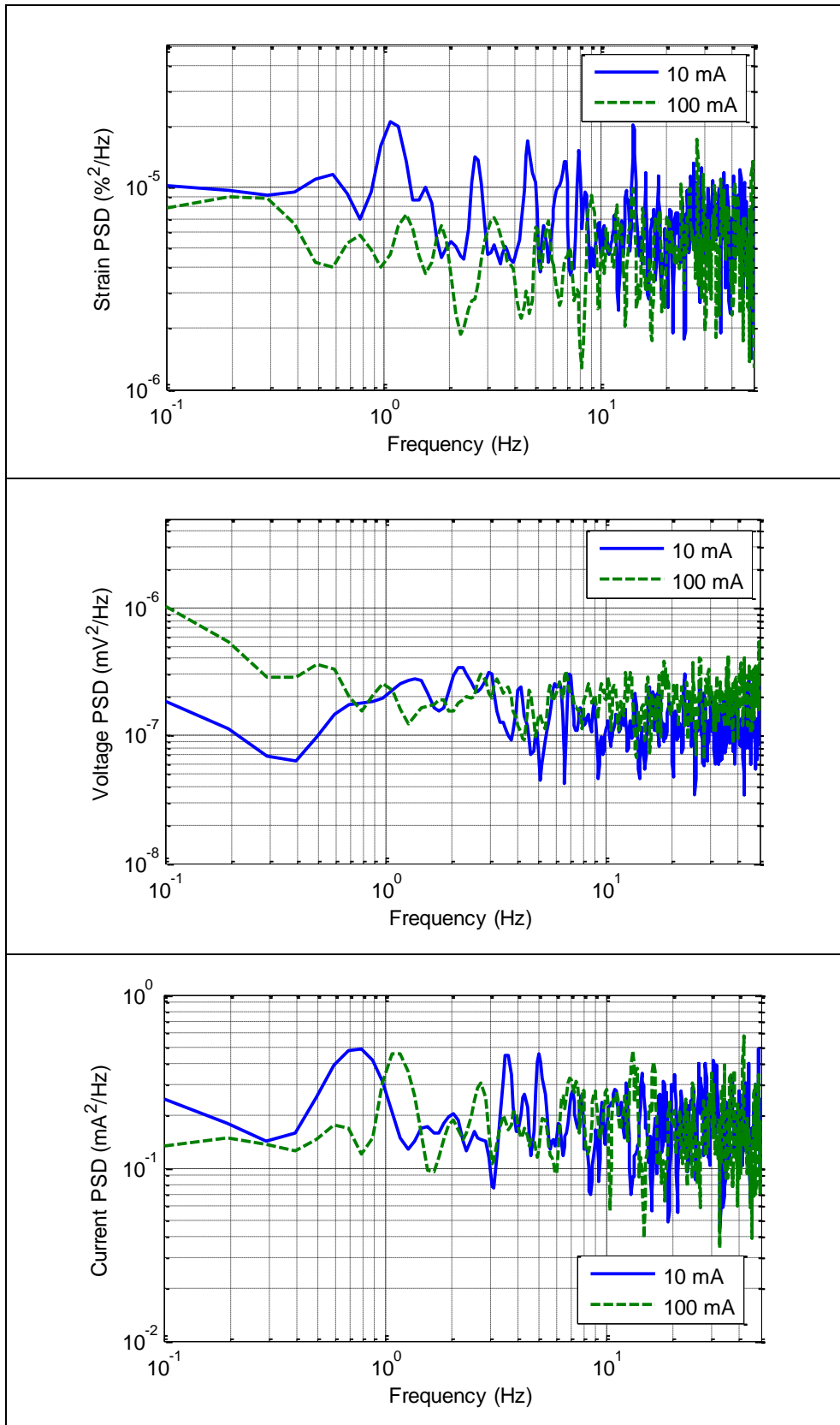


Figure 122. PSDs of raw strain, voltage, and current data

The order of the filter determines the smoothness and the phase lag of the filtered data as well as the overshoot in the initial start-up. As the order of the filter is increased, the phase lag, the initial overshoot, and calculation time increases, however, the data become smoother. Thus, a trade-off should be made. Raw data and data filtered with second-order and third-order low-pass filters are plotted (Figure 123). When the graphs are analyzed, the overshoot with the third order filter is higher, however the smoothness of the curve with third order filter is much better than the curve with the second order filter, thus third order low pass filter is chosen to be used.

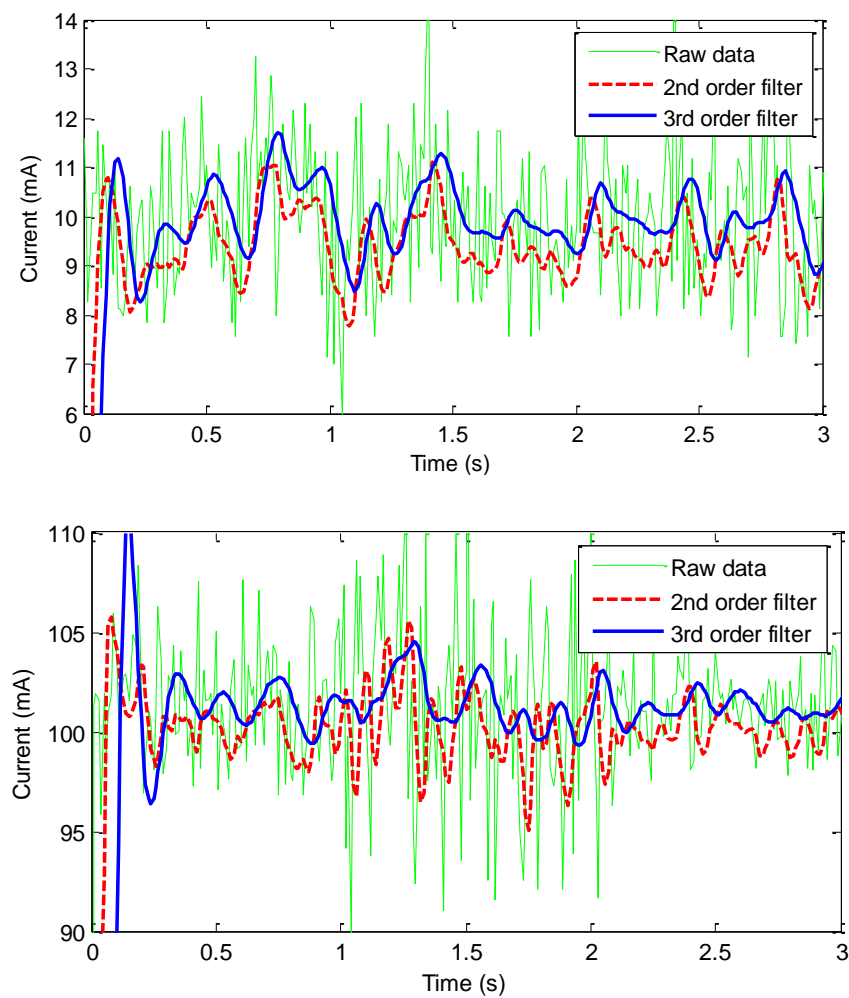


Figure 123. Raw and filtered data for 10 mA and 100 mA constant current

4.2. Strain Feedback

Firstly, the position of the SMA wire is controlled using strain feedback. In this work, PI, PI with feedforward loop, and neural network Narma-L2 control schemes are implemented and then experimented.

The Simulink model for the strain feedback is given in Figure 124. In this model strain command and feedback are fed to the controller box. Then, the control command generated by the controller passes through saturation block to ensure that the command is below 650 mA in order not to feed the wire with over current. After saturation the current command is converted to control voltage to be supplied to electronic load by passing through the driver gain block. The block named SMA wire represents the real world, i.e. electronic load, power supply, SMA wire, and calibrated resistance. The connection between the computer and the real world is maintained through the data acquisition and control card (NI 6036E) and the connector block (SCB 68). The generated command signals are sent to electronic load that adjusts its internal resistance accordingly, and that is connected to the SMA wire in series so that the current through the loop is controlled.

The data of the current passing through the wire, voltage of the wire, and displacement of the tip of the wire are collected. In strain feedback control method, the displacement of the wire is supplied to the feedback loop. After being filtered the displacement is converted to the absolute strain of the wire by subtracting the initial position of the wire and then dividing by the length of the wire. The obtained strain data are then fed back to the controller for real time control.

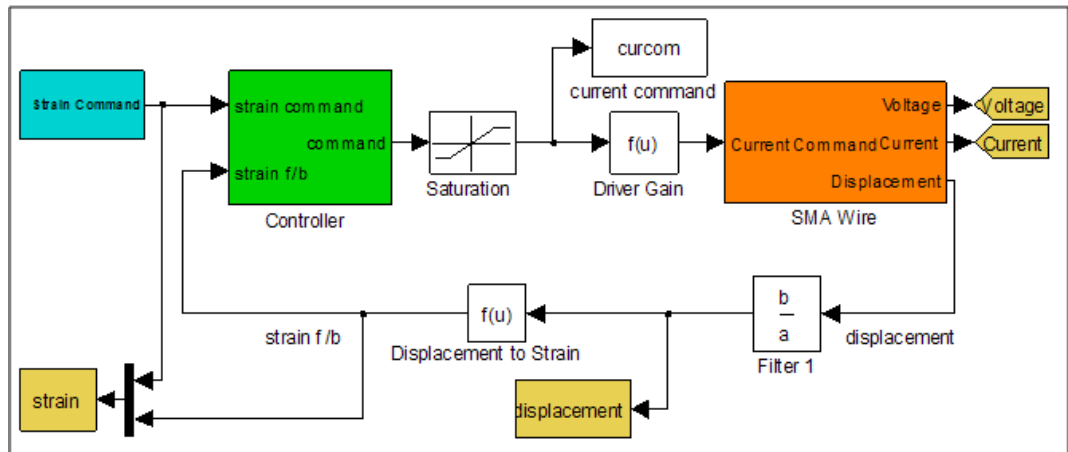


Figure 124. Simulink model for strain feedback control system

4.2.1. PI-Type Control

In order to control the strain of the SMA wire, the designed PI-type controller is implemented with $K_p=300$, $K_i=55$, and $K_f=110$ (Figure 125). In this control method, error in strain is fed through the proportional gain and the cumulative error is multiplied with the integral gain.

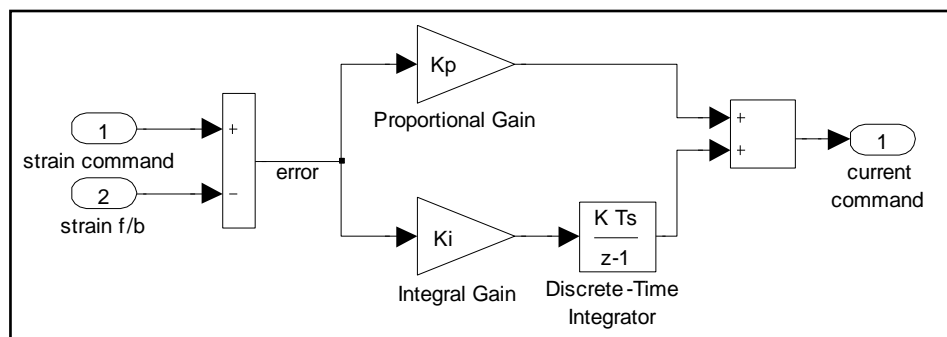


Figure 125. Simulink model for PI-type controller for strain feedback

The plots of the strain command and the response obtained during the experiments are given in Figure 126 and Figure 127.

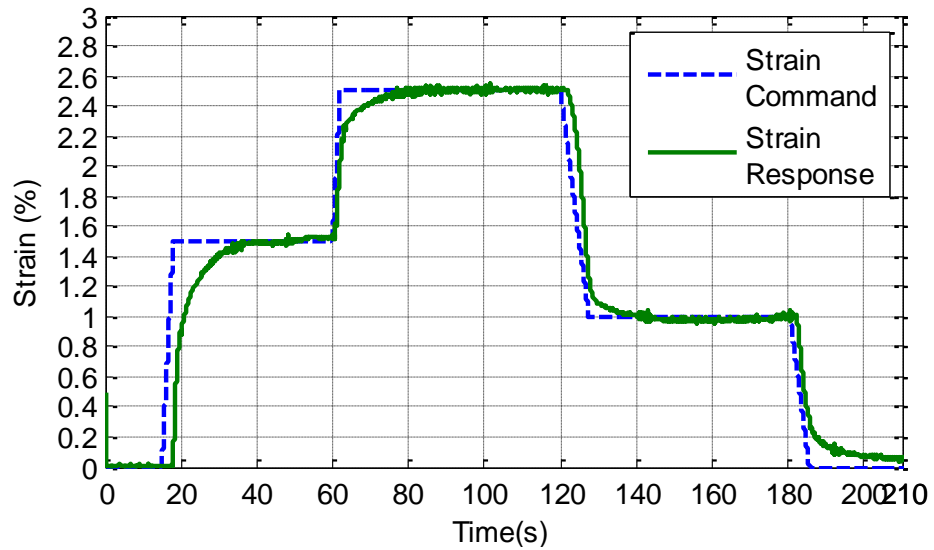


Figure 126. Strain feedback with PI control ($K_p=300$ and $K_i=55$)

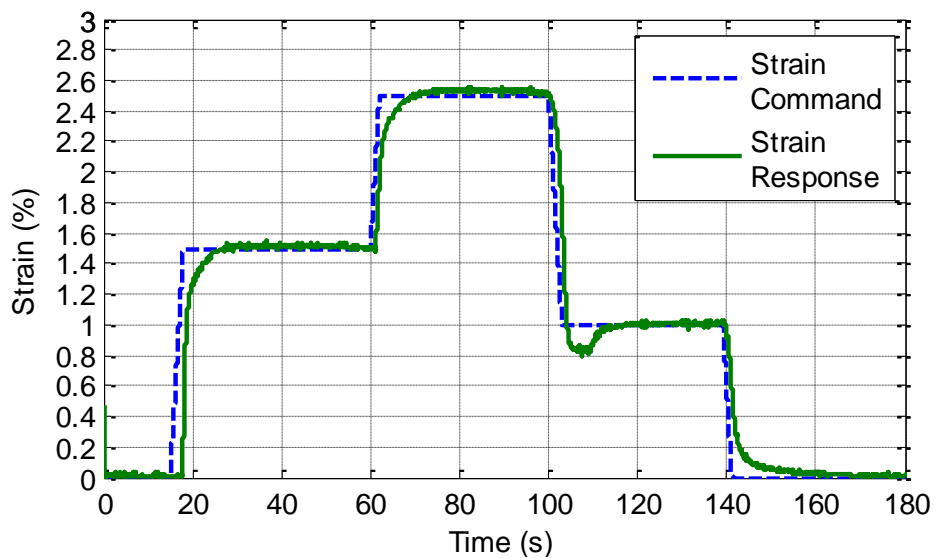


Figure 127. Strain feedback with PI control ($K_p=300$ and $K_i=110$)

When the figures are examined, it can be seen that the speed of the response increases as the selected control bandwidth (integral gain) increases, as expected; also 18 % overshoot is observed during cooling.

4.2.2. PI-Type Control with Feedforward Loop

The inverse model for strain-current relation given in section 3.3.3 is implemented in the PI control scheme (Figure 128). The feedforward gain is

adjusted to 0.8 in the feedforward loop. The experiments are conducted for $K_p=300$, and $K_i=55$. The obtained strain curve is presented in Figure 129.

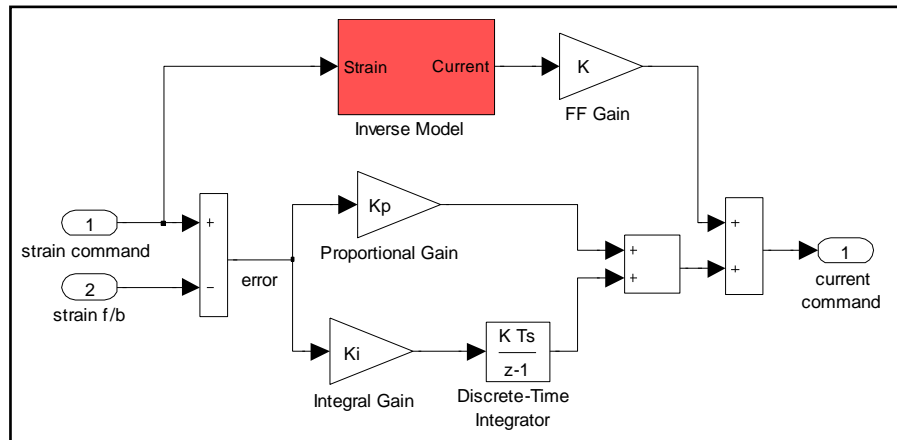


Figure 128. Simulink model for PI-type control with feedforward loop for strain feedback

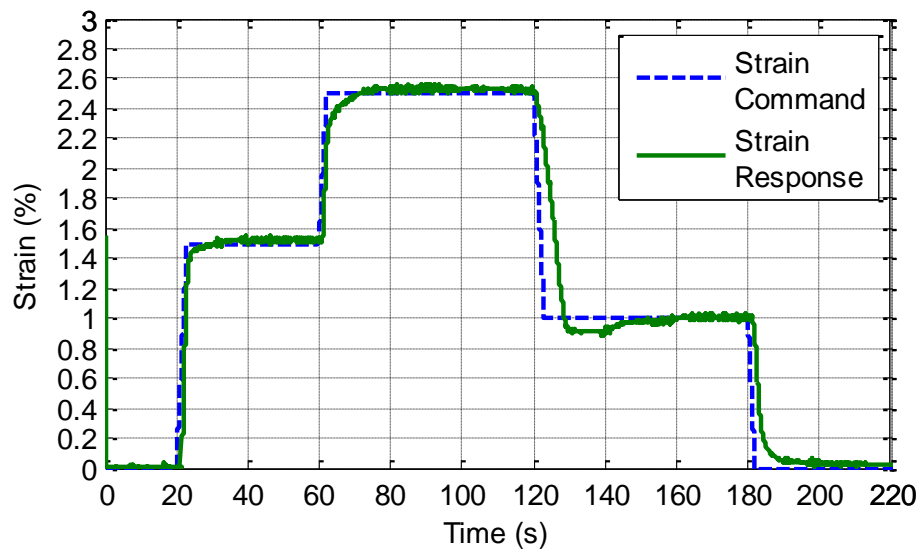


Figure 129. Strain feedback with PI control with feedforward loop ($K_p=300$ and $K_i=55$)

If Figure 126 and Figure 129 are compared the increase in the speed of the response can easily be seen. That is, the settling time of latter control system becomes smaller than the former one.

4.2.3. Neural Network Narma-L2 Controller

The controller trained as discussed in section 3.3.4 is used to control the strain of the SMA wire. The standard Narma-L2 control box in Simulink is given

in Figure 130. The strain command and the response are presented in Figure 131.

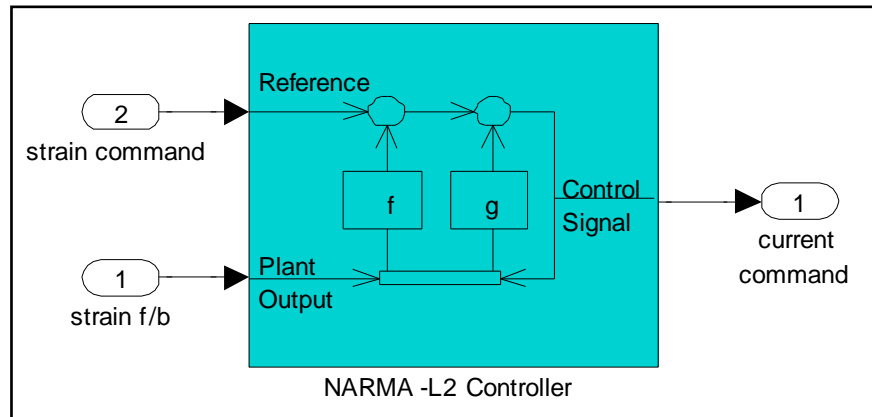


Figure 130. Simulink model for Neural network Narma-L2 control for strain feedback

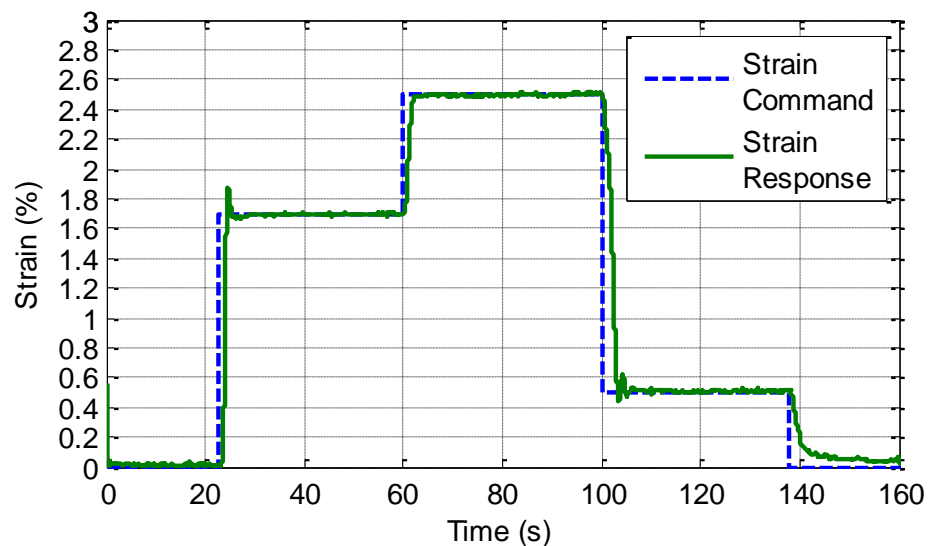


Figure 131. Strain feedback with NN Narma-L2 control

In the figure presented above it can be seen that, strain of the wire can be controlled using the neural network controller obtained in the simulations.

Results of experiments on strain feedback can be summarized as in Table 9, considering steady state error, overshoot, rise time and settling time (2 % criterion).

Table 9. Comparison of experimental results of strain control methods

Command	Controller	Steady state error (%)	Overshoot (%)	Rise time (95%) (s)	Settling time (2%) (s)
0% →1.5%	PI ($K_p=300$ and $K_i=55$)	0	0	17	25
	PI ($K_p=300$ and $K_i=110$)	0	0	8	13
	PI with FF ($K_p=300$, $K_i=55$, and $K=0.8$)	0	0	7	13
	NN Narma-L2	0	9	3	8
1.5%→2.5%	PI ($K_p=300$ and $K_i=55$)	0	0	17	22
	PI ($K_p=300$ and $K_i=110$)	0	4	8	35
	PI with FF ($K_p=300$, $K_i=55$, and $K=0.8$)	0	0	8	18
	NN Narma-L2	0	0	3	5
2.5%→1%	PI ($K_p=300$ and $K_i=55$)	0	0	18	25
	PI ($K_p=300$ and $K_i=110$)	0	13	6	15
	PI with FF ($K_p=300$, $K_i=55$, and $K=0.8$)	0	7	8	25
	NN Narma-L2	0	2.5	5	8

1%→0%	PI ($K_p=300$ and $K_i=55$)	0	0	30	60
	PI ($K_p=300$ and $K_i=110$)	0	0	15	30
	PI with FF ($K_p=300$, $K_i=55$, and $K=0.8$)	0	0	12	25
	NN Narma-L2	5	0	10	20

4.3. Resistance Feedback

Secondly, the position of the SMA wire is controlled using resistance feedback. In this work, PI, PI with feedforward loop, and neural network Narma-L2 control methods are implemented and experimented as done before.

The Simulink model for the resistance feedback is given in Figure 132. In this model resistance command and feedback are fed to the controller box. Then, the control command generated by the controller passes through saturation block. After saturation the current command is converted to control voltage to be supplied to electronic load by passing through the driver gain block.

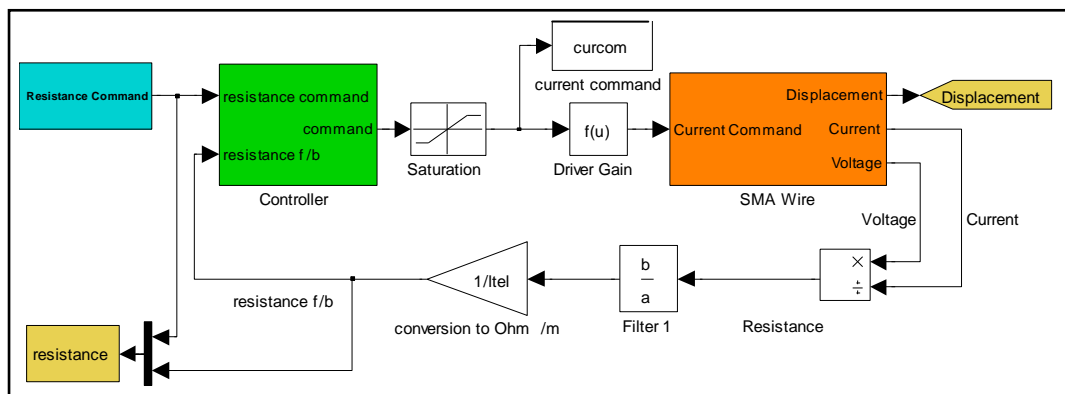


Figure 132. Simulink model for resistance feedback control system

The data of the current passing through the wire, voltage of the wire, and displacement of the tip of the wire are collected. In resistance feedback control method, the resistance of the wire, obtained by dividing the voltage across the

wire to the current passing through the wire, is supplied to the feedback loop. After being filtered the resistance is converted to the resistance of the unit length of the wire. The obtained resistance value is then fed back to the controller for real time control.

4.3.1. PI-Type Control

In order to control the resistance of the SMA wire, the designed PI-Type Controller (Figure 133) is implemented with the controller gains of $K_p=300$, $K_i=35$, and $K_f=70$.

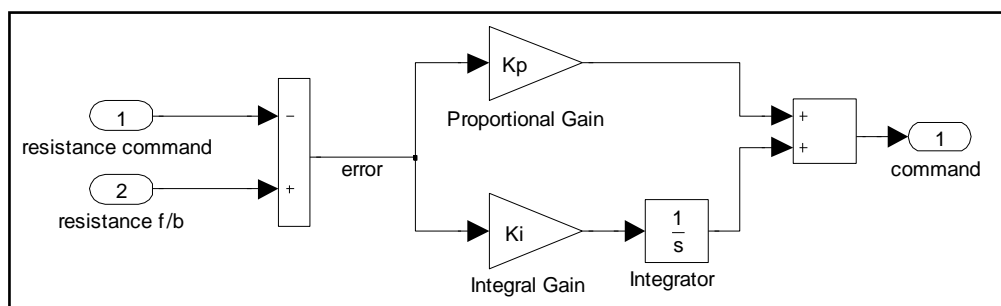


Figure 133. Simulink model for PI-type controller for resistance feedback

The resistance command and response of the wire for the two cases are submitted in Figure 134 and Figure 135, respectively.

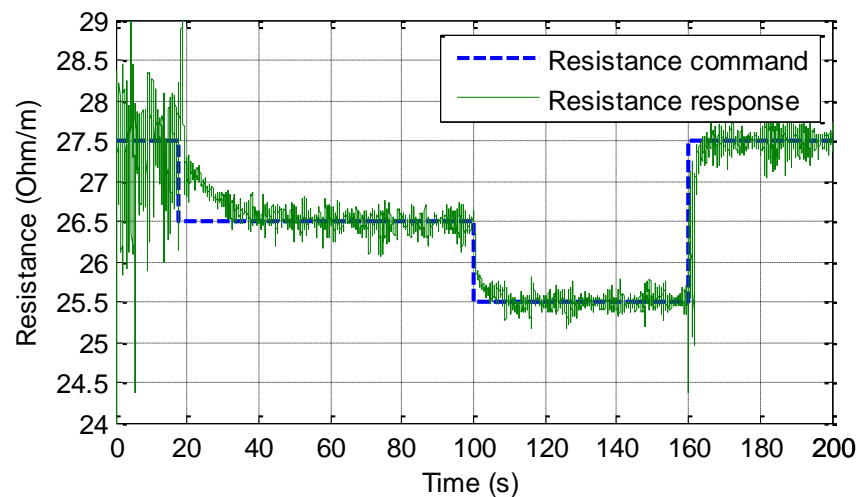


Figure 134. Resistance feedback with PI control ($K_p=300$ and $K_i=35$)

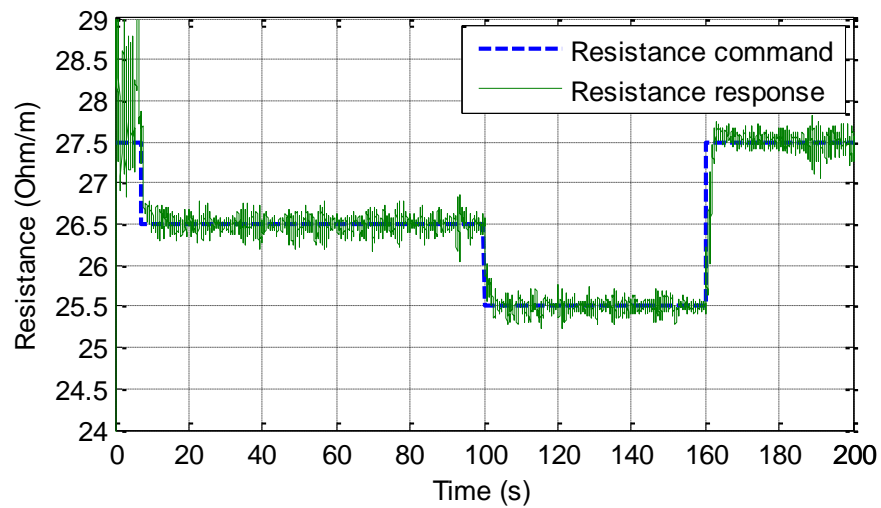


Figure 135. Resistance feedback with PI control ($K_p=300$ and $K_i=70$)

When the figures given above are examined, the noise in the data is seen, which is caused by the division operation used to calculate the resistance of the wire using current and voltage data. The noise in current and voltage data is amplified when voltage data are divided by current data.

4.3.2. PI-Type Control with Feedforward Loop

In this method, the inverse model for current-resistance relation obtained in section 3.4.3 is implemented in the feedforward loop with a feedforward gain, K , of 0.8 using $K_p=300$ and $K_i=35$. The Simulink model for PI-type control with feedforward loop is given in Figure 136.

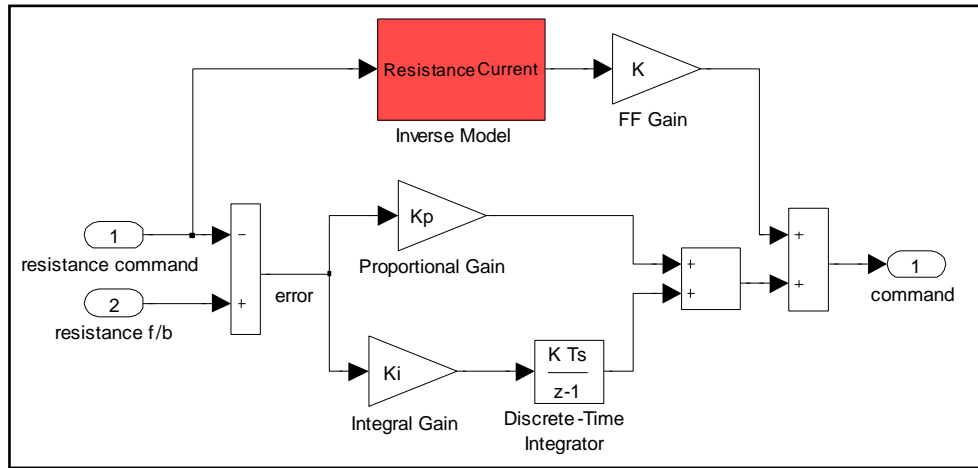


Figure 136. Simulink model for PI-type control with feedforward loop for resistance feedback

The response curve obtained in the experiments can be seen in Figure 137.

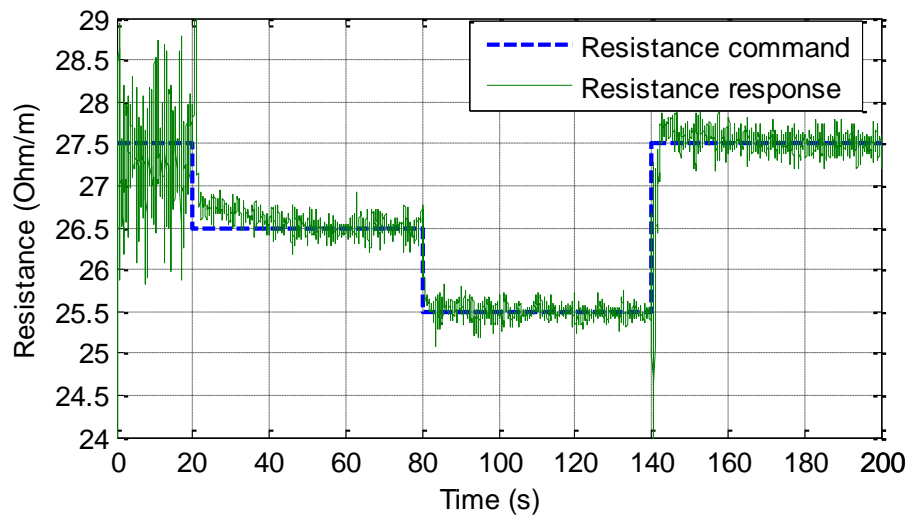


Figure 137. Resistance feedback with PI control with feedforward loop ($K_p=300$, $K_i=35$, $K=0.8$)

When Figure 134 and Figure 137 are compared, the increase in the speed of the response by addition of the feedforward loop can be observed as anticipated in the simulations.

4.3.3. Neural Network Narma L2 Controller

The NN Narma-L2 controller trained using the data from the characterization tests is employed to control the resistance of the SMA wire (Figure 138).

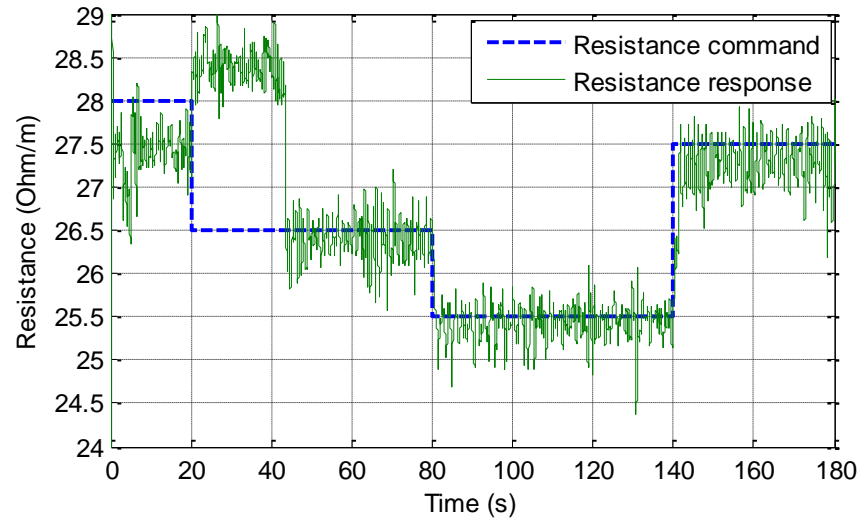


Figure 138. Resistance feedback with NN Narma-L2 control

The command and response curves presented in the plot above show that this type of controller is not suitable for resistance feedback control, due to high noise levels associated with the resistance feedback. The response is delayed and it oscillates with amplitude of 1 Ohm/m.

The summary of the results obtained in the experiments for resistance feedback control is presented in Table 10.

Table 10. Comparison of experimental results of resistance control methods

Command (Ohm/m)	Controller	Steady state error (%)	Overshoot (%)	Rise time (95%) (s)	Settling time (2%) (s)
27.5 →26.5	PI ($K_p=300$ and $K_i=35$)	0	0	14	22
	PI ($K_p=300$ and $K_i=70$)	0	0	4	7
	PI with FF ($K_p=300$, $K_i=35$, and $K=0.8$)	0	0	10	20
	NN Narma-L2	0	0	23	25
26.5 →25.5	PI ($K_p=300$ and $K_i=35$)	0	0	8	12
	PI ($K_p=300$ and $K_i=70$)	0	0	5	9
	PI with FF ($K_p=300$, $K_i=35$, and $K=0.8$)	0	0	3	7
	NN Narma-L2	0	0.4	3	10
25.5 →27.5	PI ($K_p=300$ and $K_i=35$)	0	0	7	12
	PI ($K_p=300$ and $K_i=70$)	0	0.3	4	10
	PI with FF ($K_p=300$, $K_i=35$, and $K=0.8$)	0	0.5	3	10
	NN Narma-L2	0.6	0	2	2

4.4. Power Feedback

Thirdly, the position of the SMA wire is controlled using power feedback. In the next sections the plots obtained by implementing PI, PI with feed-forward loop, and neural network Narma L2 control schemes using power feedback are presented. The Simulink model for the power feedback is given in Figure 124.

As in other cases, power command and feedback are fed to the controller box. Then, the control command generated by the controller passes through saturation block. After saturation the current command is converted to control voltage to be supplied to electronic load by passing through the driver gain block.

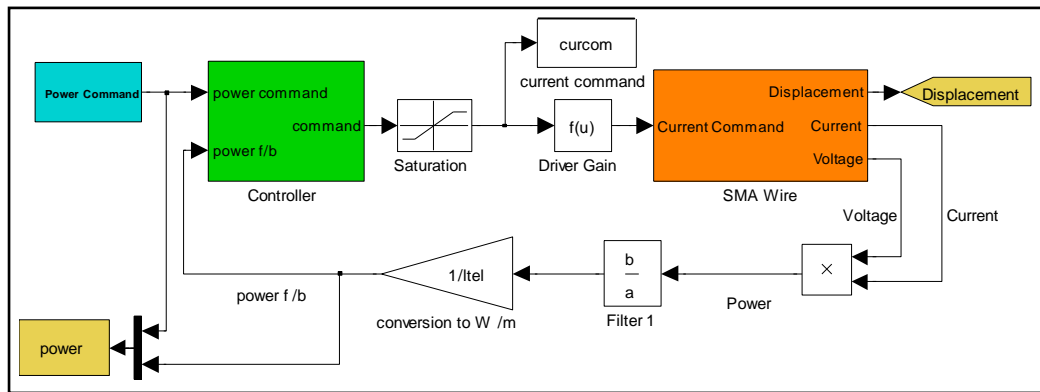


Figure 139. Simulink model for power feedback control system

The data of the current passing through the wire, voltage of the wire, and displacement of the tip of the wire are collected. In this method, the power consumption of the wire, obtained by multiplying the voltage across the wire with the current passing through the wire, is supplied to the feedback loop. After being filtered the power consumption per unit length of the wire is obtained. The obtained value is then used in the controller for comparison.

4.4.1. PI-Type Control

In order to control the power of the SMA wire, the designed PI-Type control was implemented with $K_p=100$, $K_i=49$, and $K_f=99$. The Simulink block of this controller is presented in Figure 140. The plots are presented in Figure 141 and Figure 142.

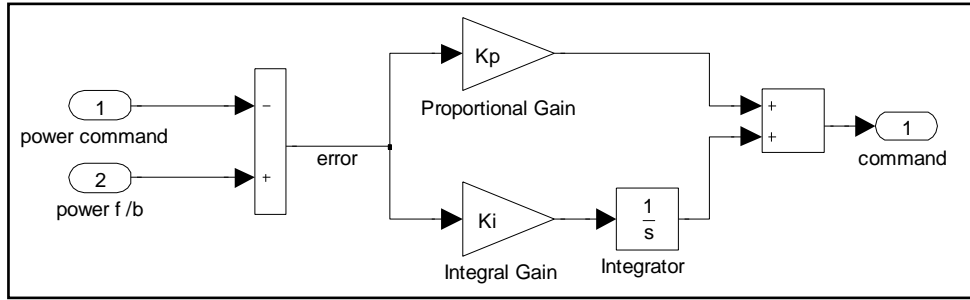


Figure 140. Simulink model for PI-type controller for power feedback

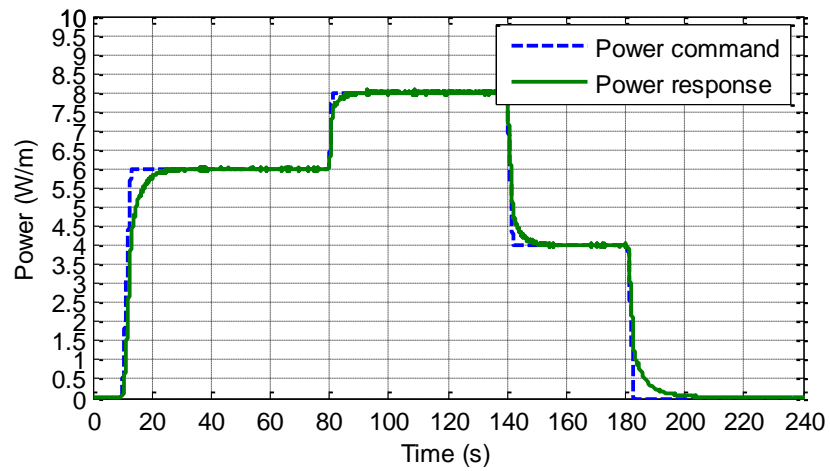


Figure 141. Power feedback with PI control ($K_p=100$ and $K_i=49$)

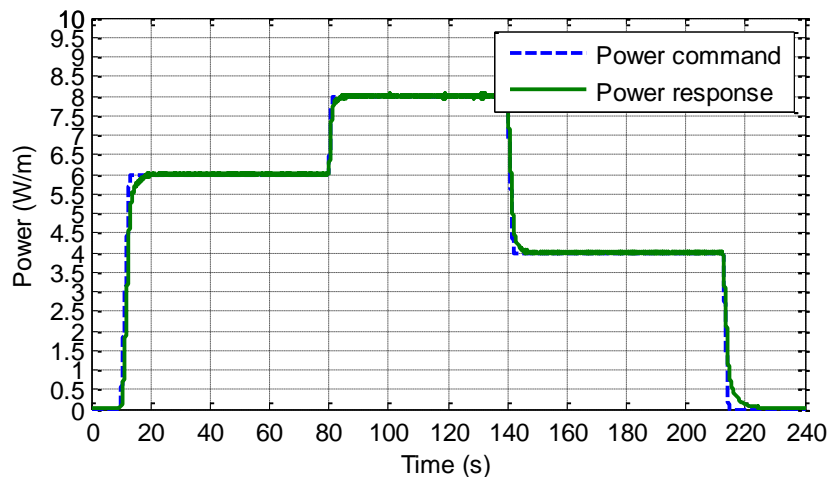


Figure 142. Power feedback with PI control ($K_p=100$ and $K_i=99$)

Power consumption of the wire can be controlled using the PI-type controllers obtained in section 0.

4.4.2. PI-Type Control with Feedforward Loop

The inverse model for power-current relation is implemented in the feedforward loop with a gain of 0.8. The Simulink model for PI-type control with feedforward loop is presented in Figure 143. The command and response curve are presented in Figure 144 for $K_p=100$ and $K_i=49$, and $K=0.8$.

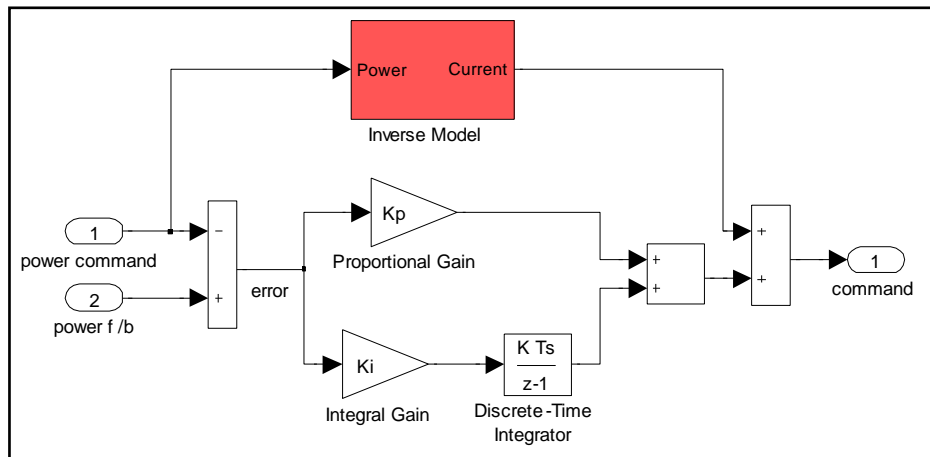


Figure 143. Simulink model for PI-type control with feedforward loop for power feedback

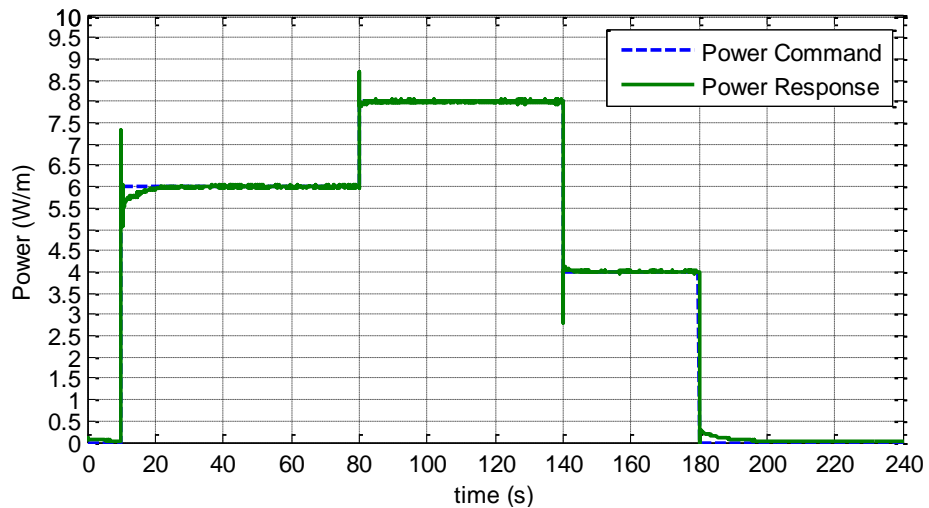


Figure 144. Power feedback with PI control with feedforward loop ($K_p=100$ and $K_i=49$)

The overshoots observed in application of this control scheme is a result of the dynamics of the system caused by electronic load and the power supply.

4.4.3. Neural Network Narma L2 Controller

The trained controller is used to control the power of the SMA wire. If the plot submitted in Figure 145 is examined it can be observed that very satisfactory results are achieved with NN Narma-L2 controller.

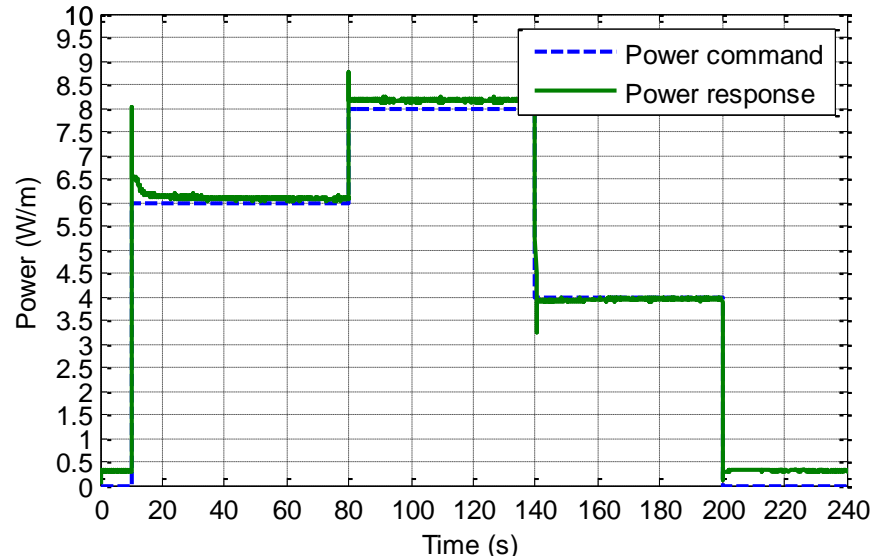


Figure 145. Power feedback with NN Narma-L2 control

The steady state error observed when the power command is zero is due to the fact that the controller output is set to be minimum 100 mA.

The summary of the results obtained in the experiments for power feedback control is presented in Table 11 considering steady state error, percent overshoot, rise time (95% criterion), and settling time (2% criterion).

Table 11. Comparison of experimental results of power control methods

Command (W/m)	Controller	Steady state error (%)	Overshoot (%)	Rise time (95%) (s)	Settling time (2%)(s)
0 → 6	PI ($K_p=100$ and $K_i=49$)	0	0	10	13
	PI ($K_p=100$ and $K_i=99$)	0	0	7	10
	PI with FF ($K_p=100$, $K_i=49$, and $K=0.8$)	0	23	2	10
	NN Narma-L2	1.5	30	1	12
6 → 8	PI ($K_p=100$ and $K_i=49$)	0	0	7	10
	PI ($K_p=100$ and $K_i=99$)	0	0	4	7
	PI with FF ($K_p=100$, $K_i=49$, and $K=0.8$)	0	10	1	3
	NN Narma-L2	2.5	10	1	2
8 → 4	PI ($K_p=100$ and $K_i=49$)	0	0	10	15
	PI ($K_p=100$ and $K_i=99$)	0	0	6	9
	PI with FF ($K_p=100$, $K_i=49$, and $K=0.8$)	0	30	1	4
	NN Narma-L2	0	20	1	18

4 → 0	PI ($K_p=100$ and $K_i=49$)	0	0	17	25
	PI ($K_p=100$ and $K_i=99$)	0	0	8	14
	PI with FF ($K_p=100$, $K_i=49$, and $K=0.8$)	0	0	10	18
	NN Narma-L2	0.3 W/m	0	1	2

4.5. Strain- Resistance Relation

As discussed in section 3.6, the aim of controlling the resistance of the wire is eventually to control the position of the wire. The strain-resistance relation obtained previously is implemented in the models so that strain inputs are converted to resistance commands thus the resistance of the wire is controlled in a closed-loop manner. The Simulink model for strain control through resistance feedback is given in Figure 146.

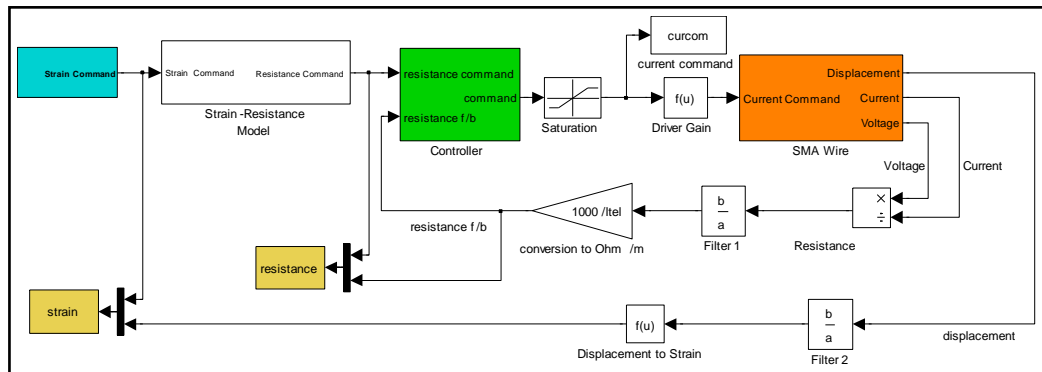


Figure 146. The Simulink model for strain control through resistance feedback

Figure 147 presents the strain command and response during the resistance control, and Figure 148 is the resistance command generated using the strain-resistance relation and the resistance response of the wire using PI controller with $K_p=300$ and $K_i=70$.

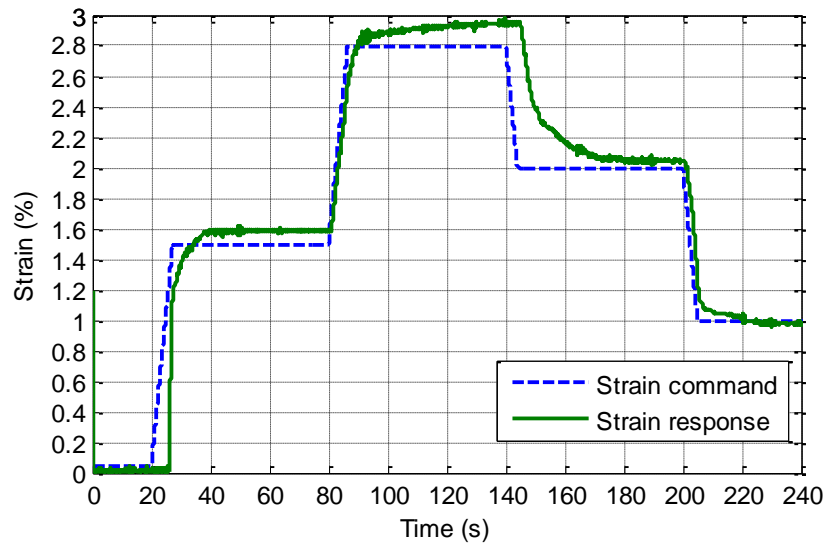


Figure 147. Strain command and response using resistance feedback with PI control ($K_p=300$ and $K_i=70$)

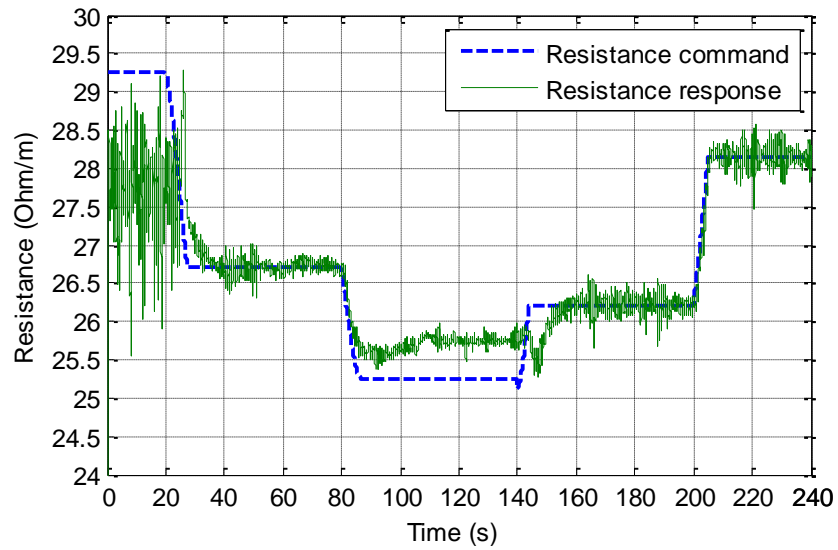


Figure 148. Resistance command and response using resistance feedback with PI control ($K_p=300$ and $K_i=70$)

When the graph given in Figure 147 is examined, strain error less than 7% is observed, so it can be concluded that using resistance for position control gives very satisfactory results.

4.6. Strain- Power Relation

As in the previous section, the same discussion applies to power feedback control. The strain-power relation obtained in section 3.7 is used to generate power commands using strain commands and power of the wire is controlled using PI controller with $K_p=100$, and $K_i=99$. The Simulink model for strain control through power feedback is given in Figure 149.

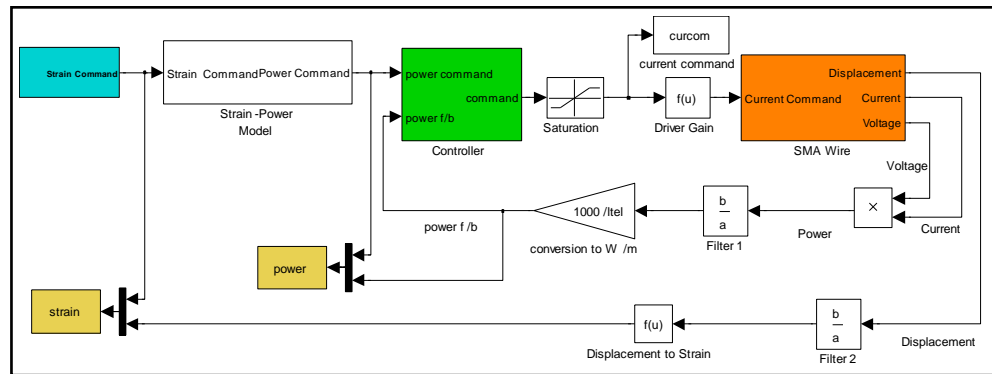


Figure 149. The Simulink model for strain control through power feedback

The strain command and response are given in Figure 150 and power command with the power response is presented in Figure 151.

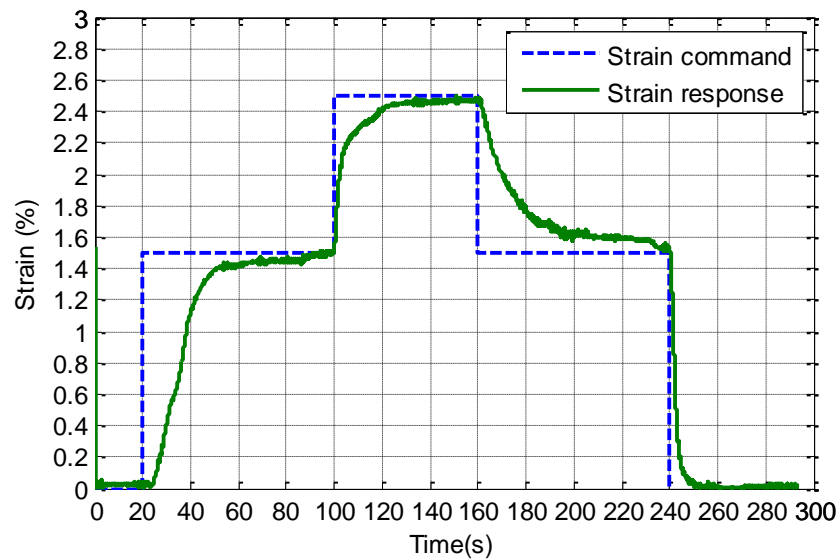


Figure 150. Strain command and response using power feedback with PI control ($K_p=100$ and $K_i=99$)

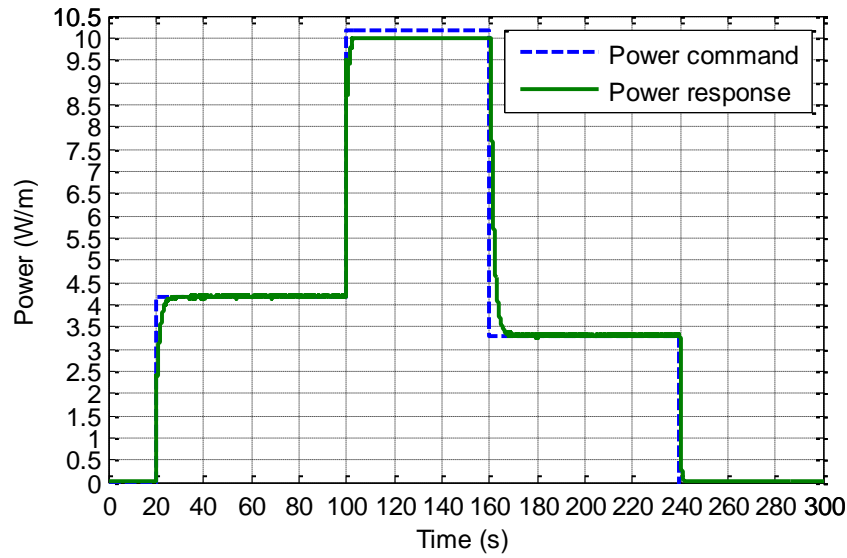


Figure 151. Power command and response using power feedback with PI control ($K_p=100$ and $K_i=99$)

Using power-strain relation strain commands can be tracked with an error less than 6.5%. However strain response is slower than the power response of the wire, so the required strain values are achieved with some delay.

4.7. Validation of Control Schemes under Different Loads

In this section, the controllers experimented in the previous sections for strain, resistance and power feedback are validated for the wire loaded with 286 gr (90 MPa) and 660 gr (210 MPa).

4.7.1. Tests with 90 MPa Stress

4.7.1.1. Strain Feedback

The strain of the wire subjected to 90 MPa stress is controlled using strain feedback firstly by PI controller whose parameters are adjusted to $K_p=300$ and $K_i=55$ (Figure 152), then by PI control with feedforward loop using a gain of 0.8 (Figure 153), lastly by neural network Narma-L2 controller trained on the data from the characterization of the wire under 140 MPa stress (Figure 154).

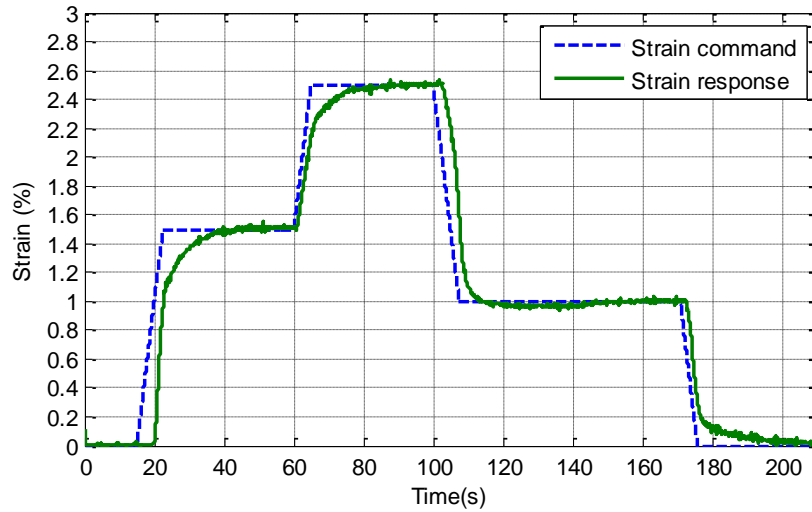


Figure 152. Strain feedback control with PI controller ($K_p=300$ and $K_i=55$) under 90 MPa stress

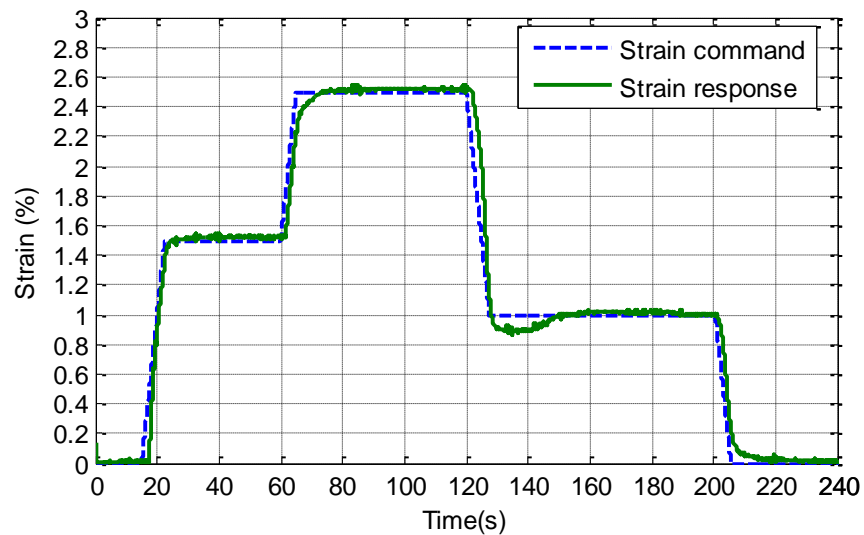


Figure 153. Strain feedback control with PI controller with feedforward loop ($K_p=300$, $K_i=55$, and $K=0.8$) under 90 MPa stress

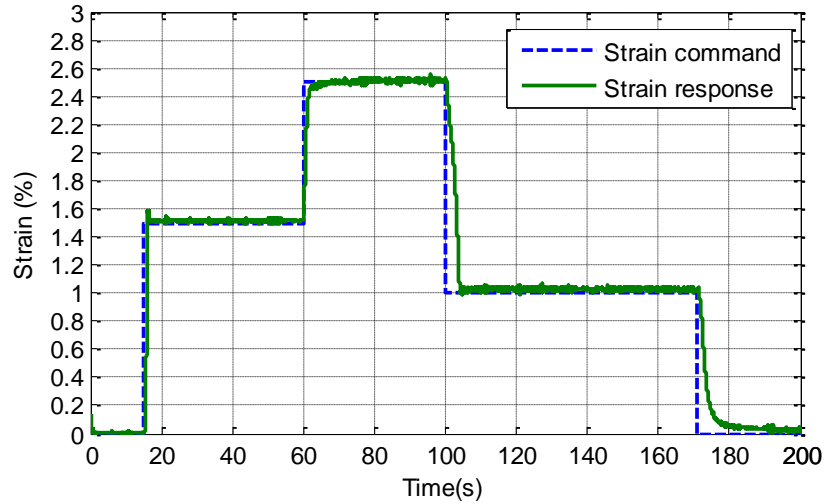


Figure 154. Strain feedback control with NN-Narma L2 controller under 90 MPa stress

As seen from the figures the controllers designed and experimented for 140 MPa stress using strain feedback can effectively control the wire under 90 MPa stress.

4.7.1.2. Resistance Feedback

Control experiments on the wire loaded with 90 MPa stress are conducted. Response using PI controller ($K_p=300$ and $K_i=35$) (Figure 155), PI controller with feedforward loop ($K_p=300$, $K_i=35$, and $K=0.8$) (Figure 156) and NN Narma-L2 controller (Figure 157) are obtained.

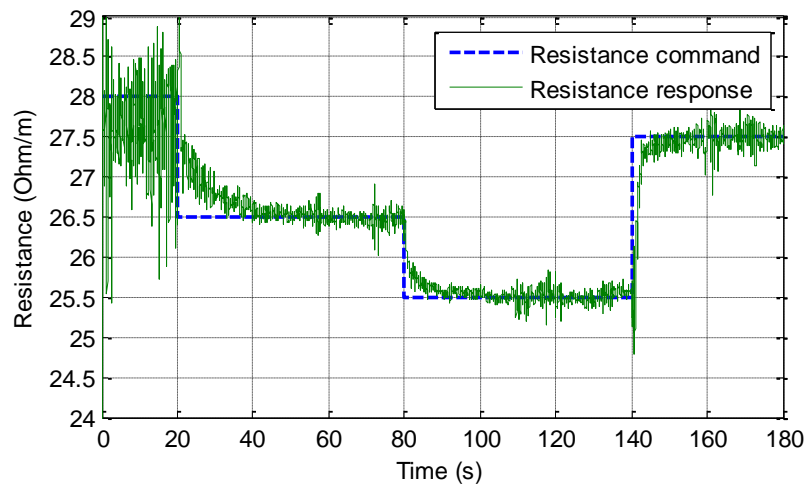


Figure 155. Resistance feedback control with PI controller ($K_p=300$ and $K_i=35$) under 90 MPa stress

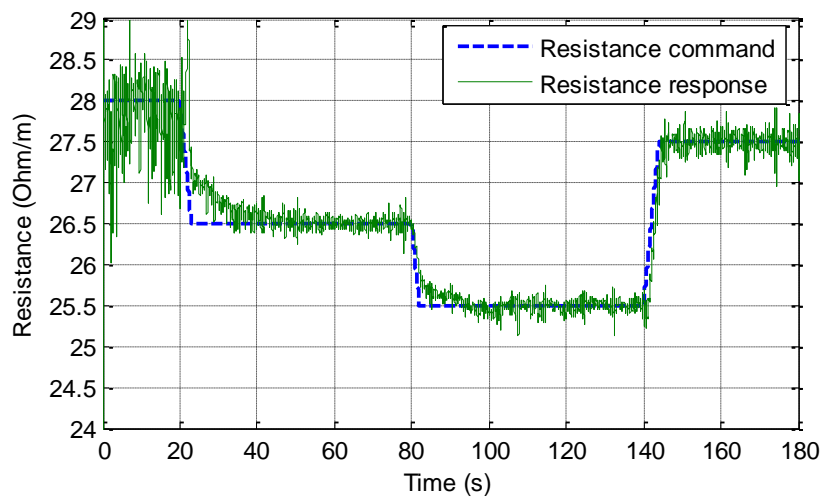


Figure 156. Resistance feedback control with PI controller with feedforward loop ($K_p=300$, $K_i=35$, and $K=0.8$) under 90 MPa stress

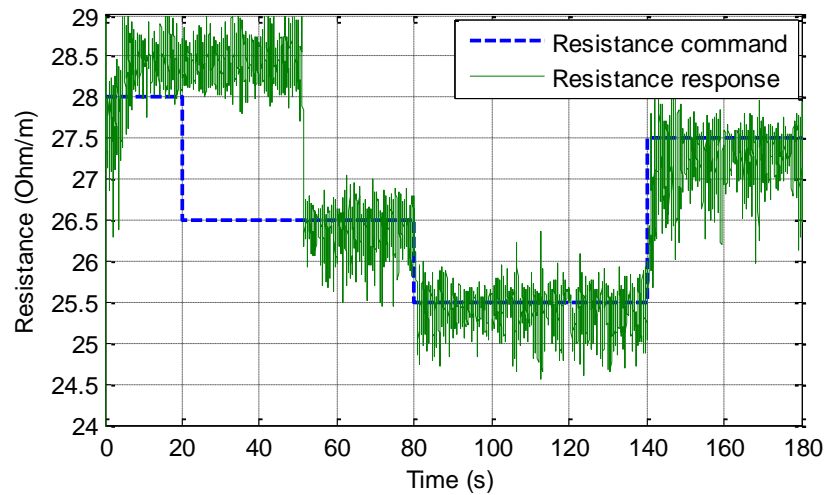


Figure 157. Resistance feedback control with NN-Narma L2 controller under 90 MPa stress

As seen in Figure 157, neural network controller gives delayed response with 1 Ohm/m oscillations.

4.7.1.3. Power Feedback

The power of the wire under 90 MPa stress is controlled using PI-Type Control ($K_p=100$ and $K_i=99$) (Figure 158), PI controller with feedforward loop ($K_p=100$, $K_i=99$, and $K=0.8$) (Figure 159) and NN Narma-L2 controller (Figure 160). In the results satisfactory control performance can be observed.

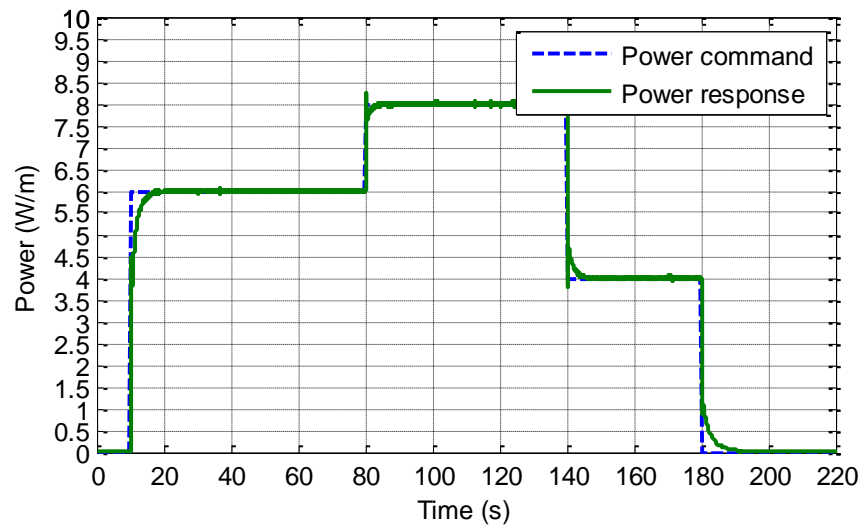


Figure 158. Power feedback control with PI controller ($K_p=100$ and $K_i=99$) under 90 MPa stress

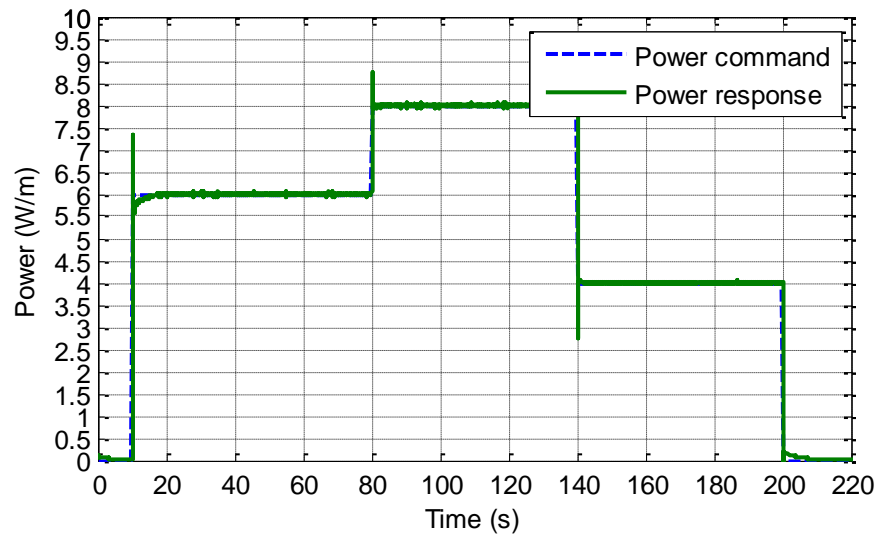


Figure 159. Power feedback control with PI controller with feedforward loop ($K_p=100$, $K_i=99$, and $K=0.8$) under 90 MPa stress

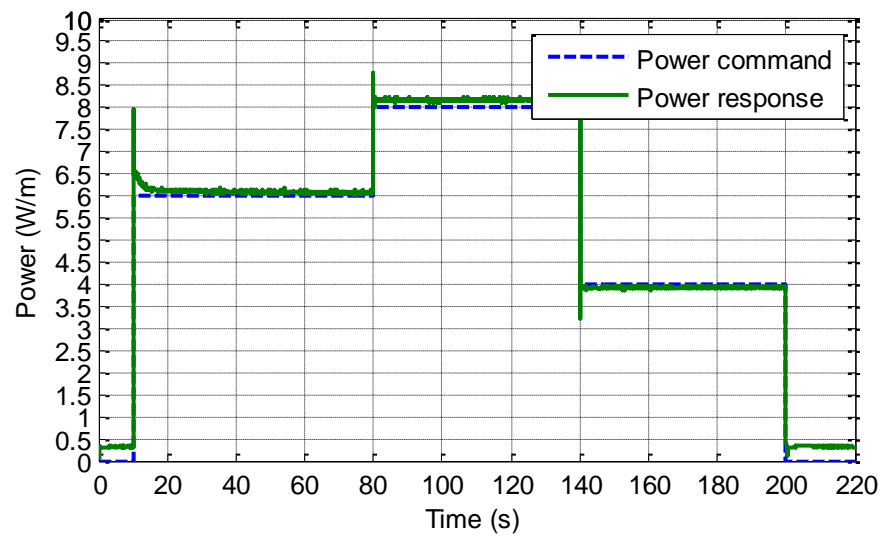


Figure 160. Power feedback control with NN-Narma L2 controller under 90 MPa stress

4.7.2. Tests with 210 MPa Stress

4.7.2.1. Strain Feedback

The strain control experiments are repeated with 660 gr load hanging on the wire, inducing 210 MPa of stress. The strain of the wire is controlled by PI controller with the calculated gains ($K_p=300$ and $K_i=55$) (Figure 161), then PI controller with feedforward loop ($K_p=300$, $K_i=55$, and $K=0.8$) (Figure 162), and lastly using NN Narma-L2 controller (Figure 163) trained with the data of the wire under 140 MPa stress.

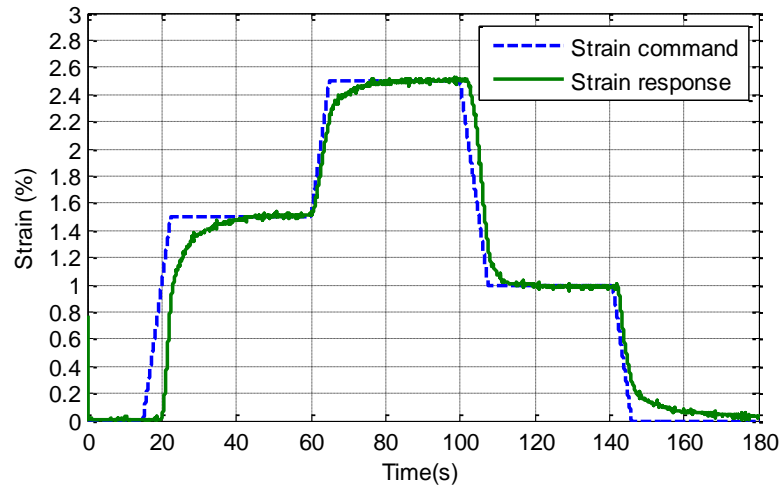


Figure 161. Strain feedback control with PI controller ($K_p=300$ and $K_i=55$) under 210 MPa stress

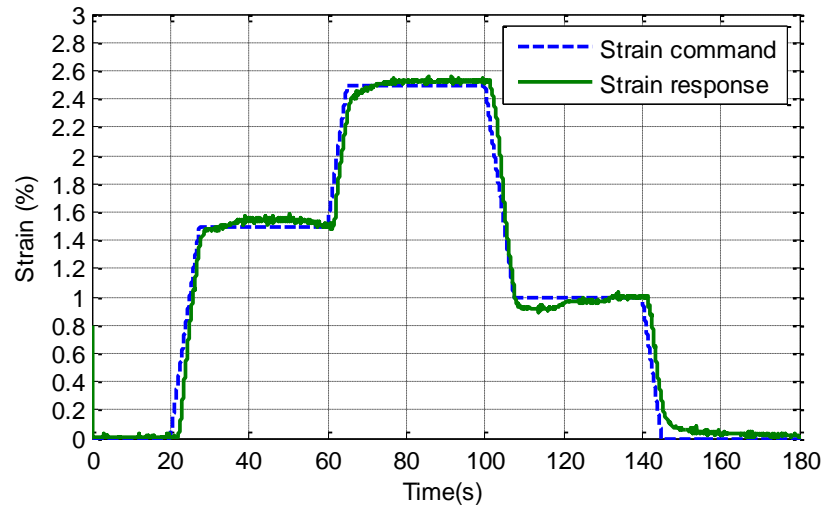


Figure 162. Strain feedback control with PI controller with feedforward loop ($K_p=300$, $K_i=55$, and $K=0.8$) under 210 MPa stress

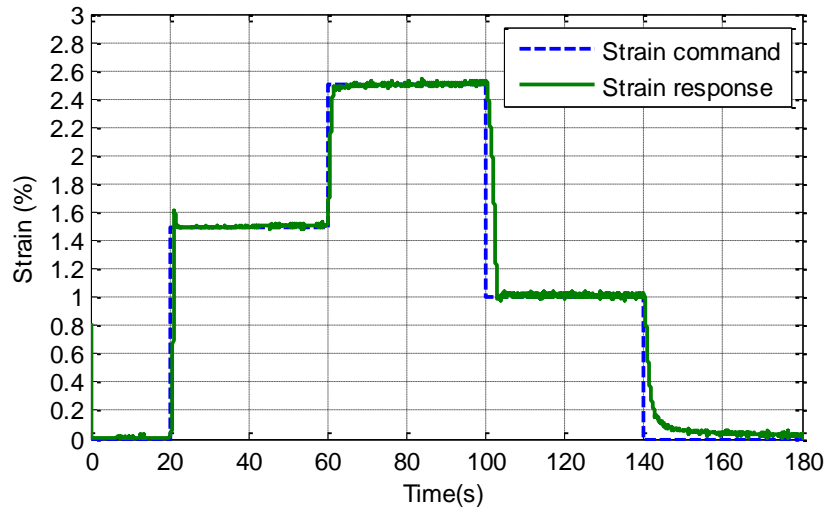


Figure 163. Strain feedback control with NN-Narma L2 controller under 210 MPa stress

4.7.2.2. Resistance Feedback

PI-type control ($K_p=300$ and $K_i=35$) (Figure 164), PI with feedforward loop ($K_p=300$, $K_i=35$, and $K=0.8$) (Figure 165), and NN Narma-L2 (Figure 166) control methods have been implemented to control the resistance of the wire under 210 MPa. However, as it can be seen in Figure 166, neural network controller is not working for this feedback variable due to high noise levels in resistance feedback.

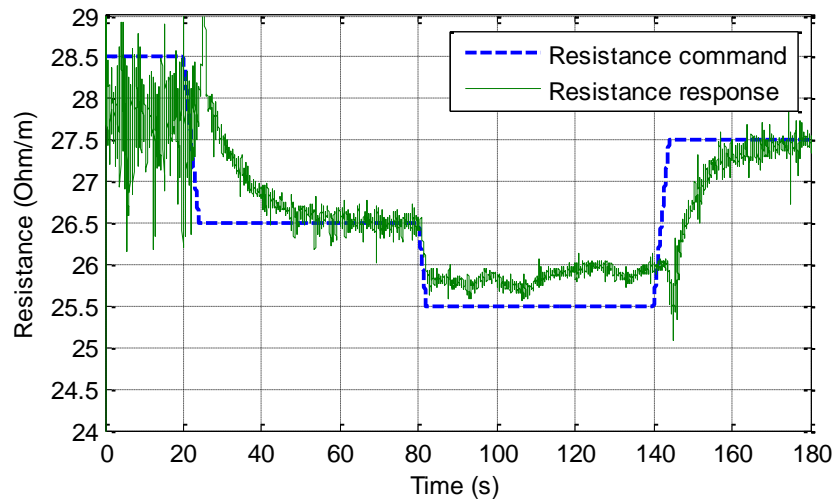


Figure 164. Resistance feedback control with PI controller ($K_p=300$ and $K_i=35$) under 210 MPa stress

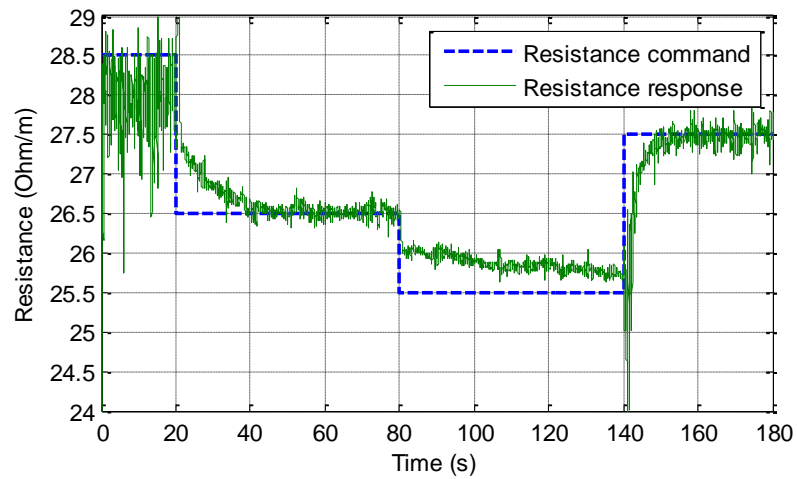


Figure 165. Resistance feedback control with PI controller with feedforward loop ($K_p=300$, $K_i=35$, and $K=0.8$) under 210 MPa stress

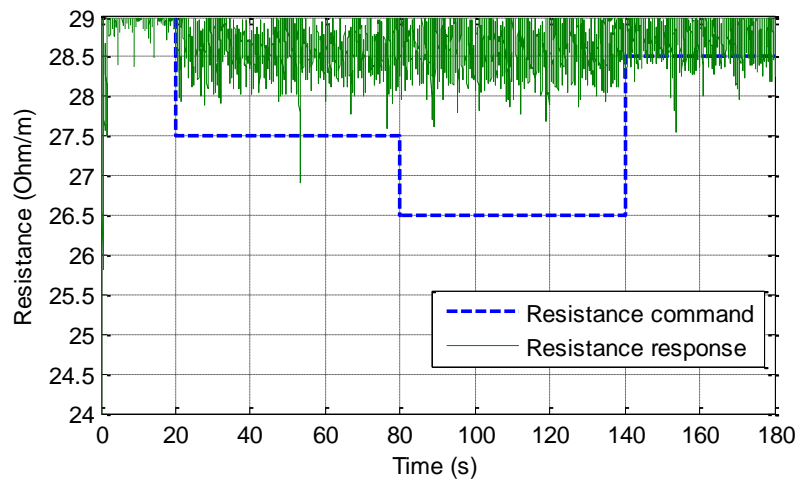


Figure 166. Resistance feedback control with NN-Narma L2 controller under 210 MPa stress

4.7.2.3. Power Feedback

The wire is also controlled using power as feedback for transformation. Here, PI controller ($K_p=100$ and $K_i=99$) (Figure 167), PI with feedforward loop ($K_p=100$, $K_i=99$, and $K=0.8$) (Figure 168), and NN Narma-L2 controller (Figure 169) has been employed.

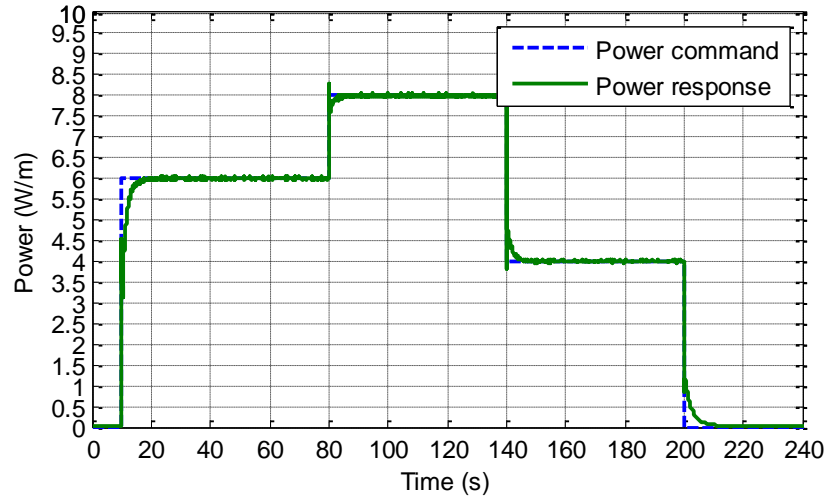


Figure 167. Power feedback control with PI controller ($K_p=100$ and $K_i=99$) under 210 MPa stress

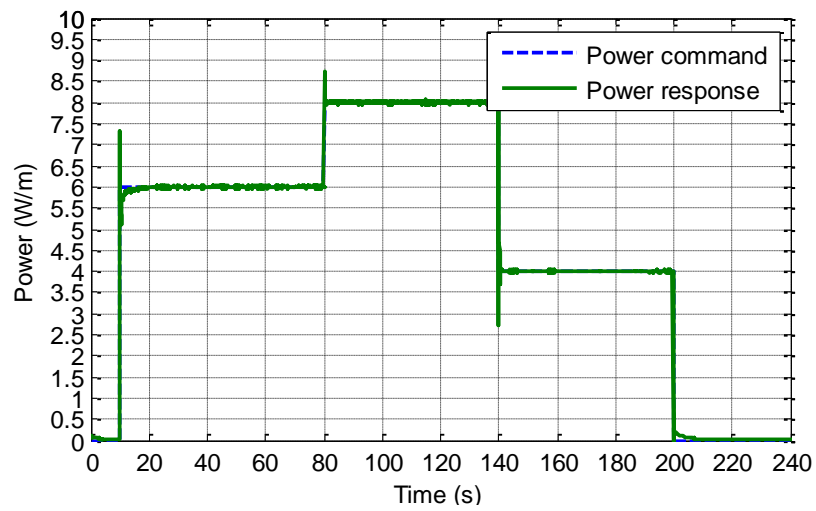


Figure 168. Power feedback control with PI controller with feedforward loop ($K_p=100$, $K_i=99$, and $K=0.8$) under 210 MPa stress

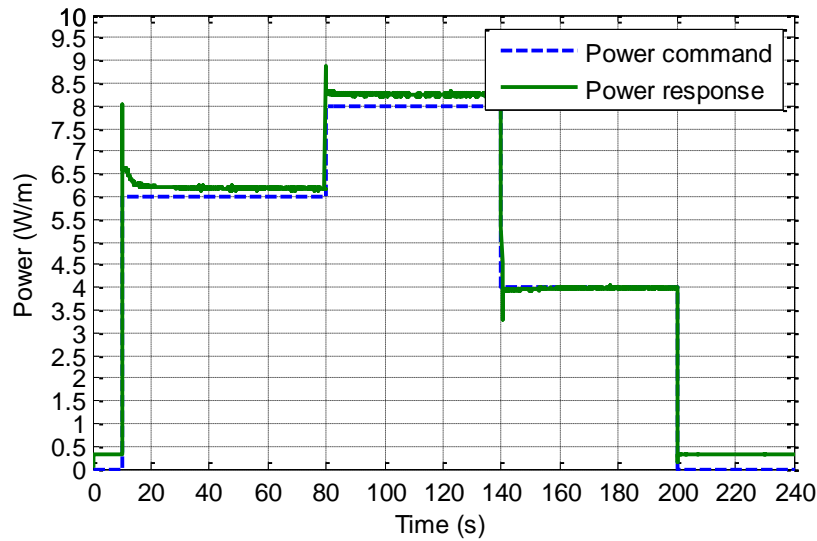


Figure 169. Power feedback control with NN-Narma L2 controller under 210 MPa stress

As can be seen from the plots all control methods work sufficiently. However a steady state error is observed in NN controller for the heating stages which is due to the difference between stresses on the wire in training data and in the application and errors observed on zero power commands is due to the minimum current limit of the controller (100 mA).

4.7.3. Tests Against a Spring

A helical tensile spring is designed to be used as resetting force against SMA wire. The spring is designed to produce a force of 7.5 N in 3% strain of the wire. The wire is characterized with the spring attached to the end. The strain, resistance and power curves are presented in Figure 170, Figure 171, and Figure 172 respectively.

It can be observed that the maximum attainable strain of the wire working against the spring, with the current limit of 800 mA, is 2.6% and minimum resistance value is 26.4 Ohm/m. This is due to the fact that the stress on the wire increases as its strength decreases, i.e. as the wire contracts (transforms to austenite form) the opposing spring force increases. As a result, the wire cannot reach 3% strain thus higher resistance values are observed. The control of the wire using strain, resistance, and power feedback are performed.

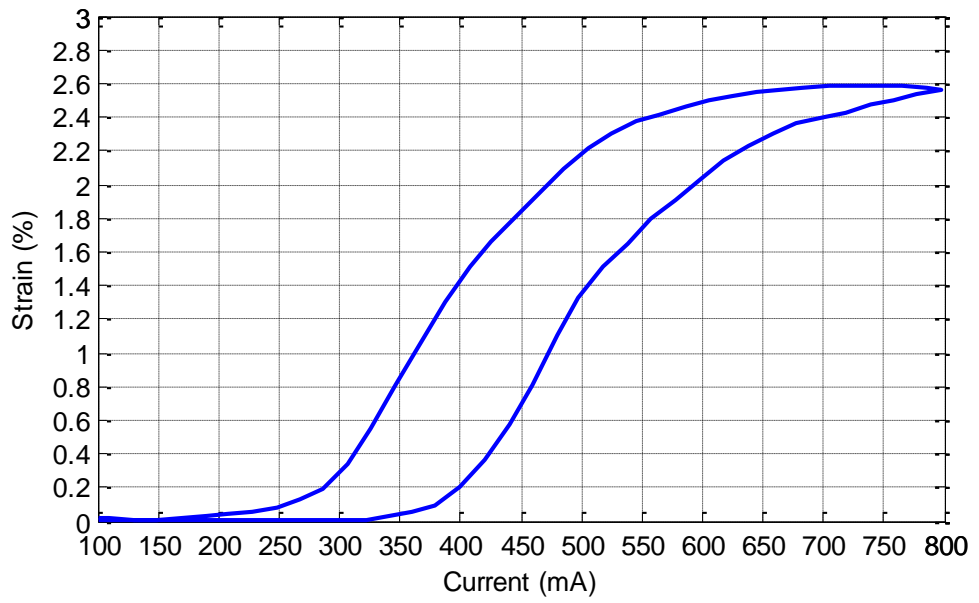


Figure 170. Strain-current curve of the wire working against the spring

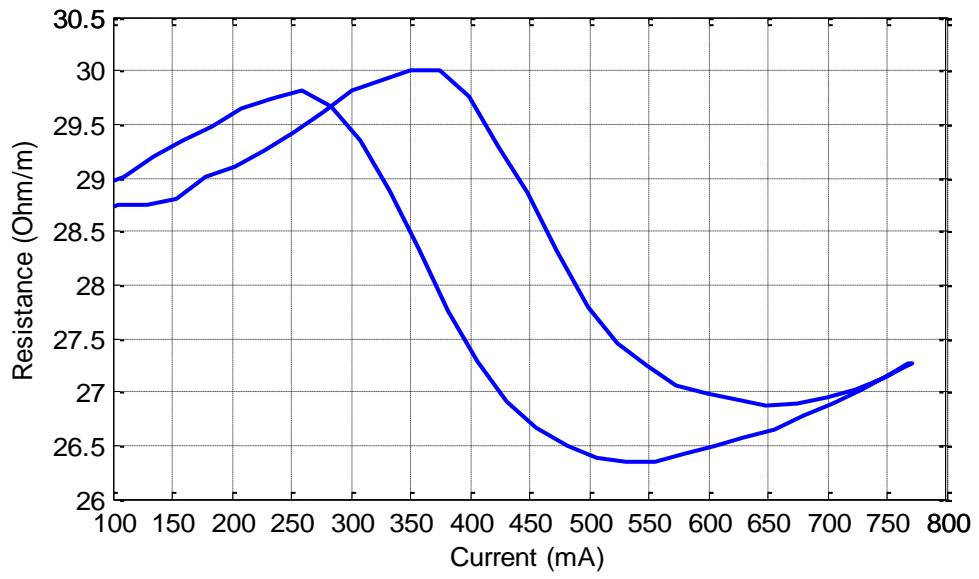


Figure 171. Resistance-current curve of the wire working against the spring

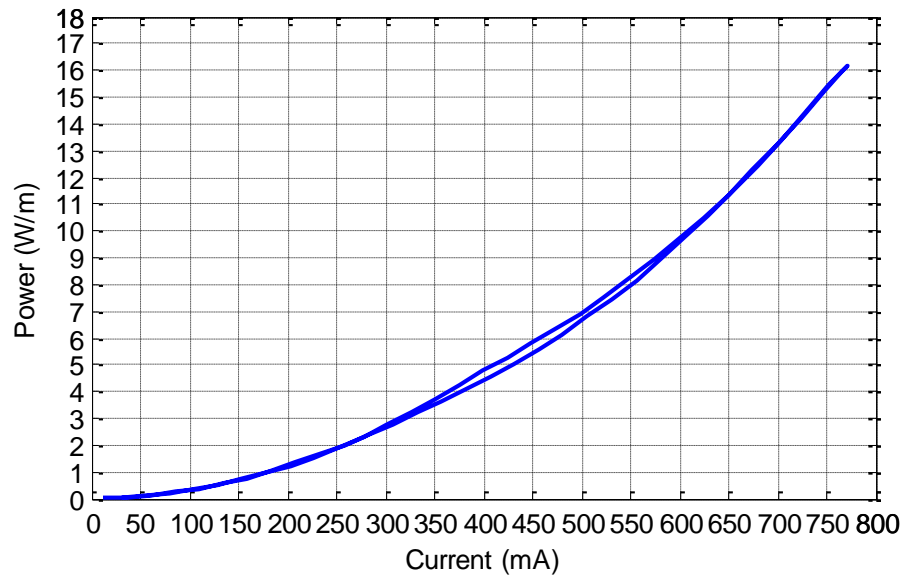


Figure 172. Power-current curve of the wire working against the spring

4.7.3.1. **Strain Feedback**

The strain of the wire is controlled by employing a PI controller with $K_p=300$ and $K_i=55$ (Figure 173), then by PI with feedforward loop whose relations are based on the data of the wire under 140 MPa stress ($K_p=300$, $K_i=55$, and $K=0.8$) (Figure 174), and using the neural network Narma-L2 controller (Figure 175).

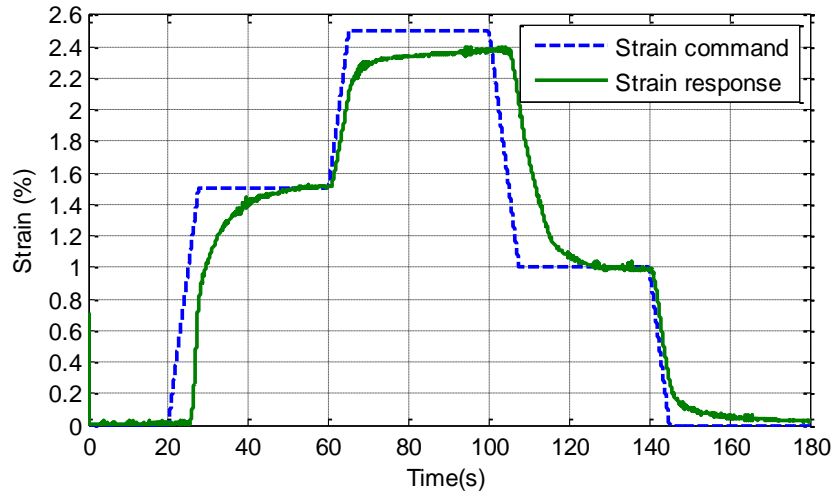


Figure 173. Strain feedback control with PI controller ($K_p=300$ and $K_i=55$) against spring

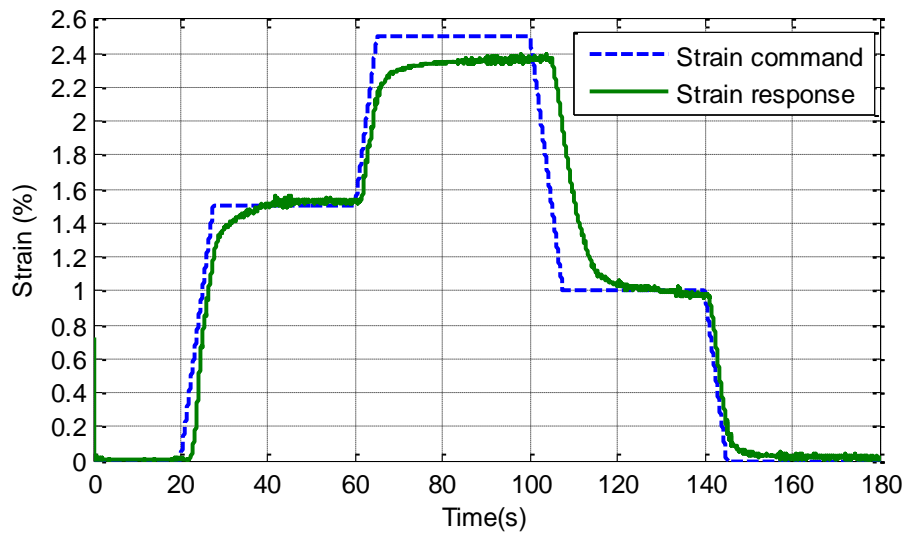


Figure 174. Strain feedback control with PI controller with feedforward loop ($K_p=300$ and $K_i=55$) against spring

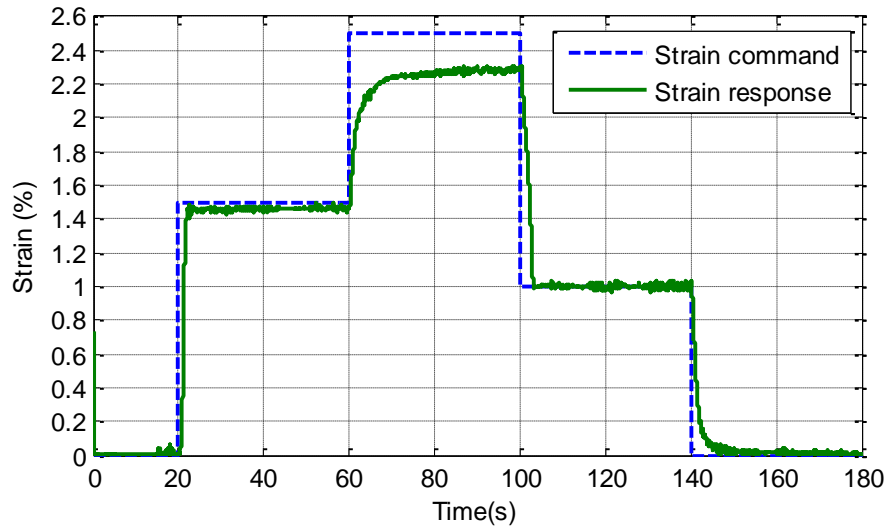


Figure 175. Strain feedback control with NN Narma-L2 controller against spring

4.7.3.2. Resistance Feedback

The resistance of the wire working against the spring is also controlled. PI-type control ($K_p=300$ and $K_i=35$) (Figure 176), PI with feedforward loop ($K_p=300$, $K_i=35$, and $K=0.8$) (Figure 177), and Narma-L2 control (Figure 178) methods are experimented. The neural network controller is not working for resistance feedback control of the wire against the spring.

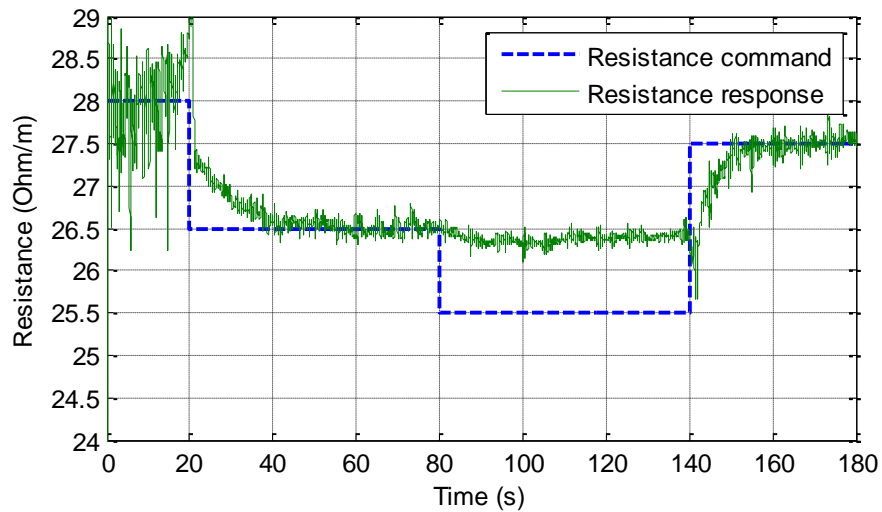


Figure 176. Resistance feedback control with PI controller ($K_p=300$ and $K_i=35$) against spring

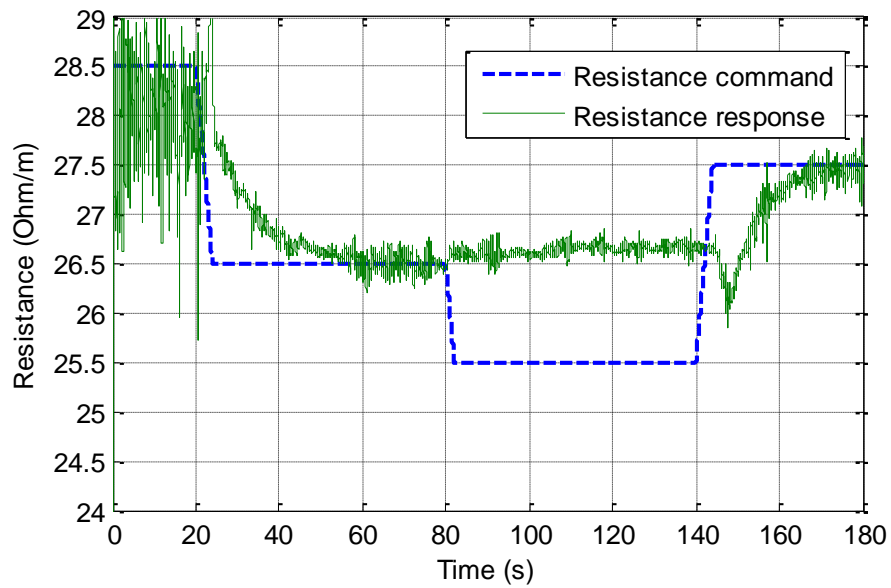


Figure 177. Resistance feedback control with PI controller with feedforward loop ($K_p=300$, $K_i=35$, and $K=0.8$) against spring

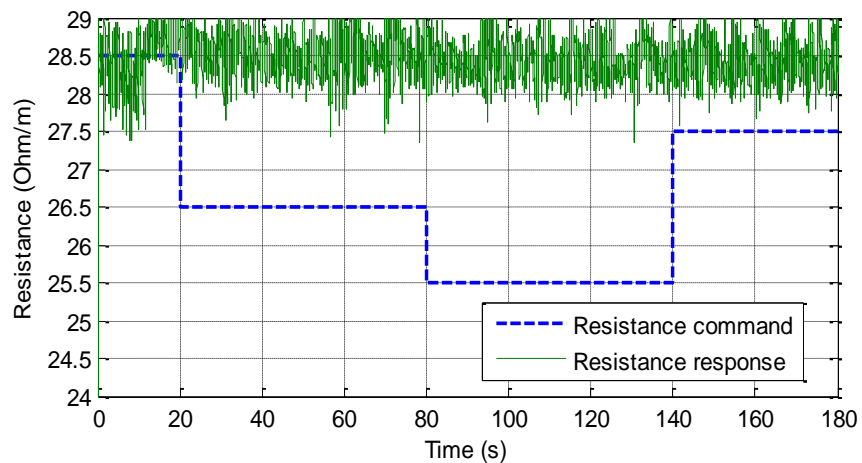


Figure 178. Resistance feedback control with NN Narma-L2 controller against spring

4.7.3.3. Power Feedback

The power of the wire working against the spring is controlled using PI control ($K_p=100$, and $K_i=99$) (Figure 179), PI with feedforward loop ($K_p=100$, $K_i=99$, and $K=0.8$) (Figure 180), and Narma-L2 control (Figure 181).

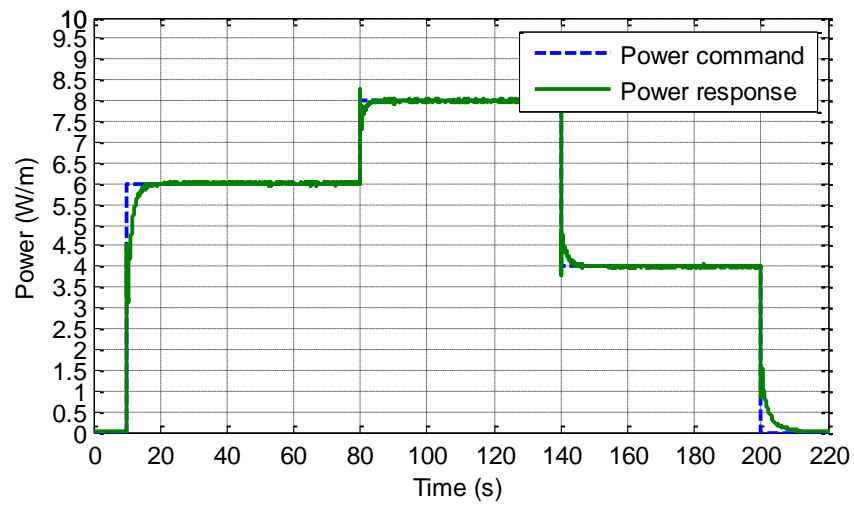


Figure 179. Power feedback control with PI controller ($K_p=100$ and $K_i=99$) against spring

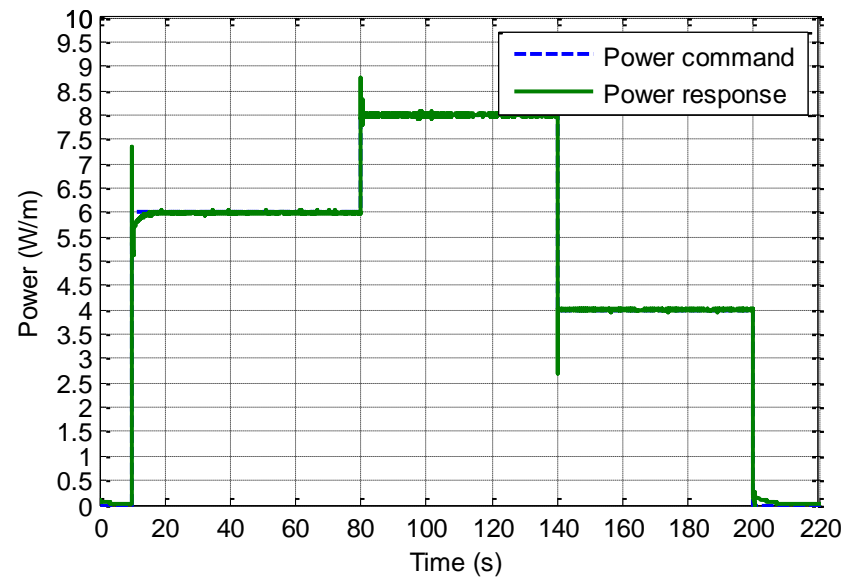


Figure 180. Power feedback control with PI controller with feedforward loop ($K_p=100$, $K_i=99$, and $K=0.8$) against spring

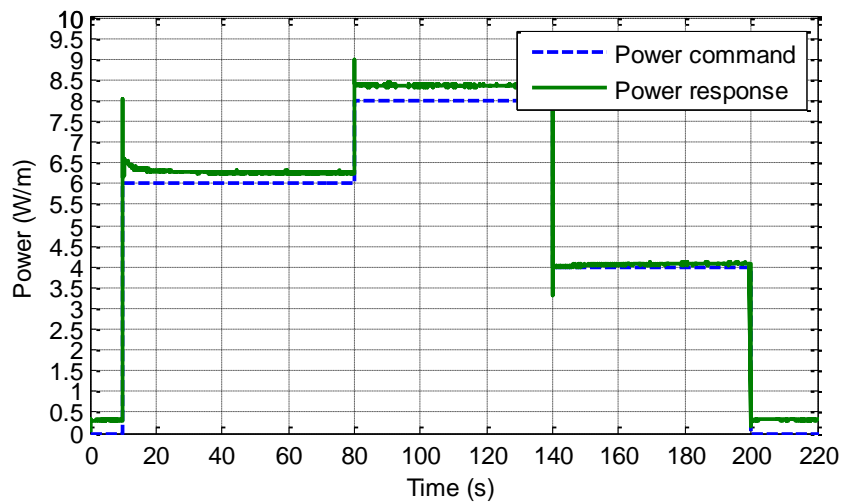


Figure 181. Power feedback control with NN Narma-L2 controller against spring

Power control methods developed for the wire working against a constant load sufficiently control the wire against a spring. The steady state error observed in NN controller is due to the difference between the nature of load in training data and in the application and errors observed on zero power commands is due to the minimum current limit of the controller (100 mA).

CHAPTER 5

DESIGN AND EXPERIMENTAL INVESTIGATION OF A LINEAR SHAPE MEMORY ALLOY ACTUATOR

In this part of the study, the design and control studies of a linear SMA wire actuator will be discussed.

In the design of an SMA actuator, limitations on strain and force should be overcome by mechanical design. The SMA actuator described in this section overcomes the limited strain of SMA's by the pulley design and sufficient force is obtained by using the SMA wires in parallel.

5.1. Actuator Design

5.1.1. Conceptual Design

The generic linear SMA wire actuator to be designed is required to displace 1 kg of load at least 10 mm.

5.1.1.1. Design for Strain Requirement

The SMA wire characterized previously is known to have a strain value of approximately 3%. For a stroke of 10 mm, minimum 333 mm of wire should be used in the actuator. Since this length is very long, pulleys should be utilized to obtain volumetric efficiency. In the design of the pulleys minimum bending radius (10 mm) should be taken into account as an important constraint. As a result, when the bending strain losses are taken into account a wire with minimum 400 mm of length should be used in the actuator.

5.1.1.2. Design for Stress Requirement

The recommended working stress of the SMA wire is 190-200 MPa, for a 0.2 mm diameter wire this corresponds to a load of 600 grams. In order to carry the desired 1 kg load (approximately 10 N) two 0.2 mm diameter SMA wires should be used in parallel.

5.1.2. Mechanical Design

Mechanical design studies started with placing the pulleys, designed considering the minimum bend radius of the wire, so as to create wire route long enough to use at least 400 mm of wire. The 2-dimensional layout of the actuator is given in Figure 182.

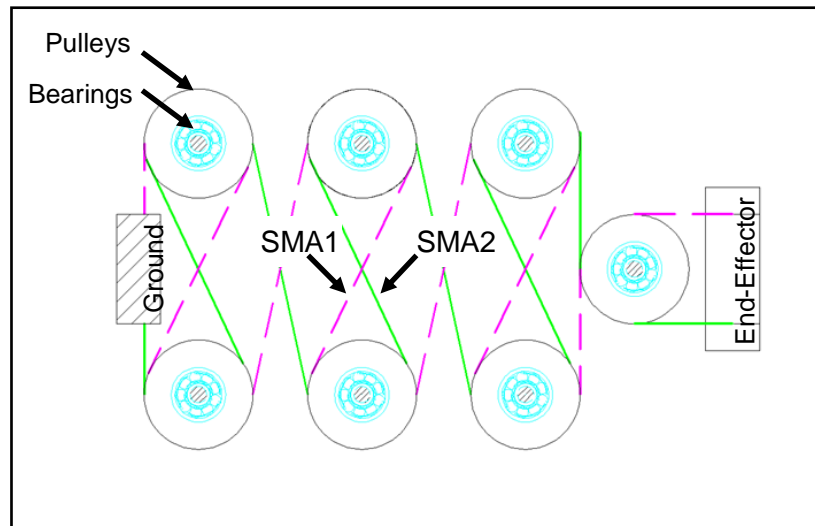


Figure 182. 2-D Layout of the actuator

For the configuration shown in Figure 182, two SMA wires of length 450 mm are used, net wire length is approximately 430 mm after current connection length losses are deducted. The wires are wound around the grooved pulleys in a 2-layer pattern, in a way that there is no contact between them. One of the ends of each wire is connected securely to the ground, while the other ends are connected to the movable end-effector. The pulleys are connected to the casing by 623 2RS coded ball bearings by SKF to reduce rolling friction.

The end-effector is guided to ensure perpendicular stroke of the actuator, and guiding is achieved by low friction material, teflon. The pulleys are made of non-conducting polyamid, and the end-effector is made of teflon to avoid electrical short circuit.

Three dimensional views of the actuator can be seen in Figure 183. A miniature displacement sensor LT0951-025 from Active Sensors LTD. (LVDT) is attached to the end-effector to obtain data for strain feedback. The shaft

between the end-effector and the LVDT core is supported by a linear ball bearing LBBR 3 from SKF, so that the sensor core is not subjected to any moment loads.

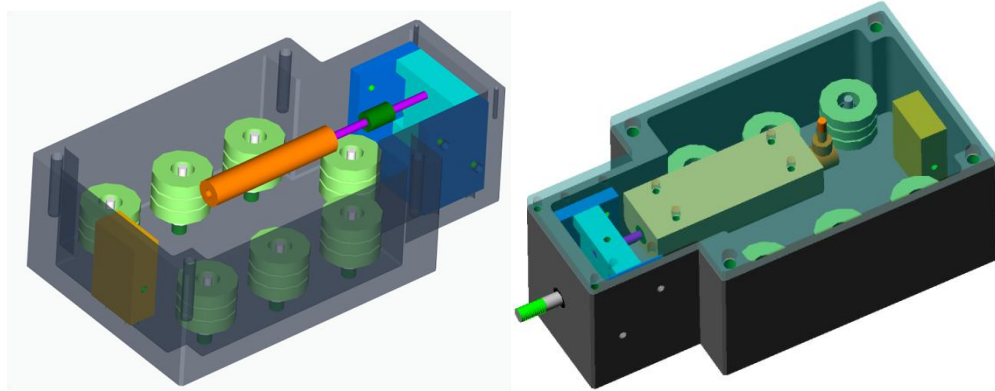


Figure 183. 3-D views of the actuator

The designed actuator is fabricated and assembled as shown in Figure 184.

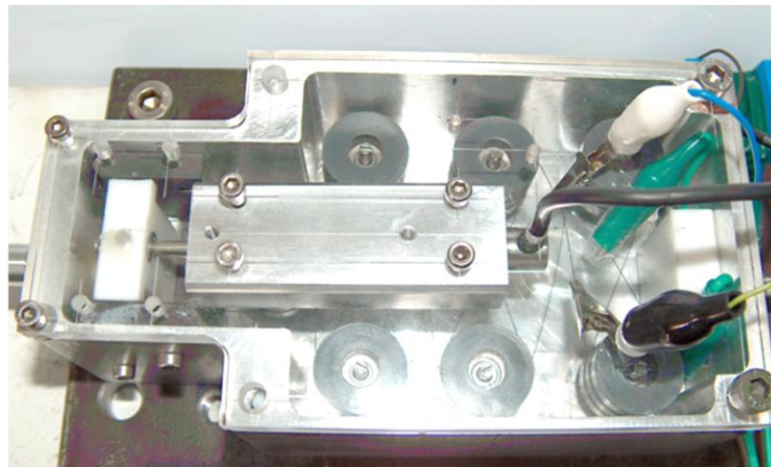


Figure 184. SMA linear actuator

5.2. Actuator Test-Bed

In order to hang the 1 kg load to the actuator a horizontal test bed is designed and fabricated. In this test-bed a pulley with a ball bearing mounting is utilized to change the direction of the load. The force on the end-effector of the

actuator is created by the tension on the rope carrying the 1 kg load. The fabricated actuator test bed can be seen in Figure 185 and Figure 186.



Figure 185. Actuator test-bed rear view

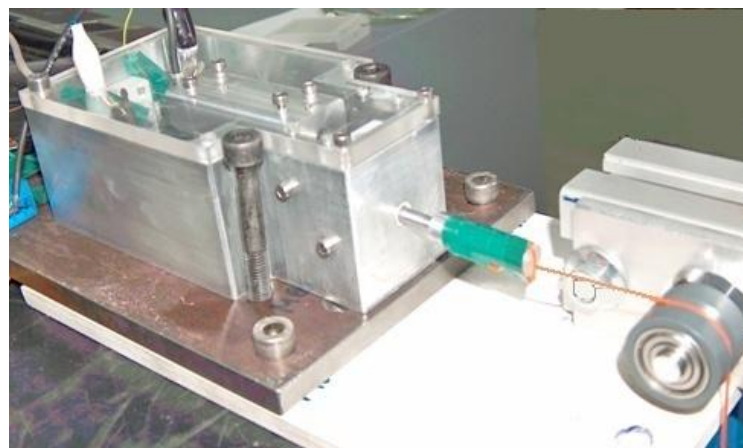


Figure 186. Actuator test-bed front view

5.3. Control Experiments on the Actuator

The actuator is characterized with the 1 kg load hung to the end-effector. The displacement and strain curves are presented in Figure 187 and Figure 188 respectively. It can be observed that the maximum displacement of 12.1 mm thus, maximum strain of 2.8%, with the current limit of 750 mA, can be attained. It can also be observed that cooling takes longer time than the cooling of a single open wire.

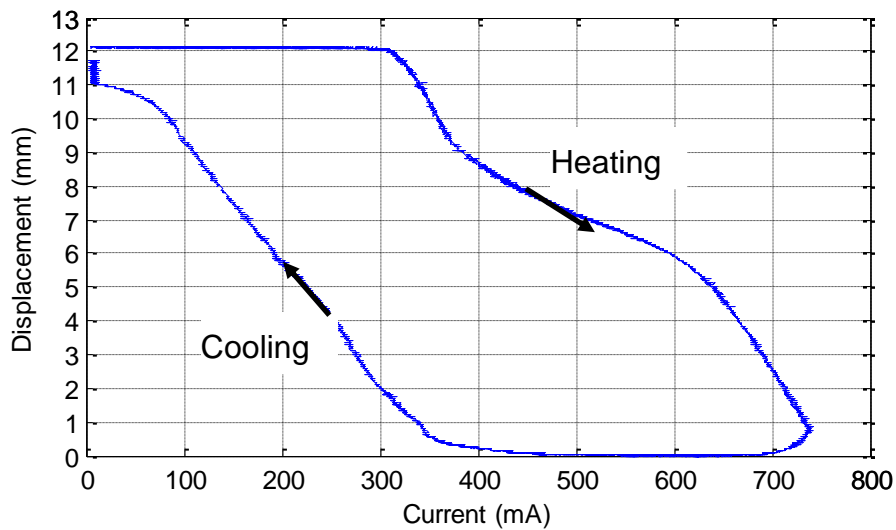


Figure 187. Displacement characteristic of the actuator

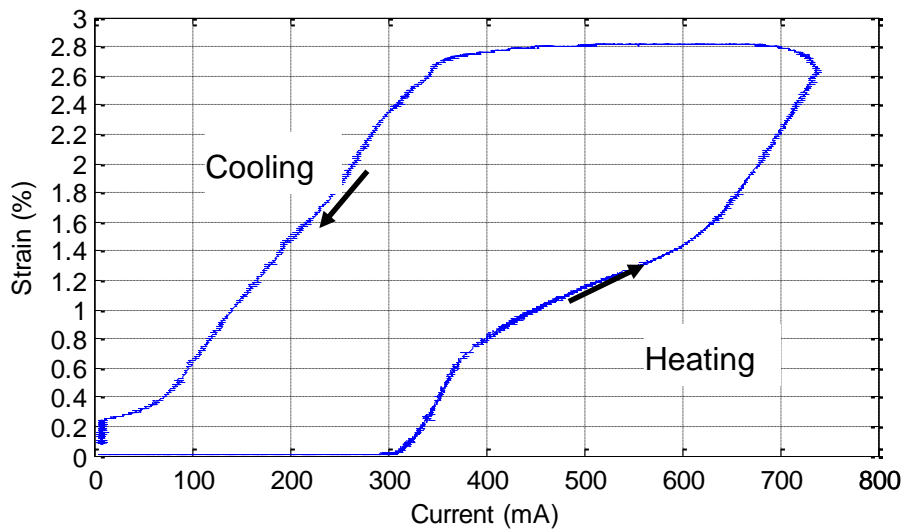


Figure 188. Strain curve of the actuator

The resistance and power consumption of the curves of the actuator are given in Figure 189 and Figure 190 respectively.

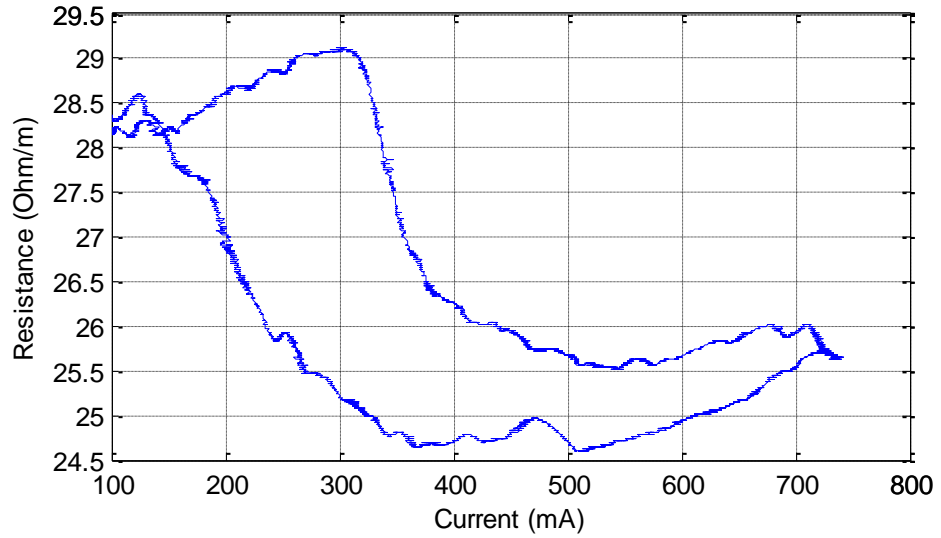


Figure 189. Resistance curve of the actuator

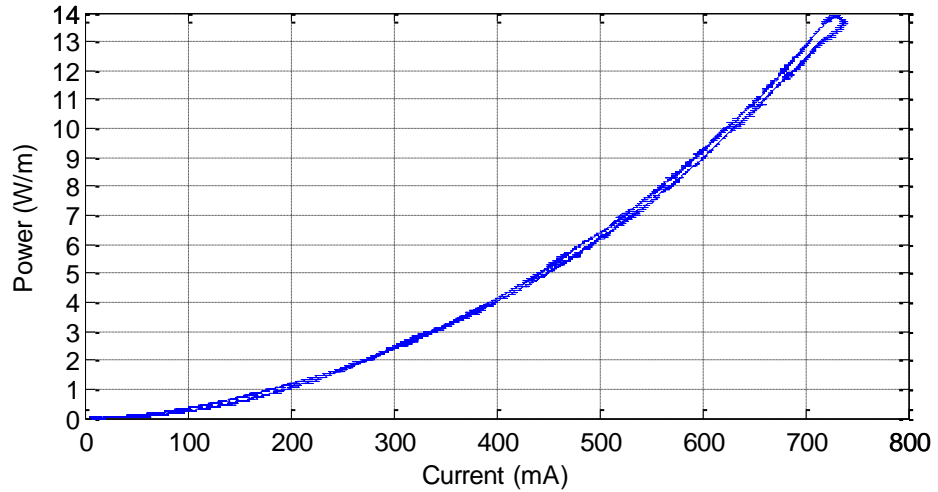


Figure 190. Power consumption curve of the actuator

The control of the wire using strain, resistance, and power feedback are performed.

5.3.1. Strain Feedback

The position of the actuator against 10 N load is controlled using strain feedback firstly by PI controller whose parameters are adjusted to $K_p=300$ and $K_i=55$ (Figure 191), $K_p=300$ and $K_i=110$ (Figure 192), then by PI control with feedforward loop using a gain of 0.8 ($K_p=300$ and $K_i=55$) (Figure 193), lastly by neural network Narma-L2 controller trained using the data from the characterization of the SMA wire under 140 MPa stress (Figure 194).

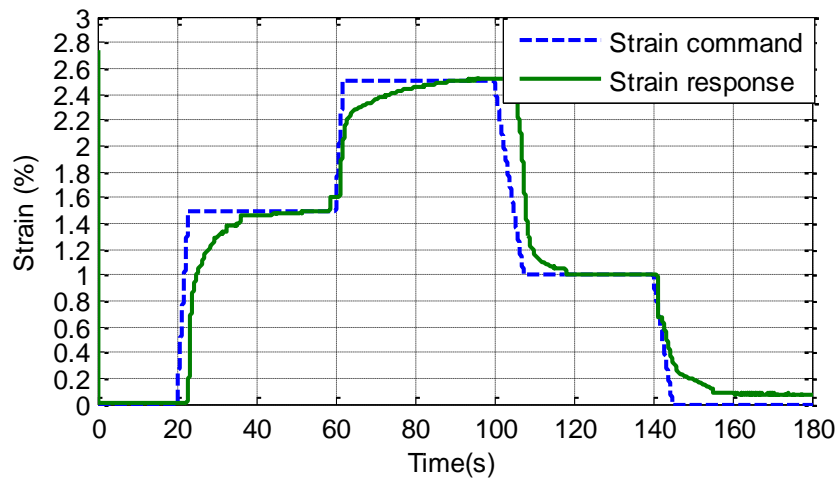


Figure 191. Strain feedback control of the actuator with PI controller ($K_p=300$ and $K_i=55$)

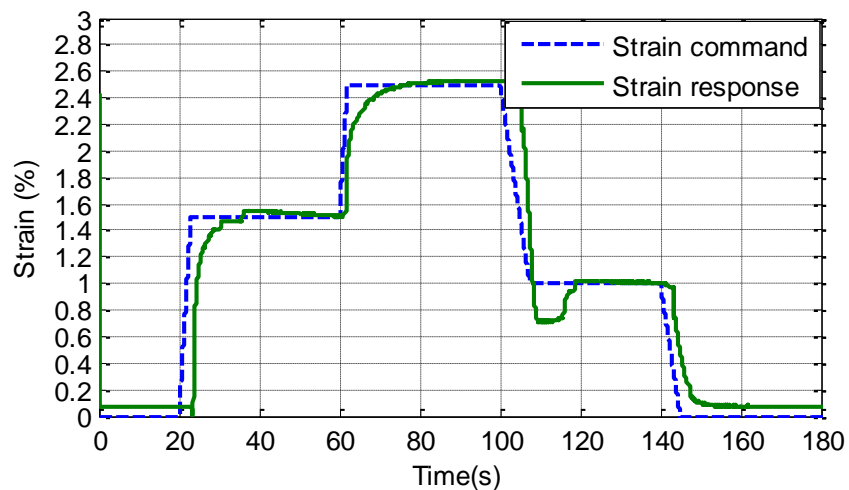


Figure 192. Strain feedback control of the actuator with PI controller ($K_p=300$ and $K_i=110$)

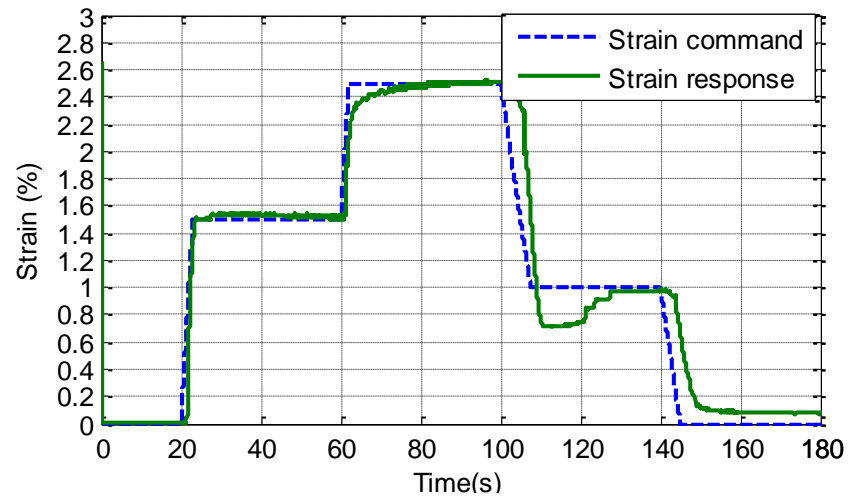


Figure 193. Strain feedback control of the actuator with PI controller with feedforward loop ($K_p=300$, $K_i=55$ and $K=0.8$)

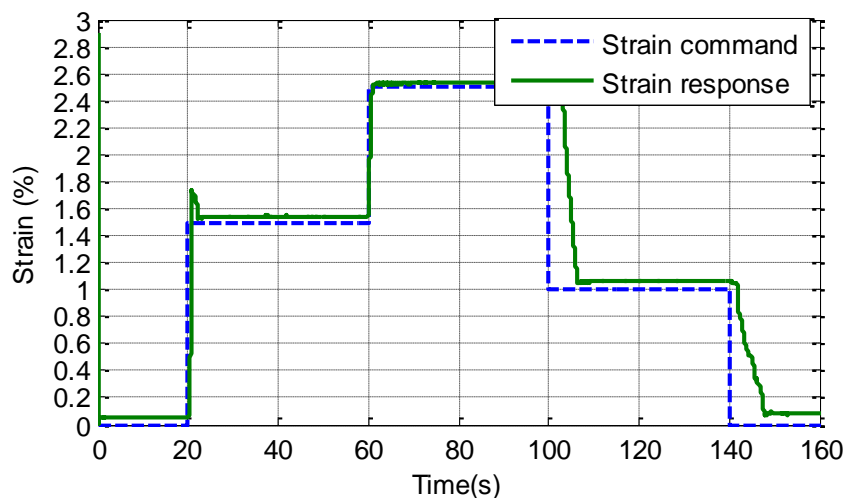


Figure 194. Strain feedback control of the actuator with NN Narma-L2 controller

As seen from the figures very satisfactory results are obtained using previously designed strain feedback controllers.

5.3.2. Resistance Feedback

Control experiments using resistance feedback are conducted on the actuator. Resistance response of the actuator using PI controller ($K_p=300$, $K_i=35$ and $K_p=300$, $K_i=70$) (Figure 195 and Figure 196, respectively), PI controller with

feedforward loop ($K_p=300$, $K_i=35$, and $K=0.8$) (Figure 197) and NN Narma-L2 controller (Figure 198) are obtained.

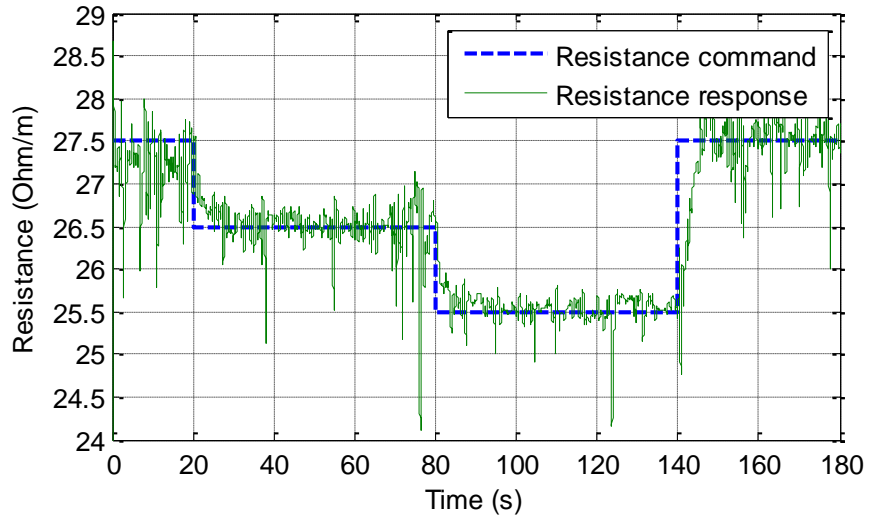


Figure 195. Resistance feedback control of the actuator with PI controller ($K_p=300$ and $K_i=35$)

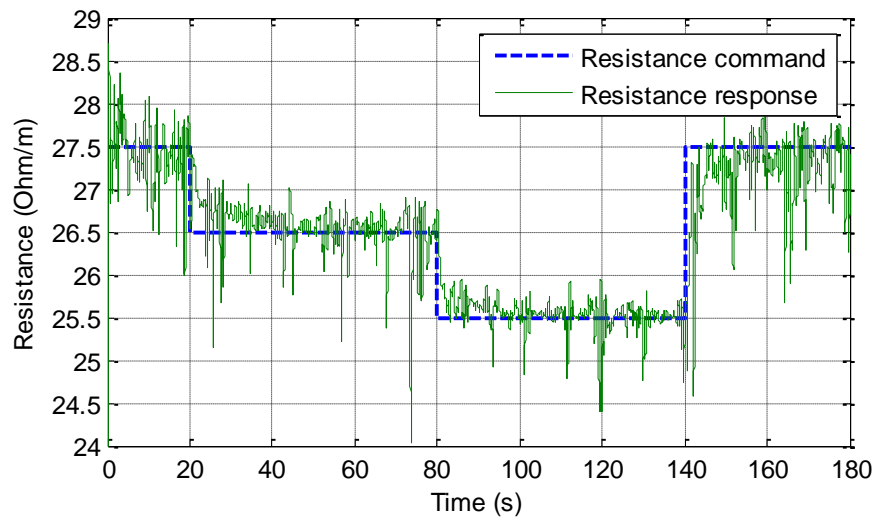


Figure 196. Resistance feedback control of the actuator with PI controller ($K_p=300$ and $K_i=70$)

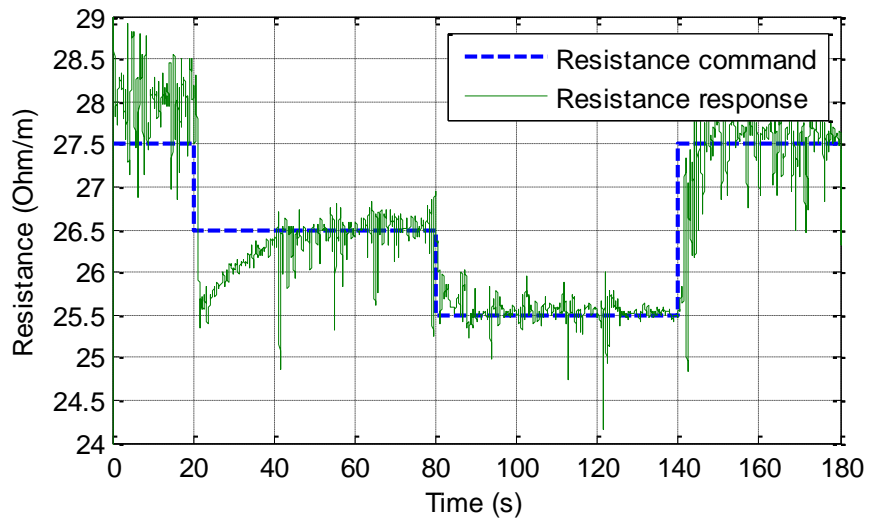


Figure 197. Resistance feedback control of the actuator with PI controller with feedforward loop ($K_p=300$, $K_i=35$, and $K=0.8$)

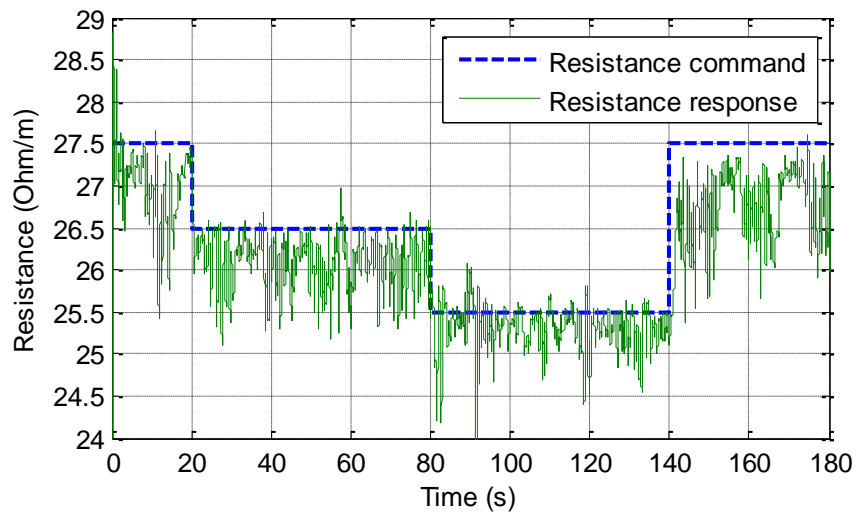


Figure 198. Resistance feedback control of the actuator with NN Narma-L2 controller

In resistance feedback control, the oscillations at an amount of 1 Ohm/m are observed in the resistance data. This affects the control effectiveness on the actuator.

5.3.3. Power Feedback

The power consumption of the actuator is controlled using PI-Type control ($K_p=100$, $K_i=49$, and $K_p=100$, $K_i=99$), (Figure 199 and Figure 200,

respectively), PI controller with feedforward loop ($K_p=100$, $K_i=49$, and $K=0.8$), (Figure 201) and NN Narma-L2 controller, (Figure 202).

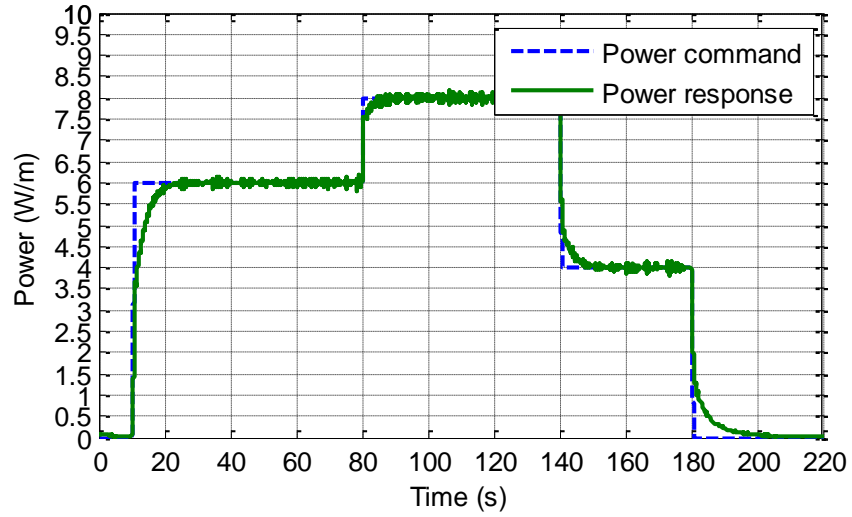


Figure 199. Power feedback control of the actuator with PI controller ($K_p=100$ and $K_i=49$)

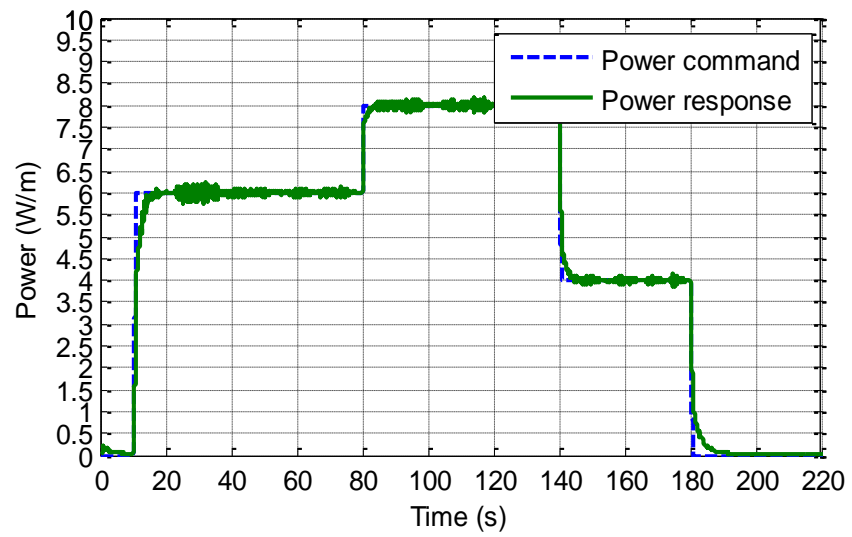


Figure 200. Power feedback control of the actuator with PI controller ($K_p=100$ and $K_i=99$)

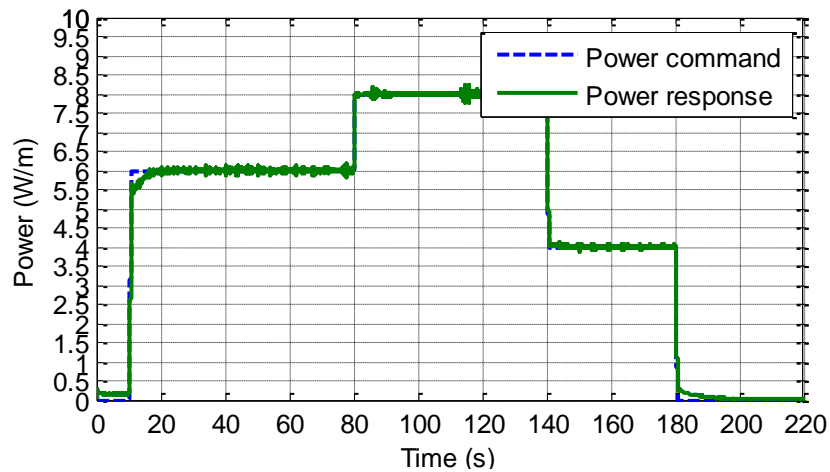


Figure 201. Power feedback control of the actuator with PI controller with feedforward loop ($K_p=100$, $K_i=49$, and $K=0.8$)

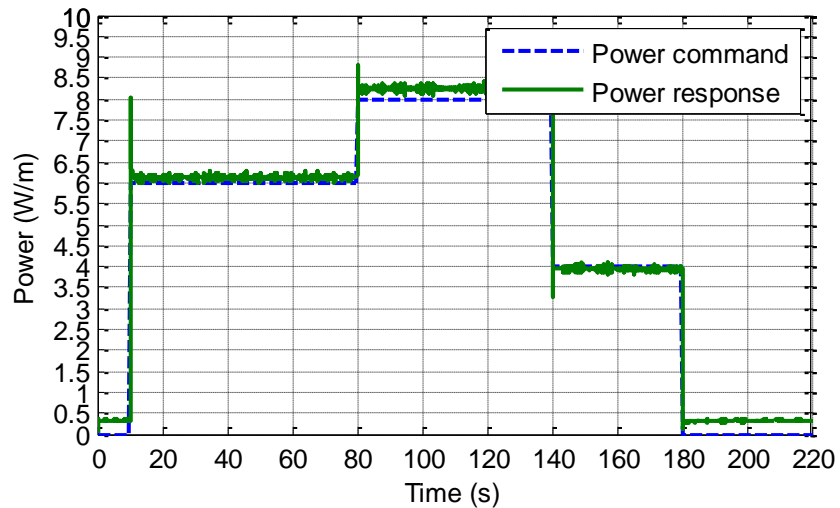


Figure 202. Power feedback control of the actuator with NN Narma-L2 controller

The steady state error observed in NN controller is due to the difference between loads in training data and in the application and errors observed on zero power commands is due to the minimum current limit of the controller (100 mA).

In the results satisfactory control performance can be observed using power as feedback.

As seen from the experiment results models developed for a single wire can be used in controlling the linear actuator designed. Displacement of the

actuator can be controlled using the sensor and strain feedback; however to control the displacement using only power or resistance feedback, thus eliminating the need for the external sensor, accurate models for power-strain and resistance-strain should be obtained.

CHAPTER 6

DISCUSSION AND CONCLUSION

6.1. Summary and Conclusions

In this dissertation, the use of shape memory alloy wires in actuators is considered. Actuators based on SMA have a high power to weight ratio and have found applications in many areas including micro mechatronics and light robotics.

Shape memory alloys are materials whose dimensions can be modified due to a temperature-dependent structural phase transition. This property can be used to generate motion or force in electromechanical devices and micro-machines. However, they have traditionally been used as “on-off” electromechanical actuators, mainly because of the difficulty in accurately controlling the martensite-austenite proportion due to the fact that the microscopic rearrangements involved in the structural changes take place quite sharply and in a highly complex and nonlinear fashion with the hysteresis appearing in the phase transition. One possible solution to this question would imply developing an accurate model for the material thermomechanical behavior, as it is made for other materials. Yet, there is no unique model to describe the behavior of the family of SMAs. The models vary greatly with composition, training, working conditions, etc. When the literature is surveyed for the models that can be implemented in control system design, only a few models, which are based on curve fit on experimental data, can be found. Hence, by this motivation, models based on the data of the selected wire for displacement, resistance and power consumption per unit length are developed. Although, strain and resistance are used as feedback variables and models can be found for them in literature, power consumption of the wire is a new internal feedback variable introduced in this study. For characterization purposes an electro-thermo-mechanical characterization set-up is built, with this set-up any wire can be trained and characterized.

In Chapter 3, the efforts on developing control strategies for SMA wires are discussed. In this context, PI type control, PI type control with feedforward loop, in which an inverse model is used in addition to enhance the response time characteristics of the controller, and Neural Network Narma-L2 controller which is a built-in block in Matlab® Simulink®, are implemented and simulations are run in computer environment using the developed models as plant of the control system.

Chapter 4 is about the experimental studies carried out using the modified characterization set-up and the control strategies developed. In this part of the dissertation, the SMA wire is controlled in a real time manner with the controllers designed for strain, resistance and power of the wire.

When the results for 140 MPa load are compared with the simulations the correlation between them can be seen in Figure 203, Figure 204, and Figure 205.

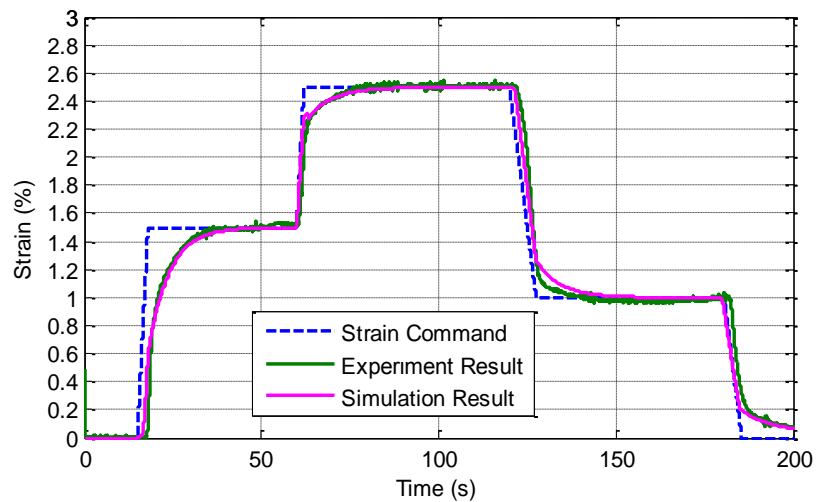


Figure 203. Strain feedback control simulation and experiment result, PI type control

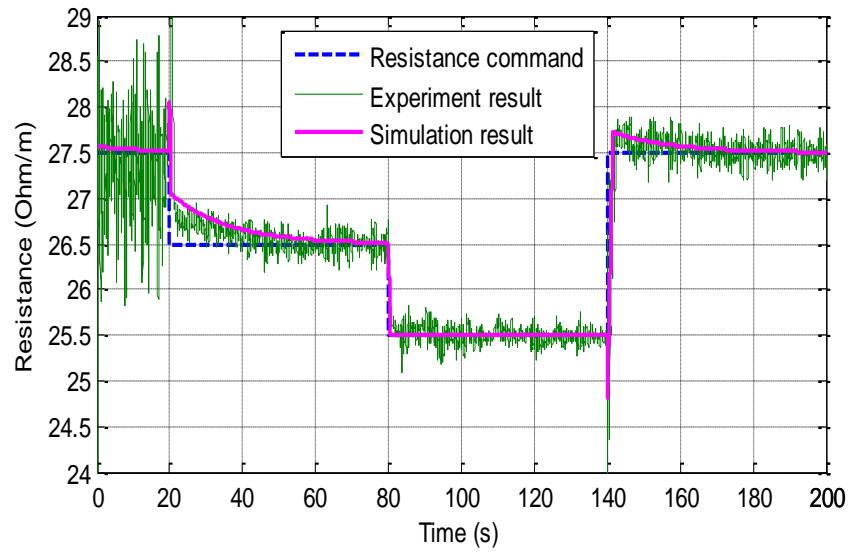


Figure 204. Resistance feedback control simulation and experiment result, PI type control with feedforward loop

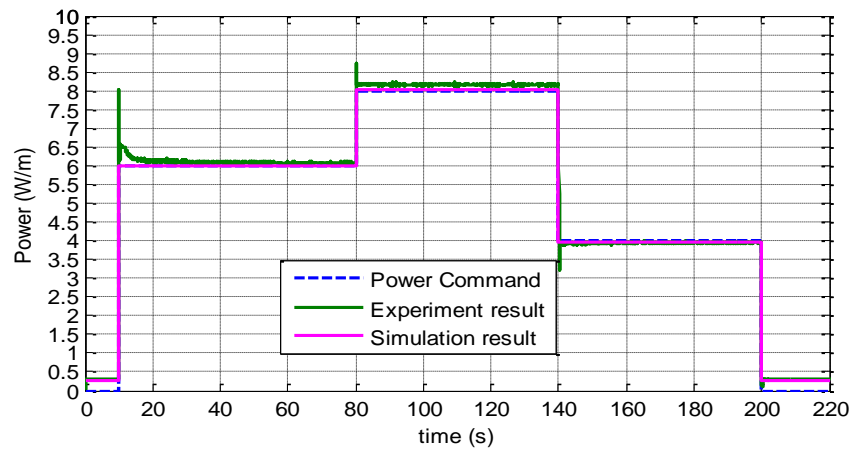


Figure 205. Power feedback control simulation and experiment result, NN controller

After experimental verification of control schemes on the wire, an actuator which can displace 1 kg of load 10 mm is designed in Chapter 5. In this design, two long SMA wires are used in parallel and pulley configuration to withstand the required load capacity and to achieve the desired stroke. Successful experiments are performed by implementing the previously developed control systems.

The power to weight ratio of the developed actuator is calculated as 0.6 W/gr of the actuating element, which takes place in the graph, presented previously, as given in Figure 206.

This linear SMA wire actuator is a case study for technology demonstration of use and control of SMA wires in actuators. In future, lessons learned during this study and outcomes of this work can guide to design and control of various SMA wire actuators employing different wires and requiring different load and stroke values.

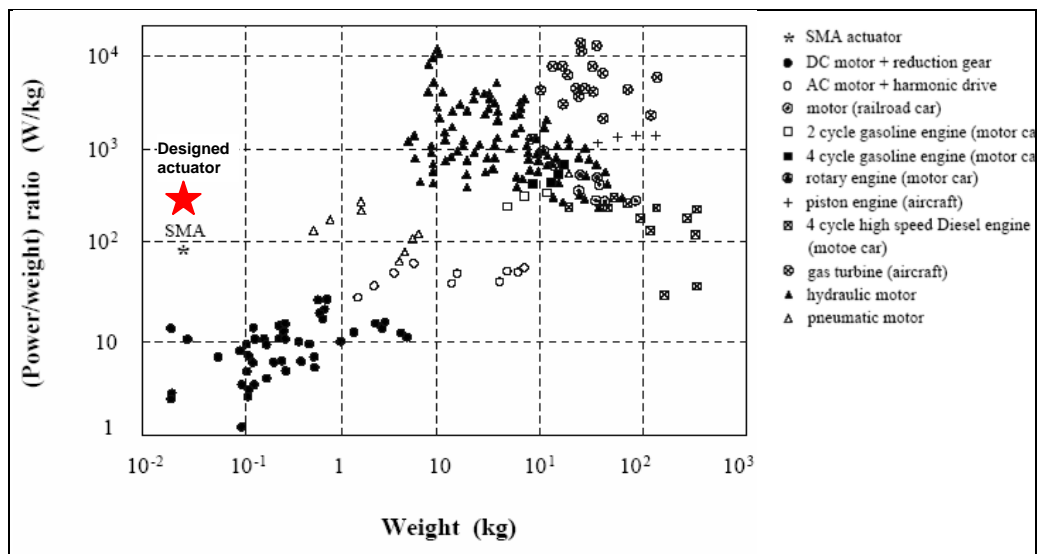


Figure 206. Power to weight ratios of common actuators

The following conclusions can be deduced from the study:

- Using current as the control variable necessitates the characterization of every diameter and composition of the wire to be used. If temperature were used as the control variable different diameters of the same composition wire could be used without the need for characterization. However, since accurate temperature measurement of thin wires is very challenging and not correct for most of the time, using temperature as the control variable would require the temperature control of the chamber or enclosed volume of the actuator in which the wire is working.
- Using length normalized feedback variables eliminates the need for re-characterization of different lengths of the same wire.

- Using dissipated power as an internal feedback variable gives better results than using resistance of the wire since the calculation of power does not amplify the noise in the data.
- Using power or resistance as self sensing feedback to control strain is useless unless accurate models for power-strain or resistance-strain are obtained under the specified working conditions.
- Strain feedback with an external sensor is the most suitable method to control the displacement if a robust performance of the actuator under different working conditions is expected.
- Among the controllers designed in this study PI type control with feedforward loop gives better result in sense of transient response (rise time and settling time). Neural network controller adopted is found to be very sensitive to the noise in the feedback data and produce steady state errors.
- In the feedback path, where very high noise effects are observed, more advanced filters such as Kalman filter would have been utilized. However, the filter used in this study is quite sufficient for systems operating in such low bandwidths.

6.2. Design Methodology for SMA Wire Actuators

The design methodology for SMA wire based actuators is different from regular actuator design in many ways. The steps of Ni-Ti wire actuator design can be outlined as follows.

- **Selection of Wire Diameter**

Considering the heating method and approximate load to be carried by the actuator a suitable wire diameter should be chosen. If the actuator is to be activated by Joule heating (passing current through the wire) respectively small diameters should be chosen to reduce activation energy and time. If the stress induced on the wire is very high, using the wires in bundle configurations or in parallel can be considered.

- **Material Characterization**

Once the wire to be used is selected, a characterization of the wire behavior should be carried out as explained in section 2.7.2., then the

relation between selected feedback variable (displacement, resistance, power) and control input (current, temperature) should be modeled. For generalization purposes, feedback variables should be in terms of unit length of the wire, so that any length of the same wire can easily be used without the need for new characterization. However, it should be noted that time response of the wire is not included in this characterization process.

- **Control System Design and Preliminary Simulations**

Control system should be designed considering a simplified wire model. At this stage, computer simulations are carried out to test the designed control system.

- **Actuator Design**

Key details of the actuator design that have to be decided include,

- The length of the wire to be used is decided by the stroke requirement and maximum recoverable strain of the wire.
- The number of the wires to be used in parallel is decided by the load capacity of the actuator. Recommended working stress of the wires is approximately 190-200 MPa, if the induced stress on a wire is greater than this value, wires should be used in parallel to prolong the actuator life.
- Electrical insulation is required if the wire is to be activated by Joule heating. The wire can be insulated from other metal components of the actuator either by covering it by insulating elements, or by coating the other metal surfaces with insulating layers. In the former case the insulator should be hard but flexible. In the latter case, only the contact points between the wire and other parts need to be insulated, however if possible wire contacting metal parts can be replaced with insulating materials. The insulators or the replaced metal parts should be able to stand high temperatures without softening and melting, to avoid the wire digs into the insulator at high temperature.

- Forced cooling options should be considered to increase bandwidth of the system, especially if the wires are actuated in a confined volume. Forced cooling can be achieved by forced air cooling, liquid immersion, heat sinks, Peltier devices, etc.
- In order to improve the performance of the actuator friction should also be considered. The surfaces that the wire works on can be chosen to be a low friction material. Also, the pulleys or shafts that are used in the design should be connected to the ground with bearings to reduce the friction.
- Suitable mechanical clamps or other type of connection should be designed to securely connect the wire to the ground and the end-effector.
- The initial condition of the wire such as pre-strain and pre-stress issues should be considered carefully.

6.3. Future Work

In the following studies, disturbances (ambient temperature, stress, etc.) and sensor noise can be modeled during the design of control schemes to increase accuracy of the simulations and robustness of the resulting system.

As another future work, the bandwidth of the actuator can be improved by increasing the rate of cooling. In this content, various active cooling methods can be explored, including forced air cooling, liquid cooling, heat sinks and even Peltier devices. Different actuator designs can be realized, using the multi-layer pulley concept. If only internal feedback variables, i.e. resistance and power, are used as feedback in the control system, sensors can be eliminated from the system, leading more compact actuators. In this dissertation wire is used as active element, if suitable characterization and modeling techniques are developed for different shape memory alloy elements, these elements can be utilized in various actuator designs.

REFERENCES

- [1] Wayman C.M., Duerig T.W., and Melton K.N., *An Introduction to Martensite and Shape Memory, Engineering Aspects of Shape Memory Alloys*. London: Butterworth-Heinemann, 1990.
- [2] Otsuka K., and Wayman C.M., Ed., *Shape Memory Materials*. London: Cambridge University Press, 1998, ISBN 0-521-44487-X.
- [3] Stoeckel D., “*The Shape Memory Effect- Phenomenon, Alloys and Applications*”, Proceedings of Shape Memory Alloys for Power Systems, pp. 1-13, 1996.
- [4] Funakubo H., *Shape Memory Alloys*. Glasgow, Bell and Bain Ltd, 1984.
- [5] Donmez B., “*The Use of Shape Memory Alloys in Aerospace Applications*”, Proceedings of AIAC-2007, Ankara, Turkey, 2007.
- [6] Duerig T.W., “*Applications of Shape Memory, Martensitic Transformations II*”, Materials Science Forum, Vols. 56-58, pp. 679-692, 1990.
- [7] Baz A. M., and Chen T., “*Active Control of the Lateral Buckling of Nitinol Reinforced Composite Beams*”, Proceedings of SPIE 2427: Active Materials and Adaptive Structures, pp. 34-48, 1995.
- [8] Kim S., “*Passive Control Techniques in Earthquake Engineering*”, Proceedings of SPIE 2445: Smart Structures and Materials, pp. 214-224, 1995.
- [9] Yoshida H., Ami N., and Nagai H., “*Development and Applications of TiNi Based Smart Structure*”, Proceedings of SPIE 4935: Smart Structures, Devices and Systems, pp. 63-69, 2002.
- [10] Turner T. L., Lach C.L., and Cano R.J., “*Fabrication and Characterization of SMA hybrid Composites*”, Proceedings of SPIE 4333: Smart Structures and Materials, pp. 343-355, 2001.
- [11] Han Y, Xing D., Xiao E., and Li A., “*Ni-Ti Wire Shape Memory Alloy Dampers to simultaneously Damp Tension, Compression, Torsion*”, Journal of Vibration and Control, Vol.11, pp. 1007-1022, 2005.

- [12] Khan M.M., Lagouda D.C., Mayes J.J., and Handerson B.K., "*Pseudoelastic Shape Memory Alloy Spring Elements for Passive Vibration Isolation*", Journal of Intelligent Material Systems and Structure, Vol. 15, No. 6, pp. 415-441, 2004.
- [13] Aiken I.D., Nims D.K., Whittaker A.S., and Kelly J.M., "*Testing of Passive Energy Dissipation Systems*", Earthquake Spectra, Vol. 9, No. 3, pp. 335-370, 1990.
- [14] Ikuta K., "*Micro/Miniature Shape Memory Alloy Actuator*", Proceedings of IEEE Conference on Robotics and Automation, Vol. 3, pp. 2156-2161, 1990.
- [15] Krishnan R.V. and Bhaumik S.K., "*Shape Memory Alloys: Properties and Engineering Applications*", Proceedings of SPIE 5062: Smart Materials, Structures and Systems, pp. 879-890, 2003.
- [16] Johnson A. D., "*State-of-the-Art of Shape Memory Actuators*", TiNi Alloy Company, San Leandro, CA, USA.
- [17] Donnellan Q. A. "*Design and Testing of Linear Shape Memory Alloy Actuator*", National Science Foundation, Summer 2005.
- [18] Bergamasco M., Salsedo F., and Dario P., "*A Linear SMA Motor as Direct-Drive Robotic Actuator*", Proceedings of IEEE Conference on Robotics and Automation, pp. 618-623, 1989.
- [19] Gorbet R.B., and Russel R.A., "*A Novel Differential Shape Memory Alloy Actuator for Position Control*", Robotica, Vol. 13, pp. 423-430, 1995.
- [20] Trasher M.A., Shahin A.R., Meckl P.H., and Jones J.D., "*Thermal Cycling of Shape Memory Alloy Wires Using Semiconductor Heat Pump Modules*", Proceedings of SPIE 1777: Smart Structures and Materials, pp. 271-280, 1992.
- [21] TiNi Aerospace Inc., <http://www.tiniaerospace.com>, last accessed on 12/09/2008.
- [22] Godard O.J., Lagoudas M. Z., and Lagoudas D. C., "*Design of Space Systems Using Shape Memory Alloys*", Proceedings of SPIE 5056: Smart Structures and Materials 2003, Smart Structures and Integrated Systems, 2003.

- [23] Fosness E., Maji A., Guerrero J., Carpenter B., and Tupper M., “*Development of Low Shock Deployment Devices for Aerospace Applications Using Shape Memory and Elastic Memory Materials*”, Proceedings of AIAA 2003-6246: Space 2003 Conference, 2003.
- [24] Lan X., Leng J., and Du S., “*Design of a Deployable Antenna Actuated by Shape Memory Alloy Hinge*”, Materials Science Forum, Vols. 546-549, pp. 1567-1570, 2007.
- [25] Shankar V., Dayananda G.N., et. al., “*Development of Electronic actuation system for Shape Memory Alloy based Aerospace Structures*”, Proceedings of SPIE 5062: Smart Materials, Structures, and Systems, 2003.
- [26] Manzo J., Garcia E., Wickenheiser A., and Horner G. C., “*Design of a Shape-Memory Alloy Actuated Macro-Scale Morphing Aircraft Mechanism*”, Proceedings of SPIE 5764: Smart Structures and Materials 2005, Smart Structures and Integrated Systems, 2005.
- [27] Kudva J.N., et. al., “*Overview of DARPA/AFRL/NASA Smart Wing Program*”, Proceedings of SPIE 3674: Conference on Industrial and Commercial Applications of Smart Structures, Technologies, pp 230-236, 1999.
- [28] eSMART, University of Alberta, <http://www.cs.ualberta.ca>, last accessed on 20/03/2008.
- [29] Song G., Ma N., Lee H., and Arnold S., “*Design and Control of a Proof-of-Concept Variable Area Exhaust Nozzle Using Shape Memory Alloy Actuators*”, Smart Materials and Structures, Vol.16, pp.1342-1347, 2007.
- [30] Eps J.J. and Chopra I., “*In-Flight Tracking of Helicopter Rotor Blades Using Shape Memory Alloy Actuators*”, Proceedings of AIAA- 99-1545: 40th AIAA Structural Dynamics and Materials Conference and Adaptive Structures Forum, 1999.
- [31] Şehitoğlu H., Gall K., and Chumalakov Y., “*Ni-Ti Experiments versus Modeling: Where do we stand?*”, Proceedings of SPIE 3992: Smart Structures and Materials, 2000.
- [32] M. Brocca, L. C. Brinson, and Z. P. Bazant, “*Three Dimensional Constitutive Model for Shape Memory Alloys Based on Microplane Model*”, J. Mech. Phys. Solids, 1999.

- [33] Funakubo H., *Shape Memory Alloys*, Glasgow, UK, Bell and Bain Ltd, 1984.
- [34] Bertram A., “*Thermo-Mechanical Constitutive Equations for The Description Of Shape Memory Effect In Alloys*”, Nuclear Engineering and Design, Vol. 74, pp. 173-182, 1982.
- [35] Wayman C.M., “*Shape Memory and Related Phenomena*”, Progress in Material Science, Vol.36, pp. 203-224, 1992.
- [36] Ho E., “*Linear Macro-Micro Positioning System Using a Shape Memory Alloy Actuator*”, University of Waterloo, 2004.
- [37] Brinson L. C., “*One-Dimensional Constitutive Behavior of Shape Memory Alloys: Thermomechanical Derivation with Non-Constant material Functions and Redefined Martensite Internal Variable*”, Journal of Intelligent Material Systems and Structures, Vol. 4, pp. 229-242, 1993.
- [38] Nascimento M. and Araújo C., “*Electro-Thermomechanical Characterization of Ti-Ni Shape Memory Alloy Thin Wires*”, Materials Research, Vol. 9, No. 1, pp. 15-19, 2006.
- [39] Huang W., “*On The Selection of Shape Memory Alloys for Actuators*”, Materials and Design, Vol. 23, pp. 11-19, 2002.
- [40] Smith S. A. et al., “*Shape Setting Nitinol*”, Proceedings of ASM International Conference on the Materials and Processes for Medical Devices, pp. 266-270, 2003.
- [41] Morgan N. B. and Broadley M., “*Taking the Art Out of Smart!—Forming Processes and Durability Issues for the Application of Ni-Ti Shape Memory Alloys in Medical Devices*”, Proceedings of ASM International Conference on the Materials and Processes for Medical Devices, pp. 247-252, 2003.
- [42] Reynearts D. and Brussels H., “*Design Aspects of Shape Memory Actuators*”, Mechatronics, Vol. 8, pp. 635-656, 1997.
- [43] Gilbertson RB., *Muscle Wires Project Book*, San Rafael, CA (USA): Mondo-Tronics Inc., 2000.
- [44] Paiva A., and Savi M.A., “*An Overview Of Constitutive Models For Shape Memory Alloys*”, Mathematical Problems in Engineering, Hindawi Publishing Corporation, Article ID 56876, pp. 1–30, 2006.

- [45] DeGiorgia V. G., and Salemb H., "A comparison of a few shape memory alloy constitutive models", Proceedings of SPIE 3667: Conference on Mathematics and Control in Smart Structures, 1999.
- [46] De la Flor S., Urbina C. and Ferrando F., "Constitutive Model of Shape Memory Alloys: Theoretical Formulation and Experimental Validation", Materials Science and Engineering A, Vol. 427, pp. 112-122, 2006.
- [47] Epps J.J. and Chopra I., "Comparative Evaluation of Shape Memory Alloy Constitutive Models with Test Data", Proceedings of AIAA-97-1194, pp. 1425-1437, 1997.
- [48] Prahland H., and Chopra I., "Comparative Evaluation of Shape Memory Constitutive Models with Experimental Data", Journal of Intelligent Material Systems and Structures, Vol. 12, pp. 383-395, 2001.
- [49] Liand C. and Rogers C.A., "One-Dimensional Thermomechanical Constitutive Relations for Shape Memory Materials", Journal of Intelligent Material Systems and Structures, Vol. 1, pp. 207-234, 1990.
- [50] Liand C. and Rogers C.A., "A Multi-dimensional Constitutive Model for Shape Memory Alloys", Journal of Engineering Mathematics, Vol. 26, pp. 429-443, 1992.
- [51] Brinson L.C. and Huang M.S., "Simplifications and Comparisons of Shape Memory Alloy Constitutive Models", Journal of Intelligent Material Systems and Structures, Vol. 7, pp. 108-114, 1996.
- [52] Kamath G.M., Dayananda G.N. and Senthilpriya R., "A Modified Thermo-Mechanical Modeling Approach for Shape Memory Alloy Behavior", Proceedings of SPIE 0277: Smart Materials, Structures and Systems, 2003.
- [53] Pons J.L., *Emerging Actuator Technologies: A Micromechatronic Approach*, Chichester, England; Hoboken, NJ, Wiley, 2005.
- [54] Prahland H., Chopra I., "Experimental Characterization of Ni-Ti Shape Memory Alloy Wires Under Complex Loading Conditions", Proceedings of SPIE 3668: Conference on Smart Structures and Integrated Systems, 1999.
- [55] Ikuta K., "Micro/Miniature Shape Memory Alloy Actuator", IEEE CH2876-1/90/000, 1990.

- [56] Tanaka Y. and Yamada A., "A Rotary Actuator Using Shape Memory Alloy for a Robot-Analysis of the Response with Load", Proceedings of IROS'91, IEEE/RSJ Intelligence for Mechanical Systems, 1991.
- [57] Pons J.L., Reynaerts D., Peirs J., Ceres R., and VanBrussel H., "Comparison of Different Control Approaches to Drive SMA Actuators", ICAR'97, 1997.
- [58] Troisfontaine N., Bidaud Ph., and Dario P., "Control Experiments on Two SMA Based Micro-Actuators", Proceedings of 5th International Symposium on Experimental Robotics, 1997.
- [59] Van der Wijst M. W. M., Schreurs P. J. G., and Veldpaus F.E., "Application of Computed Phase Transformation Power to Control SMA Actuators", Smart Materials and Structures, IOP, Vol. 6, 1997.
- [60] Asua E., Etxebarria V., and Garcia-Arribas A., "Micropositioning Control Using Shape Memory Alloys", Proceedings of IEEE International Conference on Control Applications, 2006.
- [61] Ma N., Song G., and Lee H.J., "Position Control of SMA Actuators With Internal Electrical Resistance Feedback", Proceedings of SPIE 5049: Smart Structures and Materials 2003: Modeling, Signal Processing, and Control, 2003.
- [62] Kumagai A. Liu T., and Hozian P., "Control of Shape Memory Alloy Actuators with A Neuro-Fuzzy Feedforward Model Element", Journal of Intelligent Manufacturing, Vol. 17, 2006.
- [63] Lei K. and Yam Y. "Modeling and Experimentation of a Positioning System of SMA Wires", Proceedings of SPIE 3986: Smart Structures and Materials 2000: Sensory Phenomena and Measurement Instrumentation for Smart Structures and Materials, 2000.
- [64] Song G., Chaudhry V., and Batur C., "Precision Tracking Control Precision Tracking Control Of Shape Memory Alloy Actuators Using Neural Networks and a Sliding-Mode Based Robust Controller", Smart Materials and Structures, IOP, Vol. 12, 2003.
- [65] Lu A., Grant D., and Hayward V., "Design and Comparison of High Strain Shape Memory Alloy Actuators", Proceedings of IEEE International Conference on Robotics and Automation, 1997.

- [66] Kuo B., *Automatic Control Systems*, Prentice-Hall Inc., 1995.
- [67] Erickson R.W., *Filter Circuits*, ECEN2260, 1997.
- [68] Matlab, *Neural Network Toolbox, Narma L2 Controller*, The Mathworks Inc., 2007.
- [69] Hagan, M.T., O. De Jesus, and R. Schultz, *Training Recurrent Networks for Filtering and Control*, L. Medsker and L.C. Jain, Eds., CRC Press, pp. 311-340, 1999.
- [70] Narendra K.S. and S. Mukhopadhyay, "Adaptive Control Using Neural Networks and Approximate Models", *IEEE Transactions on Neural Networks*, Vol. 1, pp. 4-27, 1990.

APPENDIX A

POLYNOMIALS THAT CAN BE USED IN POLE PLACEMENT¹

The pole placement technique is one of the methods used in the design of control systems. Basically, it is based on the placement of the poles of a closed loop system to the desired locations on the left-hand side of the complex plane. This way, it is guaranteed for the closed loop control system to be stable. Especially when the number of the controller parameters to be determined is equal to the order of the closed loop system, i.e., the highest power of the characteristic polynomial, the pole placement is a very powerful technique.

In the pole placement, the poles can be located according to certain patterns defined by some polynomials. Among them, the Butterworth and Chebyshev polynomials are the most popular ones. Using these polynomials, the poles that make the closed loop system stable can be put on the left-hand-side of the complex plane so as to set the bandwidth of the closed system (ω_c) as well. The expressions for the polynomials in terms of the Laplace operator “s” are given in Table A. 1 and Table A. 2 up to the fourth-order.

¹ Erickson, R.W., “*Filter Circuits*”, ECEN 2260, 2001

Table A. 1. Butterworth Polynomials

Order	Polynomial
1	$1 + \frac{s}{\omega_c}$
2	$1 + \sqrt{2} \frac{s}{\omega_c} + \left(\frac{s}{\omega_c}\right)^2$
3	$\left(1 + \frac{s}{\omega_c}\right) \left(1 + \frac{s}{\omega_c} + \left(\frac{s}{\omega_c}\right)^2\right)$
4	$\left(1 + 0.7654 \frac{s}{\omega_c} + \left(\frac{s}{\omega_c}\right)^2\right) \left(1 + 1.848 \frac{s}{\omega_c} + \left(\frac{s}{\omega_c}\right)^2\right)$

Table A. 2. Chebyshev Polynomials

Order	Polynomial
1	$1 + \frac{s}{\omega_c}$
2	$\sqrt{2} \left(1 + 0.7654 \left(\frac{s}{0.8409 \omega_c}\right) + \left(\frac{s}{0.8409 \omega_c}\right)^2\right)$
3	$\left(1 + \left(\frac{s}{0.2980 \omega_c}\right)\right) \left(1 + 0.3254 \left(\frac{s}{0.9159 \omega_c}\right) + \left(\frac{s}{0.9159 \omega_c}\right)^2\right)$
4	$\sqrt{2} \left(1 + 0.1789 \left(\frac{s}{0.9502 \omega_c}\right) + \left(\frac{s}{0.9502 \omega_c}\right)^2\right) \cdot \left(1 + 0.9276 \left(\frac{s}{0.4425 \omega_c}\right) + \left(\frac{s}{0.4425 \omega_c}\right)^2\right)$

When these two types of polynomials are compared, it can be seen that a Butterworth polynomial of some degree leads to a flatter response than the

Chebyshev polynomial of the same degree. It means that the magnitude curve remains almost constant at zero dB up to the corner frequency, i.e., desired bandwidth value, in the Bode magnitude diagram as shown in Figure A. 1. In this figure, the vertical axis represents the magnitude of the output to input ratio in terms of dB.

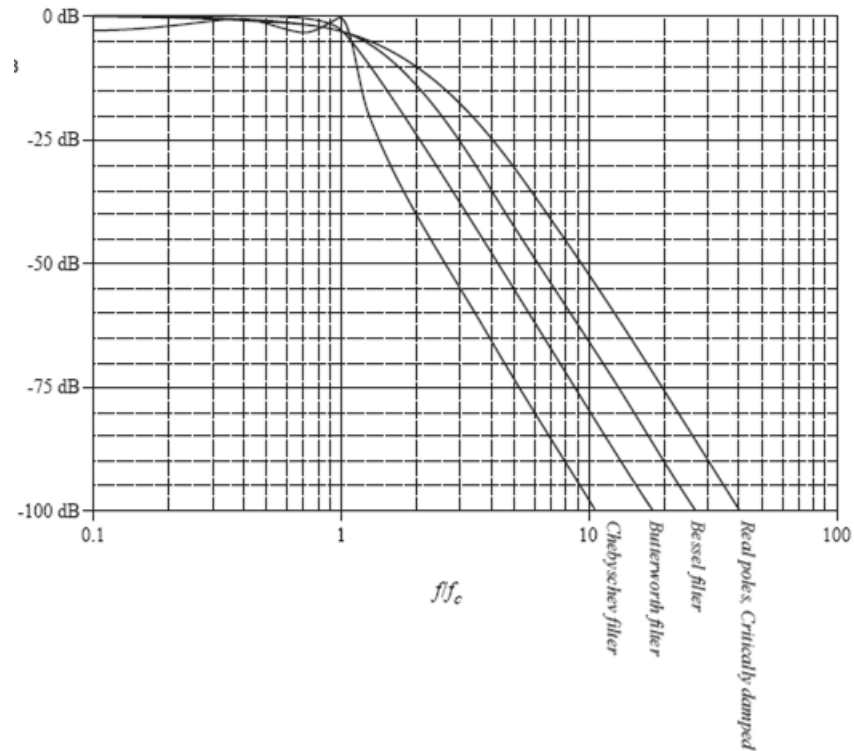


Figure A. 1. Comparison of certain fourth order polynomials [67]

Moreover, the Butterworth polynomial allows the designer to place poles on a semi-circle with the radius of ω_c that makes the poles far away to the left-hand-side of the complex plane from the pole locations proposed by the ellipse of the Chebyshev polynomial. The example pole locations proposed by the fourth-order Butterworth and Chebyshev polynomials are shown in Figure A. 2.

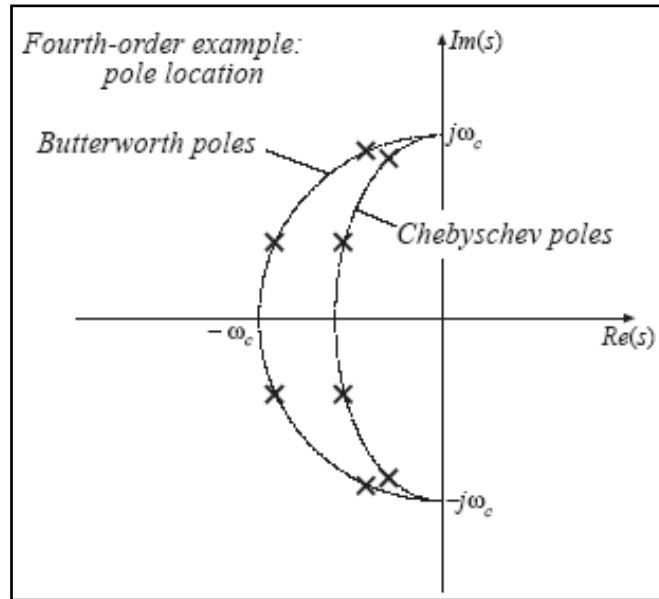


Figure A. 2. Pole locations proposed by the fourth-order Butterworth and Chebyshev polynomials [67]

CURRICULUM VITAE

PERSONAL INFORMATION

Surname, Name : DÖNMEZ (SÖYLEMEZ), Burcu
Place of birth : Ankara - TÜRKİYE
Nationality : Turkish
Work address : TÜBİTAK-SAGE
Turkish Scientific & Technical Research Council
Defense Industries Research & Development Institute
P.K. 16, 06261 Mamak ANKARA / TÜRKİYE
Phone : +90 (312) 590 91 27
Fax : +90 (312) 590 91 48-49
E-mail : bdonmez@sage.tubitak.gov.tr
Marital status : Married

EDUCATION

School	Years	Diploma, Subject and Grade
METU, Department of Mechanical Engineering, Ankara, TÜRKİYE	2004-2009	PhD., "Design and Analysis of a Linear Shape Memory Alloy Actuator", 3.72/4.00.
METU, Department of Mechanical Engineering, Ankara, TÜRKİYE	1999-2002	MSc., "An Investigation on the Gait Analysis Protocol of the 'KISS' Motion Analysis System", 3.64/4.00.
METU, Department of Mechanical Engineering, Ankara, TÜRKİYE	1995-1999	BSc., High Honor, 3.65/4.00
T.E.D Ankara Koleji Özel Lisesi, Ankara, TÜRKİYE	1992 - 1995	High Honor Student

LANGUAGE SKILLS

English: Advance Level

German: Beginner Level

WORK EXPERIENCE

<i>Organization</i>	<i>Years</i>	<i>Enrollment</i>
<i>TÜBİTAK-SAGE, Weapon Systems Group / Mechatronics Division, Ankara, TÜRKİYE</i>	<i>Sept. 2008-....</i>	Chief Research Engineer
<i>TÜBİTAK-SAGE, Weapon Systems Group / Mechatronics Division, Ankara, TÜRKİYE</i>	<i>May 2004- Sept.2008</i>	Senior Research Engineer
<i>TÜBİTAK-SAGE, Weapon Systems Group / Mechatronics Division, Ankara, TÜRKİYE</i>	<i>Sept. 2002 - May 2004</i>	Research Engineer
<i>METU, Department of Mechanical Engineering, Ankara, TÜRKİYE</i>	<i>Sept. 1999 – Sept 2002</i>	Research Assistant
<i>Babcock & Wilcox – GAMA Ankara, TÜRKİYE</i>	<i>June-July 1998</i>	Intern Engineering Student
<i>Türk Traktör Fabrikası Ankara, TÜRKİYE</i>	<i>June-July 1997</i>	Intern Engineering Student

PUBLICATIONS

1. Dönmez B., Özkan B., and Kadiođlu S., “*Şekil Bellekli Alaşımli Tellerle Hassas Konum Kontrolü*”, TOK'2008 Otomatik Kontrol Ulusal Toplantısı, İstanbul, Türkiye, November 2008.
2. Özkan B., Yıldız E.N., and Dönmez B., “*Precise Position Control of a Gimbaled Camera System*”, AIAA-GNC 2008, Honolulu, U.S.A., August 2008.
3. Dönmez B. and Kadiođlu S., “*Şekil Bellekli Alaşımli Teller için Elektro-Termo-Mekanik Karakterizasyon Cihazı*”, SAVTEK 2008, Ankara, Türkiye, June 2008.
4. Dönmez B., “*The Use of Shape Memory Alloys in Aerospace Applications*”, AIAC 2007, Ankara, Türkiye, September 2007.